Final Technical/Scientific Report

DOE Award No.: DE-FE0031637

Integrated Computational Materials and Mechanical Modeling for Additive Manufacturing of Alloys with Graded Structure Used in Fossil Fuel Power Plants

Proposal ID: FP00001427
Sponsor-Assigned Award/Protocol No: DE-FE0031637
University of Pittsburgh Institution No: 0061811
University of Pittsburgh DUNS No.: 004514360
Project/ Grant Period: November 1, 2018 – October 31, 2021
(with 1 year non-cost extension)

TECHNICAL POINT OF CONTACT

PI: **Dr. Wei Xiong**
Department of Mechanical Engineering and Materials Science
University of Pittsburgh
3700 O'Hara Street
Pittsburgh, PA 15261
Telephone: (412) 383-8092
Fax: (412) 624-4846
Email: weixiong@pitt.edu

BUSINESS POINT OF CONTACT

Dr. Jennifer E. Woodward
University of Pittsburgh
Office for Sponsored Research
123 University Place
Pittsburgh, PA 15213-2303
Telephone: (412) 624-7408
Fax: (412) 624-7409
Email: jew7@pitt.edu

SUBMITTED TO

National Energy Technology Laboratory
U.S. Department of Energy

Team: University of Pittsburgh & RaytheonTechnologies Research Center

University of Pittsburgh
Address: 3700 O'Hara Street
Pittsburgh, PA 15261

Raytheon Technologies
Address: 411 Silver Lane,
East Hartford, CT 06108

Report Submission Date: January 29, 2022

DISCLAIMER

ABSTRACT

Wire-arc additive manufacturing (WAAM) has demonstrated its unique capability of producing large-size alloy components with a significantly reduced fabrication time and enhanced geometry design freedom. In this project, the team has developed an ICME (Integrated Computational Materials Engineering) modeling framework, which supports the WAAM of the AUSC (Advanced Ultra-Supercritical) power plant components. The manufacturing design has been applied to Inconel 740H, steel P91, as well as the dissimilar alloy components between steel P91 and Inconel 740H.

The ICME model framework is developed by considering two types of modeling. First, mechanistic modeling has been applied to control the printing quality and understand the sequence of the dissimilar printing of the wall structure. The following models have been included in the developed ICME framework: finite element thermal model, grain structure model, residual stress simulation, crystal plasticity model, CALPHAD-based precipitation kinetic model, phase stability prediction, thermal expansion predictive model, and heuristic creep model. Secondary, a physics-based machine learning model has also been developed based on the ICME model structure. The machine learning model development is based on the ICME model prediction with calibration of the experiments. In addition, the WAAM has been utilized as a high-throughput experimental tool rapidly generating a gradient of alloy composition to facilitate experimental database generation for process-structure-property relationships. Such a database directly supported the ICME-enhanced machine learning, which further assisted in intermediate composition block design between P91 and 740H. A high-throughput screening study of the oxidation resistance has been performed based on such high-throughput experimentation.

Based on the computational design, several dissimilar alloy manufacturing with post-heat treatment have been performed with a comprehensive evaluation of mechanical performance, including hardness mapping, yield strength, creep resistance.

In this project, the single component of P91 and 740H processed by WAAM after heat treatment designed by ICME has demonstrated higher performance in yield strength and creep resistance than the wrought materials. The P91 sample prepared by WAAM with ICME-designed heat treatment performs better than P92 in creep resistance. The designed graded alloy printing with intermediate block shows a promising performance that exceeds the traditional welding. Moreover, the current research indicates the high need for location-specific design analysis with uncertainty quantification, an important topic that deserves more dedicated research.

The achievement of this project demonstrated the promising future of WAAM in structural alloy manufacturing for energy power plant development. Successful printing requires synergetic efforts made by manufacturing, mechanical, and materials sciences.

TABLE OF CONTENTS

LIST OF FIGURES

LIST OF TABLES

1. EXECUTIVE SUMMARY

The goal of this research is to support development of an innovative ICME (Integrated Computational Materials Engineering) modeling framework, via integration of materials and mechanical models for additive manufacturing (AM) of the AUSC (Advanced Ultra-Supercritical) power plant components. This aims to enable the design of functionally graded microstructure and properties, demonstrated via a multi wire feed AM method. Fabrication of wire-AM samples serves to enable calibration and validation of the modeling effort, while providing a path for production of optimized multi-material builds. Wire-arc additive manufacturing (WAAM) process provides a large, open platform AM and welding environment suited to material and process development. Two commercial alloys that are currently utilized in power plants namely, P91 steel and 740H superalloy were chosen for the multi-material manufacturing investigation. Single builds of these two alloys were initially characterized and an effective post-heat treatment was also designed using both simulations and experiments. Concomitantly, several modeling efforts such as grain texture prediction, thermomechanical, thermal and residual stress modeling as well as the process-structure-property relationship were undertaken since it will be beneficial in the design of graded alloys.

As a first step for multi-material manufacturing, the optimum sequence in which the materials have to be deposited one over the other (P91 on 740H or 740H on P91) was determined. Moreover, thermomechanical modeling was performed for the two deposition strategies to understand the stress distribution. Parallelly, CALPHAD (Calculation of phase diagrams)-based ICME modeling was performed to determine 3 different candidate graded alloy compositions, amongst the mixed compositions between P91 steel and 740H superalloy to act as interlayer between the constituent materials. The three computationally designed interlayer builds were characterized, and an optimum post-heat treatment was identified. From the post-heat treatment efforts, the suitable candidate material that could be further tested for understanding the creep properties was identified. In addition, a stepwise gradient sandwiched between the constituent materials was also utilized for performing high-throughput experiments which will serve as useful inputs for further alloy design efforts aided by machine learning. The optimum composition with high hardness and other related properties was identified using genetic algorithm. Besides, an alloy composition that can potentially exhibit high entropy effect was also identified using thermodynamic calculations. These two designed compositions were fabricated using WAAM. The build pertaining to the composition identified by data driven design was successful and hence, it was further characterized to determine the required properties. However, the composition designed exhibit high entropy effect exhibited location-specific solidification cracking and hence, it was correlated by computing the solidification cracking susceptibility using well established models.

As a final step, the computationally designed interlayer composition which was identified for further performance evaluation was tested for its creep and oxidation resistance. For comparison, the creep properties of the pure alloys and the deposits without interlayer as well as the oxidation resistance of pure alloys were also determined. In addition, an interlocking design for joining the P91 steel with 740H superalloy was identified using topology optimization. Further, the designed joint was fabricated using WAAM and its mechanical performance was evaluated along with further calibration.

2. GOALS OF THE PROJECT

In this project, Pitt (University of Pittsburgh) and RTRC (Raytheon Technologies Research Center) work together to develop an Integrated Computational Materials and Mechanical Engineering (ICME: integrated computational materials engineering) framework for WAAM (wire arc additive manufacturing). The ICME model framework will be calibrated using microstructure and mechanical characterization. The primary goal of the research is to establish an ICME simulation framework for AM process in order to design and guide the build of alloys with graded structure for AUSC steam components. Therefore, new process-structure and structure-property models will be developed for the graded alloys, which will be verified by supporting experiments. The research goals according to the statement of project objectives (SOPO) are as follows:

- Develop and improve ICME models for the WAAM technique to understand process-structure-property relationships
- ICME design modeling of graded alloys with gradient composition profile
- Topology optimization for alloys with graded structure with specific geometries used in the AUSC steam component
- Perform uncertainty analysis for ICME model-prediction and design allowables

3. ACCOMPLISHMENTS

The road map used for the design of graded alloys using WAAM which can potentially be employed as an A-USC power plant component by integrating mechanical and materials modeling is summarized in Fig. 1. In this report, the accomplishments reached throughout the project period will be detailed followed by a brief summary comprising the milestones achieved for each task listed above.

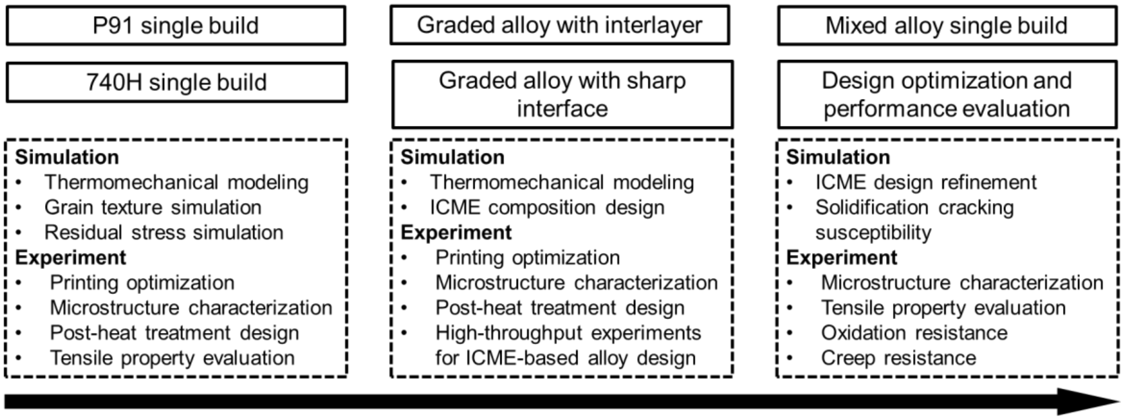

Figure 1. The design roadmap used development of new graded alloys using WAAM with improved performance.

This report is structured based on the design strategies that the team uses for development of the dissimilar alloy component printing using the WAAM processes. In the beginning of the project, the team focused on developing both printing and heat treatment recipes of the successful wall shape P91 and 740H samples. As shown on the left column of Fig. 1. Experimental designs have been performed to ensure the success of single build of P91 and 740H samples. In addition, the the mechanical simulation has been performed to guide the understanding of thermal history influences on structure-property relationships.

After successfully printed the single build of individual P91 and 740H samples with designed post-heat treatment, the ICME modeling has been further applied to support the experimental study of graded alloy printing between P91 steel and 740H superalloy. Before designing the interface printing, the combined simulation and experiments identified the best printing sequence. P91 is printed as the bottom structure on the P91 substrate to avoid cracking by comparing with the choice that using the 740H as the bottom part with P91 building on the top. Therefore, the consequent printing designs are all following the printing sequence from P91 as the initial printing from bottom to the 740H on the top. Particularly, the ICME design was focused on design a graded composition interlayer between the P91 and 740H single alloy blocks. By comparison, the sharp interface by naturally deposit 740H on top of P91 without composition control of the interface between these two alloys are also studied. During the topology design optimization, the team introduced an interlock geometry for the interface to evaluate the strength improvement.

In order to evaluate the best design of dissimilar alloy component, significant efforts have been made to optimize the phase transformation during heat treatment and its influence on materials performance including oxidation, tensile strength and creep resistance. The heterogeneity has been observed in the tensile bar tests indicate the requirement of location specific design, which require more design efforts in the future.

3.1 Material Selection

The team surveyed available materials in search of suitable feedstock materials for the WAAM process, targeting a range of AUSC relevant alloys. WAAM utilizes spooled wire, typically in the range of 0.030 to 0.062 inch (0.75 to 1.6 mm) diameter. Continuous spooled wire is required, unlike manual gas tungsten arc welding (GTAW) which can operate with cut sections of wire or rod feedstock. The WAAM platform utilizes a wire feeder which is programmed to deposit material along a robotic toolpath. For nickel-based alloys, Inconel 740H material was selected and determined that a single vendor has this material available: Special Metals Welding Products Company (Newton, NC). Two spools of wire were procured to support the current project. Special Metals has published guidelines [1] for welding of 740H, which will be referenced as a guideline for selection of WAAM process conditions. Standard chemistry/composition for this material is shown in Fig. 2, along with the actual composition of the feedstock wire received and used in the current effort.

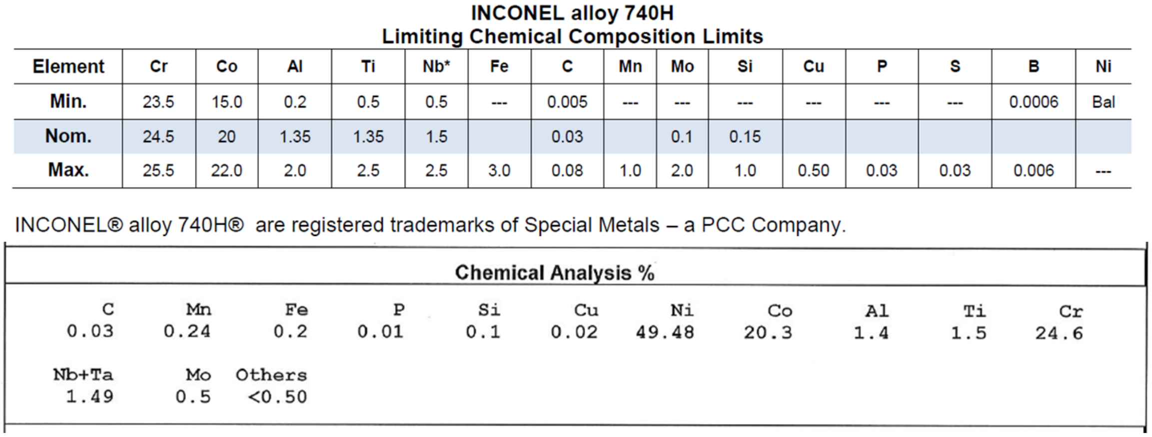

INCONEL alloy 740H
Limiting Chemical Composition Limits

Element	Cr	Co	Al	Ti	Nb*	Fe	C	Mn	Mo	Si	Cu	P	S	B	Ni
Min.	23.5	15.0	0.2	0.5	0.5	---	0.005	---	---	---	---	---	---	0.0006	Bal
Nom.	24.5	20	1.35	1.35	1.5		0.03		0.1	0.15					
Max.	25.5	22.0	2.0	2.5	2.5	3.0	0.08	1.0	2.0	1.0	0.50	0.03	0.03	0.006	---

INCONEL® alloy 740H® are registered trademarks of Special Metals – a PCC Company.

Chemical Analysis %

C	Mn	Fe	P	Si	Cu	Ni	Co	Al	Ti	Cr
0.03	0.24	0.2	0.01	0.1	0.02	49.48	20.3	1.4	1.5	24.6

Nb+Ta	Mo	Others
1.49	0.5	<0.50

Figure 2. Wire composition used for Inconel 740H superalloy in this study.

For creep resistant steel/stainless, the P92/P91 family was identified. During the survey of materials and suitable suppliers, it was determined that few vendors produce P92 steel in spooled-wire form suitable as feedstock for WAAM. It was suggested that current P92 wire material does not have the required cleanliness for WAAM, and frequently contains added deoxiders (e.g, silicon) which are included to improve GMAW/MIG welding operations. The added deoxiders have a tendency to degrade creep performance, and negatively impact deposit quality during the WAAM process. As such, it was suggested to focus on the more common P91 (i.e., ER90S-B91) steel which can be sourced in a high-cleanliness condition suited to WAAM. The differences in alloy composition between P92 and P91 are minimal, and the developed ICME tools aim to be flexible to accommodate future changes in alloy selection. Therefore, the framework/ICME methods remain relevant. EuroWeld Ltd. (Mooresville, NC) was identified as a source, and two spools of P91 wire were procured. The AWS classification for this wire is ER90S-B91. The material test report was retrieved from the vendor, which will provide composition to support the modelling effort, and is shown in Fig. 3, with the composition for the wire lot used in the current effort.

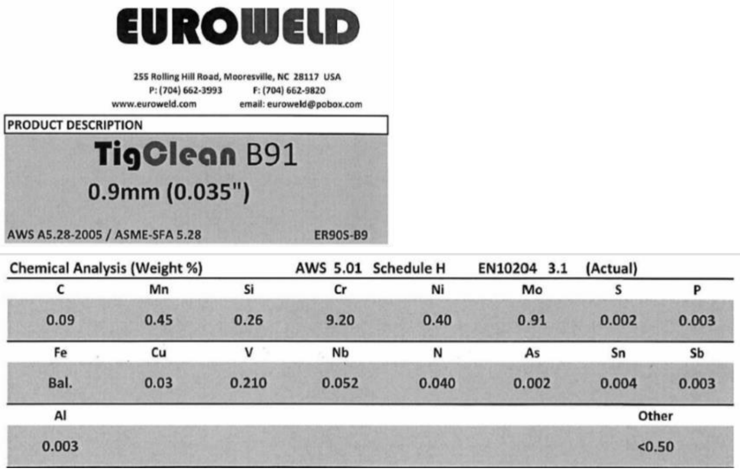

EUROWELD

255 Rolling Hill Road, Mooresville, NC 28117 USA
P: (704) 662-3993 F: (704) 662-9820
www.euroweld.com email: euroweld@pobox.com

PRODUCT DESCRIPTION

TigClean B91
0.9mm (0.035")
AWS A5.28-2005 / ASME-SFA 5.28 ER90S-B9

Chemical Analysis (Weight %) AWS 5.01 Schedule H EN10204 3.1 (Actual)

C	Mn	Si	Cr	Ni	Mo	S	P
0.09	0.45	0.26	9.20	0.40	0.91	0.002	0.003
Fe	Cu	V	Nb	N	As	Sn	Sb
Bal.	0.03	0.210	0.052	0.040	0.002	0.004	0.003
Al						Other	
0.003						<0.50	

Figure 3. Wire composition used for P91 steel in this study.

A preliminary literature survey for both alloys indicated preferred preheat conditions, interpass temperatures, and general welding process conditions. Preheat, along with specified inter-pass temperatures are recommended for the P91 material [2], the conditions which help to guide the ICME approach to process condition selection. Post-weld heat treatments are also indicated, providing methods for tailoring the material properties. Conversely, the literature recommendations for 740H included limited inter-pass temperatures [1], thereby recommending a cool-down between subsequent layers of the WAAM process. In general, the literature notes IN740H benefits from interpass temperatures below 175°C, while P91 benefits from interpass temperatures in the range of 200°C to 300°C.

3.2 Experimental investigation of single build P91 steel and Inconel 740H superalloy

In this project, RTRC has built several long vertical samples with different building parameters as the starting point to identify the best possible printing parameters which will be suitable for multi-material manufacturing using WAAM. For mechanical property evaluation for the WAAM deposited IN740H and P91 materials, deposition parameters were developed for fabrication of bulk deposits of greater size and cross-section, necessary for extracting a range of test coupon geometries. In order to remain relevant to the previously demonstrated processing conditions, the deposits relied on the same energy/power, travel speed, and wire feed rates. However, in order to generate a thicker cross section, a square raster/fill pattern was employed. This is commonly utilized in AM, often referred to as a square raster or "lawnmower" type fill pattern, shown schematically in Fig. 4. For the WAAM coupons, the build does not utilize of an outside perimeter/contour path, which is more common in powder deposition and powder bed AM methods. Alternating layers have mirror images of the fill pattern.

Table 1: Building parameters of 740H superalloy and P91 steel using WAAM

Layer	***Voltage (V)***	***Current (A)***	***Travel speed (mm/s)***	***Wire feed (m/min)***	***Hatch spacing (mm)***
			G10 (Inconel 740H)		
Layer 1	*20.9*	*220*	*3.5*	*2.5*	*3*
Layer 2	*20.9*	*200*	*4*	*2.5*	*3*
Layer 3-25	*20.9*	*158*	*5*	*2.5*	*3*
			G9 (P91 steel)		
Layer 1	*20.9*	*220*	*3.5*	*2.75*	*3*
Layer 2	*20.9*	*200*	*4*	*2.75*	*3*
Layer 3-25	*20.9*	*158*	*5*	*3.10*	*3*

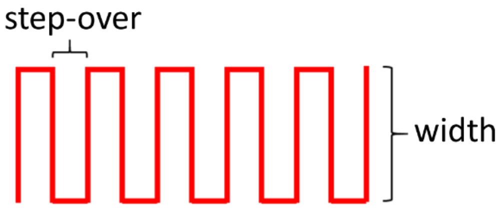

Figure 4. Schematic of the fill pattern used.

A range of test deposits were generated, in order to best optimize the fill pattern line spacing dimension for both materials. Here, the fill pattern width was 16 mm, while the line spacing (step-over) was 3 mm for both materials. The finished deposits are on the order of 22.5 mm wide for the P91 and 24 mm wide for the IN740H. The differences in width are due to the melt pool behavior of each material. The IN740H flows differently, stretching the overall width slightly larger despite the same toolpath. Each deposit was built to a height of roughly 100 mm (approximately 50 layers) and is suited to extraction of samples for mechanical properties and heat treatment characterization, discussed in later sections. An additional benefit of the square fill/raster pattern is observed in the greater stability of the melt pool, as compared to the single-width deposits. As shown in the figures, the deposit surfaces display a periodic texture, with no bulging, sagging, or overflow of the melt pool. This is common across WAAM and other arc based AM methods (in addition to welding), where a weave motion of the torch serves to further stabilize the arc and thus melt pool. The builds with the optimum printing parameters for both pure 740H superalloy (G10) and P91 steel (G9) were identified and characterized further. The parameters used for building 740H and P91 alloys that were studied extensively in this project are summarized in Table 1.

3.2.1 Characterization of as-built Inconel 740H superalloy

The sample G10 that correspond to the IN740H superalloy was printed using WAAM process with a square raster pattern, unlike the zig-zag pattern. In order to identify the anisotropy in properties and microstructure 2 different planes were studied namely, longitudinal (build) and transverse planes as shown in Fig. 5. Figure 6 shows the scanning electron microscopic images in backscattered electron mode (BSE-SEM) for the as-built G10 sample. A typical columnar growth is observed, and the dendrites have grown almost parallel to the building direction. Also, the presence of precipitates mostly in the interdendritic region is found in all the three regions of the sample. From the magnified images shown on the right-hand side, it can be observed that there are two precipitates with different contrast (white and grey) and shapes (blocky and discontinuous). The line scans performed across different precipitates using energy dispersive spectroscopy

(EDS) are shown in Fig. 7. From the composition profile across the precipitates, it is evident that the white and discontinuous precipitate is a Nb-rich phase i.e., the Laves phase. The grey and blocky precipitate corresponds to the carbide phase, (Nb, Ti)C with excessive depletion of Ni. Hence, the presence of Nb-rich Laves phase and (Nb,Ti)C carbides has been confirmed in the as-built IN740H superalloy processed using WAAM.

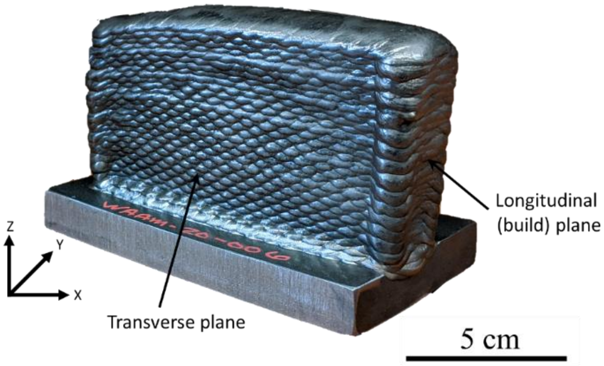

Figure 5. Inconel 740H superalloy fabricated using WAAM showing the different planes studied.

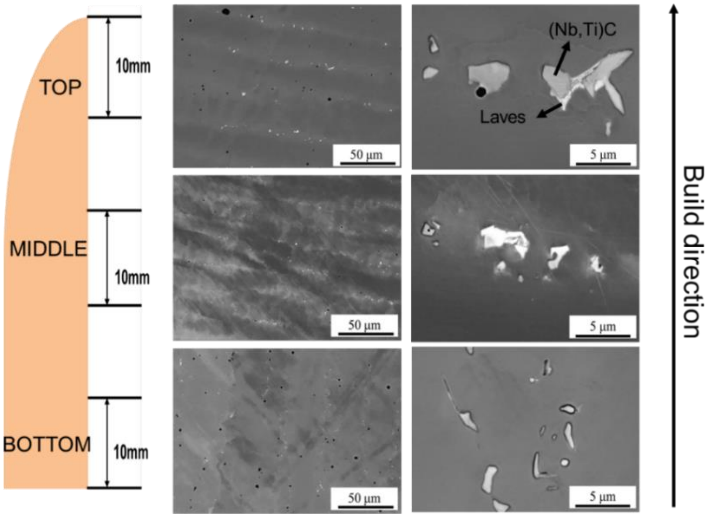

Figure 6. BSE-SEM micrographs of as-built G10 sample corresponding to IN740H superalloy showing the columnar dendritic growth and the presence of precipitates in the longitudinal/build plane.

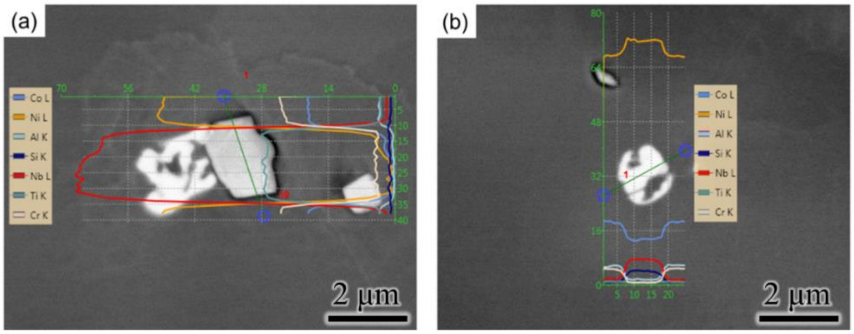

Figure 7. EDS line scans across different precipitates in as-built G10 sample. (a) (Nb,Ti)C, and (b) Nb-rich Laves phase.

The inverse pole figure (IPF) and pole figures (PF) of (001), (101) and (111) planes in the top middle and bottom portions of as-built IN740H in the longitudinal and transverse planes are shown in Figs. 8 and 9. From Fig. 8, it is clearly evident that there is strong texture across the sample, however, it is found to vary in different regions in the longitudinal plane. In region L1 i.e., the topmost portion of the sample was found to possess grains mostly oriented close to the (001) plane, as seen from the IPF and PF maps. There is strong texture found in this region since the maximum texture intensity is the highest. During additive manufacturing, the process of melting and solidification of the alloy leads to epitaxial growth of columnar grains showing a strong cubic texture in the building direction due to the high temperature gradient and rapid cooling rate as reported for other additively manufactured Ni-base superalloys. In region L2, the grain size has drastically increased and oriented close to the (001) and (111) planes as seen from the IPF and PF maps. The maximum texture intensity in this region is less than that of region L1. The drastic increase in grain size can be attributed to the following reason. In general, heat tends to accumulate in a build as the processing time increases. As the build height increases, further away from the substrate, the heat transfer is directed through previously deposited layer, which usually results in slower cooling rate. Extended times at elevated temperatures causes coarsening of microstructural features, relaxation of residual stresses as well as dislocation motion and annihilation. In region L3, which is in the middle portion of the sample, the grains are more refined in comparison with region L2. Some of the grains are oriented mostly along the (111) planes and the remaining grains are oriented along the planes in between (001) and (101) planes in this region. On the other hand, in region L4 of the middle portion shows grains that are oriented along (001) plane and few grains along the (101) and (111) directions as seen from the IPF and PF maps. Moreover, there is a drastic reduction in maximum texture intensities from region L3 to L4. In region L5 of the bottom portion, the grains are oriented closely along the (001) planes, while in region L6, the grains are oriented along (001), (101) and (111) planes. Region L6 possesses the most random texture across the sample with the least texture intensities.

The IPF and PF maps for different regions along the transverse plane is shown in Fig. 9. In region T1, the topmost part of the top portion of the sample in the transverse plane, the grains are oriented mostly along the (101) and (001) planes, with very few grains along the (111) plane. This region does not show any strong texture, which is in contrary to region L1, the topmost part of the top potion in the longitudinal plane which showed the strongest texture. However, in region T2, the grain size has drastically increased and the texturing transforms to (110) planes mostly, with few small grains along the (001) plane as seen from the IPF and PF maps. The maximum texture intensity has increased more than twice as we move from region T1 to T2 in the top portion of the transverse plane in as-built IN740H superalloy processed using WAAM. The regions T3 and T4 in the middle portion of the sample along the transverse plane, the grains are found to be extremely coarse and oriented along the planes between (001) and (101), possibly (102) planes, with very few grains oriented along the (101) plane. The maximum texture intensities were very high in comparison with other regions of the sample. This indicates that very strong texture is found in the middle portion of the sample in the transverse plane, unlike the longitudinal plane, where highest texturing was found in the top portion of the sample. In region T5 present in the bottom portion of the sample, The grains are oriented mostly along (001) plane as well as planes between (001) and (111) planes, and few grains oriented along (101) and (111) planes, indicating the presence of a weak texture. The maximum texture intensity has reduced drastically in comparison with the middle portion of the sample. In region T6, that is close to the mild steel substrate, the grains are found to be oriented along (101) planes and planes between (111) and (101). This region is found to possess the least maximum texture intensity among all the other regions in the transverse plane of as-built 740H superalloy.

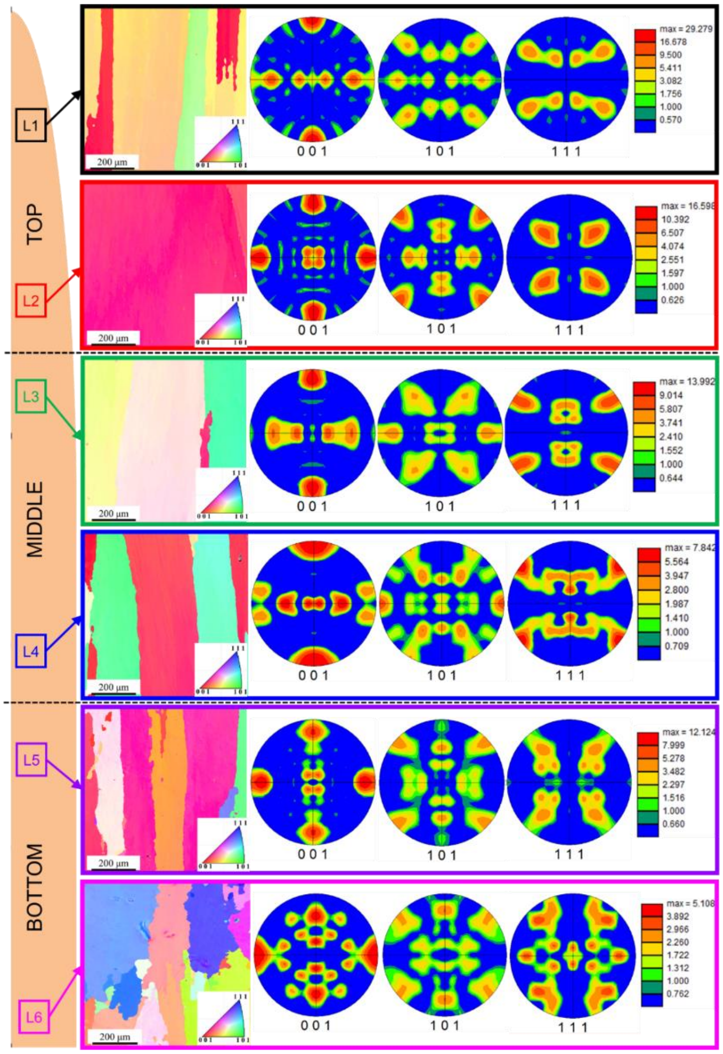

Figure 8. IPF and PF maps in different regions of longitudinal plane of as-built Inconel 740 superalloy.

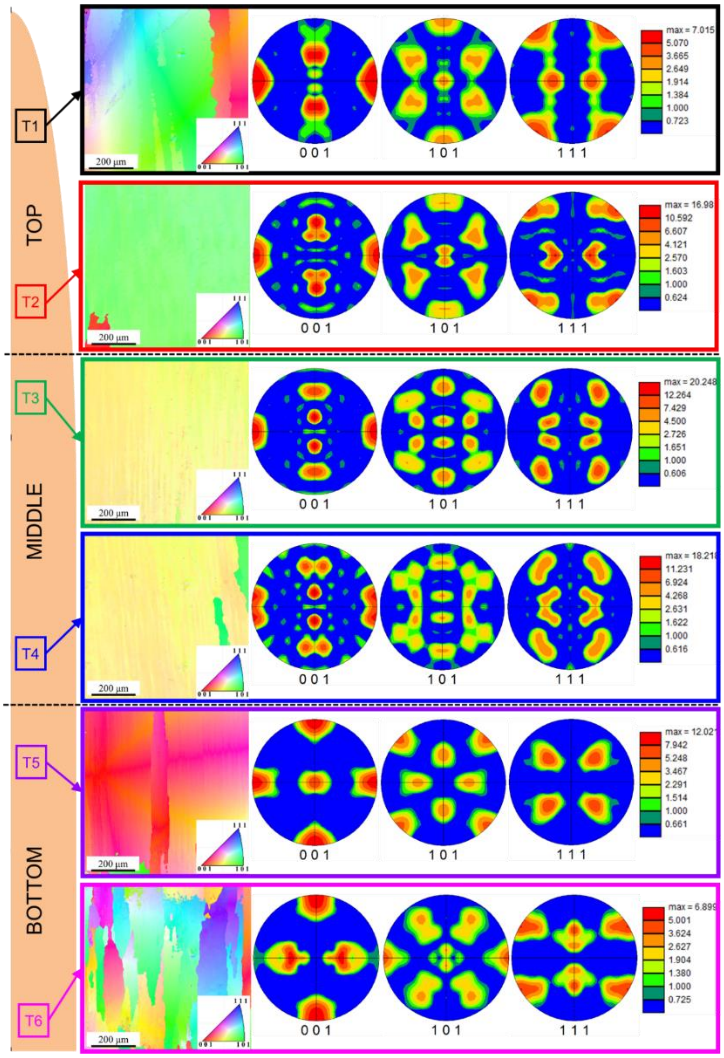

Figure 9. IPF and PF maps in different regions of transverse plane of as-built Inconel 740 superalloy.

The as-polished surfaces of the top, middle and bottom portions of the samples along the longitudinal and transverse planes were used for obtaining the hardness maps for these samples using an automated Vicker's microhardness tester. 500 indents were made across the samples to obtain the hardness maps. The hardness maps obtained from different portions of the sample along the transverse and longitudinal planes of the sample are shown in Fig. 10. The average microhardness in the top portion was found to be between 268 and 282 HV in the longitudinal plane and between 295 and 315 HV in the transverse plane. This shows that there is not much difference in the microhardness values of the top portion of the transverse and longitudinal planes of the sample. On the contrary, the average hardness is between 346 and 359 HV in the longitudinal plane while, it is between 349 to 380 HV in the transverse plane for the middle portion of the samples. These values are much higher than the microhardness values in the top portion of the sample in both the planes. However, the average hardness is much higher for the transverse plane in comparison with the longitudinal plane. Moreover, it is clearly evident from the hardness map for the middle portion of the transverse plane that it can divided into 2 regions, the upper region with high hardness (380 HV) and lower region with low hardness (349 HV). The microhardness of the bottom portion of the sample in the longitudinal plane is found to reduced drastically with a hardness between 237 to 277 HV, with certain region with hardness as low as 197 HV in the region close to the substrate. On the other hand, the average hardness of the bottom portion of the transverse plane, the hardness in the upper region is nearly 362 HV and further reduces to 334 HV in the lower regions. In regions close to the substrate, the microhardness is between 306 and 278 HV. Hence, it is evident that the hardness in the bottom portion of the transverse plane is higher than that of the hardness of the bottom potion of the longitudinal plane. Besides, the hardness of the bottom portion is found to be the least in comparison with the top and middle portions in both longitudinal and transverse planes of the as-built IN740H superalloy.

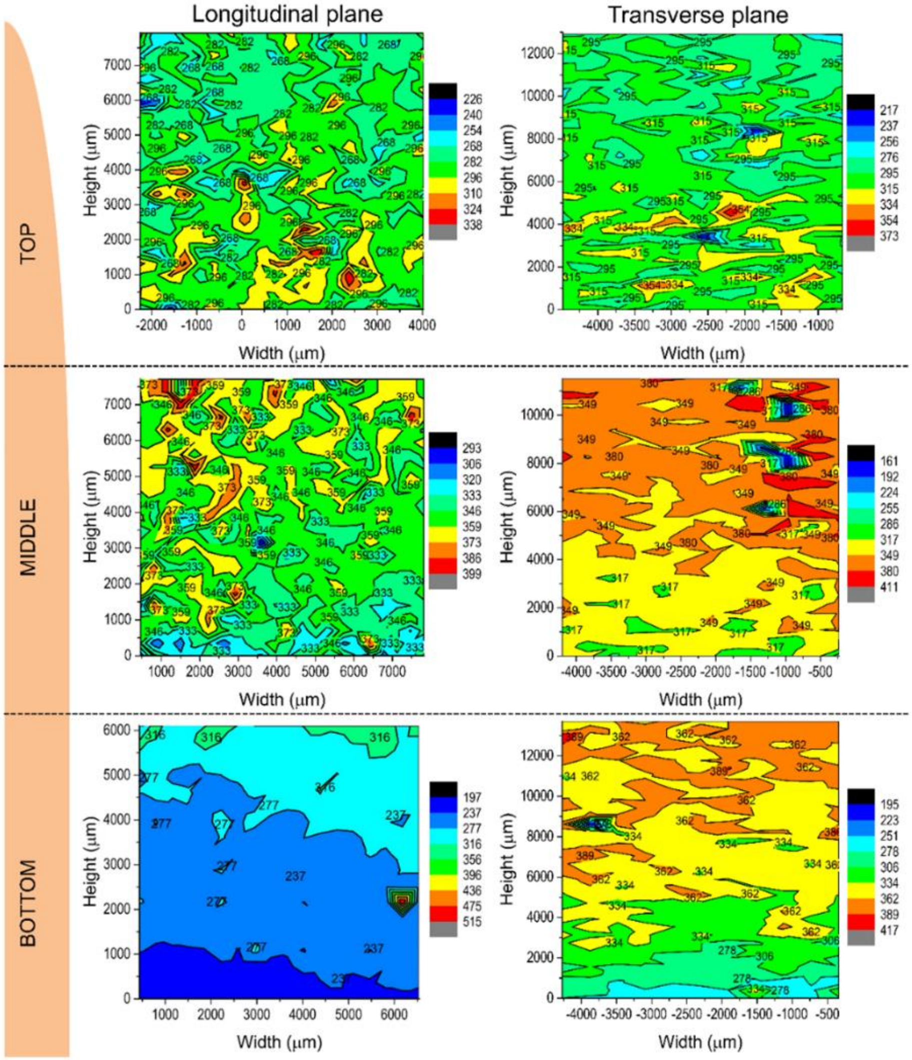

Figure 10. Hardness maps from the top, middle and bottom potions of the sample in the longitudinal and transverse planes of as-built Inconel 740H superalloy.

3.2.2 Characterization of as-built P91 steel

Build G9 (shown in Fig. 11) with high density is selected for further studying the microstructure and mechanical properties for P91 steel fabricated using WAAM. The microstructure of as-built P91 steel is shown in Figs. 12 and 13. Fig. 12 presents the metallographic analysis of the as-built P91 steel. Two distinct phases, i.e., the dark martensite and the bright δ-ferrite, can be identified, since martensite with fine and complex structure was heavily etched, while the plain δ-ferrite was etched evenly. The δ-ferrite can be observed readily in the entire build. Its volume fraction decreases from top to bottom, as illustrated in A, B, and C locations along building direction Z (Fig. 5c-e). This is because the cooling rate at the top layers is typically higher than the bottom layers. Thus, it is favorable for the δ-ferrite formation in the top layers. This result is consistent with the result reported by Pandey et al. [3], who found that a fast cooling in a wide solidification range can promote the δ-ferrite formation. At the bottom layers, the grains transit from fine columnar to equiaxial morphology due to the effect of multiple thermal cycles during WAAM deposition. The as-built sample has a strong heterogeneous microstructure along Z direction. On the XY plane of the middle location (Fig. 12(b)), the bright δ-ferrite is usually surrounded by dark martensite lath. Therefore, the observations in the middle location on both XY and XZ planes show a typical microstructure consisting of δ-ferrite and martensite in the as-built samples of WAAM.

Figure 13 shows the microstructure observed along building direction on the XZ plane from the middle location of this build (Fig. 13(a)) under OM and SEM. The black and white regions in Fig. 13(a) are dominant with martensite and δ-ferrite with different orientations, respectively. The plain area from the white and black regions in Fig. 13(a) is the δ-ferrite, while the complex lath in the uneven area indicated as the "black region" of Fig. 13(a) is lath martensite. It indicates that the microstructure mostly consists of δ-ferrite and fine lath martensite. In addition, there are few MX precipitates distributed in matrix and grain boundaries of the as-built sample, as pointed out with yellow dashed circles shown in Figs. 13(d), 13(f) and 13(g). The EDS analysis of composition on point1 is given in Fig. 13. Although this particle is too small to gain a precise measurement, precipitates are enriched in Nb, which can be confirmed as MX.

Figures 14 and 15 depict the EBSD analysis of as-built P91 in the XZ and XY planes, respectively. It is obvious that the grains are very large with strong texture (Fig. 14(a)). In the orientation and band contrast maps at high magnification (Figs. 14(b) and 14(d)), it can be observed that the dominant grain misorientation is low angle grain boundaries (LAGB), with 69.5%. The grains with LAGB is martensite, which has a lower image quality value (Fig. 14(e)). The LAGB indicates high dislocation density in the martensite resulting from the diffusionless transformation from austenite. On the contrary, δ-ferrite has very clean and bright grains with no low angle grain boundaries (Fig. 14(d)). Consequently, it has a higher image quality value. Fig. 14(c) shows the grain orientation spread (GOS) in the as-built component, which indicates the residual stress in the grains. It can be seen that there is very high residual stress in most of the grains, especially in martensite grains that have higher dislocation density. In the XY plane, prior austenite grains (PAG) of larger size can be observed in the IPF map (Fig. 15(a)), while there is no fcc phase in the as-built material, which indicates the absence of retained austenite (Fig. 15(b)). The PAG size is found to be around 200 μm after reconstruction using the ARPGE software package [4, 5] with the EBSD data as the input (Fig. 15©). There are numerous sub-grains of martensite in the PAGs. These martensite grains have two kinds of preferred orientation namely, {001} and {111}, which is shown in the pole figure (Fig. 15(e)) and inverse pole figure (Fig. 15(f)). They are colored with red and blue in the IPF, respectively. Therefore, two kinds of bcc structures are present, i.e. δ-ferrite and martensite in the as-built component, with an inhomogeneous microstructure. There is more inhomogeneity in the XZ plane than that in the XY plane, while strong texture exist in the whole build.

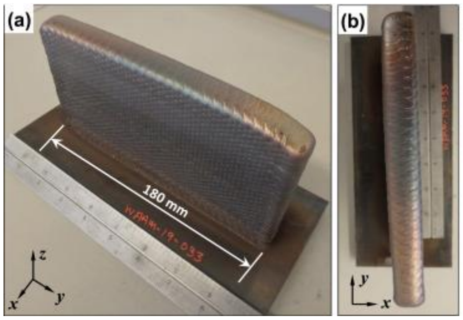

Figure 11. The final build block of P91 steel: (a) side view and (b) top view.

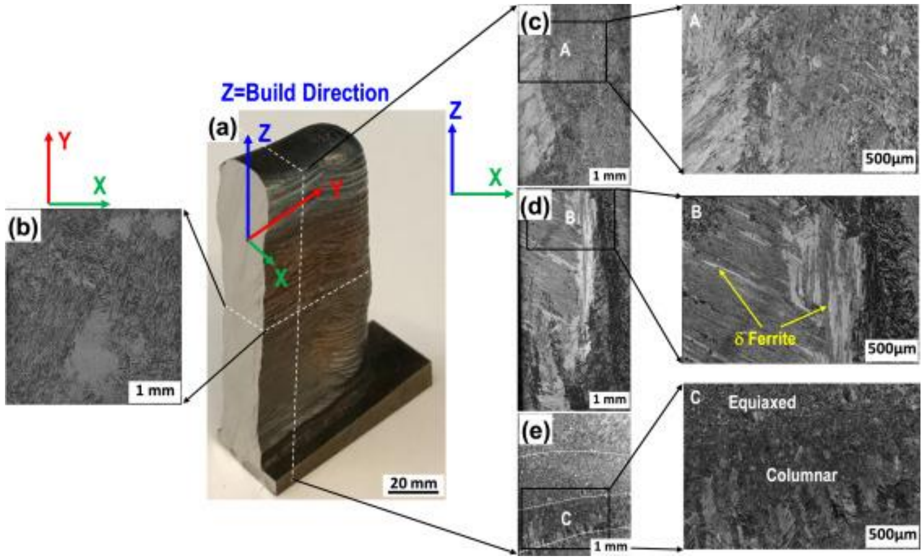

Figure 12. Optical morphologies of the as-built P91 steel: (a) overview of cut part, (b) morphology in the middle location on XY plane, (c) morphology at the top location, (d) morphology at the middle location and (e) morphology at the bottom location on XZ plane.

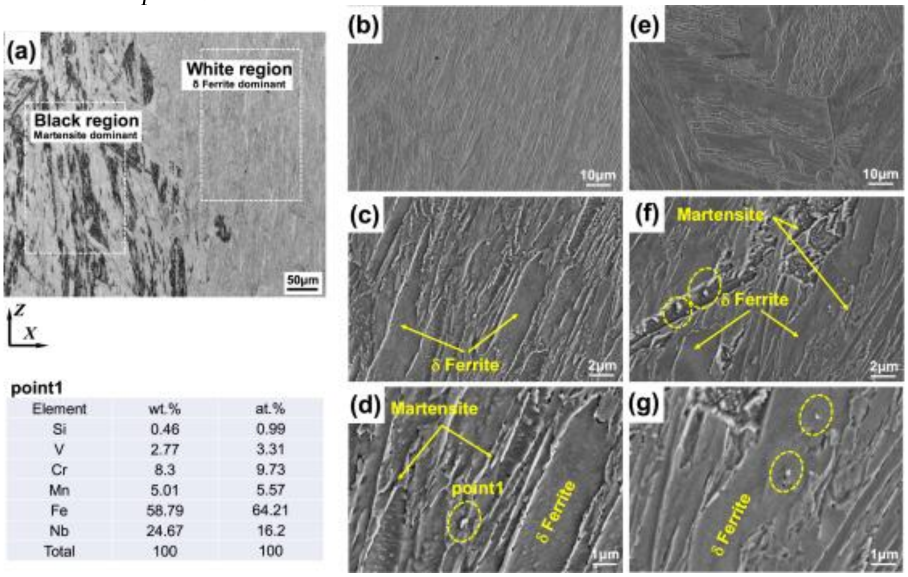

point1

Element	wt.%	at.%
Si	0.46	0.99
V	2.77	3.31
Cr	8.3	9.73
Mn	5.01	5.57
Fe	58.79	64.21
Nb	24.67	16.2
Total	100	100

Figure 13. The microstructure at the typical middle location on XZ plane of the as-built P91 steel: (a) OM overview, (b-d) SEM morphologies at different magnifications in white region and (e-g) SEM morphologies at different magnifications in black region (EDS analysis of point1 is listed in the bottom left).

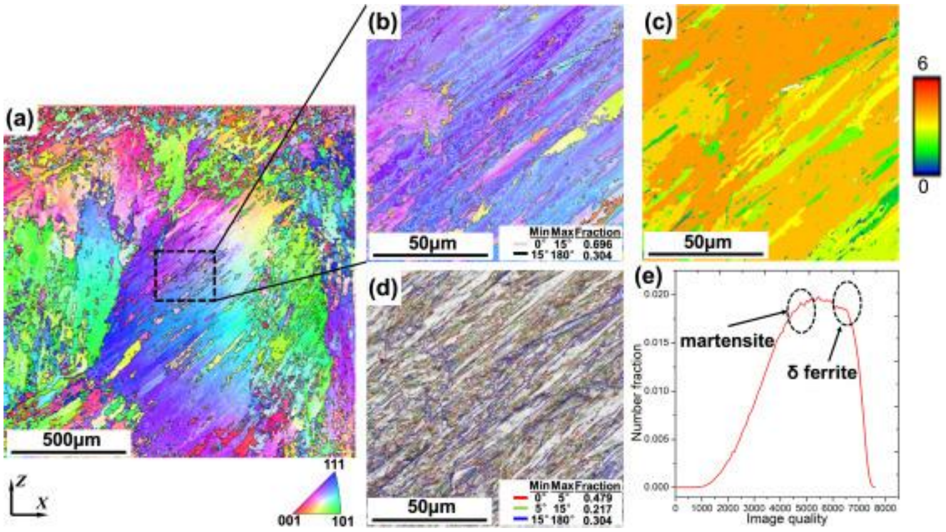

Figure 14. EBSD analysis in XZ plane of as-built P91 steel: (a) orientation map of inverse pole figure (IPF) at low magnification, (b) high magnification of (a), (c) grain orientation spread (GOS), (d) band contrast map with grain boundary misorientation and (e) image quality of (a).

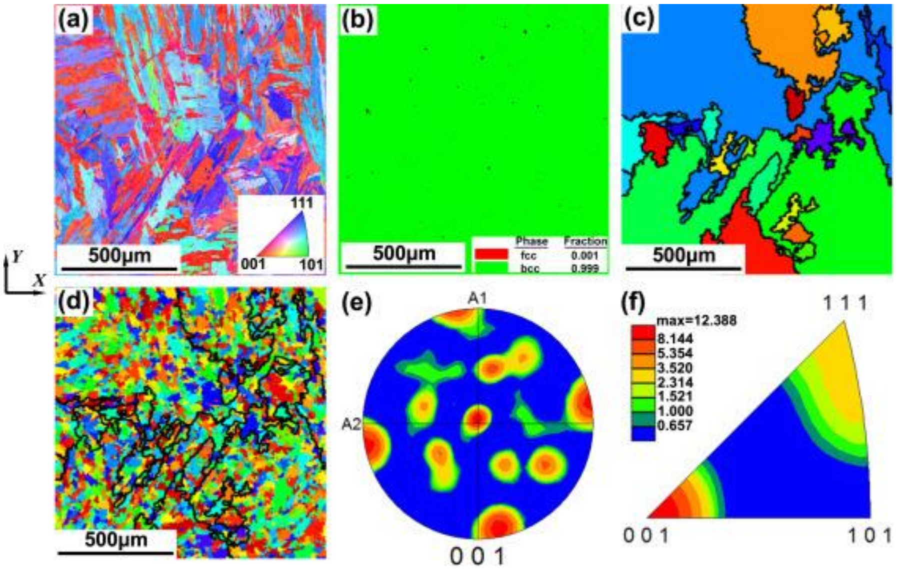

Figure 15. EBSD analysis at typical middle location on XY plane of the as-built P91 steel: (a) orientation map of inverse pole figure (IPF), (b) phase map of (a), (c) reconstruction of prior austenite grain boundaries (PAGB), (d) sub-grains in PAG, (e) pole figure and (f) inverse pole figure.

3.2.3 Post-heat treatment design for WAAM Inconel 740H superalloy

From the results obtained from the microstructure characterization of the as-built Inconel 740H superalloy, it is evident that the secondary precipitates such the Laves phase needs to be removed and the columnar dendritic structure needs to be transformed to a lesser anisotropic structure, so that better mechanical and creep properties can be attained in these alloys. Also, during the WAAM process, repeated rapid heating and cooling can produce a steep thermal gradient, which leads to the formation of residual stresses In addition to this, better distribution of the strengthening particles such as γ’ and $M_{23}C_6$ precipitates needs to be achieved in order to improve the strength. Therefore, a post-heat treatment process needs to be designed for 740H superalloy fabricated using WAAM. A two-step post-heat treatment involving solution treatment and aging will be adopted and the time and temperature needed for each step will be optimized. The equilibrium phase fraction plot and the Scheil solidification diagram were calculated using the Thermo-Calc software with the TCNI8 database for the IN740H alloy, as shown in Fig. 16. It was observed from the phase fraction plot that at 1100 and 1200ºC, the major phase is the γ (disordered FCC), with minor amounts of the NbC phase. Hence, these two temperatures will be appropriate for dissolving the Nb-rich Laves phase. Also, from the Scheil diagram, it is evident that the incipient melting temperature is found to be close to 1120ºC.

In order to determine the optimum temperature and time required to homogenize 740H superalloy, DICTRA simulations were performed. The thermodynamic and kinetic databases that were used are for these calculations are TCNI8 and MOBNI4, respectively. Since it was identified that the homogenization temperature can be either 1100 or 1200ºC, the calculations were performed for both the cases. The simulations were performed for 10^6 seconds with 200 grid points. Additional inputs such as width of the cell, position of grid points within the cell and composition at each grid point were chosen from the line scan obtained using energy dispersive spectroscopy (EDS). The maximum inhomogeneity in composition was found in the region of the matrix with Laves phase and hence, it was considered for obtaining the optimum homogenization temperature and time. EDS line scan was performed in the region with Laves phase in the γ (FCC) matrix to obtain the required inputs for the DICTRA simulations. The initial composition measured using the EDS line scan from a region with Laves phase is shown in Fig. 17. It can be observed that the Laves phase is rich in Nb, Ti, Si and Ni. The total length of the line where the measurement was performed is 16.33 μm, which will be considered as the width of the cell for the DICTRA simulation. The calculated composition profiles for various elements as a function of distance at various time periods in the region with Laves phase at 1100 and 1200ºC are shown in Figs. 18 and 19. It can be observed that the composition of Nb and Ti (which shows maximum segregation) reaches near the homogeneous composition around 60 minutes i.e., 1 hour at 1100ºC. On the other hand, the composition of Nb and Ti attains a composition close to the homogenous composition in 30 minutes at 1200ºC. In both the cases, the composition of Si reaches the homogeneous composition at 10 minutes due to its rapid kinetic behavior. Based on these observations, the solution treatment was performed at 1100 and 1200ºC for 1, 2 and 3 hours followed by water quenching in order to dissolve the Laves phase and remove the residual stress developed during the WAAM process.

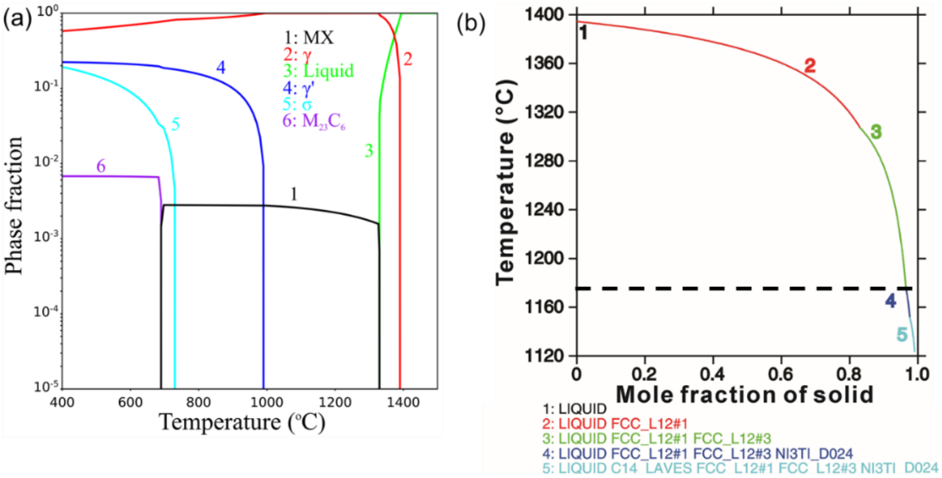

Figure 16. (a) Equilibrium phase fraction plot and (b) Scheil diagram calculated for Inconel 740H superalloy wire composition.

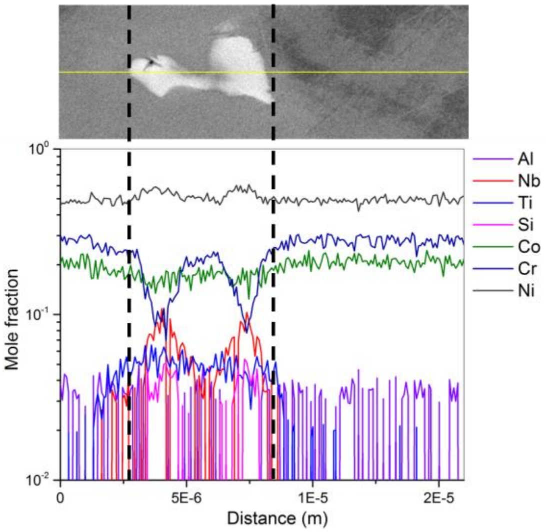

Figure 17. Initial composition from a region with Laves phase obtained using EDS.

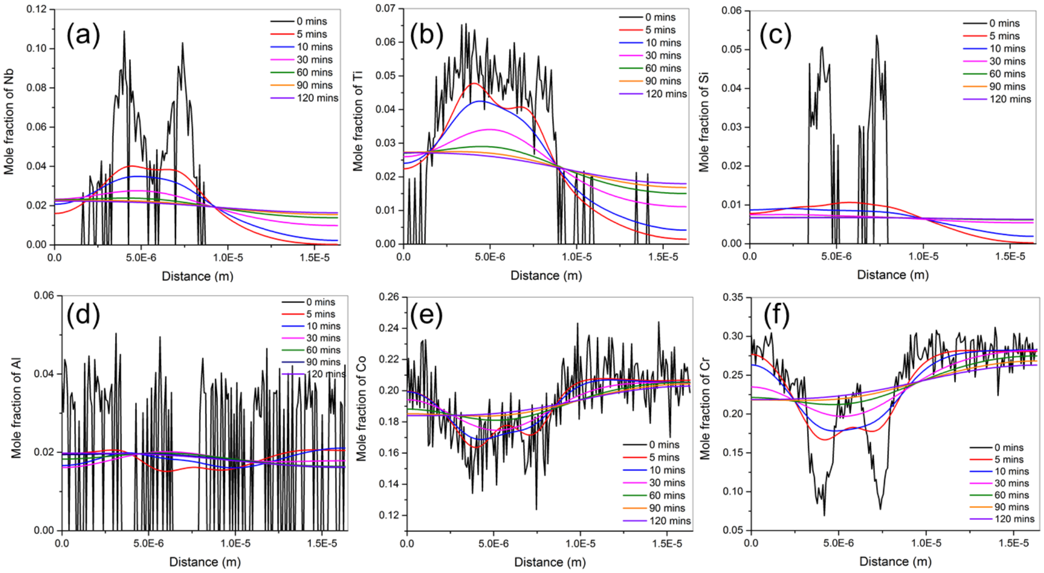

Figure 18. Composition profile as a function of distance at different time periods at 1100ºC for (a) Nb, (b) Ti, (c) Si, (d) Al, (e) Co and (f) Cr.

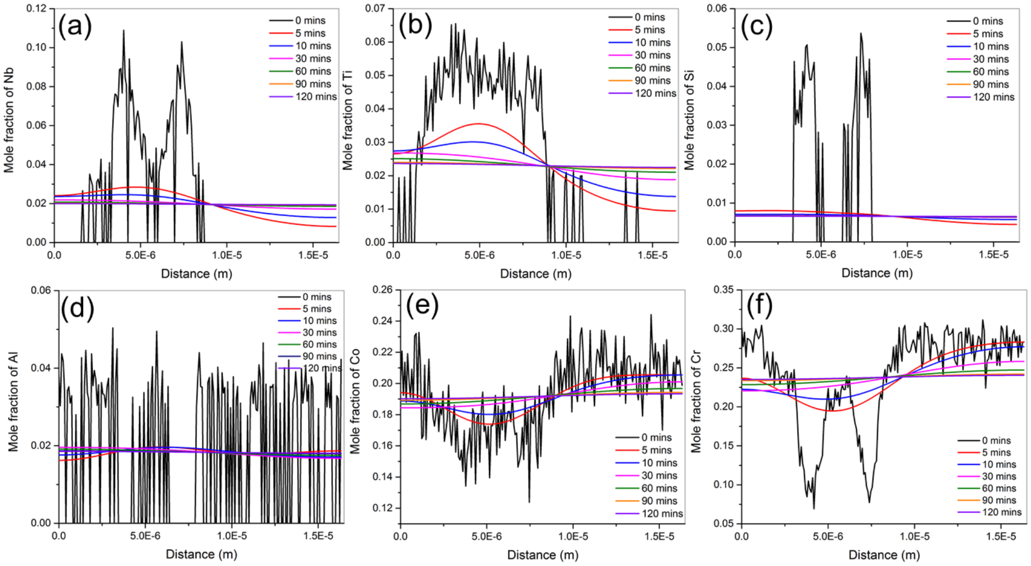

Figure 19. Composition profile as a function of distance at different time periods at 1200°C for (a) Nb, (b) Ti, (c) Si, (d) Al, (e) Co and (f) Cr.

The variation of hardness across the sample after solution treatment at 1100 and 1200°C at different time periods are shown in Fig. 20(a). It is evident that a high hardness is attained after solutionizing at 1100°C for all the time periods in comparison with the samples solutionized at 1200°C. According to You *et al*., at 1210°C, the dissolution of all the second phases occurs, leading to a homogenized microstructure in the IN740H superalloy processed by electron beam melting [6]. It was also reported that the ideal condition for solution heat treatment for IN740H alloys was found to be 1210°C for a time period longer than 30 minutes. The average hardness of the G10 sample subjected to solution treatment at 1100 and 1200°C as a function of time is shown in Fig. 20(b). The higher hardness after solutionizing at 1100°C is due to the incomplete dissolution of the second phase particles, especially, the Laves phase. On the other hand, the reduced hardness exhibited by samples solutionized at 1200°C is due to the complete dissolution of the second phase particles into the matrix.

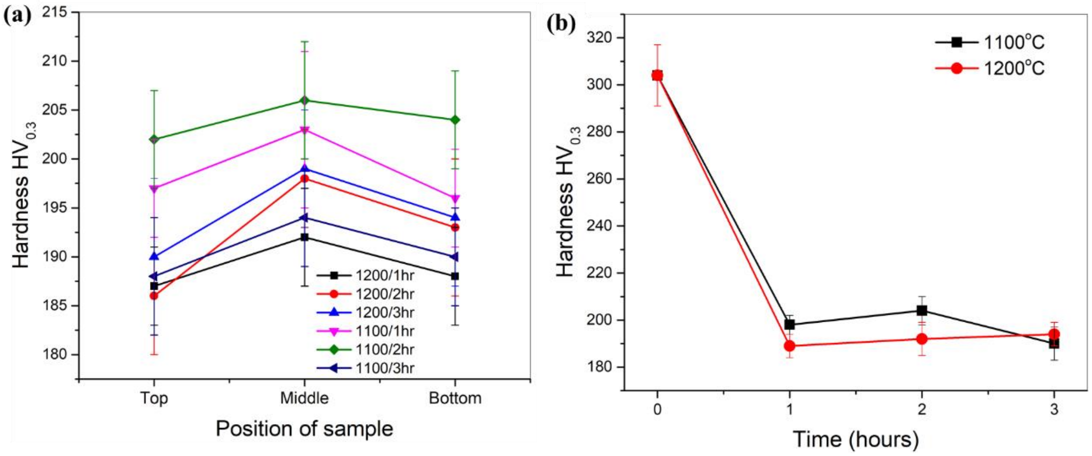

Figure 20. (a) Average hardness at different positions and (b) average hardness as a function of time for Inconel 740H samples homogenized at 1100 and 1200°C for different times.

The BSE-SEM micrographs of the G10 samples solutionized at 1200^{o}C for 1, 2 and 3 hours are shown in Fig. 21, respectively. After 1 hour of solution treatment, annealing twins are found to form only in the middle region of the sample, and the top, as well as the bottom regions, still maintained the columnar structure. This indicates that this time period was not sufficient to homogenize the sample. Annealing twins were found to form in all the regions of the sample after solutionizing for 2 hours. Similar behavior in 740H superalloy after annealing has also been observed by Zielinski *et al* [7]. According to Zhang *et al*. [8], there are three types of annealing twins that can form in the 740H superalloy. They are twins at the corner of the grain boundary, twins across grains and incomplete twins without grain penetration. From the BSE-SEM images, it can be observed that after 2 hours of solution treatment at 1200^{o}C leads to the formation of incomplete twins without grain penetration with widths ranging from 1 to 5 µm. Also, the formation of recrystallized grains in all the regions is also evident. Large annealing twins with a width more than 10 µm can be observed in all the regions of the sample that was solutionized at 1200^{o}C for 3 hours. It is also expected to possess excessive grain growth due to heat treatment at high temperatures for a longer time. The IPF superimposed over IQ map (IPF+IQ map for better contrast), kernel average misorientation (KAM), grain maps and the pole figure obtained using EBSD from the middle region of the G10 sample subjected to solution treatment for 2 hours at 1200^{o}C is shown in Fig. 22. The presence of annealing twins with incomplete growth into the recrystallized grain is evident from the IPF+IQ map. KAM values close to 0^{o} correspond to blue color and values close to 2.5° are denoted by green color. From the KAM map (Fig. 22(b)), it is clear that the recrystallized grains with annealing twins exhibit larger misorientation in comparison with grains without twins. Also, the twinned regions with larger width have high misorientation and the twinned regions with smaller width possess almost zero misorientation. The pole figure presented in Fig. 22(d) indicates that there is lesser anisotropy due to the formation of recrystallized grains during solution treatment. Hence, the optimum solution treatment temperature and time were determined to be 1200^{o}C and 2 hours, respectively.

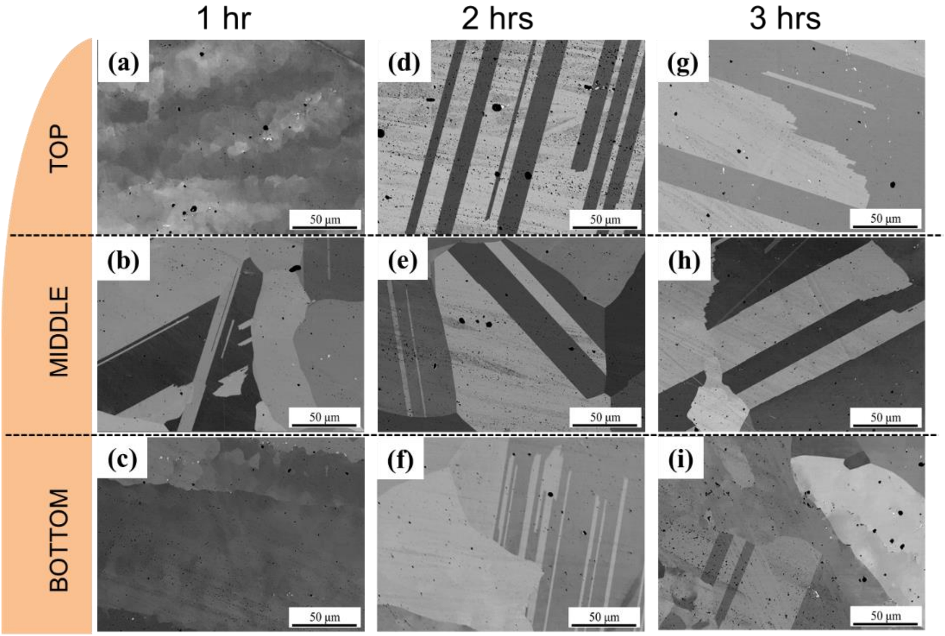

Figure 21. BSE-SEM micrographs of Inconel 740H samples homogenized at 1200^{o}C for (a-c) 1 hr, (d-e) 2 hrs and (g-i) 3 hrs from different positions of the sample.

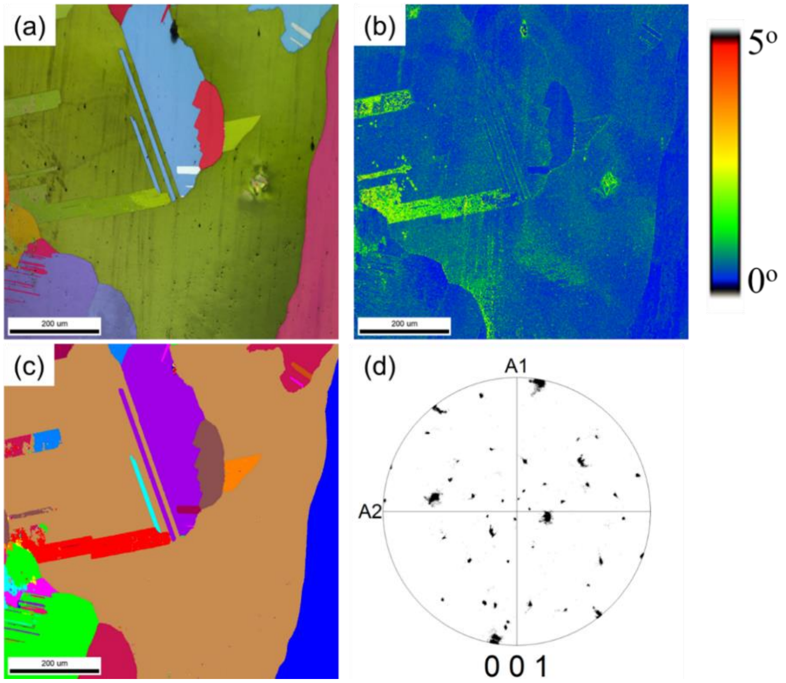

Figure 22. (a) IPF+IQ, (b) KAM, (c) Grain maps and (d) pole figure obtained using EBSD from the middle region of the G10 sample solution treated at 1200°C for 2 hours.

The second step of the post-heat treatment schedule is aging heat treatment. This is an important step as it leads to precipitation strengthening of 740H superalloy due to the supersaturated solid solution developed after solution heat treatment at 1200°C for 2 hours. The aging temperature was determined with the equilibrium phase fraction plot for the 740H superalloy shown in Fig. 16(a). It was found that at 730°C, there is no formation of the σ phase and γ' second phase particles will lead to the strengthening. Also, it was found in the literature that the typical aging temperature for hot-rolled 740H alloys lies in the range of 730-800°C for a time period between 4-16 hours. An aging temperature of 760°C was chosen in order to achieve strengthening due to precipitate formation. The G10 alloys were solutionized at 1200°C for 2 hours and subsequently aged at 760°C for 4, 8, 12 and 16 hours followed by air cooling. The hardness with respect to the position of the sample and the average hardness of the sample as a function of aging time are shown in Figs. 23(a) and 23(b). It was found that the peak hardness was achieved after aging for 12 hours. *In a nutshell, the optimum two-step post-heat treatment schedule for Inconel 740H processed using WAAM is as follows: 1) Solution treatment at 1200°C for 2 hours; 2) Aging at 760°C for 12 hours.*

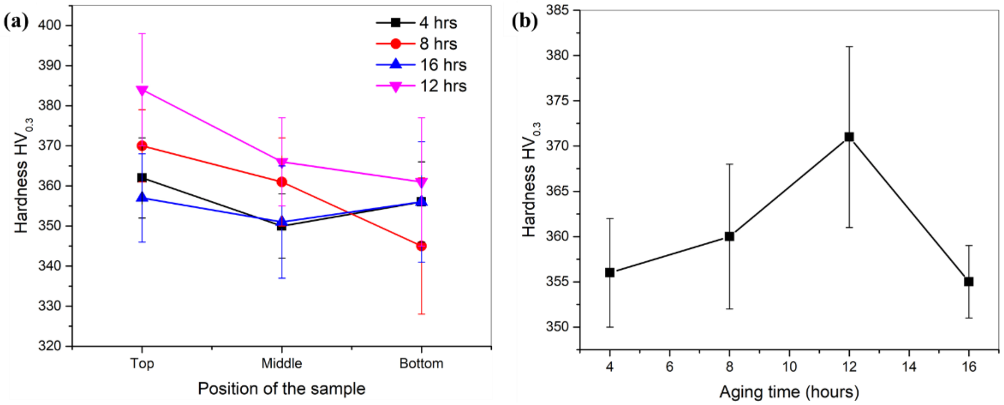

Figure 23. (a) Average hardness as a function of sample position and (b) average hardness as function of aging time for IN740H samples aged at 760°C.

3.2.4 Post-heat treatment design for WAAM P91 steel

To homogenize the as-built microstructure and get a uniform property in P91 steel fabricated using WAAM, δ-ferrite needs to be dissolved. Furthermore, MX precipitates are supposed to be eliminated, because the carbon dissolved from MX back to the matrix is beneficial to the precipitation of $M_{23}C_6$ that has the most significant contribution to the creep properties of P91 during the aging heat treatment. Fig. 24 gives the step diagram (equilibrium phase fraction vs. temperature) of P91 steel. It is obvious that MX can be dissolved completely by increasing the temperature to 1200°C. According to the equilibrium phase fractions at lower temperatures, it can be seen that MX is able to completely transform to $M_{23}C_6$ and other phases at around 760°C. It is also the temperature at which the highest fraction of $M_{23}C_6$ is observed. Therefore, we chose the homogenization temperature as 1200°C, followed by the aging heat treatment at 760°C that is high enough to promote the formation of a higher fraction of $M_{23}C_6$. In order to optimize the post-heat treatment, the homogenization time was tested in the range of 1 h to 3 h and the aging time was tested from 2 h to 8 h to identify the optimal microstructure and properties.

The hardness of WAAM P91 steels homogenized at 1200°C with different times is shown in Fig. 25. From the plot, it reveals that the as-built sample has the lowest hardness with an average of 387 HV, due to large amounts of δ-ferrite forming in the as-built matrix. The hardness decreases from the bottom to top locations, as illustrated in the inset of Fig. 25. This phenomenon results from the heterogeneous microstructure, i.e., the increasing content of δ-ferrite with the building height increasing. After 1 h homogenization, the average hardness increases to 440 HV, while there is still a notable difference of 20 HV from the bottom to top locations, and the bottom location still displays the highest hardness. The sample with 2 h homogenization shows the highest hardness with an average value of 445 HV for the entire section. The hardness distribution is more uniform, with a difference within 10 HV from bottom to top locations. When the homogenization is prolonged to 3 h, the hardness in the entire part is nearly uniform, with a decrease to 433 HV.

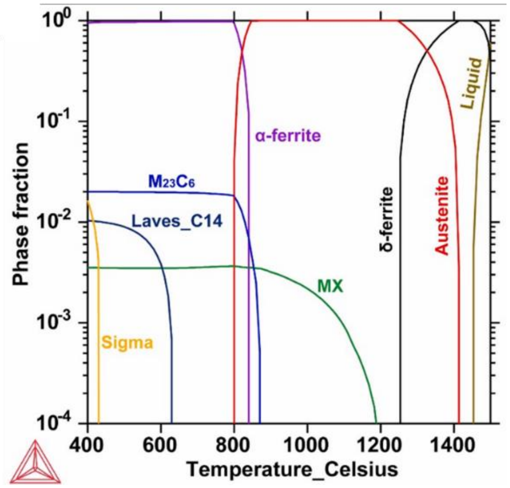

Figure 24. Calculated step diagram (equilibrium phase fraction vs. temperature) for P91 steel wire composition.

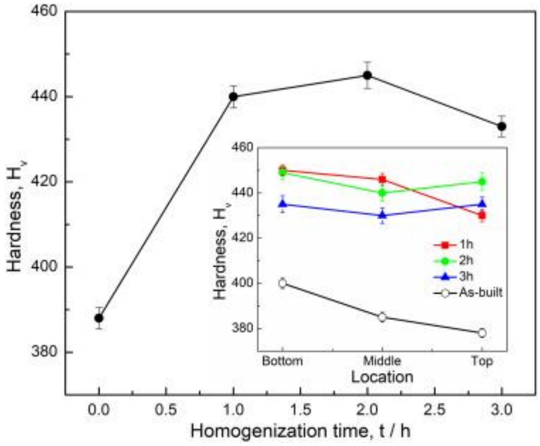

Figure 25. The average hardness of WAAM P91 steels homogenized at 1200°C with different times (inset shows the hardness of different locations with different homogenization times).

The microstructural evolution of WAAM P91 steels during homogenization with different times is shown in Fig. 26. After homogenized at 1200°C, the δ-ferrite disappears replaced by lath martensite, which leads to the significant increase in hardness compared to the as-built sample. For 1 h homogenization, there are still a few δ-ferrite at the middle and top locations (Figs. 26(a) and 26(b)). This is due to the higher content of δ-ferrite in the as-built matrix. Due to the remaining δ-ferrite, the top location has the lowest hardness. The homogeneity of martensite lath is decreased from bottom to top locations, which is also reflected from the preferred orientations of martensite lath. The poor homogeneity in the whole part results in the big difference of hardness from bottom to top locations, which inferred that 1 h is not long enough to eliminate the heterogeneous structure. Fig. 27 shows TEM micrographs of different homogenized samples. The TEM foils were taken from the middle locations, which have typical microstructure under stable building conditions. In the as-built matrix (Fig. 27(a)), the martensite has many dislocation tangles, while the δ-ferrite forms along the martensite, with few dislocation tangles. The MX forms in both of martensite and δ-ferrite, which is confirmed by the diffraction pattern (the inset of Fig. 27(a)). Homogenization at 1200°C completely dissolves the MX, replaced by the entire BCC structure as shown in the diffraction pattern of the inset of Fig. 27(b). Most of the matrix is martensite lath with a smaller width, and few δ-ferrite still remains in the matrix, which is consistent with the SEM observation. It further confirms that 1 h homogenization is not sufficient to dissolve all of δ-ferrite. When the homogenization is 2 h, there is no δ-ferrite remaining in the entire part. The prior austenite grain boundaries (PAGBs) are clear in the SEM morphologies, as indicated with red arrows. The PAGs are fully filled with martensite laths (Figs. 26(d-f)). Moreover, the martensite is homogenized at different locations, with uniform laths. The width of martensite lath is even finer compared to homogenization for 1 h, with a width of 200 nm (Fig. 27(c)). This results from the homogenized martensite in the part restraining the lath growth, as indicated in Fig. 10f. It can also introduce higher dislocation density in the martensite, which is identified in Fig. 11c. The homogeneity with finer martensite causes the sample with 2 h homogenization has a higher hardness with less deviation. The microstructure of WAAM P91 steel homogenized for 3 h presented in Figs. 26(g-i) shows PAGs grow after long homogenization time. It shows a completely homogenized microstructure from bottom to top locations. The martensite lath coarsens and becomes blocky shapes, which lead to a decrease in hardness. Whereas, it still has a high dislocation density within martensite owing to the water quench (Fig. 27(d)). This results in a higher hardness than the as-built sample.

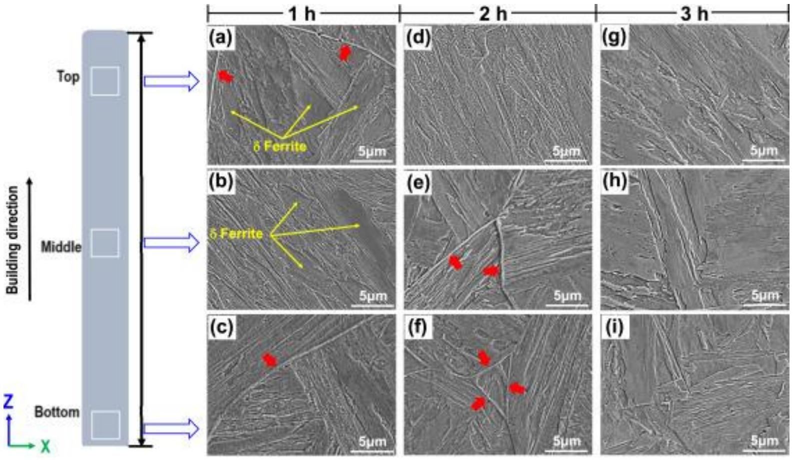

Figure 26. Microstructure evolution at different locations of WAAM P91 steels homogenized at 1200°C with different times: (a-c) 1 h, (d-f) 2 h and (g-i) 3 h. (red arrow indicates the prior austenite grain boundary).

To further study the grain distribution and residual stress in the part after homogenization, EBSD analysis was performed at the middle location with the representative microstructure, as shown in Fig. 28. IPF orientation maps indicate that the martensite size decreases remarkably after homogenization compared to the as-built sample. Furthermore, the 2 h homogenized sample has the finest martensite blocks and laths. Based on GOS maps, the heterogeneity of the GOS distribution is decreased in the grains with the homogenization time increasing. The average value drops from 3.5 to 2.3. This fact indicates the residual stress is gradually reduced with longer homogenization time. Pole figures in three different homogenized samples exhibit the texture in the {001} plane is decreased from 6.040 to 2.488. The texture in 2 h homogenized sample is slightly stronger than that in 3 h homogenized sample. The reconstruction of PAGs is analyzed as shown in Fig. 29. It is obvious that the as-built sample has a large PAG size of 300 μm. After homogenization, the PAG size decreases to 167 μm, while 2 h homogenized sample has the smallest PAG size of 108 μm. Then the PAG size increases, with a value of 135 μm at 3 h homogenization. The finest and homogenized PAGs and martensite lath contribute the highest hardness for 2 h homogenization sample. Therefore, homogenization at 1200°C for 2 h is the optimal process.

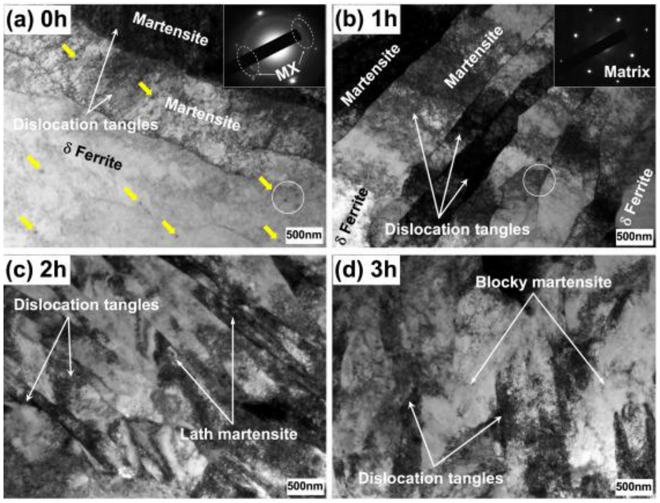

Figure 27. TEM morphologies at typical middle locations of WAAM P91 steels homogenized at 1200°C with different times: (a) as-built-0 h, (b) 1 h, (c) 2 h and (d) 3 h. (yellow arrow: MX precipitates, white circle: selected diffraction

area. The diffraction patterns from white circles in the insets of (a) and (b) indicate that MX presents in the matrix of the as-built steel and disappeared in the matrix of the homogenized steel).

Fig. 30 shows the aging behaviors on the microstructure of WAAM P91 steels aged at 760°C with different aging times. The precipitation of $M_{23}C_6$ was observed clearly in aged samples, as indicated with red dashed circles in SEM morphologies. Most of them distribute in the matrix, grain boundaries, and sub-grain boundaries of martensite lath. Some particles with a very small size of less than 50 nm (yellow arrows) are precipitated in the matrix or sub-grain boundaries of martensite lath. These small precipitates along martensite boundaries were reported to be MX in the previous work, which is the main strengthening phase for P91 steel. As the aging time increases, the size of $M_{23}C_6$ is increased, while their distribution has a big difference. Most of $M_{23}C_6$ precipitates along grain boundaries, being coarsened near each other (Fig. 14b-d). The evolution of $M_{23}C_6$ during aging heat treatment is summarized in Fig. 31. The volume fraction and diameter of $M_{23}C_6$ increase as the aging time increases. The number density of $M_{23}C_6$ reaches the highest value at 4 h. However, the $M_{23}C_6$ coarsens and clusters with less dispersive distribution in the grain boundaries. According to the microstructural evolution of aged samples, the hardness change is presented in Fig. 32. After 1 h aging, the hardness, HV value, drops to 239 from 445 in the as-homogenized state. This is because of the tempered martensite losing dislocation density and supersaturation of elements such as Cr, Mo and C during aging. This significantly impairs the solution strengthening effect, which decreases the hardness. After aging for 2 h, the hardness slightly increases to 248 HV. It is anticipated that more precipitation of MX comes out from the martensite and $M_{23}C_6$ has not been coarsened. When the aging time is above 2 h, the hardness decreases rapidly, due to increased precipitation and coarsening of $M_{23}C_6$ which severely softens the material. Therefore, the 2 h aged sample with the fine distribution of MX and M23C6 precipitates shows the highest hardness. Hence, *the optimum two-step post-heat treatment schedule for P91 steel processed using WAAM is as follows: 1) Solution treatment at 1200^{o}C for 2 hours; 2) Aging at 760^{o}C for 2 hours.*

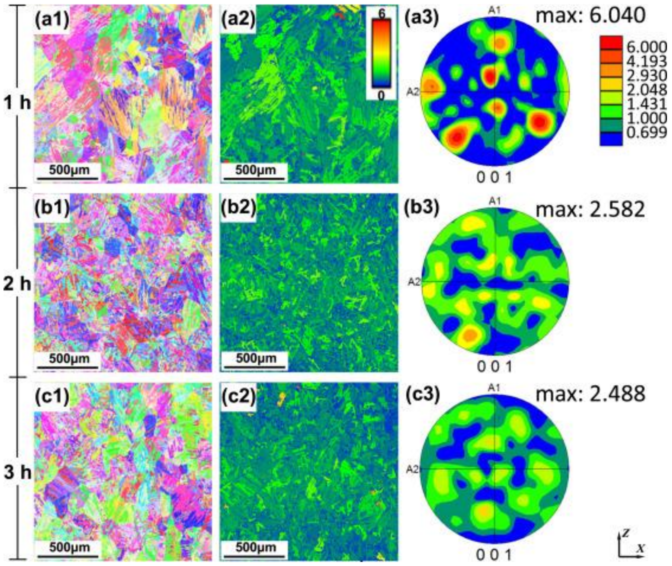

Figure 28. EBSD analysis on XZ plane of WAAM P91 steels homogenized at 1200°C with different times: (a) 1 h, (b) 2 h and (c) 3 h. (a1-c1: IPF maps, a2-c2: GOS maps, a3-c3: pole figures).

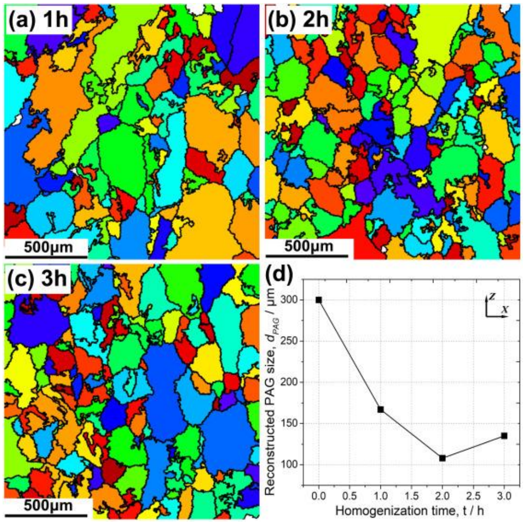

Figure 29. The reconstruction of prior austenite grains (PAGs) based on EBSD data of WAAM P91 steels homogenized at 1200°C for 1 h (a), 2 h (b), 3 h (c), and (d) evolution of PAG size.

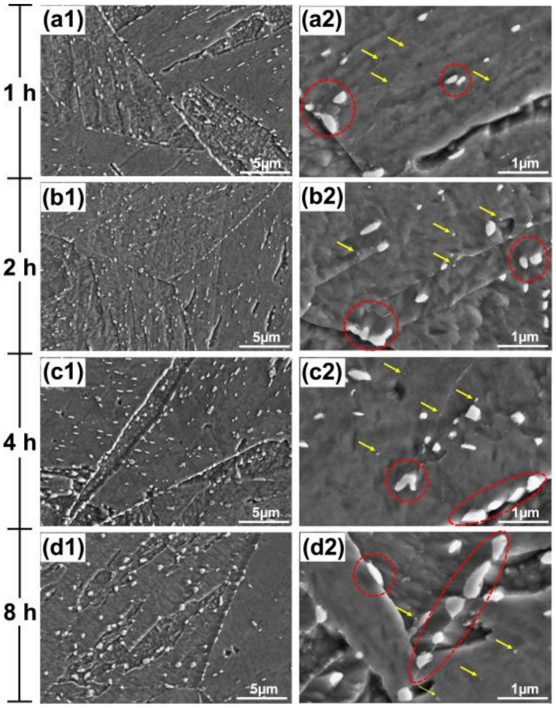

Figure 30. SEM morphologies on microstructure of WAAM P91 steel aged at 760°C with different aging times: (a) 1 h, (b) 2 h, (c) 4 h and (d) 8 h. (a1-d1: low magnification, a2-d2: high magnification; red dashed circle-$M_{23}C_6$*, yellow arrow-MX)*.

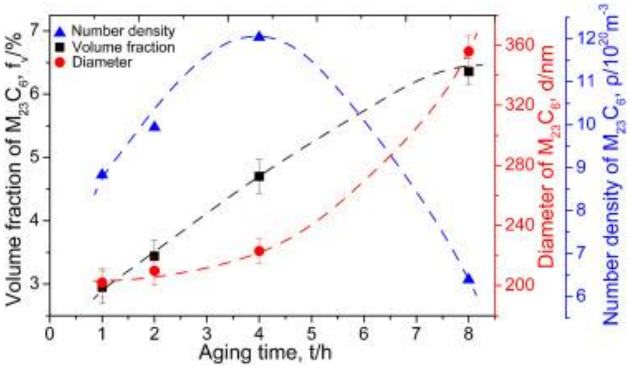

Figure 31. Precipitation evolution of $M_{23}C_6$ in the aged WAAM P91 steels versus aging time at 760°C.

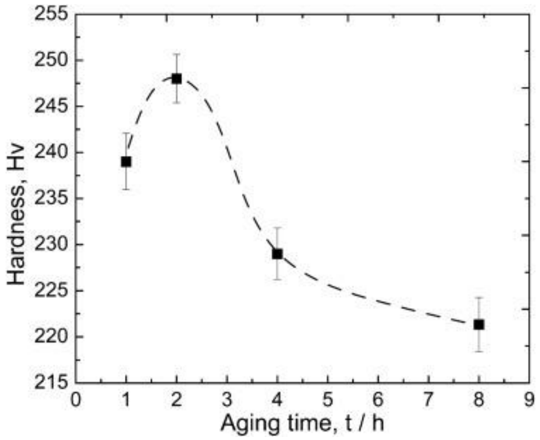

Figure 32. Hardness evolution of WAAM P91 steels aged at 760°C with different times.

3.2.5 Evaluation of mechanical properties

In order to evaluate the effectiveness of the designed post-heat treatment, mechanical testing was performed before and after heat treatment for single build P91 steel and Inconel 740H superalloy. Z-direction tensile bars (i.e., oriented in the build height direction) were extracted via electrical discharge machining (EDM) from the two bulk WAAM deposits. This machining method was selected to maximize the material available from the deposit (i.e., no wasted material from saw cuts and traditional milling). The orientation and geometry of the tensile bars are shown in Fig. 33, alongside the original WAAM deposited bulk coupon for reference. In order to remove the EDM surface (recast layer), each tensile bar was lightly ground on every surface to produce a smooth finish. This serves to also remove any sharp edges, which may result in stress concentration during tests. Each sample is marked with reflective tags, which enable a laser extensometer to be used to monitor elongation during the test. This non-contact elongation measurement is more robust compared to clip-on extensometers and can accommodate larger elongation without suffering slipping. Samples were tested in a 120 kip servo-mechanical load frame at crosshead rate of 0.05 inch per minute at room temperature.

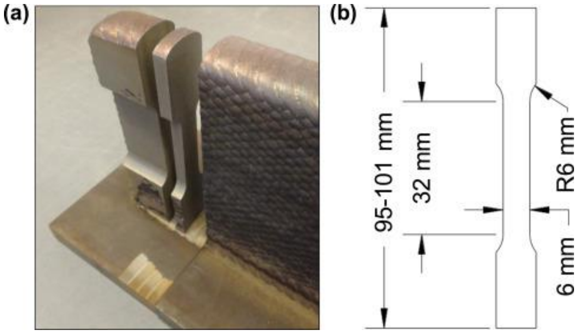

Figure 33. Design of tensile bars: (a) geometry of the tensile bar from the as-built P91 steel and (b) dimensions of the tensile bar.

The stress-strain curves obtained for the as-built and post-heat treated P91 steel is shown in Fig. 34. The tensile properties obtained from these curves are summarized in Table The as-built sample has a very high strength with the ultimate strength (UTS) of 1242 MPa and yield strength (YS) of 985 MPa, which is twice that of standard wrought P91 steel at room temperature. This is attributed to the strengthening effects of the high density of dislocations and MX precipitates. Whereas, the ductility of the as-built sample is only half of the standard wrought material, which results from the heterogeneous structures and strong texture leading to easy cracking during deformation. The fractography shows that the main fracture mode is cleavage, with a typical river-pattern fracture surface (Figs. 35(a-c)). Some intergranular fracture features along grains are obvious, as indicated by red arrows. Different orientations of river-patterns imply different orientated martensite blocks in the as-built sample. At high magnification, it is clear that plenty of precipitates are bare or embedded in the fracture walls, which is MX according to the above characterization and simulation results. In addition, it shows a typical ductile fracture feature in some zones (Fig. 35(d)). This zone might have low residual stress and texture, contributing to better deformation. As magnified in Figs. 35(e-f), the dimples have decreased depth with a relatively large size of 1 µm. There are several small precipitates clustered in the big dimples (yellow dashed circles). These precipitates are supposed to be MX. The micro-cracks are initiated at these precipitates and developed as a severe deformation area during the tensile process, which is beneficial to the ductility compared with the cleavage fracture mode. On the contrary, after the optimal heat treatment, the sample has a remarkably improved ductility of 19.4%, which is similar to standard wrought P91 steel. It has a much better combination of strength and ductility. Meanwhile, the UTS of the heat-treated sample is 774 MPa and the YS is 686 MPa, which far surpasses the strength of the standard wrought P91 steel by more than 200 MPa. The fracture surface is full of fine dimples, which is a typical ductile fracture mode (Fig. 36). The dimples are deeper with a finer size of around 500 nm. From high magnified images, it can be found that each dimple enfolds several precipitates. The precipitate is detected with enriched elements of Cr and Mo, and there is no enrichment of Nb or V (Fig. 36(f)). This demonstrates that these precipitates belong to M23C6 of which the typical rich elements are Mo and Cr. Beside the regular and small dimples, some big dimples are observed in severe deformation zones along the grain boundaries, as indicated in Fig. 19a. These dimples are attributed to large M23C6 particles (Fig. 36(c)) in them, because the $M_{23}C_6$ is easy to coarsen at grain boundaries. Therefore, the uniform fractures and dispersive distribution of precipitates results in an excellent combination of high strength and high ductility for the heat-treated P91 WAAM sample.

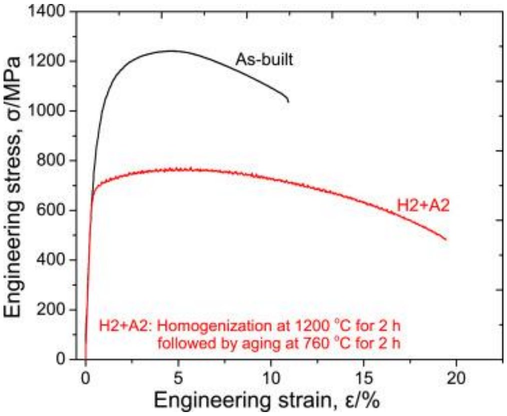

Figure 34.Tensile curves for as-bult and post-heat treated WAAM P91 steel.

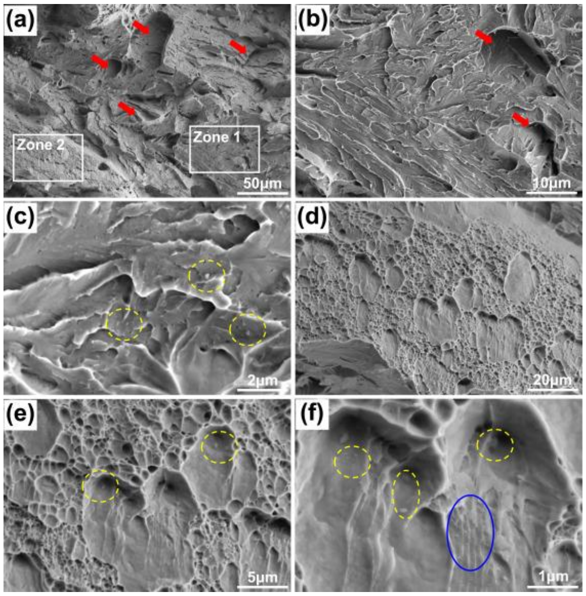

Figure 35. Surface fracture of the as-built tensile sample: (a) fracture overview at the low magnification, (b) and (c) SEM morphologies of Zone 1, and (d-f) SEM morphologies of Zone 2 at different magnifications. (red arrow-grain boundary, yellow dashed circle-MX in the matrix, blue circle-MX with very fine size along martensite lath boundary).

Table 2: Tensile properties of as-built and post-heat treated WAAM P91 steel.

Sample	***YS (MPa)***	***UTS (MPa)***	***Elongation (%)***
As-built	*985*	*1242*	*10.9*
Post-heat treated	*686*	*774*	*19.4*
Wrought	*415*	*585*	*20*

The tensile properties of as-built and post-heat treated of WAAM Inconel 740H superalloy is summarized in Table 3 and the engineering stress-strain curves are shown in Fig. 37. There is slight improvement in the YS and UTS with the optimized post-heat treatment. However, the ductility has reduced probably due to the hardness induced by the γ’ precipitates. The YS and ductility for the as-built and post-heat treated Inconel 740H superalloy are above the design targets specified by ASME Boiler and Pressure Vessel Code. However, the tensile properties are not superior in comparison with the tensile properties prescribed for Inconel 740H by Special Metals Co. This is possibly because from the hardness at different locations for the aged samples, it was found that the hardness in the middle portion was lower than the top and bottom locations. Since the gauge length of the sample is in the middle portion, the tensile properties are expected to be lower. The precipitation behavior could be probed further for understanding this observation.

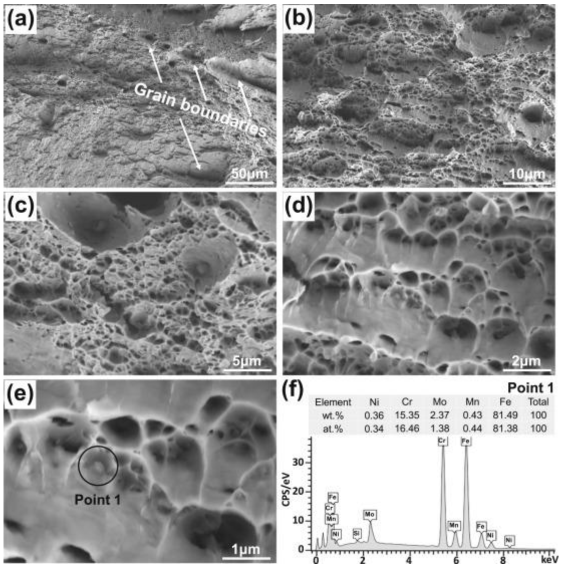

Element	Ni	Cr	Mo	Mn	Fe	Total
wt.%	0.36	15.35	2.37	0.43	81.49	100
at.%	0.34	16.46	1.38	0.44	81.38	100

Figure 36. Surface fracture of post-heat treated tensile sample: (a) fracture overview at the low magnification, (b-e) SEM morphologies at different magnifications and (f) EDS analysis of Point 1 in (e).

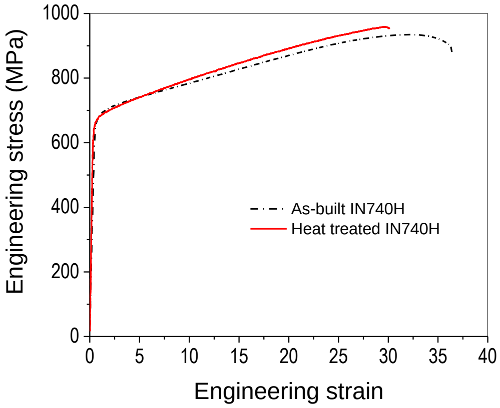

Figure 37. Tensile curves for the as-built and post-heat treated WAAM Inconel 740H superalloy.

Table 3:Tensile properties of as-built and post-heat treated WAAM Inconel 740H superalloy

Sample	***YS (MPa)***	***UTS (MPa)***	***Elongation (%)***
As-built	*649±19*	*925±14*	*37.5±2.4*
Post-heat treated	*655±18*	*963±11*	*29.5±1.2*
ASME Minimum	*620*	-	*20*

For high thermal energy density processes such as WAAM, the heat source movement is modelled as a double ellipsoid (Eq. 1). To model the wire deposition under a high energy electric arc in WAAM, the double ellipsoid heat source is synchronized with the element birth technique. A brief description of the thermal model for WAAM is provided below.

3.3 Mechanical modeling for single build Inconel 740H superalloy and P91 steel

3.3.1. Process-scale thermal model for WAAM

For high thermal energy density processes such as WAAM, the heat source movement is modelled as a double ellipsoid (Eq. 1). To model the wire deposition under a high energy electric arc in WAAM, the double ellipsoid heat source is synchronized with the element birth technique. A brief description of the thermal model for WAAM is provided below.

$$Q = \frac{6\sqrt{3}\eta P f}{abc\pi\sqrt{\pi}} exp\left(-\frac{3(x_0 + v_s t - x')^2}{a^2} - \frac{3(y' - y_0)^2}{b^2} - \frac{3(z' - z_0)^2}{c^2}\right) \quad (1)$$

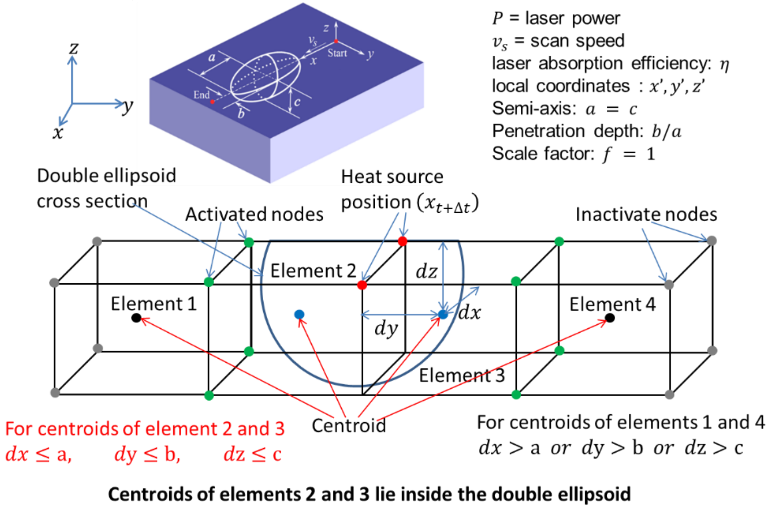

Figure 38. Schematic of element activation with heat source movement.

First, the location of the heat source at any time instant is identified, e.g., for a predefined time increment (Δt); the instantaneous location of the heat source along x axis is defined as $x_{t+\Delta t} = x_t + v_s\Delta t$, where v_s is the scan velocity. The centroids of the elements associated with the heat source position ($x_{t+\Delta t}$) are identified as shown in Fig. 38. For an element to be eligible for re-activation, its centroid should lie within the double ellipsoid bounded by the dimensions a, b, and c along the three axes. Thus, as illustrated in Figure 1, elements 2 and 3 are activated whereas; elements 1 and 4 remain inactive. The activation of elements for multiple layer deposition in WAAM is demonstrated in Fig. 39.

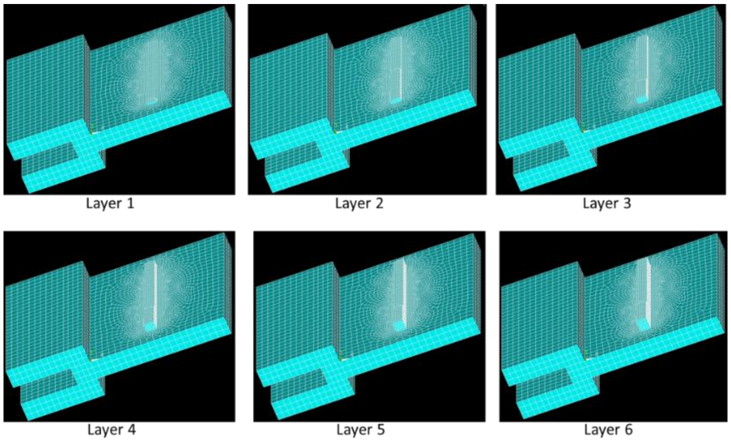

Figure 39. Demonstration of element activation for WAAM.

Specific to each of the alloys (P91 and Inconel 740H), the thermal model needs to be calibrated for the input power (P) and the double ellipsoidal heat source parameters (a, b and c) using the melt-pool dimensions measured experimentally. Therefore, the essential melt-pool dimensions required for calibration are length, depth, height, and width as shown in Fig. 40. The melt-pool length, depth and height will be measured using a high-speed camera in the side view during deposition at UTRC. For the melt-pool width dimension the solidified width, post deposition will be considered for model calibration. In addition to the melt-pool dimensions, the thermal model will be calibrated/validated by the far field temperature profile measured using thermocouples at the locations specified in Fig. 41. Note that, the results from the thermal model will be used to determine the grain evolution and for the part-scale residual stress analysis due to the process. Therefore, it is essential for the thermal model to accurately predict thermal gradients and cooling rates in the computational domain to calculate the in-process stresses using the inherent strain theory.

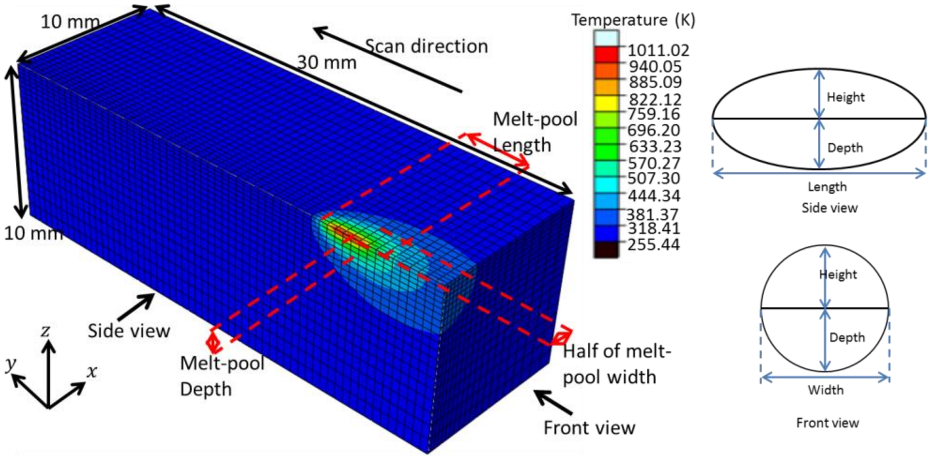

Cut section of computational domain

Melt-pool dimensions

Figure 40. Thermal model of WAAM with melt-pool dimensions.

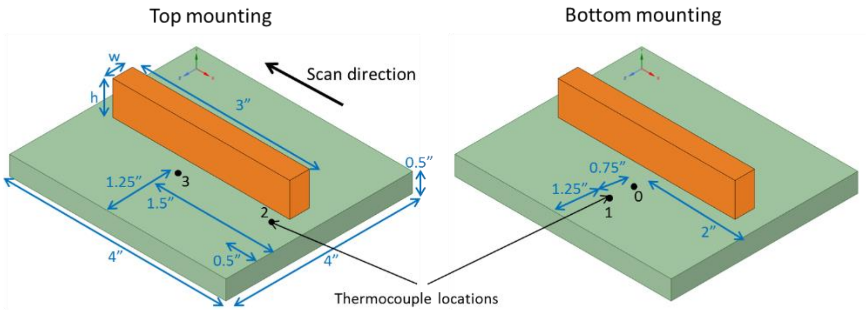

Dimensions indicated by blue color, thermocouple locations indicated by black color

- Thermocouple 2 (TC2 at the start of scan) to capture the temperature profile at the boundary

Figure 41. Thermocouple locations for measurement of far field temperature profile.

Thermal model: Calibration

The following major activities were performed for calibration of the thermal model to obtain a full thermal detailed simulation of the WAAM process:

a) The Goldak's heat source in the model was modified to add a front and rear parameter to capture the long tail of hot wire behind the torch.
b) The material properties and process parameters were adjusted to obtain a better process simulation
c) The model geometry was modified from a half model to a full model
d) A temperature-based inherent strain model was idealized.

The significant results from the thermal model are discussed in the following paragraphs.

a) The Goldak double ellipsoid heat source was modified to divide the heat source in a front and rear section. This captures the effect of having a tail behind the heat source that is at a higher temperature than the rest of the wire. The new parameters are shown in the image (Fig. 42) as a1 and a2 with the rest of the parameters remaining the same. The parameters for the front and rear distance were extracted from the infrared measurements conducted by RTRC.

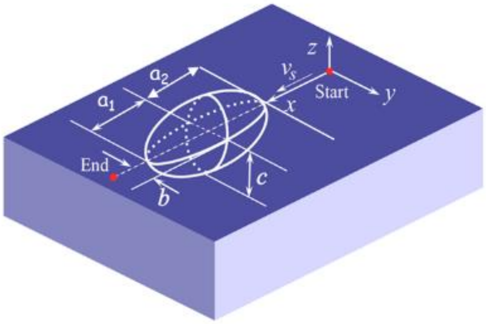

Figure 42. Goldak heat source.

b) The material properties and parameter for the materials were updated. The revised mechanical properties for Inconel 740H and A36 low carbon steel were added into the model. All the values were taken from published literature. The absorptivity parameter was modified into an arc efficiency parameter and given a value of 0.7. The absorptivity refers to the amount of energy that gets transferred from the laser into the material, because wire arc uses a welding power source, in WAAM the parameter is referred to as welding efficiency. The value of the efficiency depends on the welding technology being used and some properties inherent to the system. This value is usually between 0.7 and 0.85. All those changes added accuracy to the thermal model as seen in Fig. 43.

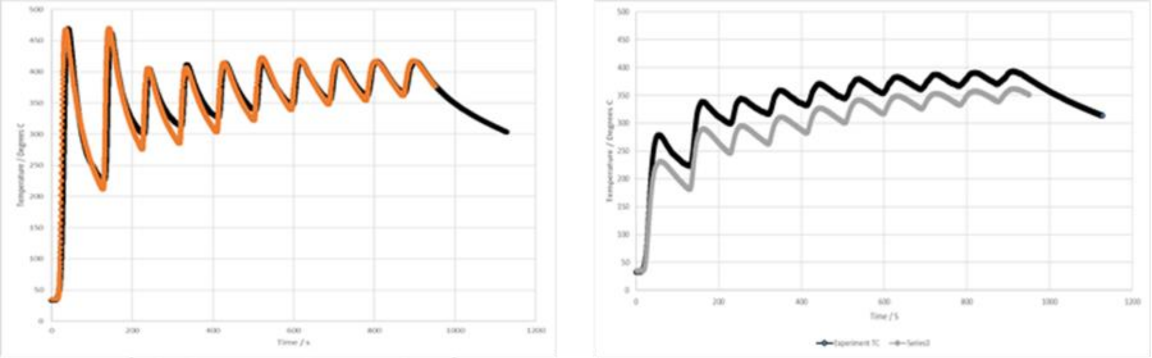

TC 0 (right under wire)

TC 1

Figure 43. Thermocouple data from the thermocouples at the bottom.

The focus of the calibration has been the two thermocouples at the bottom of the substrate. Those thermocouples were selected because they are free from the influence of plasma. Some of the data from the thermocouples at the top is believed to be modified by the plasma gas and not only the heat conduction from the wire.

c) The geometry of the entire substrate plate and the clamp was implemented and meshed. The new model is slower because of the additional elements in it. Figure 44 shows the temperature distribution during the printing process with the gray section being the dead elements that have not been printed yet.

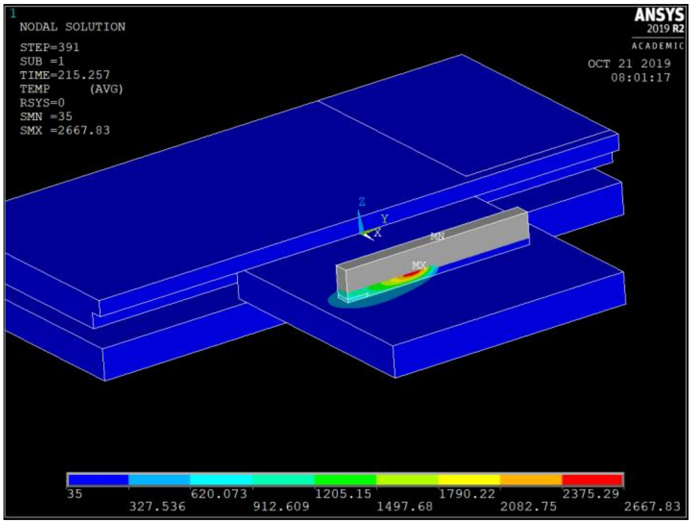

Figure 44. Thermal finite element analysis.

e) A new method for calculating the deformation caused by residual stresses has been idealized. This is needed because it would be impossible to perform a full simulation of a large WAAM part due to extended computation times. The solution needs to reduce the amount of simulation time without compromising model quality. A temperature-based inherent strain method was idealized to incorporate this technique into the WAAM process.

The method starts by performing a layer-by-layer thermal simulation of the entire part being studied. The layer-by-layer method applies heat to all the elements at once to obtain results in an accelerated way. Then, the average temperature of every layer is extracted.

Detailed simulations are then performed for each different average temperature found. The detailed simulation consists of a two-layer representative model from where the inherent strains are extracted. Finally, the corresponding inherent strains are applied to the entire part depending on the average temperature of the part. Further development of this method could allow us to reduce the number of detailed of simulations needed by clumping layers with similar temperatures together.

3.3.2. Heat source calibration

In order to calibrate the model heat source, the ICME team requested thermal measurements be performed on a range of WAAM deposits. Substrates were instrumented with thermocouples to capture the heat input during the deposition process of multi-layer buildup for different conditions with both materials. A schematic of the substrates is shown in Fig. 45, including thermocouple locations (orange) and the deposit location (blue). The build direction was held constants for all tests (i.e., single direction deposits).

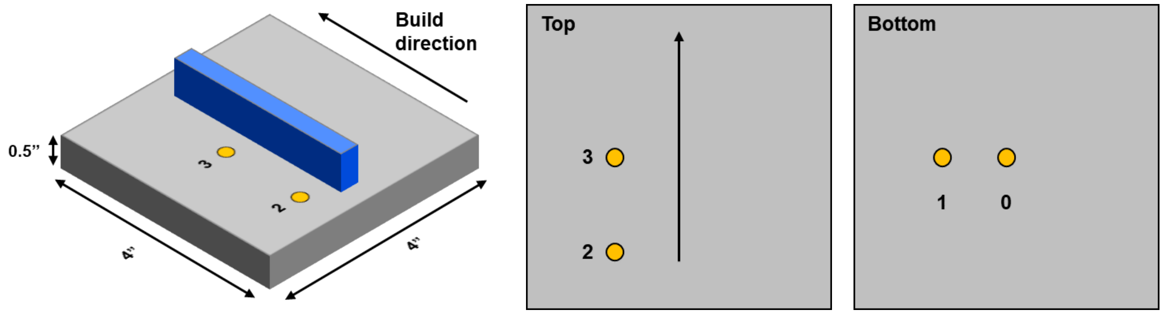

Figure 45. Thermocouple locations on the substrate for WAAM heat source calibration.

The first test on the thermocouple instrumented substrates was operated with the wire feeding disabled. This provided a representation of only the WAAM heat source to assist in model calibration. The process was operated with different plasma powers, representative of the range of power settings used in deposition of the test coupons. Here, the melt pool size is observed, which contains only melted substrate material. Subsequent tests introduced wire feeding for 10 layer deposits. Between layers, 60 seconds of cooling time was used to best represent the test coupons shown above. For each material, two deposits were produced. The first with higher power conditions, and the second with lower power conditions. The higher power conditions resulted in deposit widths on the order of 10 mm, while the lower power conditions were in the range of 6 to 8 mm. Example thermocouple data is shown in Fig. 46, along with the resulting 10 layer deposit (higher power, wide deposit).

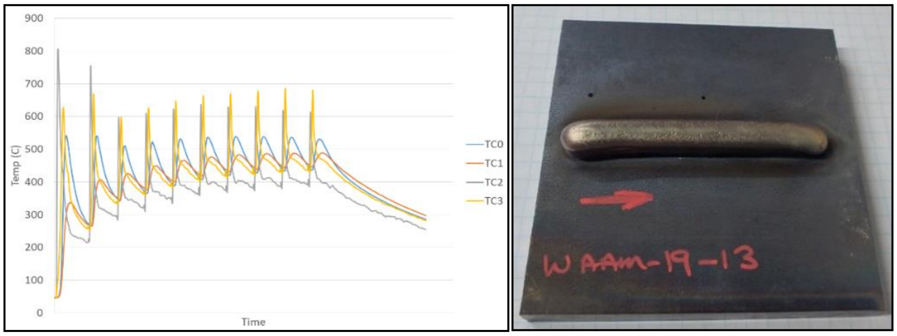

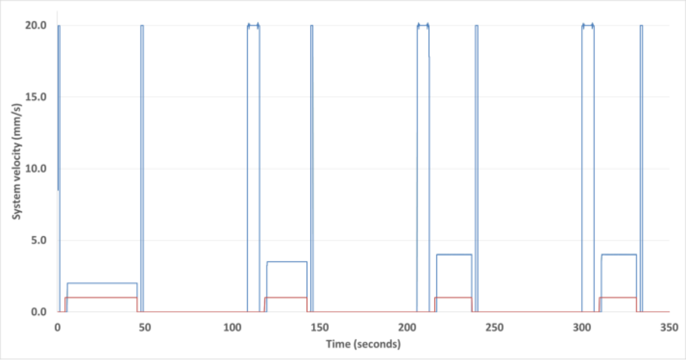

Figure 46. Thermal measurements from the four thermocouples (left) and the resulting 10 layer deposit (right) and System motion (velocity) for the first four layers of the IN740H "wide" deposit. Blue denotes the travel speed (mm/s), and red denotes whether the heat source (plasma) was on or off.

For the thermal measurements, the substrate was elevated off of the table, and clamped only along one edge (i.e., cantilevered). This provided access to the back surface for thermocouple placement, in addition to a controlled heat sink effect for the modeling team. For each layer, the melt pool was imaged and measured, to give the modeling team further calibration information along with the thermal data. To better assess the sequencing/timing during the process, process monitoring was utilized to depict the duration of the deposition as well as the dwell periods more accurately between layers (with resulting cooling). The robotic motion platform used for WAAM enables capture of actual process parameters, including travel speed along the toolpath. It was determined that the prescribed 60 second wait between layers resulted in an actual 74.5 second dwell, due to the system motion while retracting the robot away from the deposit and then returning to restart a subsequent layer. This data was used along with a confirmation of the travel speed and full cycle time, to provide a more accurate input to the model configuration. An example of the system motion is shown in Fig. 46. The system retract speed (20 mm/s) can be seen when moving into position and away from the deposit, adding to the overall dwell period between deposits. The red line indicates when the welding/deposition powder supply was on, during each deposit layer.

3.3.3. *Residual stress measurement using XRD*

Five locations on the surface of the substrate and on the deposit were selected for measurement of the residual stress in WAAM process. X-ray diffraction (XRD) measurements were conducted at American Stress Technologies, Inc. with a Stresstech Xstress 3000 Xrobot. Figure 47 shows the schematic of the XRD measurement locations marked as X1-5 and the thermocouple measurement locations as TC.

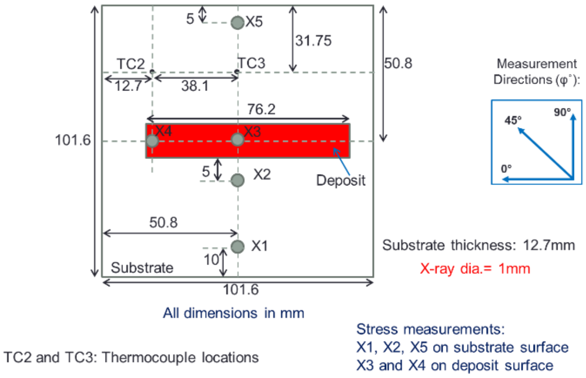

Figure 47. Schematic of XRD measurement locations.

Residual stresses were measured for In740H and B91 deposit, in compliance with experimental standards listed in Table 4 for the measurements parameters listed in Table 5. Most measurements were made with the goniometer in the modified psi configuration using the nominal tilt angles ψ of (0°, 18.4°, 26.6°, 33.2°, and 45°). In cases where the tilt range was limited due to mechanical interference, the goniometer Configuration was changed to omega-mode with tilt angles ψ of (0°, 18°, 25.9°, 32.4°, and 43.8°) to allow collimator "touch-off" and/or tilt access.

Table 4: Experimental standards

EN 15305	*Test Method for Residual Stress Analysis by X-ray Diffraction*
ASTM E915-16	*Standard Test Method for Verifying the Alignment of X-Ray Diffraction Instrumentation for Residual Stress Measurement*
SAE HS-784	*Residual Stress Measurement by X-Ray Diffraction*

Table 5: XRD measurement parameters

Tube Power	*30 kV x 6.6 mA, 100 %*
Collimator Size	*1 mm Ø*
Exposure Time	*6 seconds*
Meas. Directions (φ°)	*0, 45, 90*
Nominal Tilt Angles ($\pm\psi^{\circ}$)	*see text*
Oscillation	$\varphi \pm 4^{\circ}$
Peak Shift Analysis	*Cross-correlation*
Parabolic Level	*75 %*
Background/Threshold	*Linear, 48 px, 20 %*
d vs. $\sin^2\psi$ *analysis*	*Elliptical least squares fit*
Smoothing	*none*
Peak limits	*none*

Tables 6 and 7 lists the measured stresses along $0°, 45°, 90°$ for IN740H deposit and B91 deposit respectively. The reported uncertainty for each measurement only describes the quality of the fit of the d vs. $sin^2\psi$ data.

Table 6: Measured stresses along 0°,45°,90° for IN740H deposit

	Location [n]	σ_0 *[MPa]*	$\Delta\sigma_0$ *[MPa]*	σ_{45} *[MPa]*	$\Delta\sigma_{45}$ *[MPa]*	σ_{90} *[MPa]*	$\Delta\sigma_{90}$ *[MPa]*
Steel	*1*	*-78*	*3*	*-46*	*3*	*0*	*6*
	2	*114*	*9*	*100*	*5*	*85*	*7*
	5	*-73*	*3*	*-47*	*3*	*-3*	*4*
In70H	*3*	*-523*	*103*	*-459*	*97*	*-849*	*130*
	4	*-579*	*55*	*-553*	*72*	*-916*	*125*

Table 7: Measured stresses along 0°,45°,90° for B91 deposit

	Location [n]	σ_0 *[MPa]*	$\Delta\sigma_0$ *[MPa]*	σ_{45} *[MPa]*	$\Delta\sigma_{45}$ *[MPa]*	σ_{90} *[MPa]*	$\Delta\sigma_{90}$ *[MPa]*
Steel	*1*	*30*	*5*	*-9*	*8*	*-26*	*5*

	2	239	9	158	6	58	8
	5	-15	5	-36	5	-56	2
B91	3	116	32	113	43	41	64
	4	105	49	126	39	49	63

For the stress measured in the three directions ($\varphi = 0°, 45°, 90°$) the stress tensor components are:

$$\sigma_{11} = \sigma_0 \tag{2}$$

$$\sigma_{22} = \sigma_{90} \tag{3}$$

$$\tau_{12} = \pm\left(\sigma_{45} - \frac{\sigma_0 + \sigma_{90}}{2}\right) \tag{4}$$

From the stress tensor components $\sigma_{11}, \sigma_{22}, \tau_{12}$, the maximum principal stress (σ_{max}) and the minimum principal stress (σ_{min}) can be calculated as:

$$\sigma_{max}, \sigma_{min} = \frac{\sigma_{11} + \sigma_{22} \pm \sqrt{(\sigma_{11} - \sigma_{22})^2 + (2\tau_{12})^2}}{2} \tag{5}$$

For all directions, positive angles are clockwise and negative angles are counterclockwise. φ_{max} describes the direction of σ_{max} with respect to the 0° measurement direction. The direction of the principal plane (φ_{max}) is given by equation (5). Tables 8 and 9, lists the calculated principal stresses for In740H and B91 deposits respectively.

$$\varphi_{max} = \frac{1}{2} tan^{-1} \frac{2\tau_{12}}{\sigma_{11} - \sigma_{22}} \tag{6}$$

Table 8: Calculated principal stresses for IN740H deposit

	Location [n]	σ_{max} [MPa]	$\Delta\sigma_{max}$ [MPa]	σ_{min} [MPa]	$\Delta\sigma_{min}$ [MPa]	φ_{max} [°]
Steel	1	1	4	-79	4	85
	2	114	7	85	7	-2
	5	-1	3	-75	3	83
In70H	3	-406	116	-966	116	-27
	4	-490	92	-1005	92	-25

Table 9: Calculated principal stresses for B91 deposit

	Location [n]	σ_{max} [MPa]	$\Delta\sigma_{max}$ [MPa]	σ_{min} [MPa]	$\Delta\sigma_{min}$ [MPa]	φ_{max} [°]
Steel	1	32	5	-28	5	11
	2	240	7	58	7	-3
	5	-15	3	-56	3	0
B91	3	130	48	27	48	-21
	4	134	54	20	54	-30

Thermal model: Improvement

The Inconel thermal model was improved by changing the deposition direction and position to match the experiments conducted by RTRC. The IN740H sample that is being used to calibrate the model was measured with respect to the substrate plate and the location of the deposit was updated in the model. The thermal model results show good correlation between the experimental and the model results.

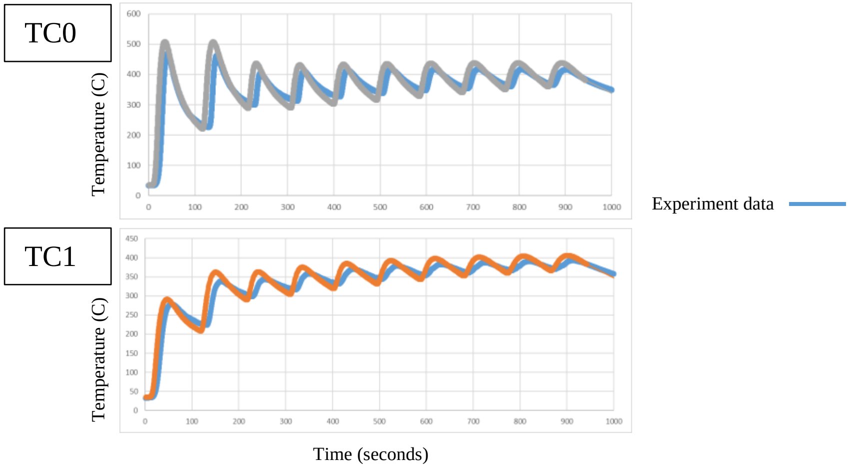

Figure 48. Inconel 740H thermocouple data for TC0 and TC1. Experiment data is shown in blue.

Additionally, the quasi-static mechanical model for Inconel 740H was implemented but the calibration process is not yet completed. X-ray diffraction (XRD) measurements of the samples printed by RTRC are being used to calibrate the model. The major challenge in this calibration is that due to the large grains that are form in Inconel 740H when printed using WAAM, the standard deviation of the stress measurements is very large (~100MPa). The other challenge in this calibration is that we are not certain about the mechanical properties of the substrate A36 steel. The stress results are shown in Table 4 which compares the XRD measurements against the model.

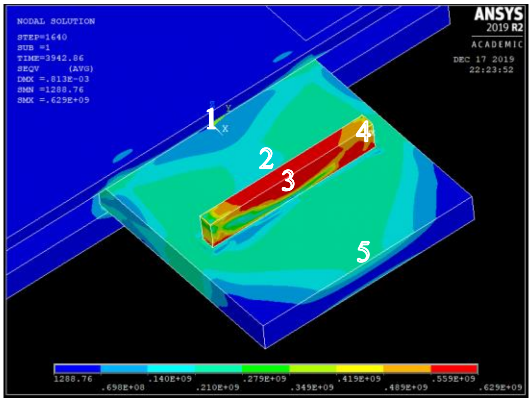

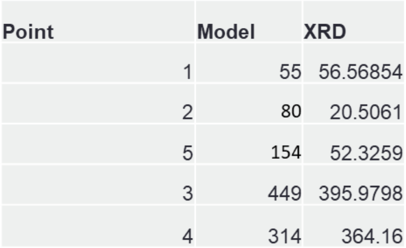

Point	Model	XRD
1	55	56.56854
2	80	20.5061
5	154	52.3259
3	449	395.9798
4	314	364.16

Figure 49. Stress distribution and a table comparing the model and experimental stress results in megapascals.

The team decided to start the calibration process of the P91 steel model to help determine the correct mechanical and thermal properties of the A36 steel substrate plate. Both models (IN740H and P91 steel) use the same material for the substrate plate, so the team would be able to confirm the calibrated properties from one model in the other model. Using this approach and the experience gained with the IN740H model, the team was able to quickly calibrate the thermal model for the P91 steel. The results from this calibration are shown below in Fig. 50. It should be noted that only one thermocouple is shown because the second thermocouple from the bottom of the plate detached at the beginning of the deposition process and no data is available. Similarly, to In740H, the thermocouples on the top are not being used because the model does not account on the influence of the plasma on them.

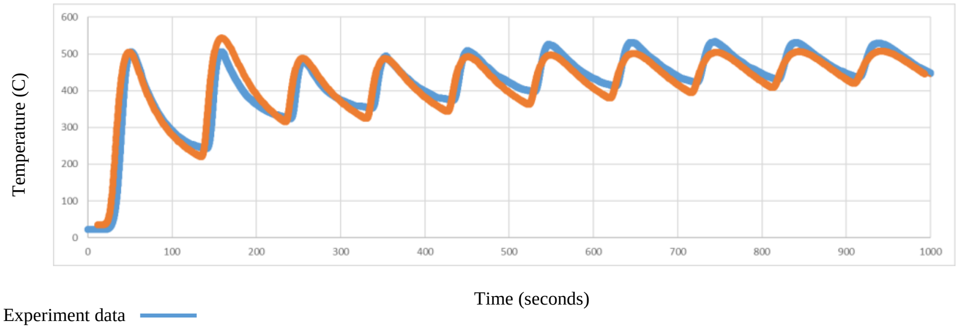

Figure 50. P91 steel thermocouple 0.

The team worked to calibrate the mechanical model for the P91 steel. It should be noted that the actual material that is used during the deposition is B91 steel, which is the welding filler used for P91 steel. There are not many studies into B91 material properties and because of this, the properties used for the thermal and mechanical model are for P91 steel. The results in Fig. 51 below show the stress distribution at the end of the deposition and show a table comparing the model against the XRD data. There is a large error between the model and the experiment, and so the team is continuing to calibrate the model.

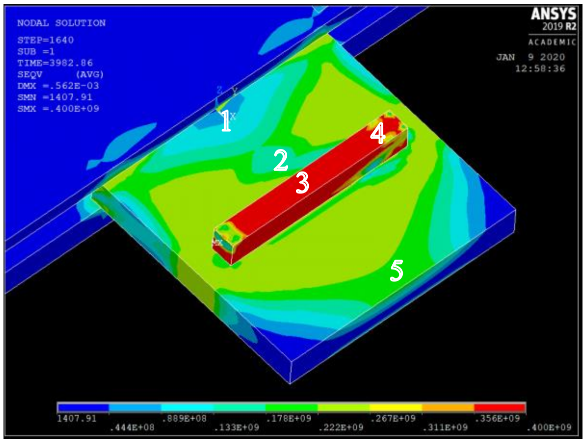

Point	Model	XRD
1	81	52
2	190	216
3	400	118
4	181	124
5	219	50

Figure 51. P91 stress distribution and stress results in megapascals.

The yield strength seems to be the property that controls the residual stress values, so the team has been working on modifying this property to reduce the error. The challenge is that the simulation becomes unstable and will stop converging when the yield strength for the steel becomes too low. To avoid this, the team is trying to improve the calibration of the yield strength by using hardness data. Although a hardness test cannot provide an exact yield strength value, we can use the data to understand the relative difference between the yield strength of the different materials. The team has performed hardness tests on both P91 and 740H but has not obtain results from the A36 substrate plate. Once this test is complete, the team will continue with the calibration process of the mechanical model.

3.3.4. *Thermomechanical modeling for single material deposition*

The thermal calibration for the single material build was completed by matching the thermocouple data to Pitt's transient heat model. The mechanical calibration was conducted by matching X-ray diffraction (XRD) data obtained from sample WAAM-19-11 and WAAM-19-13. The XRD measurements were performed by American Stress Technologies (Pittsburgh, PA). The location of the points where XRD was conducted are shown in Fig. 52, ranging from X1 to X5. X1 point is the side that was clamped and used to secure the build plate.

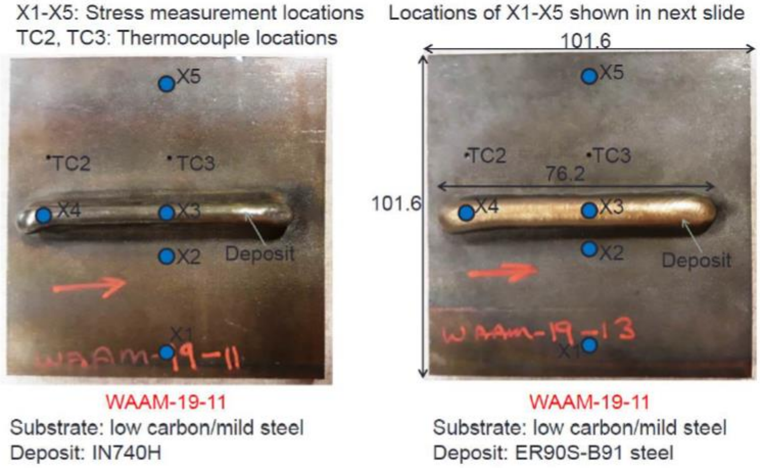

Figure 52. Location of XRD measurement points.

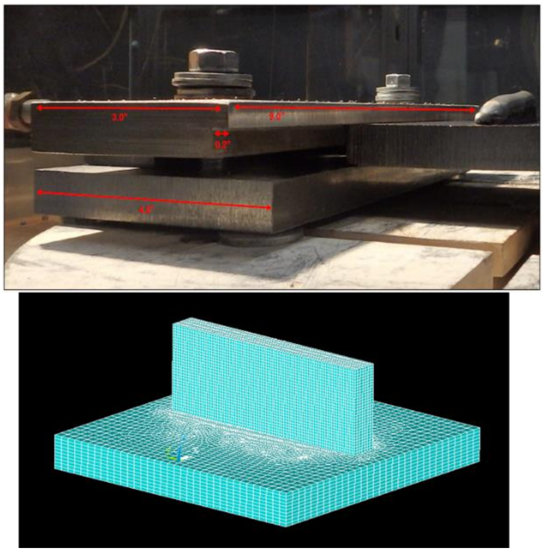

Figure 53. Clamps used to deposit single material wall (Top), Model of the clamp on ANSYS APDL (bottom).

The clamp used to hold the substrate plate during the deposition of the single material samples is pictured below in Fig. 53. The clamp was not explicitly modeled in ANSYS to reduce the number of elements in the model and increase the solver's speed. Instead, a boundary condition that represents the clamp was created by fixing the elements on the one edge of the substrate.

The quasi-static mechanical model uses the birth and dead technique to activate the elements following the deposition path. The necessary birth and dead calculations are performed during the thermal model and were explained in detail in previous reports. The In740H material properties were obtained from Special Metals Corporation (New York, NY). The model was solved using ANSYS APDL and the results are presented in Fig. 54. The XRD locations 1, 3 and 4 were correctly matched while locations 2 and 5 have a higher error. Location 5 is on the edge of the c-clamp, and it has a large error possibly due to not modeling the c-clamp completely. Point 2 in the XRD has a smaller error and a cause can be attributed to the A36 steel in the substrate going through a phase transformation or being stress relieved by the effect of the plasma from the torch. Because the XRD points on the deposit (IN740H) were closely matched, the results were accepted as adequate.

In the case of P91, the initial results had a large error in all XRD points. Artificially lowering the yield stress was not an option given than the residual stress was only about 125MPa compared to a yield stress of over 600 MPa. The team realized that there could be a phase transformation that is lowering the residual stress. During the printing, the deposited material undergoes multiple thermal cycles. Repeated heating and cooling result in solid-state phase transformations, a kind of microstructure evolution that can affect the residual stress distribution of the as-built part. For IN740H, the influence of the phase transformation can be neglected. But for P91, in view of the significant discrepancy between the simulation and experimental results, the phase transformation needs to be considered.

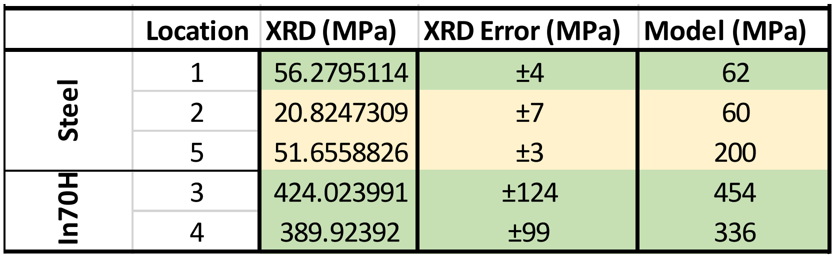

	Location	XRD (MPa)	XRD Error (MPa)	Model (MPa)
Steel	1	56.2795114	±4	62
	2	20.8247309	±7	60
	5	51.6558826	±3	200
In70H	3	424.023991	±124	454
	4	389.92392	±99	336

Figure 54. Results from single-material deposition of IN740H.

There are two types of phase transformations in each thermal cycle. When the material is heated up, the microstructure gradually transforms from ferrite to austenite (austenitic transformation). During the cooling process, the austenite is then transformed to martensite (martensitic transformation). Since the former has less effect on the stress field, in this study, only the martensitic transformation is modeled. The effects of martensitic transformation mainly include 1) volume expansion due to the lattice structure change (from face-centered cubic to body-centered tetragonal system); 2) yield strength change; 3) transformation-induced plasticity due to the atomic migration and reconstruction. The total strain increment including these effects is computed as follows,

$$\Delta\varepsilon_{total} = \Delta\varepsilon_{el} + \Delta\varepsilon_{pl} + \Delta\varepsilon_{th} + \Delta\varepsilon_{vol} + \Delta\varepsilon_{trip} \qquad (7)$$

where, $\Delta\varepsilon_{el}$, $\Delta\varepsilon_{pl}$, and $\Delta\varepsilon_{th}$ are elastic strain, plastic strain, and thermal strain increment, respectively. $\Delta\varepsilon_{vol}$ and $\Delta\varepsilon_{trip}$ are strain increments caused by volume expansion and transformation-induced plasticity, respectively. The strain increment accounting for volume expansion can be calculated by,

$$\Delta\varepsilon_{vol} = \varepsilon_0 \Delta f_m \quad (M_f < T < M_s) \qquad (8)$$

where, $\varepsilon_0 = 3.75 \times 10^{-3}$ is the total strain increment of volume change if all austenite transforms to martensite. Δf_m is martensitic volume fraction increment and is given by modified Koistine-Marburger formula,

$$\Delta f_m = 1.141\left[-0.011 e^{0.011(T-M_s)}\Delta T\right] \quad (M_f < T < M_s) \tag{9}$$

where, T is the current material temperature. ΔT is the temperature increment. $M_s = 375°C$ is the starting temperature at which the martensitic transformation begins $M_f = 185$°C is the ending temperature at which the transformation completes. It assumes that the material contains only austenite when it starts to cool down and all of them is transformed to martensite when the temperature reaches M_f. It means that f_m changes monotonously from 0 to 1 in each thermal cycle. As for $\Delta\varepsilon_{trip}$, a simplification is adopted. The influence of the transformation-induced plasticity is considered by reducing the yield strength when the temperature drops below M_s. ANSYS user material subroutine USERMAT is utilized to calculate and apply the strain increments of $\Delta\varepsilon_{vol}$ and $\Delta\varepsilon_{trip}$ and the change of yield strength. By doing so, the effect of the phase transformation on the stress field is included. The results from B91 steel with the phase transformation are shown in Fig. 55. The model was solved in ANSYS APDL using material properties

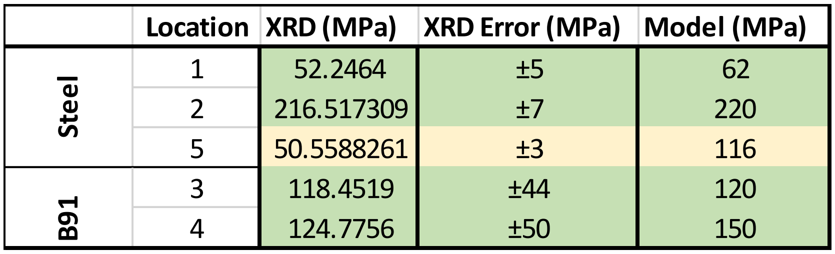

	Location	XRD (MPa)	XRD Error (MPa)	Model (MPa)
Steel	1	52.2464	±5	62
	2	216.517309	±7	220
	5	50.5588261	±3	116
B91	3	118.4519	±44	120
	4	124.7756	±50	150

Figure 55. Results from single-material deposition of P91 steel.

The two single material models were tuned based on residual stress data from the XRD measurements. Tensile testing at room temperature was performed by RTRC on different samples that were build using a more complex deposition path and not just a straight-line path. The results show that the yield strength of these samples is higher than the yield strength used to tune the models as shown in Fig. 56. This is because the more complex deposition path increases the strength of the part during tensile testing.

	Tensile Test		**Model**
Material	**Yield Stress (MPa)**	**UTS (MPa)**	**Yield Stress (MPa)**
Inconel 740H	641	896	424
Steel P91	875	1241	600

Figure 56. Tensile test results by RTRC compared with the modeling results.

3.3.5. *Grain structure predictions*

To predict the size, shape (elongation direction and aspect ratio) and texture of polycrystalline grains in metal Wire-Arc Additive Manufacturing (WAAM), a Discrete Dendrite Dynamics (DDD) model is developed. In metal AM, due to the relatively high thermal gradient present across the deposited layers, columnar grains with stable columnar dendrites in one primary direction are commonly observed. The grain growth model predicts the grain size, shape and texture of the columnar grains based on the melt-pool geometry and the temperature profile of the melt pool will be obtained from a thermal modeling. The thermal model defines the liquidus isotherm (melt pool geometry) at each time step as the quasi-steady melt-pool with a constant geometry for each track. Additionally, the cooling rate, and thermal gradient along the boundary of the melt pool, is also obtained from the thermal model. In FCC and BCC, the columnar dendrite arm grows along one of the $< 001 >$ axes, which most closely align with the local thermal gradient $(\overline{G_i})$. Therefore, in a polycrystalline material, the final dendrite direction at a location (x_i, y_i, z_i) is along one of the $\bar{m}_{hkl,j}$ directions of the initial seed crystal ($j = 1{:}\, N_{seed}$), such that $cos\varphi = (\bar{m}_{hkl\ j} \cdot \bar{G}_i)/|\bar{G}_i|$ is the maximum. The grain growth model integrates the dendrite lines grown along the same direction to determine the overall crystallographic orientation distribution (grain texture) and shape of the solidified metal. At present, the grain growth model uses centroidal Voronoi tessellation for a relatively high initial number of seed crystals ($N_{seed} = 100{,}000$) to generate fine-grained random-textured polycrystalline base metal seed crystal orientations. In the future, the actual polycrystalline base metal seed crystal orientation information obtained from EBSD measurements will be used to simulate the grain growth and hence calibrate the grain growth model, if required.

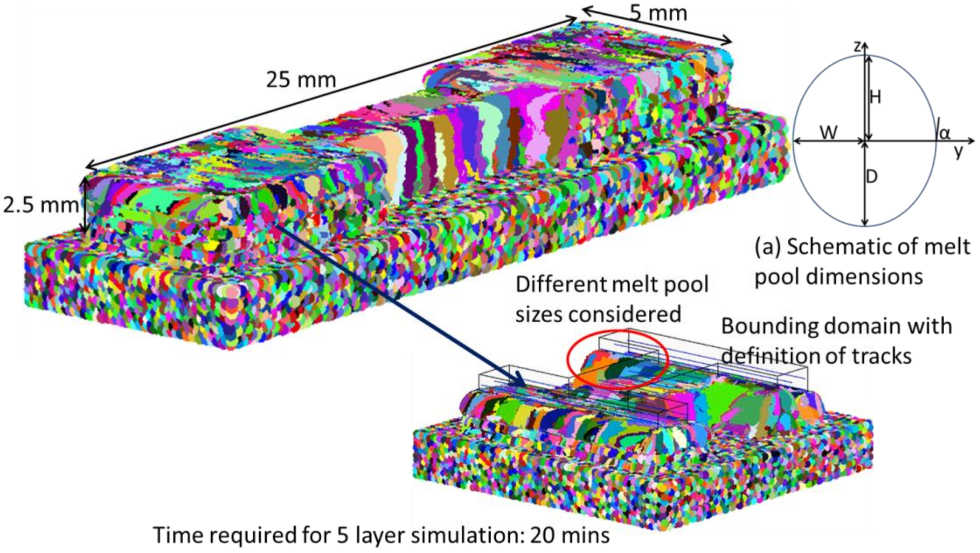

Figure 57. Predicted grains in a tensile bar.

In the WAAM technique of metal AM, the trailing part (solidification front) of the quasi-steady melt pool can be modeled as a segment of an ellipsoid and described by five geometrical parameters (W, L, D, H, α), with W being half the maximum width, L being the maximum length, D being the maximum depth, H being the maximum height of the melt pool and α being the angle between the substrate surface and the tangent of the melted trace in the transverse cross-section. The melt-pool dimensions, represented as a schematic of the transverse melt-pool cross-section in the insight (a) in Fig. 57, determine the grain size in the solidified metal. In WAAM, the varying thermal energy input to the system during wire deposition will lead to variations in the melt pool geometry. Therefore, in the current model, the variation in melt pool shape is employed by changing the melt-pool dimensions (W, L, D, H, α) as shown in Fig. 57. In future, the melt-pool dimensions, $W, D,\ H$ and α, measured experimentally from the transverse cross-section of WAAM deposited single tracks will be used as input in the grain growth model. For demonstration, the grains in a tensile bar with 5 scan layers and scan direction of 0° are predicted using the current model (Fig. 57) in MATLAB. In the model, the scanning tracks are defined within the bounding domain (tensile bar specimen shape). To simulate the varying melt pool sizes (5 in this case) for different tracks, the model initially stores the melt pool information (W, L, D, H, α). This melt pool information is then randomly mapped to different scanning track number, prior to the grain growth simulation. Thus, based on the grain texture for the track and the melt pool information for track, the size, shape, and texture of polycrystalline grains is predicted.

Following the grain growth prediction for a tensile bar, the DDD model is used to simulate the grain growth in a 63mm × 6mm × 50mm size column as shown in Fig. 58. The substrate is mild steel with the deposit of IN740H with the build direction (BD) along the z-axis. The inputs required in the grain growth model are the melt pool width, depth, and height. These values were obtained from the optical measurements conducted by Dr. Xiong's group at Pitt, on the WAAM processed In740H sample. In consultation with RTRC, it was known that a raster period of 2.5 mm used in the original pattern. However, due to the fast raster movement, the melt pool tends to stretch the full width of the deposit. Hence to reduce the computational cost, single line scan pattern with a melt pool width of 6 mm is used, as shown in Fig. 58.

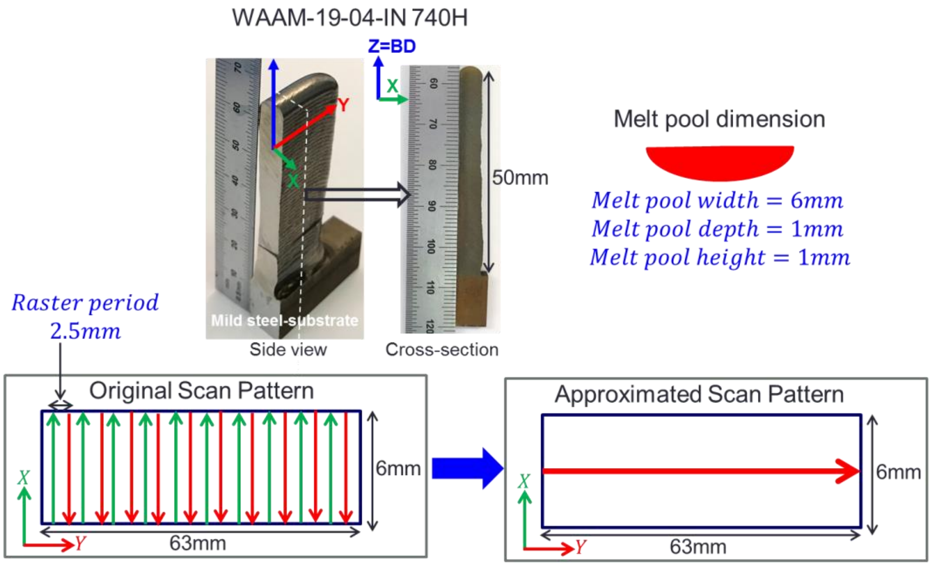

Figure 58. Melt pool dimensions and scan pattern used for grain growth simulation.

Comparison of grain texture

For the WAAM processed IN740H sample, the cross section of the microstructure and the pole figures were measured using EBSD at various locations along the height (Figs. 59 and 60). In these Figures, only 1/4th of the simulated domain is displayed, due to memory limitation in MATLAB R2018b. Short columnar grains along the build directions in the bottom section (Fig. 59) are observed from EBSD. The same is also predicted by the grain growth model. Additionally, the pole figures at the highlighted location are also compared. Expectedly, dispersed poles are predicted by the model and compared well with the EBSD measurements. Figure 60 compares the texture at a middle location along the column height. Columnar grains along the build direction are predicted by the grain growth model. The distinct pole distribution for [001], [111] and [110] predicted by the grain growth model matches exactly with the EBSD measurement. To develop microstructure-property relationship for uniform alloy composition, the microstructure of In740H was predicted using the grain growth model. The microstructure of P91 will be predicted and the microstructure-property relation for IN740H and P91 will be established.

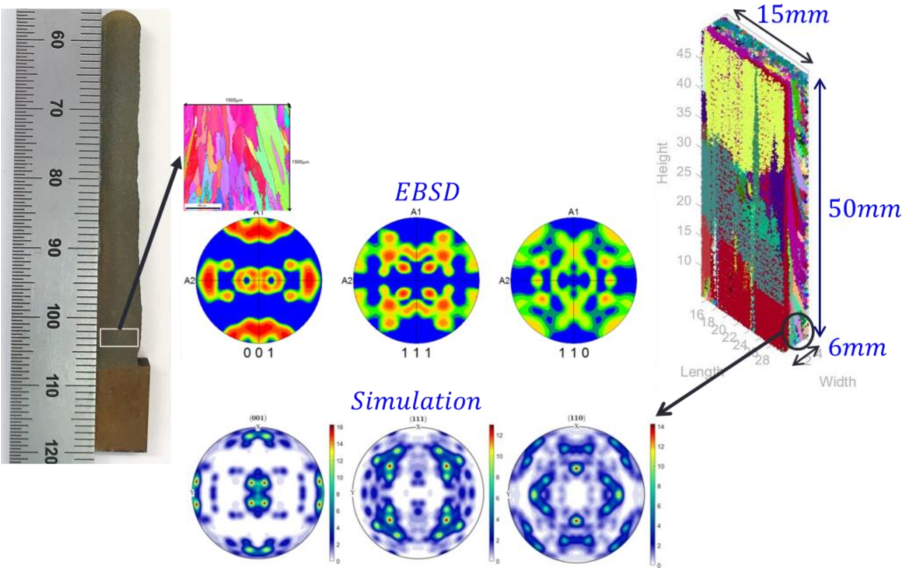

Figure 59. Comparison of texture at bottom.

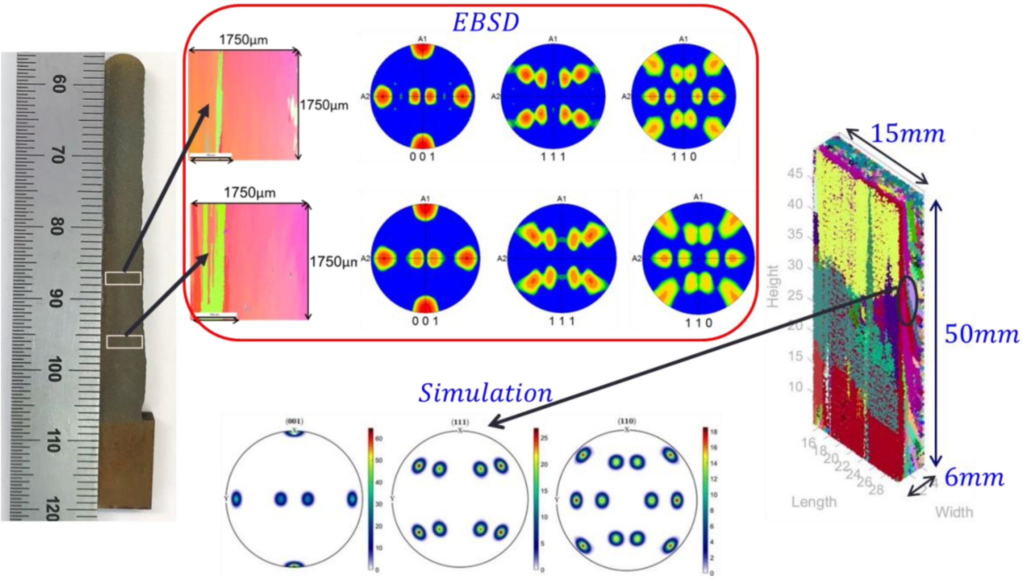

Figure 60. Comparison of texture in middle.

3.3.6. Process-Structure-Property relationship in WAAM

Anisotropy in mechanical properties of the printed components is a common feature associated with WAAM. This is due to the presence of elongated grains along the build direction. The epitaxial columnar grain growth model can predict the shape, size, orientation, and texture of the polycrystalline grains in a 63mm × 6mm × 50mm size In740H column. As shown in Fig. 61, the present work discusses the relation between microstructure and properties of IN740 components manufactured by WAAM. In this work, the mean field polycrystal plasticity model, by Liu et al. [9], for prediction of uniaxial stress-strain relation is briefly discussed. The input to the polycrystal plasticity model is the shape, size, and orientation of the polycrystalline grains. Additionally, using the microstructure input at different locations along the height of the IN740H column, the variation in the stress-strain relation is predicted, in this work.

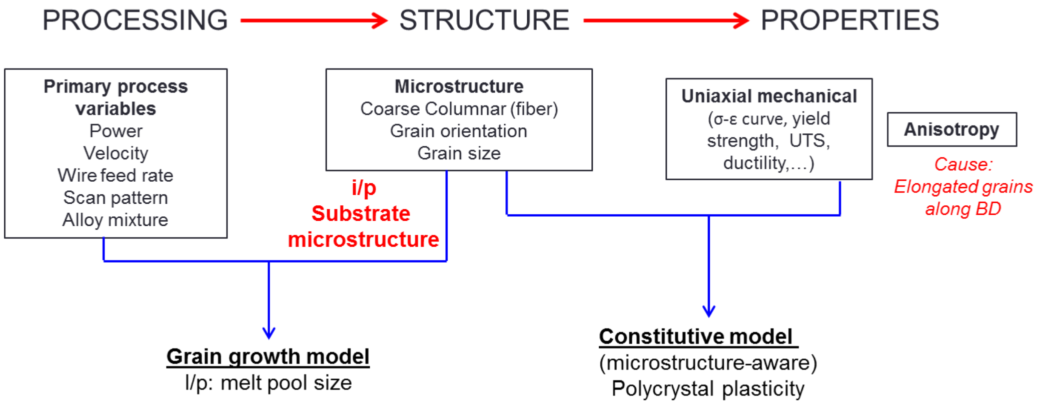

Figure 61. Schematic of process-structure-property relation in WAAM.

Polycrystal plasticity model

The FEM based polycrystal plasticity model simulates the deformation of the part along a certain strain path, with each integration point (IP) corresponding to a polycrystal material point consisting of many grains. The deformation of each IP is calculated by the Taylor's iso-strain homogenization scheme which assumes homogeneous deformation within each grain. The deformation of each constituent grain is solved using the single crystal plasticity formulation on the slip systems level. The constitutive equations on the slip system level consist of a rate equation and a hardening law. The rate equation relates the slip rates $\dot{\gamma}^{\alpha,N}$ to the Cauchy stress tensor σ^N of the N^{th} grain through a flow rule given by:

$$\dot{\gamma}^{\alpha,N} = \dot{\gamma}^{0,N}\left|\frac{(b^{\alpha,N}\otimes n^{\alpha,N}) : \sigma^N}{\tau_c^{\alpha,N}}\right|^{\frac{1}{m}} sign\left(\frac{(b^{\alpha,N}\otimes n^{\alpha,N}) : \sigma^N}{\tau_c^{\alpha,N}}\right) \tag{10}$$

where, $\dot{\gamma}^{0,N}$ is the reference strain rate, $b^{\alpha,N}$ is the slip direction vector, $n^{\alpha,N}$ is the slip plane normal vector for slip system α of grain N in the current configuration and m is the rate sensitive parameter. $\tau_c^{\alpha,N}$ is the critical resolved shear stress (CRSS) of the slip system α representing its resistance to shearing. In the polycrystal plasticity model, the evolution of CRSS is dependent on the shape, size and the crystallographic orientation of the constituent grain using a hardening rule given by:

$$\tau_c^{\alpha,N} = \tau_0^{\alpha} + (\tau_1^{\alpha} + \theta_1^{\alpha}\Gamma^N)\left[1 - \exp\left(\frac{\theta_0^{\alpha}}{\tau_1^{\alpha}}\Gamma^N\right)\right] + K_1(d^{\alpha,N})^{-1/2} + K_2(l)^{-1/2} \tag{11}$$

where, Γ^N is the accumulated shear strain in the grain, τ_0^{α} is the CRSS at the onset of plasticity, θ_0^{α} is the initial hardening rate and θ_1^{α} is the asymptotic hardening rate. The effect of grain shape and orientation is incorporated using a modified micro-Hall-Petch term (grain size effect due to slip systems). The elongated columnar grains are modeled as ellipsoids with two short axes and a third long axis as shown in Fig. 62(a). The morphology (size and shape) is represented by an effective grain size $d^{\alpha,N}$, an aspect ratio $R^{\alpha,N}$ (ASR), and the elongation direction (orientations of major axis in the morphological coordinate system) $\theta^{\alpha,N}$. The effective grain size is defined as $d^{\alpha} = f(n^{\alpha}, a, b, c)$ and n^{α} is the grain orientation (defined in terms of the Euler angles) relative to the semi-principal axes a, b, c of the ellipsoid grain. The microstructure data format input required for the polycrystal plasticity model is same as the Orientation (Imaging) Microscopy (OIM) data format from EBSD, as shown in Fig. 62(b). Hence, the microstructure data from EBSD along with the polycrystal plasticity model can be used to predict the mechanical properties of samples manufactured using WAAM.

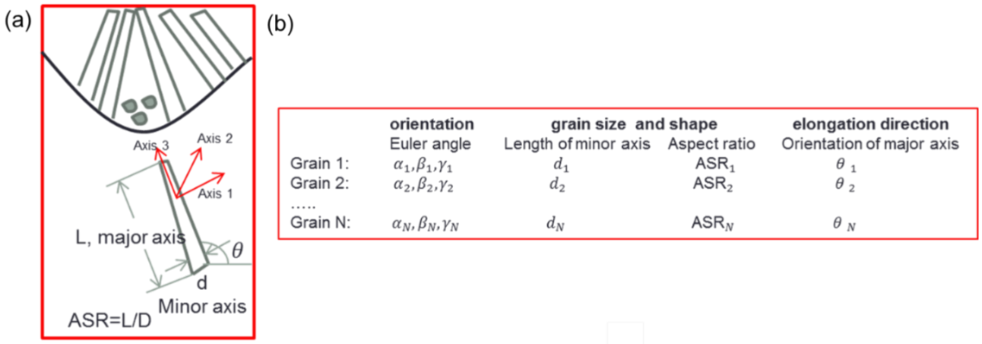

	orientation	grain size and shape		elongation direction
	Euler angle	Length of minor axis	Aspect ratio	Orientation of major axis
Grain 1:	$\alpha_1,\beta_1,\gamma_1$	d_1	ASR$_1$	θ_1
Grain 2:	$\alpha_2,\beta_2,\gamma_2$	d_2	ASR$_2$	θ_2
…..				
Grain N:	$\alpha_N,\beta_N,\gamma_N$	d_N	ASR$_N$	θ_N

Figure 62. (a) Schematic of grain assumed as an ellipsoid, (b) build in format of OIM.

Variation of property along the height

Combining the epitaxial columnar grain growth model and the polycrystal plasticity model the microstructure-property relation for uniform alloy composition (IN740H) is established. Fig. 63(a) shows the difference in the microstructure at different heights in the column. Note that, the microstructure of the 63mm × 6mm × 50mm In740H column was predicted using the grain growth model. Fig. 63(a) also, shows the simulation results of the tensile stress–strain curves along the build direction for columnar grains. The difference in the stress-strain curves due to different effective grain size between the bottom and middle regions of the column, is evident from Fig. 63(a). The model predicts higher hardening rate in the middle region even though the difference in yield stress is insignificant. Figure 63(b) shows that significant anisotropy exists in the middle regions of the column compared to the bottom regions due to difference in the grain shape in the two regions. The results presented in the current report demonstrates the extent of the polycrystal plasticity model, with improvements possible with the calibration of the model.

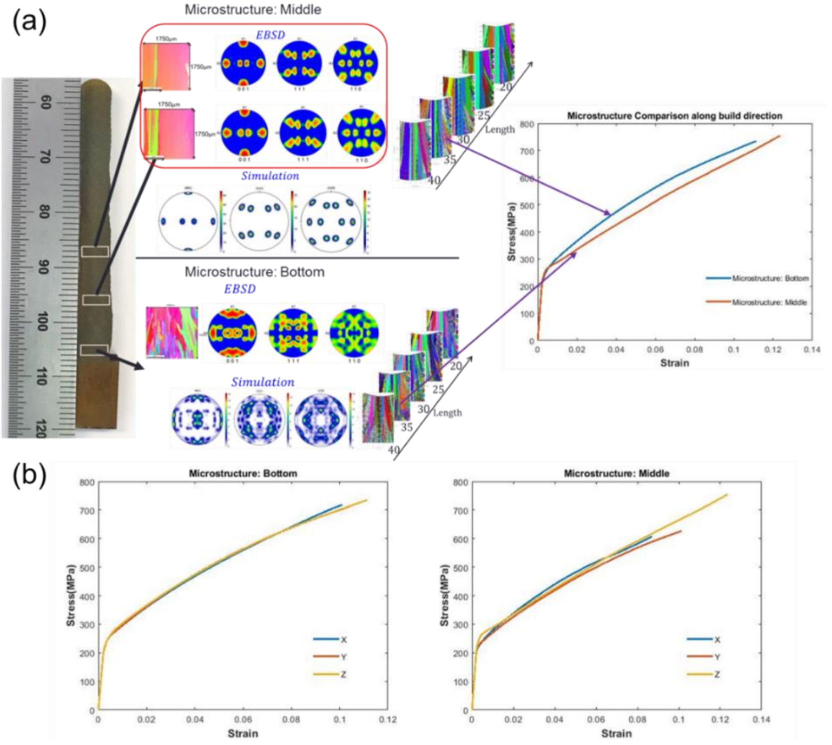

Figure 63. Comparison of microstructure-property relation along the height.

3.4 Computational design and experimental investigation for graded alloys

3.4.1 Optimum deposition sequence for graded alloys with sharp interface

Characterization of as-built graded alloys with sharp interface

The parameters used to build the gradient alloys between P91 steel and IN740H superalloy using WAAM is summarized in Table 10. Two types of graded alloy builds (named G7 and G8) were obtained using different printing strategy as shown in Fig. 64. Sample G7 was built by depositing 15 layers of P91 steel with an interpass cooling of 60 seconds over the mild steel substrate and subsequently allowed to cool for 120 minutes (2 hours). After the cooling period, 15 layers of IN740H superalloy was deposited over the P91 steel with an interpass cooling of 60 seconds. On the other hand, sample G8 was built by depositing 15 layers of IN740H superalloy over the mild steel substrate with an interpass cooling of 60 seconds, followed by cooling for 20 minutes. Successively, 15 layers of P91 steel was deposited with an interpass cooling of 60 seconds. This approach was followed mainly to study the effect of the sequence of deposition on the characteristics of the gradient zone.

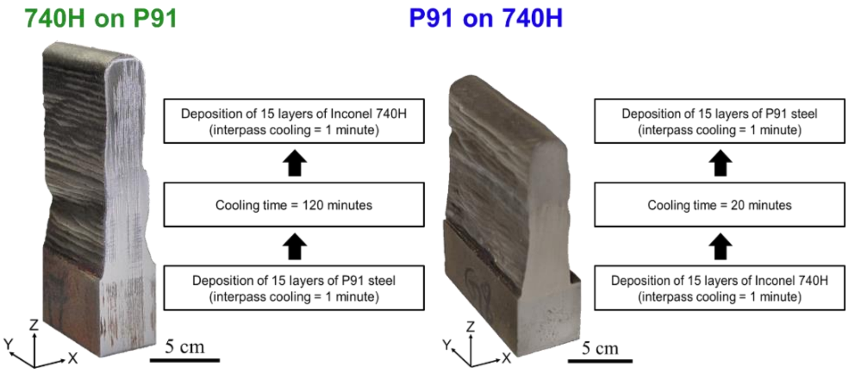

Figure 64. Deposition strategies used for 740H on P91 (G7) and P91 on 740H (G8) builds.

Table 10: Building parameters for deposition of graded alloys with sharp interface using WAAM

Layer	***Voltage (V)***	***Current (A)***	***Travel speed (mm/s)***	***Wire feed (m/min)***	***Hatch spacing (mm)***
		G7 (740H on P91)			
Layer 1	*20.9*	*255*	*2*	*3.10*	*1*
Layer 2	*20.9*	*245*	*3*	*3.10*	*1*
Layer 3	*20.9*	*230*	*3*	*3.10*	*1*
Layer 4	*20.9*	*220*	*3.5*	*3.10*	*1*
Layer 5	*20.9*	*200*	*4*	*3.10*	*1*
Layer 6-15	*20.9*	*188*	*4*	*3.10*	*1*
Layer 16	*20.9*	*188*	*4*	*3.10*	*1*
Layer 17	*20.9*	*180*	*4*	*2.50*	*1*
Layer 18	*20.9*	*175*	*4*	*2.50*	*1*
Layer 19	*20.9*	*170*	*4*	*2.50*	*1*
Layer 20-25	*20.9*	*165*	*4*	*2.50*	*1*
Layer 25-30	*20.9*	*158*	*4*	*2.50*	*1*
		G8 (P91 on 740H)			
Layer 1	*20.9*	*255*	*2*	*2.50*	*1*
Layer 2	*20.9*	*245*	*3*	*2.50*	*1*
Layer 3	*20.9*	*230*	*3*	*2.50*	*1*

Layer 4	*20.9*	*220*	*2.5*	*2.50*	*1*
Layer 5	*20.9*	*210*	*4*	*2.50*	*1*
Layer 6-8	*20.9*	*200*	*4*	*2.50*	*1*
Layer 9-10	*20.9*	*193*	*4*	*2.50*	*1*
Layer 11-15	*20.9*	*180*	*4*	*2.50*	*1*
Layer 16	*20.9*	*210*	*4*	*3.10*	*1*
Layer 17-20	*20.9*	*200*	*4*	*3.10*	*1*
Layer 21	*20.9*	*195*	*4*	*3.10*	*1*
Layer 22-30	*20.9*	*190*	*4*	*3.10*	*1*

The BSE-SEM micrograph of the as-built G7 and G8 samples in the gradient zone is shown in Fig. 65. A marked difference in contrast of the heat-affected zone (HAZ) in comparison with the P91 and IN740H alloys is evident in G7. The width of the gradient zone was measured to be ~ 60 μm using image analysis. The smaller width of the HAZ is due to the longer cooling period (120 mins) between the deposition of the P91 steel and the IN740H superalloy. However, the gradient zone is larger with an average size of nearly 2200 μm in the G8 and cracks were visible in the gradient zone. The larger gradient zone formed in this sample is due to the shorter cooling time (20 minutes) between the deposition of IN740H superalloy and P91 steel. The microhardness maps measured with a load of 300 grams and dwell time of 10 seconds for the G7 and G8 samples are presented in Fig. 66. It can be observed that the hardness is the lowest at the interface between P91 and 740H in the G7 sample. On the other hand, the hardness was lower in both the large gradient zone formed at the interface between the P91 and 740H and between the 740H and the mild steel substrate in the G8 sample. The composition across the G7 and G8 samples along the build direction was determined using EDS, as shown in Fig. 67. It is evident that there is a long-range diffusion of Fe into the IN740H alloy for ~3000 μm, which will be considered as the gradient zone for the G7 sample. In the G8 sample, It can be observed that there is a sudden decrease of the Ni composition and a drastic increase in the Fe content as it shifts from the 740H superalloy region to the gradient zone. Concomitantly, a significant decrease in the Cr and Co content is also evident in the interface between the 740H superalloy and the gradient zone. On the other hand, the transition in composition of the major elements such as Fe, Ni, Co and Cr are rather smooth as it shifts from the gradient zone to the P91 steel. Moreover, it can be clearly seen that the composition of Fe, spikes downward in certain regions along with a simultaneous increase in the composition of Nb and Ti throughout the gradient zone. The regions with spikes in the composition profiles of Fe, Nb and Ti, corresponds to the MC carbides, hence, confirming the presence of this phase throughout the sample. The IPF and phase maps obtained using EBSD for the G7 and G8 samples across the gradient zone are shown in Fig. 68. A large area spanning 750 x 750 μm^2 was scanned in order to capture the HAZ in G7 sample. It is evident from these maps that the HAZ is martensitic with the BCT structure similar to the steel. Also, there is very little dilution between the P91 steel and the IN740H superalloy. In the G8 sample, a very large region spanning 3000 x 3000 μm^2 area was scanned to capture the whole gradient zone in this sample. The black dots indicate the microhardness indents that act as markers to identify the gradient zone. It was observed that the gradient zone has an FCC structure similar to the superalloy. However, the grains are large and equiaxed, in contrast to the long columnar grains formed by the IN740H superalloy. Also, the dilution between the gradient zone and P91 steel is very small.

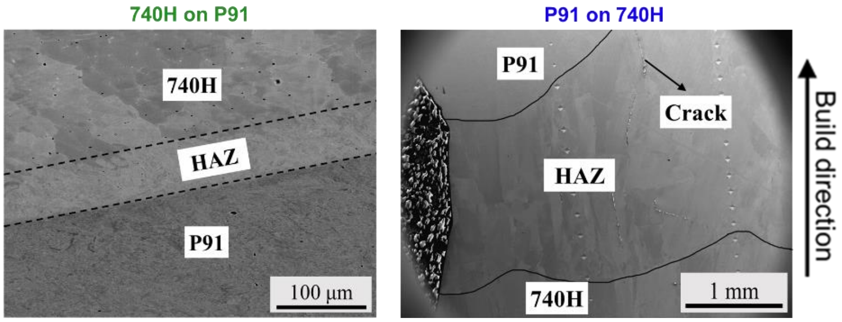

Figure 65. BSE-SEM micrographs across the interface for 740H on P91 (G7) and P91 on 740H (G8) builds.

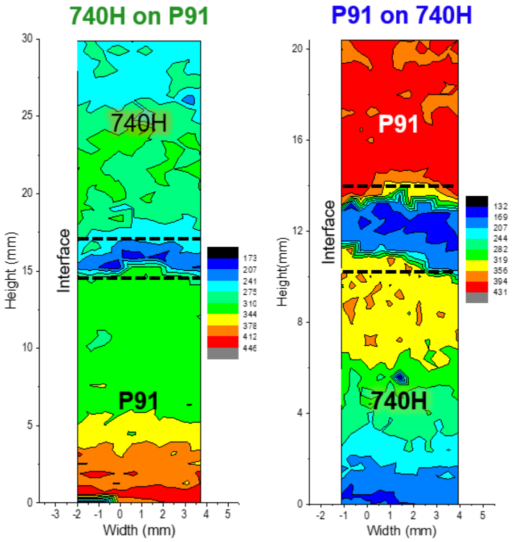

Figure 66. Microhardness maps for 740H on P91 (G7) and P91 on 740H (G8) builds.

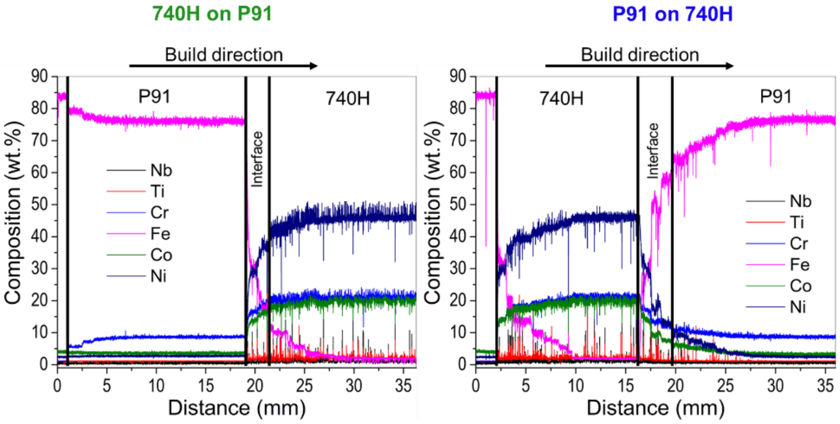

Figure 67. Composition profile across the build direction for 740H on P91 (G7) and P91 on 740H (G8) builds.

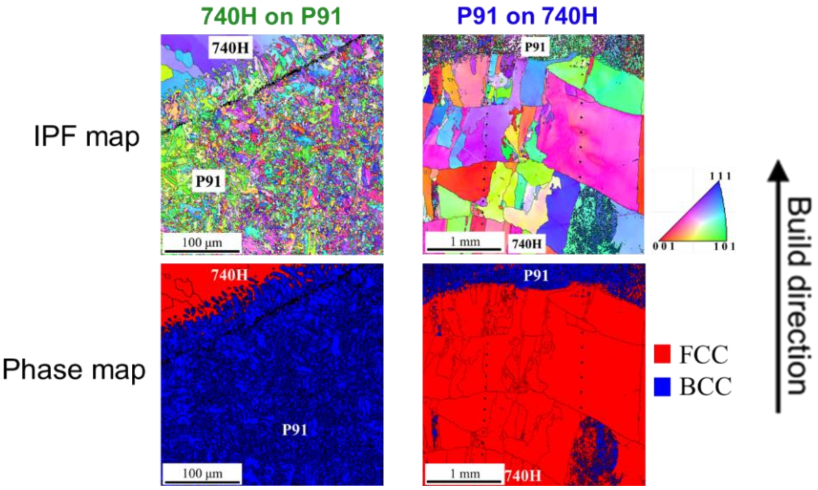

Figure 68. IPF and Phase maps obtained using EBSD across the gradient zone for 740H on P91 (G7) and P91 on 740H (G8) builds.

In order to investigate the microstructure across the gradient zone in as-built G7 gradient alloy further, EBSD was performed. The IPF map as well as the image quality (IQ) superimposed with phase (IQ+Phase) maps across the interface is shown in Figs. 69(a) and 69(b), respectively. From the IPF map (Fig. 69(a)), it can be observed that certain regions close to the gradient are black, which means that the orientation could not be determined due to the high dislocation density that leads to poor pattern quality of the Hough transform. The IQ+Phase map (Fig. 69(b)) shows a thick dark band close to the gradient zone. As per the definition, IQ is inversely proportional to the dislocation density, i.e., a phase with high dislocation density has low IQ which appears dark in the IQ map and vice versa. The IQ map for the BCC phase is shown in Fig. 69(c). It can be seen there is one peak in the low IQ region (Peak 1) and another in the high IQ region (Peak 2). Comparing the IQ+Phase map and the IQ plot for the BCC phase, it can be inferred that peak 1 corresponds to martensite with high dislocation density i.e., the dark band close to the gradient zone. Peak 2 denotes the remaining martensite in the P91 steel with lower dislocation density. The formation of martensite with very high dislocation density can be attributed to the accumulation of carbon from the interior regions of the P91 steel into the areas close to the gradient zone due to diffusion. With this additional understanding of the microstructure and hardness of as-built gradient alloys, it is proven that G7 is expected to possess better properties than G8 sample.

From these results for G7 and G8 graded alloys built using different deposition sequence and printing strategies by the WAAM process, it can be concluded that the G7 graded alloy is a successful build in comparison with the G8, due to the following reasons. The first reason is the cracking observed in the gradient zone of the G8 graded alloy Secondly, the gradient zone is very large is G8 in comparison with G7 graded alloy, with lower hardness in comparison with the P91 and IN740H alloys on either side. This is because it possesses an FCC structure with lower dislocation density in comparison with the BCC structure with higher dislocation density exhibited by the gradient zone of the G7 graded alloy. Also, the grain size in the gradient zone of G8 is very large in comparison with G7 graded alloy. All these factors will eventually lead to poor mechanical properties in the G8 graded alloy. *Hence, deposition of 740H over P91 is found to be the optimum deposition sequence.*

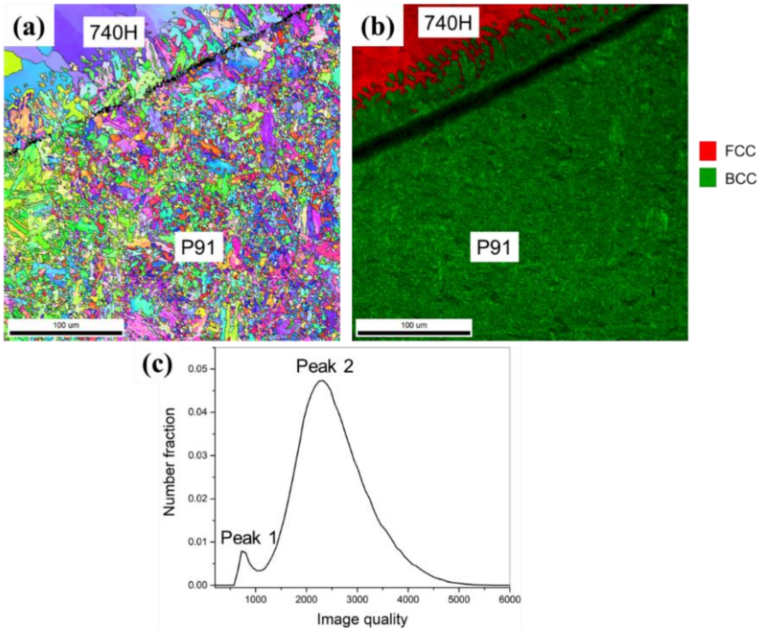

Figure 69. (a) IPF, (b) IQ+Phase and (c) IQ plot for BCC phase obtained from EBSD for 740H on P91 (G7) build.

The magnified view of the cracks as viewed under SEM in the gradient zone of the G8 sample is shown in Fig. 70(a). In order to probe into the nature of the cracks, EBSD analysis was performed in the cracked region of the gradient zone. The IPF and kernel average misorientation (KAM) maps obtained from EBSD in the cracked region of the gradient zone are shown in Fig. 70(b) and 70(c), respectively. It is clearly evident from the IPF map that the cracks propagate along the grain boundaries and hence, it is intergranular in nature. KAM is a measure of local misorientations that can be retrieved directly from the EBSD data, and it represents the average misorientation around the measurement point with respect to a defined set of nearest neighbors or nearest and second-nearest neighbor points. The KAM values are a qualitative representation of the residual stresses in a particular region. In Fig. 70(c), the red, green and blue colors correspond to misorientation angles of 5°, 2° and 0°, respectively. Regions with high KAM values can be correlated with the presence of high local strains and vice versa. From Fig. 70(c), it is obvious that there are red spots within the crack which corresponds to regions of high strains as the KAM value is high. However, in the region around the crack, the blue regions dominate, which indicate low KAM value and hence, lower strains. Therefore, one can expect that the build-up of local strains during the deposition is relieved by the formation of cracks in the gradient zone. It can be inferred that one of the reasons for crack formation in the gradient zone of the P91/740H bimetallic deposit is the accumulation of local strains during the WAAM process. The cracks might have formed possibly due to the low thermal conductivity of 740H superalloy (10.2 W/mK). During WAAM, the heat generated during the deposition usually dissipates by conduction through the component or substrate, forced convention through the shielding gas, or radiation to the surrounding environment. Heat conduction through the previously deposited layers or the substrate will result in maximum heat dissipation during the deposition in comparison with the other factors. Since the thermal conductivity of the 740H superalloy is lower than P91 steel, it cannot dissipate the heat through conduction effectively from the gradient zone. This might lead to the formation of thermal residual stresses resulting in the build-up of local strains that leads to crack formation. In addition, due to the lower thermal conductivity, the accumulation of heat increases the cooling time, thus reducing the cooling rate. The composition measured using EDS in the area around the cracked region is shown in Fig. 71. It can be observed from the EDS maps around the crack that the composition of major alloying elements such as Fe, Ni, Cr, and Co are uniform (Figs. 71(b-e)). However, from Fig. 71(f) it is evident that clusters of the second phase are present within the cracked region that is enriched in Nb. Thus, the EDS map for Nb suggests the presence of metal monocarbides containing Nb, i.e., MC phase, in the vicinity of the cracked region. From the IPF map obtained from the cracked region (Fig. 70(b)), it was found that the cracks are intergranular, which is caused by the presence of MC carbides in the grain boundaries.

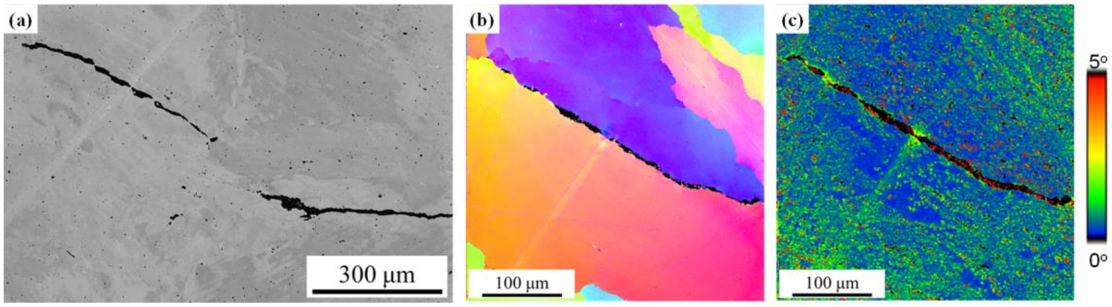

Figure 70. (a) SE-SEM micrograph of the crack as well as (b) IPF and (c) KAM maps obtained using EBSD from the cracked region in the gradient zone of P91 on 740H (G8) build.

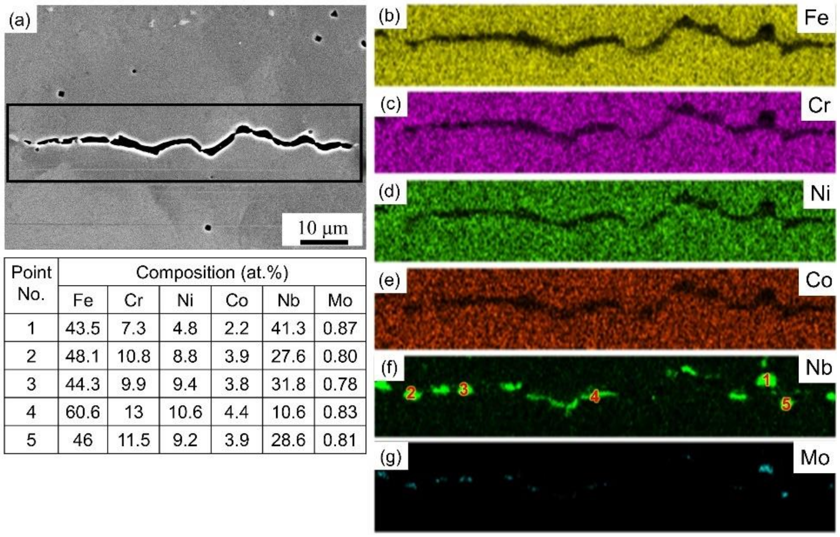

Point No.	Composition (at.%)					
	Fe	Cr	Ni	Co	Nb	Mo
1	43.5	7.3	4.8	2.2	41.3	0.87
2	48.1	10.8	8.8	3.9	27.6	0.80
3	44.3	9.9	9.4	3.8	31.8	0.78
4	60.6	13	10.6	4.4	10.6	0.83
5	46	11.5	9.2	3.9	28.6	0.81

Figure 71. (a) SE-SEM micrograph showing the crack in the gradient zone and the area EDS maps for the boxed region in the SEM micrograph for elements (b) Fe, (c) Cr, (d) Ni, (e) Co and (f) Nb and (g) Mo. The table summarizes the composition of the points highlighted in (f) showing the accumulation of Nb close to the cracks which can be attributed to MC carbide.

In order to deduce the reason for cracking in the gradient zone of the G8 sample, non-equilibrium Scheil simulations are performed for the mixed compositions of P91 and 740H in the gradient zone to determine the volumetric coefficient of thermal expansion (CTE), freezing range and the phases that form at the end of solidification (liquid content less than 1%). The composition of the interfacial region, which is a mixture of P91 steel and 740H superalloy, was determined by calculating the weighted mean for each element for varying content of P91 steel (in steps of 1%) and used as input for the Scheil simulations. In total, 101 Scheil simulations were performed for the mixed compositions in the gradient zone, and the results obtained are shown in Fig. 72. The Scheil-Gulliver model predicts that around 30 wt.% P91, there is a reduction in the volumetric CTE and an increase in freezing range due to the disappearance of the η phase. Further, there is a drastic reduction in volumetric CTE and freezing range around 60 wt.% P91 due to the formation of the ferrite phase and disappearance of Laves (Fe_2Ti) phase. From 60 wt.% P91, the volumetric CTE starts to increase, reaching a peak around 85% P91, which is due to the disappearance of MC carbide. At this point, the freezing range is found to be the lowest. After this point, the volumetric CTE decreases, and the freezing range increases till the composition of the gradient zone reaches pure P91 steel. Accordingly, it can be inferred that the formation of MC carbides leads to the drastic change in the volumetric CTE followed by the formation of the ferrite phase. The formation of other intermetallic phases such as η and Laves phases cause a subtle change in the volumetric CTE as well as the freezing range. The other possible reason for the cracking observed in the gradient zone of the P91/740H bimetallic structure is the decohesion around the MC carbides, which act as inclusion sites. Based on the mixed compositions of the gradient zone, Scheil simulation shows that the formation of MC carbide and ferrite phases from the liquid during solidification leads to a drastic change in the volumetric CTE as well as the freezing range. The presence of MC carbides in the gradient zone has been confirmed from the composition profile obtained using EDS across the gradient zone and the composition maps obtained around the cracked region. From the phase map obtained using EBSD, the ferrite (BCC) phase was not observed significantly in the gradient zone. The η and Laves phases are not expected to form due to the faster cooling rates during the WAAM process. Hence, the drastic change in volumetric CTE and freezing range due to the formation of MC carbides during the solidification can be attributed to the cracking in the gradient zone.

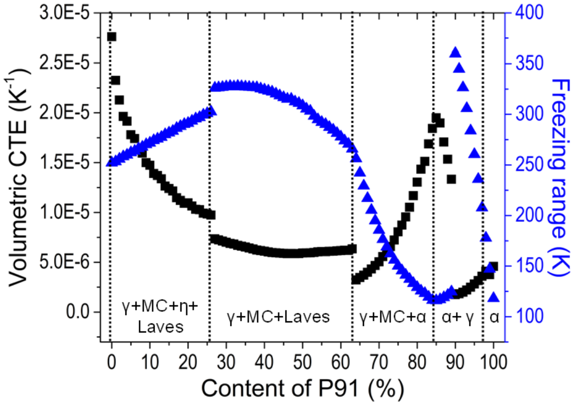

Figure 72. Variation of volumetric CTE and freezing range as a function of content of P91 steel in the gradient zone of the G8 sample calculated using Scheil simulations.

Post-Heat treatment design for graded alloys with sharp interface

As the first step in the design of post-heat treatment schedule for the graded alloys processed using WAAM, the optimum homogenization temperature as well as time needs to be determined. With the aim of maintaining identical homogenization temperature and time designed for the P91 steel and 740H superalloy, the homogenization step was performed at 1200°C for 2 h followed by water quenching for the G7 alloy. BSE-SEM images after homogenization for 2 hours is shown in Fig. 73. From, Fig 73(b), it is clearly evident that a secondary phase is forming a few microns below the gradient zone in the P91 steel. In order to identify the nature of the second phase that has formed in the P91 steel, EBSD was performed. The IPF maps superimposed with low angle grain boundaries (LAGB, $0.5^o < \theta < 15^o$) and IQ+Phase maps are shown in Fig. 74. From the IPF map (Fig. 74(a)), it can be clearly observed that there are certain grains just below the gradient zone in the P91 steel without any LAGB present within the grains. This characteristic is typical for the ferrite phase as it forms through a transformation involving diffusion, unlike the martensitic transformation that is diffusionless and can form laths with LAGB with their grains. Moreover, from the

IQ+Phase map (Fig 74(b)), it can be seen that certain grains with high IQ appear brighter than the surrounding martensitic regions which confirms that the secondary phase could be ferrite.

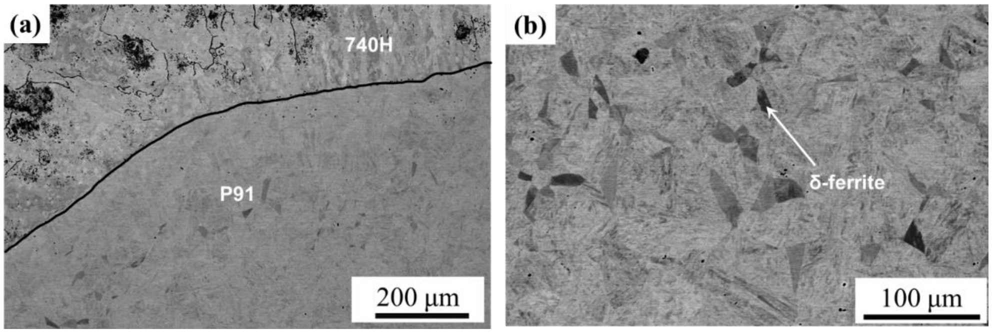

Figure 73. BSE-SEM images of (a) interface across P91 steel and 740H and, (b) region below the gradient zone showing the presence of secondary phases in G7 gradient alloy homogenized at 1200^{o}C for 2 hours.

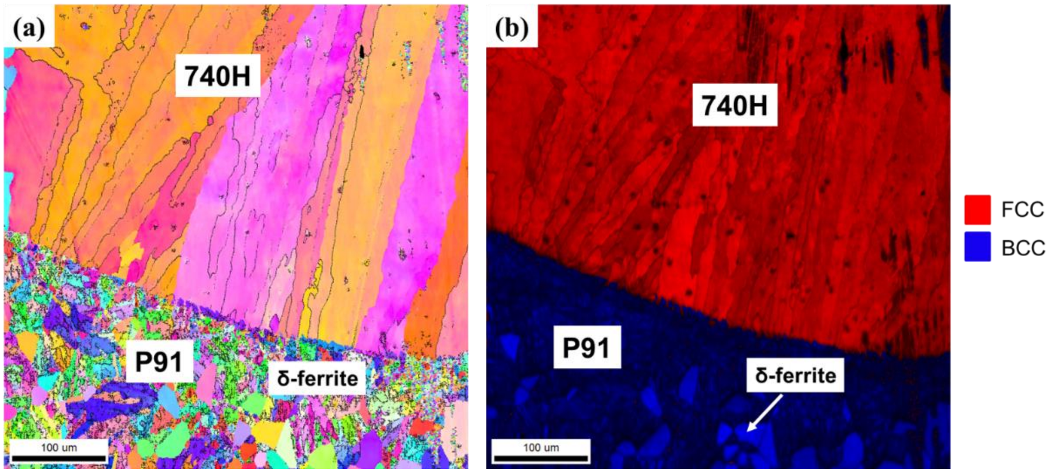

Figure 74. (a) IPF and (b) IQ+Phase maps obtained using EBSD across the interface for G7 gradient alloy homogenized at 1200^{o}C for 2 hours.

To probe further to determine the nature of the secondary phases that formed during the homogenization for 2 hours, EBSD was performed in an area within the P91 steel with the presence secondary phases at higher magnification. The IPF maps superimposed with LAGB and the IQ+Phase maps and the IQ plot for the BCC phase are shown in Fig. 75. From the IQ plot for BCC phase (Fig. 75(c)), two peaks are observed, one in the low IQ range (Peak 1) and the other in high IQ range (Peak 2). It is known that ferrite has lower dislocation density than martensite since the latter forms through a diffusionless transformation and hence, ferrite has higher IQ than the martensite. Therefore, in Fig. 75(c), Peak 1 and Peak 2 corresponds to martensite and ferrite, respectively. Depending on the temperature at which the sample was heat treated and the alloy composition, it can be identified whether it is α-ferrite or δ-ferrite. It is well known that δ-ferrite can form in the heat affected zone during the welding of P91 steel due to the high Cr content. Since, the gradient alloy was homogenized at 1200^{o}C, the possibility to form α-ferrite is ruled out at such high temperature. From these observations, it can be inferred that the secondary phase that formed in the P91 steel below the gradient zone is δ-ferrite. With the aim of suppressing the formation of δ-ferrite below the gradient zone in the P91 steel, the homogenization time was reduced to 1 hour. The BSE-SEM image across the interface is shown in Fig. 76(a) and it is evident that there is no second phase formation after homogenization at 1200^{o}C for 1 hour. The IPF and IQ+Phase maps obtained from EBSD across the interface also confirms that there is no δ-ferrite formation as shown in Figs. 76(b) and 76(c), respectively.

Hence, the optimum homogenization temperature and time were determined to be 1200°C and 1 hour, respectively, for the G7 graded alloy.

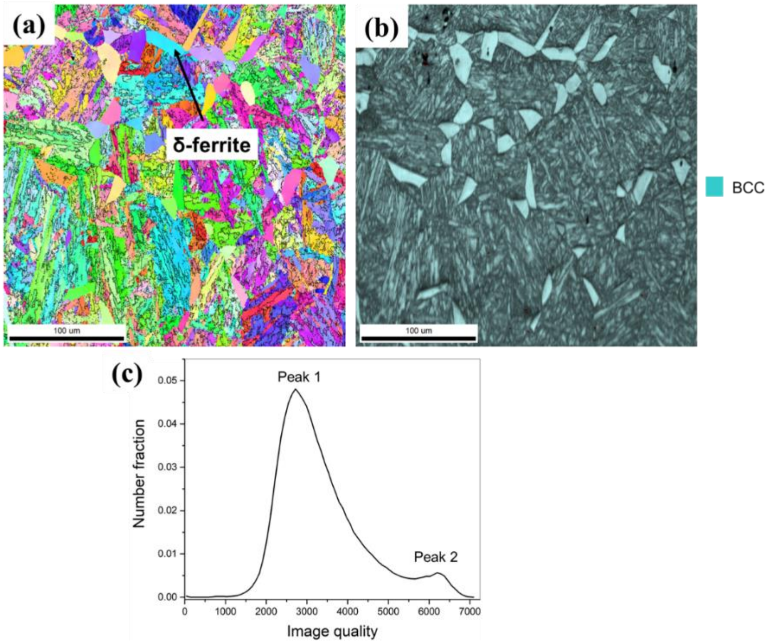

Figure 75. (a) IPF, (b) IQ+Phase maps and (c) IQ map for BCC phase obtained from EBSD from the region below the gradient zone in G7 gradient alloy homogenized at 1200°C for 2 hours. The presence of secondary phase i.e., δ-ferrite is revealed.

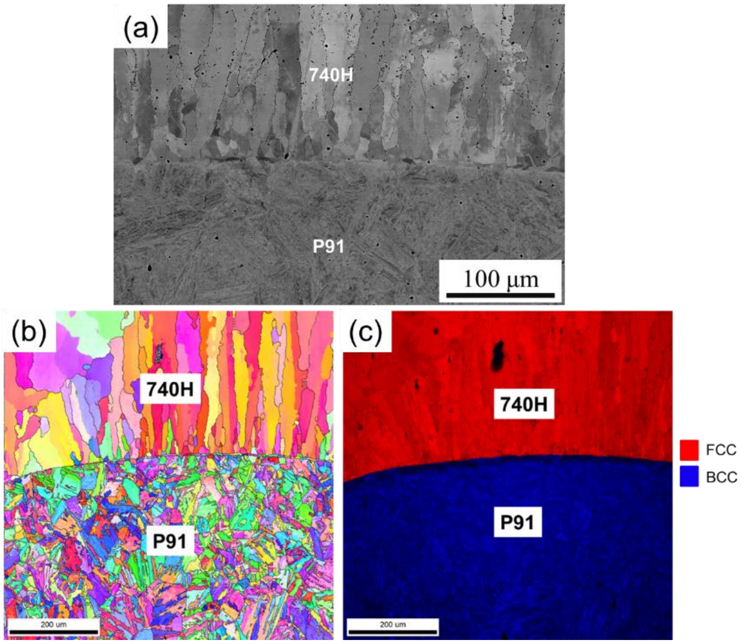

Figure 76. (a)BSE-SEM micrograph (b) IPF and (c) IQ+Phase maps obtained using EBSD across the interface for G7 gradient alloy homogenized at 1200°C for 1 hour.

The second step of the post-heat treatment schedule is the aging heat treatment. This is an important step as it leads to precipitation strengthening in the 740H superalloy, P91 steel and gradient zone, due to the supersaturated solid solution that formed after homogenization. The aging temperature was chosen to be 760°C in order to maintain a temperature that is consistent with the aging temperature optimized for P91 steel and 740H superalloy. However, the aging time was varied between 2 to 12 hours, followed by air cooling. The hardness maps for the graded alloy samples aged at 760°C for different time periods is shown in Fig. 77. It can be observed that after 2 hours of aging, P91 steel has higher hardness while the 740H superalloy had lower hardness since its optimum aging time at 760°C is 12 hrs. In addition, a soft zone with low hardness was found at the interface between the P91 steel and 740H superalloy. This could possibly be due to the accumulation of Fe close to the interface and the 2 hours of aging time was not sufficient to remove the Fe accumulation. After 12 hours of aging, 740H superalloy has higher hardness since it's the optimum aging time. However, the hardness of P91 steel has reduced considerably due to the coarsening of martensite as well as the strengthening precipitates. The hardness profiles after 4 and 8 hours of aging is intermediate between the hardness after aging for 2 and 12 hours. Hence, microstructure characterization needs to be performed to identify the optimum aging time between 4 and 8 hours.

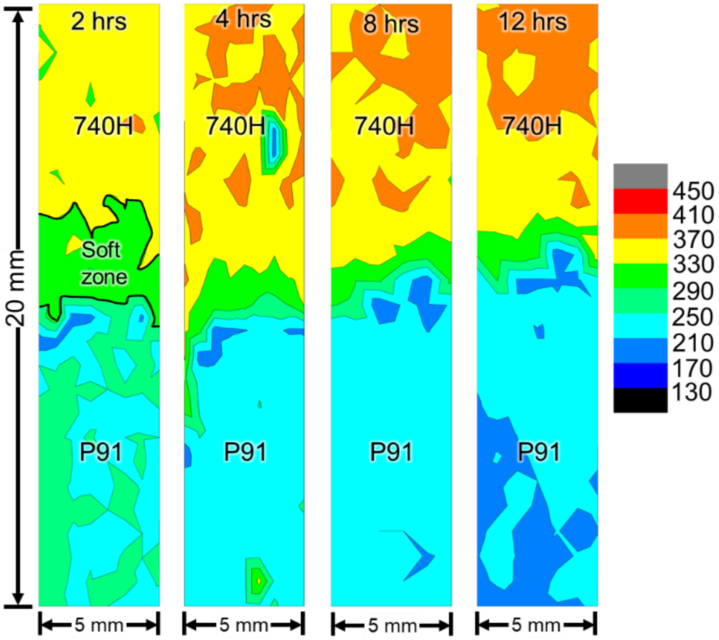

Figure 77. Hardness maps after aging the graded alloys with sharp interface at 760°C for different time periods.

The BSE-SEM images for the 4 hours aged sample is shown in Fig. 78. Two types of precipitates were observed, one is the black precipitates close to the interface between the P91 steel and graded alloy and the other is the white precipitates which are found farther away from the interface. Two different morphologies of the black precipitates were found, where one was blocky and square shaped while, the other is small and continuous found along the grain boundaries. EDS mapping in these areas were utilized to determine the nature of these precipitates. The area EDS maps for the small and continuous black precipitates along the grain boundaries are shown in Fig. 79. From these maps, it is clearly evident that the small black precipitates are carbides that are rich in Ti and Nb. Similarly, the square shaped blocky back precipitates correspond to the carbides that is rich in Ti and Nb as shown in Fig. 80. The area EDS maps for the white precipitates are shown in Fig. 81. It can be seen that the white precipitates are rich in Nb, Ti and Mo which corresponds to the Laves phase. The 8 hours aged sample also showed the same types of precipitates and the BSE-SEM micrographs for this sample is shown in Fig. 82. However, there were marked differences in the distribution of these precipitates along the graded alloy block in the 4 and 8 hours aged samples. In the 4 hours aged sample, the density of small carbides close to interface between P91 steel and graded alloy is higher (Fig.

78(a)) in comparison with the 8 hours aged sample. However, the precipitates in the graded block of the 4 hours aged samples is predominantly Laves phase while, at the middle of the 10% P91 graded alloy aged for 8 hours consists for tiny black precipitates that correspond to the carbides. Fine carbides are expected to lead to better creep resistance since they can pin the grain boundaries and restrict the grain growth. Since the 8 hours aged sample has higher carbide fraction throughout the graded alloy, it is expected to have better creep resistance and hence, taken as the optimum aging time. *In a nutshell, the optimum two-step post-heat treatment schedule for P91/740H gradient alloy processed using WAAM is as follows: 1) Homogenization at 1200°C for 1 hour; 2) Aging at 760°C for 8 hours.*

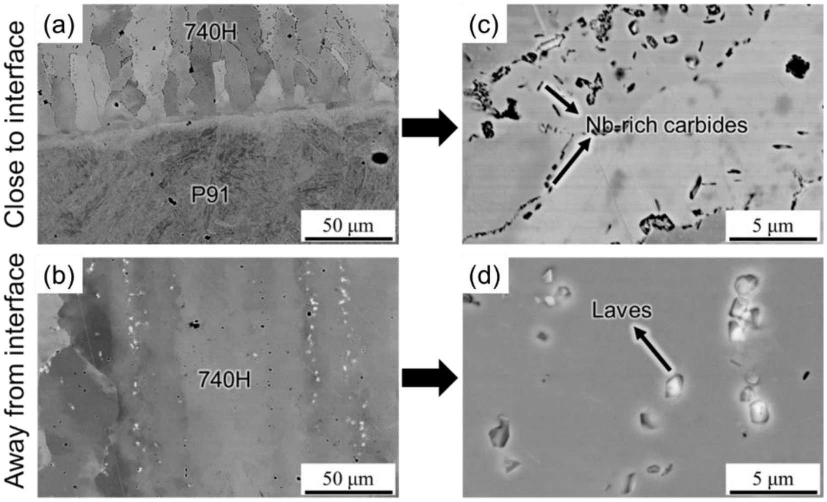

Figure 78. BSE-SEM micrographs for graded alloy with sharp interface aged at 760°C for 4 hours. (a) Interface between P91 and graded alloy showing the presence of black precipitates in the graded alloy close to the interface, (b) Middle of the 740H block farther from the interface showing the presence of white precipitates, (c) Closer look at the black precipitates near the interface showing the presence of two morphologies namely, small and continuous precipitates and blocky square shaped precipitates and (d) Closer look at the white precipitates that form farther away from the interface with irregular morphology.

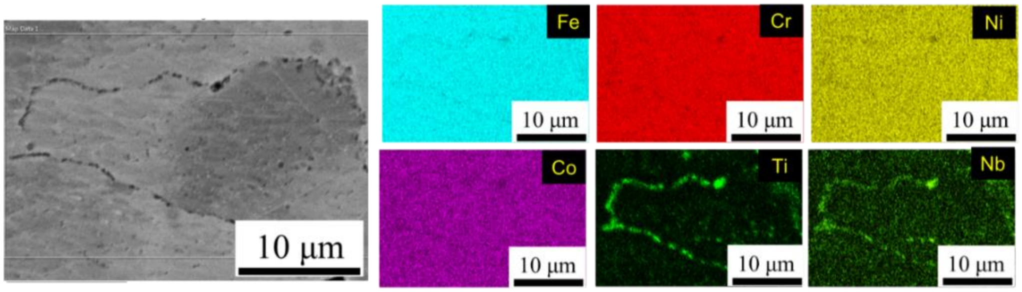

Figure 79. EDS maps in the region close to the interface between P91 steel and graded alloy with black precipitates in the graded alloy with sharp interface aged at 760°C for 4 hours confirming that the small and continuous precipitates are carbides rich in Nb and Ti.

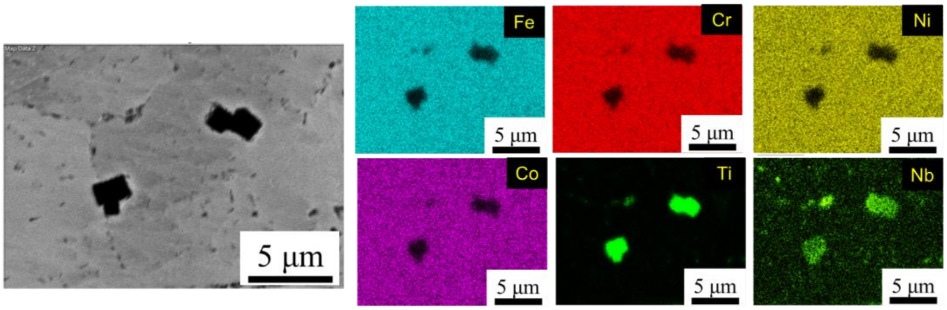

Figure 80. EDS maps in the region close to the interface between P91 steel and graded alloy with black precipitates in the graded alloy with sharp interface aged at 760^oC for 4 hours confirming that the blocky square shaped precipitates are carbides rich in Nb and Ti.

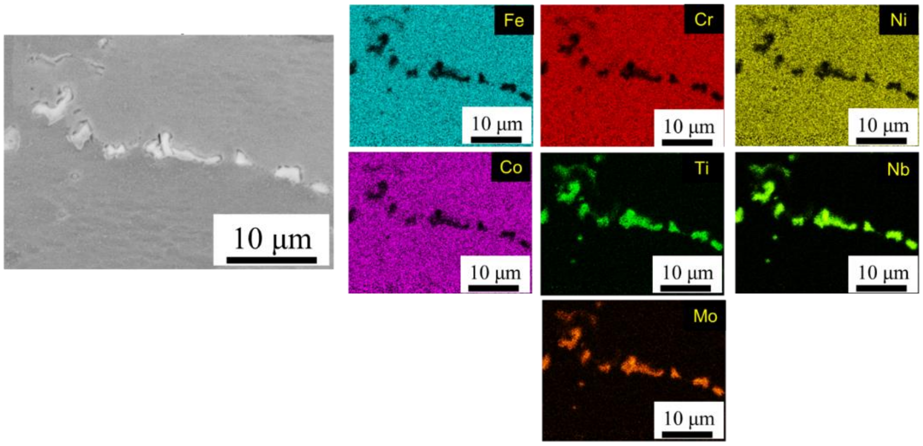

Figure 81. EDS maps in the region farther from the interface between P91 steel and graded alloy with white precipitates in the graded alloy with sharp interface aged at 760^oC for 4 hours confirming that the irregular shaped precipitates are Laves phase rich in Nb, Ti and Mo.

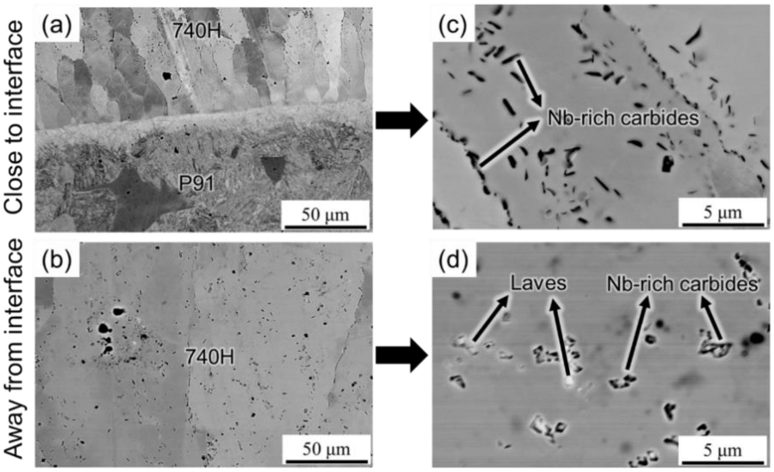

Figure 82. BSE-SEM micrographs for graded alloy with sharp interface aged at 760^oC for 8 hours. (a) Interface between P91 and graded alloy showing the presence of black precipitates in the graded alloy close to the interface, (b) Middle of the 740H block farther from the interface showing the presence of small black precipitates, (c) Closer look at the black precipitates near the interface showing the presence of two morphologies namely, small and continuous precipitates and blocky square shaped precipitates and (d) Closer look at the black precipitates that form farther away from the interface with irregular morphology.

3.4.2 *Thermomechanical modeling for multi-material deposition*

The multi-material deposition consisted of 15 layers of material 1 followed by 15 layers of material 2. The samples were deposited on a large substrate plate that was secured on the ends as shown in Fig. 83. The exact printing parameters were not recorded by RTRC and so, certain parameters were carried from the single material build into this one.

Figure 83. Multi-material deposition sample.

The set-up for the simulation was like the single material deposition, but the boundary conditions were adjusted to reflect the new printing conditions (Fig. 84). The amperage, speed and deposit dimensions were recorded by RTRC and implemented to this model. The heat source parameters were taken to be the same as the single material deposition, given that we do not have the data to calibrate the thermal model.

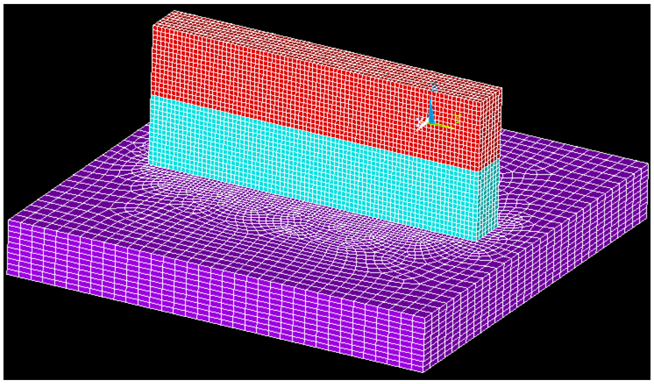

Figure 84. Multi-material deposition setup.

The goal of the multi-material simulation is to study the behavior at the interface between the two materials. The analysis performed by Dr. Xiong's group at Pitt, revealed that when depositing Inconel over steel, the boundary layer is thin and has a fine micro-structure. The difference in hardness values between IN740H and P91 is due to some Fe diffusion. On the other hand, when depositing P91 over Inconel, the boundary layer is thicker, the micro-structure is coarser and there are cracks present in the interface.

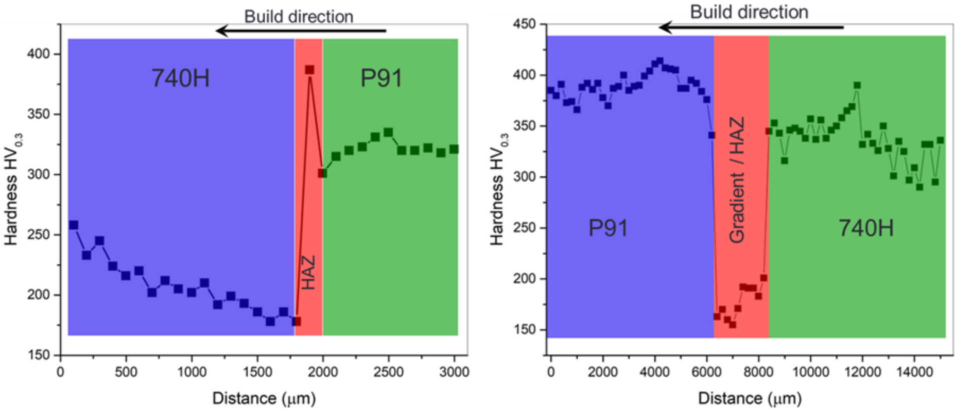

Figure 85. Microhardness results from multi-material samples.

It should be noted that both samples had a cooling time when the materials were switch, but the Inconel over Steel cooled for 120 minutes, while the steel over Inconel was only 20 minutes. This occurred due to external circumstances and the team is trying to determine if the difference in wait time influenced the different boundary layer. Furthermore, Inconel has a conductivity, 3 times lower than the conductivity of the P91 steel. When depositing the steel on top of the Inconel, heat accumulates at the boundary layer as the Inconel is not able to conduct the heat down towards the substrate. This could be one of the main factors that determines the width of the boundary layer. The team encountered stability problems when trying to solve the multi-material models and a subroutine had to be implemented in ANYS APDL. Line Search, a subroutine that scales the maximum displacement that occurs at a node was turned on. This automatically adjust the scale factor to stabilize the solution. The team is also investigated the effect of adding an independent material property for the boundary zone. For the case with cracking, the results seen with the hardness testing indicates that boundary zone has lower mechanical properties than P91 or Inconel 740H. These lower mechanical properties could be the cause for the cracking.

Bi-material deposition

Bi-material deposition prints, where a single wall was created using both materials. In the previous section, the team explained how the single material model by adding a phase transformation scheme for the P91 steel was completed. Also, the team described the bi-material deposition prints and went over the differences of the P91 on Inconel VS Inconel on P91. For ease of understanding, some of the same description was added below. The bi-material deposition consisted of 15 layers of material 1 followed by 15 layers of material 2. The samples were deposited on a large substrate plate that was fixed on the ends. The exact printing parameters were not recorded by RTRC and hence, certain parameters were carried from the single material build into the bi-material build. The set-up for the simulation was like the single material deposition, but the boundary conditions were adjusted to reflect the new printing conditions. The amperage, speed and deposit dimensions were recorded by RTRC and implemented to this model. The heat source parameters were taken to be the same as the single material deposition, given that we do not have the data to calibrate the thermal model.

The goal of the multi-material simulation is to study the behavior at the interface between the two materials. The analysis performed by Dr. Xiong's group at Pitt, revealed that when depositing Inconel over steel, the boundary layer is thin and has a fine micro-structure. The difference in hardness values between 740H and P91 is due to some Fe diffusion. On the other hand, when depositing P91 over Inconel, the boundary layer is thicker, the micro-structure is coarser and there are cracks present in the interface. Because of this difference, the P91 over Inconel model was updated. A new heat affected zone (HAZ) section was created at the boundary region, the material properties for this area were taken as an average of the properties of the two materials. It should be noted that both samples had a cooling time when the materials were switched, but the Inconel over steel cooled for 70 minutes, while the steel over Inconel was only 20 minutes. This occurred due to external circumstances and the team is trying to determine if the difference in wait time influenced the different boundary layer. Furthermore, Inconel has a conductivity 3 times lower than that of the P91 steel. When depositing the steel on top of the Inconel, heat accumulates at the boundary layer as the Inconel is not able to conduct the heat down towards the substrate. This could be one of the main factors that determines the width of the boundary layer.

The team encountered stability problems with the solution. The addition of the line search subroutine in ANSYS APDL fixed the problems with the model. The thermal model for the bi-material deposition showed that the interface region thermal history varies depending on the order the material is deposited. As seen in Fig. 86, the temperature in layer 16 (first layer of the second material) is higher for the P91 on Inconel due to the low thermal conductivity of the Inconel. A moving average (see Fig. 87) was taken on the temperature graphs, to show that over time, the average temperature is consistently higher for the P91 on Inconel sample even without only accounting for the peaks.

The cracks seen in the steel on Inconel deposit could be cause by the higher temperature experienced at the boundary region. For certain materials, it is important for the weld to cool below the transformation temperature between layers, as too high of an inter-pass temperature will allow the weld to remain austenitic. If this occurs, less hydrogen will escape that may cause cracking upon final transformation. The mechanical model results show that the residual stress in Inconel varies depending upon deposition order. In the steel on Inconel print, the P91 is deposited on top of the Inconel and then during the cooling period, it goes through a phase transformation. The phase transformations cause a stress relaxation in the P91 steel but an increase in stress in the Inconel. The stress in the Inconel reaches 600MPa and the stress in P91 steels lowers to about 300MPa. The behavior in the HAZ (boundary region) and the P91 side was very similar as seen by the stress graphs in Fig. 88.

Meanwhile, in the steel on Inconel print, the steel is deposited and goes through a first phase transformation during the cooling period, then the Inconel is deposited on top of this. Once the Inconel deposition is completed, the materials cool down and the steel goes through a second phase transformation. The steel is constraint on the bottom by the substrate plate and on the top by the Inconel, so it does not have the same degree of freedom to relax. As seen in Fig. 89, the stress in the Inconel and P91 steel remains close to 400 MPa. Figure 90 shows the stress state before and after the transformation of the steel for both deposition cases. The difference in the stress state could be the cause for the cracking and might not be influenced by the thermal history. The model cannot confirm the cause for the stress and more experiments are required to confirm the theory. The experiment should be focused on repeating the deposition of the steel on Inconel samples with temperature monitoring, as to ensure each layer is cooling to the correct interlayer temperature. If the cracking still occurs, then a gradient approach should be used for this boundary region.

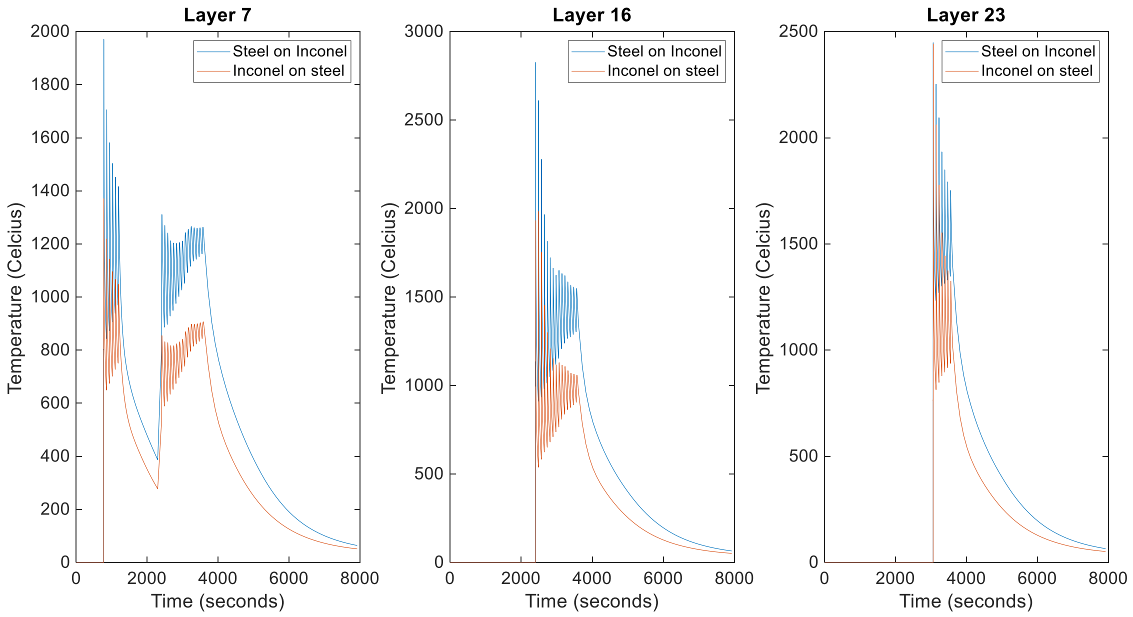

Figure 86. Thermal model results of the bi-material simulation.

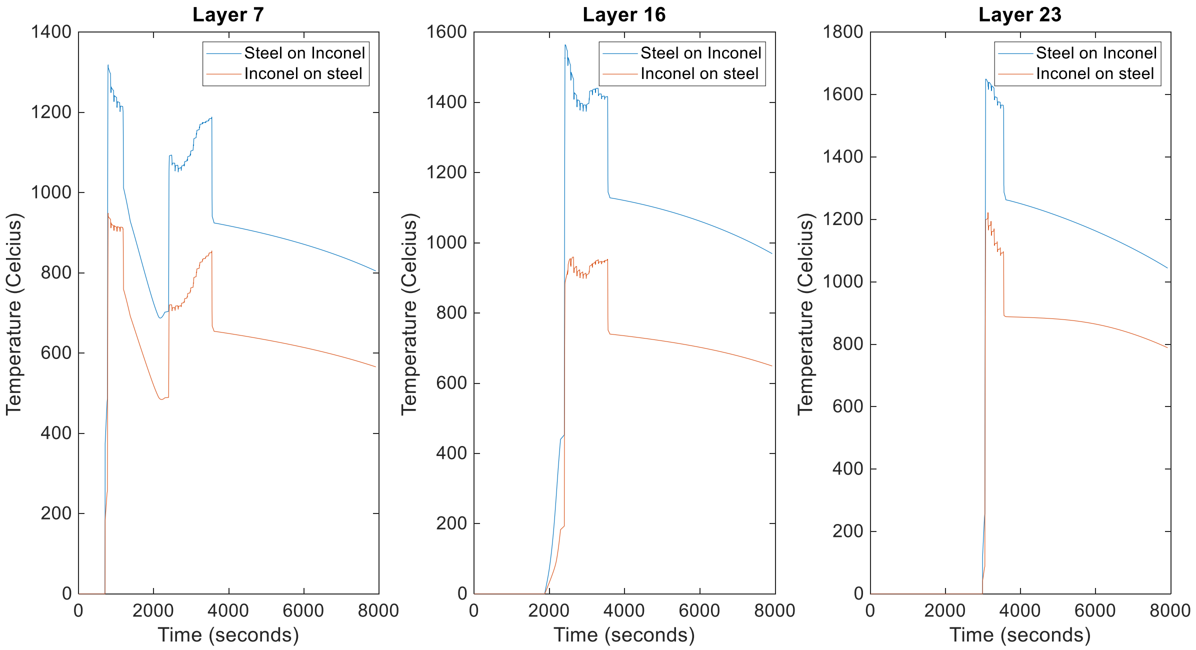

Figure 87. Thermal model results of the bi-material simulation with a moving average.

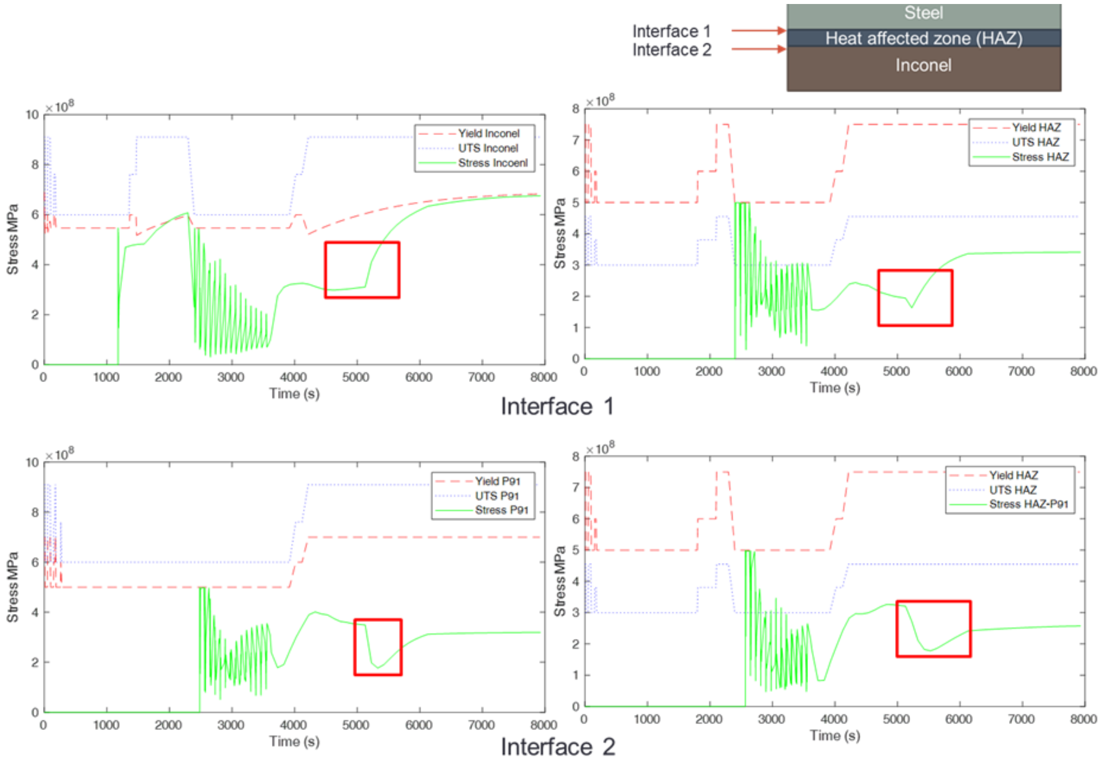

Figure 88. Stress history at the two interfaces of the P91 on Inconel deposit. Interface 1 is between Inconel and HAZ. Interface 2 is between HAZ and P91.

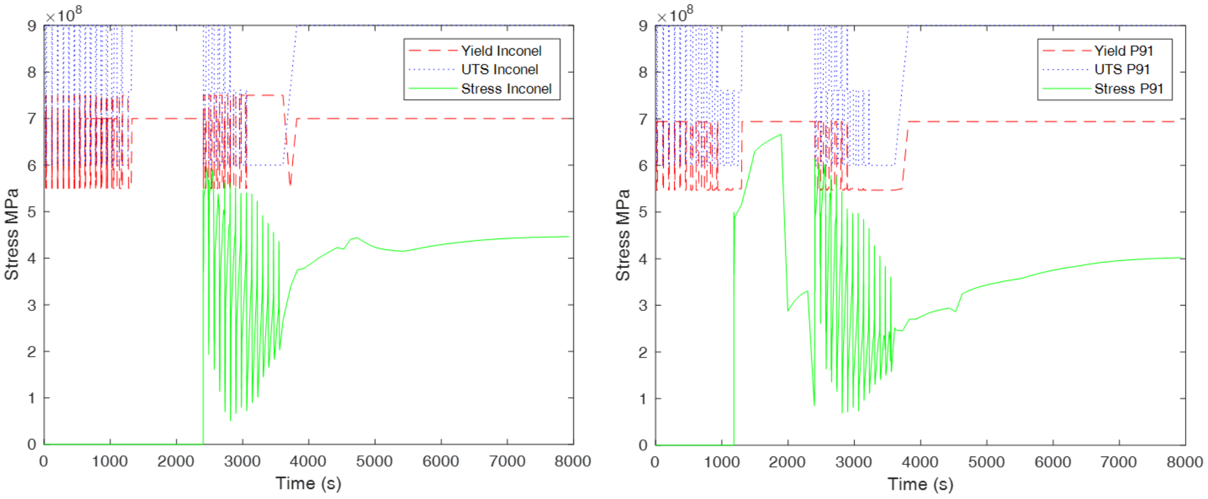

Figure 89. Residual stress history for the Inconel on P91 deposition.

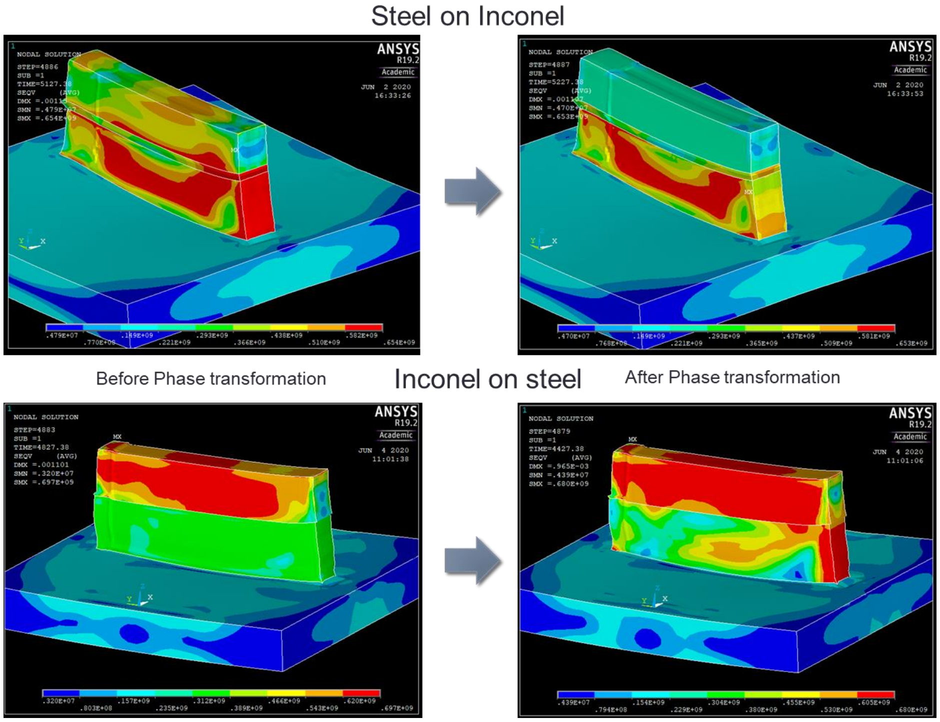

Figure 90. Stress state before and after the P91 transformation for both bi-material deposits.

3.4.3 Computational design and WAAM of graded P91/740H alloys with interlayer

ICME design of graded alloy interlayer

Since the creep resistance is a vital property for the 740H/P91 gradient alloy, we evaluated the creep resistance of the gradient composition. It was found that the creep resistance remains very high if the P91 content does not exceed 30%. Generally, an alloy with excellent creep resistance should have enough pinning precipitates such as $M_{23}C_6$ in P91 and γ' in 740H, to limit the dislocation movement, and it should also have a low diffusivity to achieve a lower diffusional creep rate. However, predicting creep resistance based on the microstructure requires numerous parameters and it is hard to predict for the gradient builds due to the variation in the microstructure. As a result, we adopted a creep resistance model purely based on the chemical composition which was proposed by Reed [10]. In this model, the time required for dislocations to escape from the pinning atoms for an element *i* is determined by the critical activation energy Q_i which is proportional to the activation energy for interdiffusion $\widetilde{Q_i}$ [11,12]. The total time for circumventing a unit length of dislocation within the matrix phase t_{total} can be written as Eq. 12 [10]:

$$t_{total} \propto \sum_{i}^{n} \frac{x_i}{\exp\left(-\frac{Q_i}{RT}\right)} \propto \sum_{i}^{n} \frac{x_i}{\exp\left(-\frac{\widetilde{Q_i}}{RT}\right)} \propto \sum_{i}^{n} \frac{x_i}{\widetilde{D_i}} \qquad (12)$$

Where *R* is the gas constant, *T* is the testing temperature, x_i is the atom fraction of solute *i* in the matrix phase, $\widetilde{D_i}$ is the interdiffusion coefficient in the matrix phase, and $\sum_i^n \frac{x_i}{\widetilde{D_i}}$ represents the merit index for creep resistance M_{creep}. In this work, Thermo-Calc software with TCFE9 and MOBFE4 databases was used to estimate the matrix composition and interdiffusion coefficient for each component at 600 °C for the 740H/P91 gradient alloy. According to Fig. 91(a), the matrix phase remains to be FCC until the P91 content reaches 60%, after which the phase fraction of BCC begins to increase. When the P91 content is higher than 80%, BCC becomes the dominant phase and the FCC phase disappeared when P91 content is more than 95%. The composition change for FCC and BCC is presented in Fig. 91(b). The solvent in BCC is always Fe as long as BCC exists. However, Ni is enriched in the FCC phase when the gradient composition is closer to the 740H side. Later the dominant element changes to Fe when more P91 is added to the gradient composition. We also calculated the M_{creep} for both FCC and BCC phases with different reference elements. Based on Fig. 91(c), it is clear that the M_{creep} does not show a big difference with the same matrix phase for different reference element. However, the creep resistance shows a big difference between BCC and FCC phases. In the whole gradient zone, FCC always has a better creep resistance than the BCC phase since the FCC phase has a close-packed structure. To evaluate the M_{creep} in terms of the gradient composition, we use the following equation [10] to calculate the M_{creep} for each composition by considering the phase fraction of FCC, BCC and their ability to resist the creep deformation:

$$M_{alloy} = M_{BCC} \times X_{BCC} + M_{FCC} \times X_{FCC} \tag{13}$$

Where M_{alloy}, M_{FCC}, M_{BCC} is the merit index of the alloy, FCC, BCC, respectively. Also, X_{FCC} and X_{BCC} are the phase fraction of FCC and BCC, respectively. According to the calculated M_{alloy} shown in Fig. 91(d), we found that the creep resistance remains stable from P91 content between 0% to 70% and the creep resistance for all compositions within the gradient zone is always higher than pure P91.

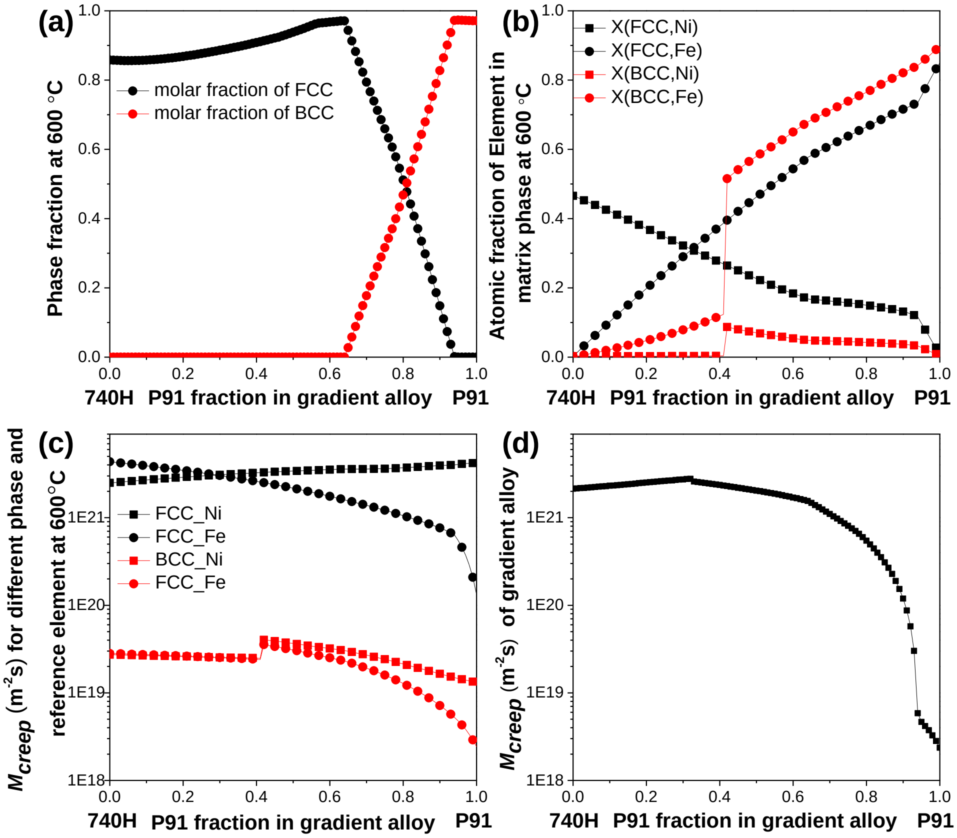

Figure 91. CALPHAD method calculated diagrams at 600 °C for gradient P91-740H alloy (a): molar fraction of BCC and FCC phases, (b) atomic fraction of Fe and Ni in BCC and FCC phases, (c) The merit index for creep resistance of FCC and BCC by setting the Fe and Ni as reference materials respectively, (d) The merit index for creep resistance of the alloys.

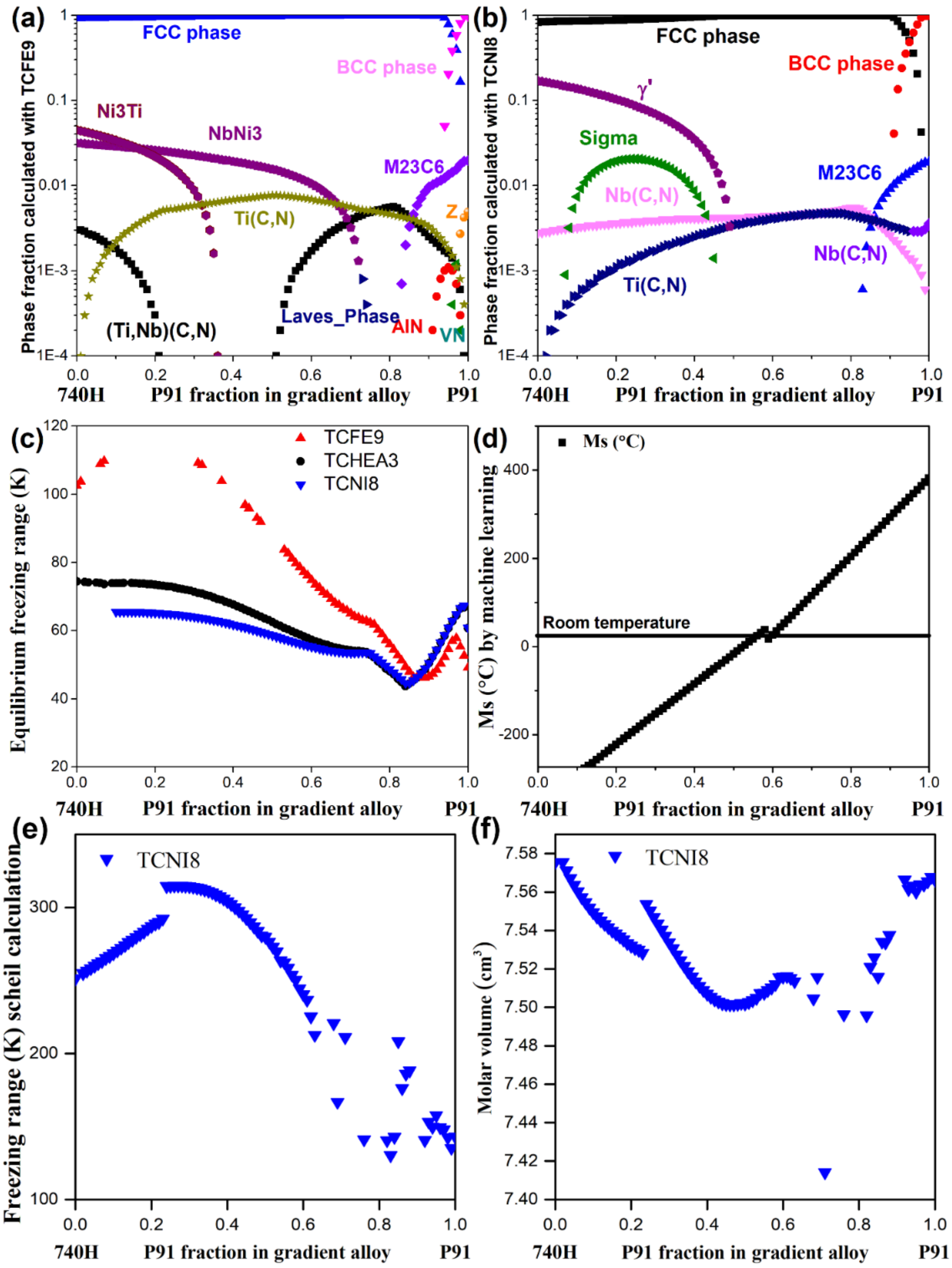

Figure 92. Phase fraction prediction for gradient alloys at aging temperature (760 °C) through CALPHAD approach with (a) TCFE9 and (b) TCNI8 database, (c) the equilibrium freezing range predicted for the gradient alloys and (d) the martensite start temperature predicted for gradient alloys using in-house machine learning model,(e) the freezing range predicted for gradient alloys using Scheil calculation, (f) the molar volumn of alloys at the incipient melting temperature

We also calculated the equilibrium phase fraction for the gradient alloys at the homogenization and aging temperatures using the TCFE9 and TCNI8 commercial databases available in Thermo-Calc software. For homogenization temperature, no detrimental phases have been found for both the TCFE9 and TCNI8 databases. However, we found that the results from the two databases show a discrepancy at the aging temperature, see Figs. 92(a) and (b). For example, the TCNI8 shows that the σ phase exists in the IN740H side while the TCFE9 shows that the $NbNi_3$ and Ni_3Ti phases form. Also, for the P91 side, the TCFE9 predicts the formation of the Laves phase while the TCNI8 does not. This is because TCNI8 is the database for Ni-based alloys and TCFE9 performs better for steel. We adopt the results calculated using TCFE9 for the P91 side and the results calculated using TCNI8 will be applied for phase prediction in the IN740H side. Thus, we propose that during the gradient alloy printing, it is preferred to avoid the composition between 20%-30% P91 which leads to the formation of a large amount of σ phase that is brittle. Figures 92(c) and 92(e) show the equilibrium freezing range calculated using the three databases (TCNI8, TCFE9 and TCHEA3) and the non-equilibrium freezing range calculated by the Scheil model using TCNI8. Some data points are missing due to the error in calculation. Although there are some discrepancies in the absolute value, the trend is basically the same. As more P91 is added to the gradient alloy, the freezing range begins to decrease and reach the lowest value when P91 is around 80%. And it is also clear that for the gradient composition, the freezing range will not be too high provided the region between 10% to 40% P91 is avoided, which is the same region where the σ phase will form at the aging temperature. We also calculated the martensite start temperature M_s using our in-house machine learning-based model. All calculated temperatures that were lower than 0 K are set to be at 0 K. The calculated M_s temperature for P91 is 382°C while the reported value is 385°C [13]. As a result, we trust our model for an accurate prediction of M_s temperature. According to Fig. 92 (d), it is clear that if the content of P91 is lower than 40%, M_s is lower than room temperature indicating the pure FCC structure for the as-built sample. On the contrary, if the P91 content is high, there is a chance to form an untempered martensitic structure during the cooling process after aging. Fig. 92(f) shows the molar volume of the alloy at an incipient melting temperature. It is known that the change of molar volume is not large except for one outlier around 75% P91.

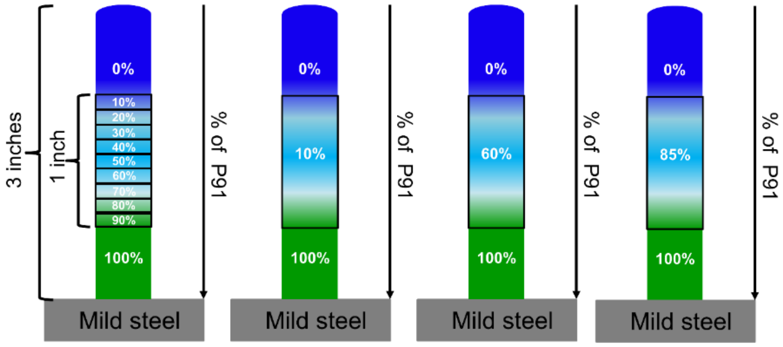

Figure 93. The proposed gradient compositions to be printed

Based on the above discussion, we planned to print several gradient builds in the next reporting period as the schematic shown in Fig. 93. The first gradient build is from 0% to 100% P91 with a 10% increment. This build serves as a benchmark and will provide microstructural information for the gradient alloy for model verification. The second one is 10% P91 between pure P91 and IN740H, where there is no sigma phase and still has a large amount of γ' precipitate. We believe that this gradient performance should be comparable to the IN740H single build. Then, a gradient of 60% P91 is inserted between pure IN740H and P91, where there is no detrimental as well as beneficial particles such as γ' and $M_{23}C_6$. This gradient helps us to study whether our creep modeling is correct and also whether the creep resistance remains high if P91 content is lower than 70%. The last gradient we plan to study is the 85% P91 between pure P91 and IN740H, which may reveal the influence of the $M_{23}C_6$ on mechanical property and the newly formed martensite after aging.

To support fabrication of gradients in alloy composition between the P91 and IN740H, the WAAM system was configured for twin-wire feeding. This setup, shown in Fig. 94, enables simultaneous feeding of the

IN740H and P91 materials into the WAAM melt pool. Feed rates of each wire are individually controlled during the deposition process, and can be adjusted layer-by-layer, or even within a single layer on a location-by-location basis to enable graded compositions in several directions.

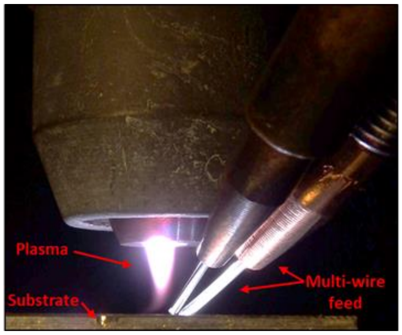

Figure 94. Twin-wire feed configuration for the RTRC WAAM system.

The first recommended composition/blend of 60% P91 composition was initially selected for trials. This is 60% by weight of P91, combined with 40% IN740H. The overall mass deposition rate was held constant at 2 pounds per hour, with deposition parameters comparable to both the single material P91 and IN740H conditions developed in earlier work. The modeling team suggested allowing the sample to cool between layers, to reduce diffusion and grain growth, which is more prevalent at elevated temperatures. An IR camera was used to monitor the bulk deposit temperature between layers, adjusting the dwell/wait time between layers to ensure the bulk deposit was below 175°C prior to starting another layer. The selection of the interpass temperature is challenging, as literature recommends temperatures below 175°C for IN740H, however, recommends maintaining interpass temperatures of 200°C to 300°C for P91 welds to avoid crack formation. Each sample consisted of roughly 1-inch height buildup of P91 steel, followed by the prescribed gradient/blend. After 1-inch of gradient, the remainder of the coupon was completed with IN740H material. The selected material blends were identified from modeling and prediction of phases/microstructure. The alloy compositions are noted in weight percent of P91 alloy. For the WAAM deposits, a square raster pattern was employed to create a wide and stable deposit. A schematic of the raster pattern. For these coupons, a raster pattern width of 10 mm, and step-over of 3 mm were used, along with torch travel speed of 5 mm/s. Figure 95 shows the two wire feeds entering the leading edge of the melt pool. For all samples, the deposition rate was held constant at 2 pounds per hour. This deposition rate was also used in the previous samples composed of bulk IN740H and P91, from which tensile coupons were extracted. As an example of the wire feed rates during blending and deposition of single materials, the wire feed rate in the 100% P91 section was 3.1 m/min. In the 60% gradient coupon, the middle section was deposited with P91 wire feed at 1.88 m/min, and IN740H wire feed at 0.97 m/min. These feed rates were calculated, taking into account the different wire feedstock diameters (0.035 inch P91, and 0.039 inch IN740H) and material densities.

Figure 95. Image from the deposition process with twin-wire feed.

The resulting coupons for all four gradient/blends are shown in Fig. 96. Each coupon was deposited onto a 0.5 inch thick mild steel substrate, which was fixtured firmly onto an aluminum base plate/table. The deposits were produced under an inert argon atmosphere, to reduce oxidation. Oxygen content was monitored and held below 70 ppm. Interestingly, the layer height for each gradient was slightly different, resulting in variability in heights of the middle section of the deposit. Likewise, the P91 and IN740H also have different melt pool behavior, resulting in differences in layer height and surface appearance. In general, the P91 deposits at a layer height near 2 mm, while the IN740H is slightly less (around 1.8 mm). In the gradient sections, the layer height varied with different alloy blends. To accommodate, the layer height of the toolpath was manually adjusted in during the sample deposition, to maintain the appropriate torch and wire feed standoff distance. The differences in layer height as a function of material can best be observed in the side view of the sample. The linear gradient coupon is shown in Fig. 97.

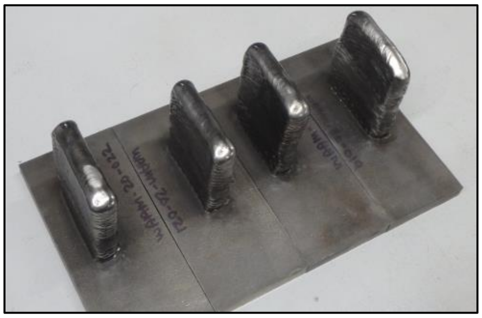

Figure 96. WAAM coupons with various material gradients/blends.

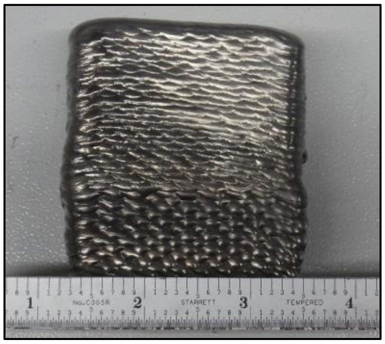

Figure 97. WAAM coupon with P91 base, linear gradient middle, and IN740H upper layers. Note difference in layer and melt pool appearance as the alloy/blend ratio is changed.

Among the four samples, the deposit at 60 wt.% P91 blend exhibited one slight crack near the end of the deposit section. Interestingly, this is the same alloy blend which exhibited tendency for cracking in the previous quarterly report, indicating that the 60% blend may be more susceptible to cracking than the other gradients/compositions. Deposition conditions for all four samples remained fixed, with the exception of the gradient/blended deposition section in the middle of the buildup. Build parameters are noted below, for the WAAM equipment. All conditions utilized a 1.1 liter/minute plasma gas flow (argon), 15 mm standoff distance, and were deposited under inert/argon environment to limit oxidation of the sample. The base layer is produced at slightly elevated power and slower travel speed, to ensure good fusion to the substrate.

Lower section: 100% P91

- Layer 1: 220A, 3.5 mm/s travel speed, 2.9 m/min wire feed
- Layer 2: 200A, 4 mm/s travel speed, 2.9 m/min wire feed

- Layer 3 thru 1-inch height: 166A, 5 mm/s travel speed, 3.1 m/min wire feed

Gradient section:
- 166A, 5 mm/s travel speed
- Wire feed defined by gradient/blend composition
- 1-inch through 2-inch height

Upper section: 100% IN740H
- 166A, 5 mm/s travel speed, 2.44 m/min wire feed
- Until 3-inch total height

In order to achieve the blended compositions, the following wire feed setpoints were used in the twin-wire feeding arrangement. Note, the Inconel 740H wire is 0.039 inch diameter, while the P91 is 0.035 inch diameter. These sizes, along with the material densities, were used to calculate the relative weight % and resulting wire feed values to achieve desired blends. For all samples, the deposition rate was held constant at 2 pounds per hour. This deposition rate was also used in the previous samples composed of bulk IN740H and P91, from which tensile coupons were extracted.

85% P91 Blend
- 2.67 m/min P91 wire, 0.37 m/min IN740 wire

60% P91 Blend
- 1.88 m/min P91, 0.97 m/min IN740 wire

10% P91 Blend
- 0.31 m/min P91, 2.19 m/min IN740

Linear Gradient
- Layer 14 & 15: 90%: 2.83 m/min P91 + 0.24 m/min IN740H
- Layer 16: 80%: 2.51 m/min P91 + 0.49 m/min IN740H
- Layer 17: 70%: 2.20 m/min P91 + 0.73 m/min IN740H
- Layer 18: 60%: 1.88 m/min P91 + 0.97 m/min IN740H
- Layer 19: 50%: 1.57 m/min P91 + 1.22 m/min IN740H
- Layer 20: 40%: 1.26 m/min P91 + 1.46 m/min IN740H
- Layer 21: 30%: 0.94 m/min P91 + 1.70 m/min IN740H
- Layer 22: 20%: 0.63 m/min P91 + 1.95 m/min IN740H
- Layer 23 & 24: 10%: 0.31 m/min P91 + 2.19 m/min IN740H

Characterization of as-built graded alloys with interlayer

The computationally designed graded alloy interlayers namely, 10, 60 and 85 wt.% P91 were printed according to the design proposed in Fig. 93, were characterized in their as-built condition to understand the microstructure and properties. No visible cracks or porosity is observed at the interface and throughout the sample. The composition profile obtained using EDS line scan along the build direction in the XZ plane is shown in Fig. 98. It can be seen that the composition of the graded alloy is close to the nominal composition evaluated by applying the rule of mixtures between P91 and 740H. This proves that there is good composition control during the twin-wire feeding process to fabricate graded alloys using WAAM. The dips in the Fe, Ni and Cr curves correspond to the presence of secondary phase, either Laves or MC carbide. Moreover, dissolution of Fe into the 740H is observed for some distance away from the interface between 85 wt.% P91 graded alloy and 740H. Similar behavior was also observed in the sharp gradient build where 740H was deposited over P91. Further, hardness map was generated by performing series of indents in the as-polished XZ plane along the build direction as shown in Fig. 99. A total of 800 indents (load: 300 grams, dwell time: 10 seconds) were made on the sample surface in order to generate these maps. It is clearly evident that the hardness is predominantly uniform throughout the samples for 10 and 85 wt.% P91 graded alloy samples. However, at the interface between graded alloy and 740H in 85 wt.% P91 sample as well as the interface between P91 and graded alloy in 10 wt.% P91 sample, the hardness is very low, which will affect the mechanical performance of these alloys. The IPF and phase maps obtained using EBSD at the interface between P91 and graded alloy in 10 and 60 wt.% P91 as well as the interface between graded alloy and 740H in 85 wt.% graded alloy is shown in Fig. 100. It is clearly evident that the 85 wt.% P91 graded alloy has a BCC structure while the 10 and 60 wt.% P91 graded alloys have a FCC structure. However, as per the CALPHAD prediction, the 85% P91 alloy should consist of FCC phase as the matrix phase. However, due to the rapid cooling, the FCC phase transforms to martensitic phase, which is seen as BCC in the phase map. It is also observed that minor amount of δ-ferrite is found in the P91 steel region close to the interface between P91 and graded alloy in 10 and 60 wt.% P91 samples. Moreover, secondary phases were observed in the graded alloy region. From the energy dispersive spectroscopy (EDS) area scans, it was found that these secondary phases were Laves and MC carbide as shown in Figs. 101 and 102. The Laves phase was found to be rich in Nb, Mo and Ti and deficient of Fe and Ni with an irregular morphology (Fig. 101). On the other hand, the MC carbides were found to have a perfectly cubic morphology that is rich in Ti and Nb as well as devoid of Fe, Ni and Cr (Fig. 102). The Laves phases will be detrimental to the mechanical and creep properties of the graded alloy and hence, it is imperative that a post-heat treatment is required for the as-built graded alloy samples for further improving the properties

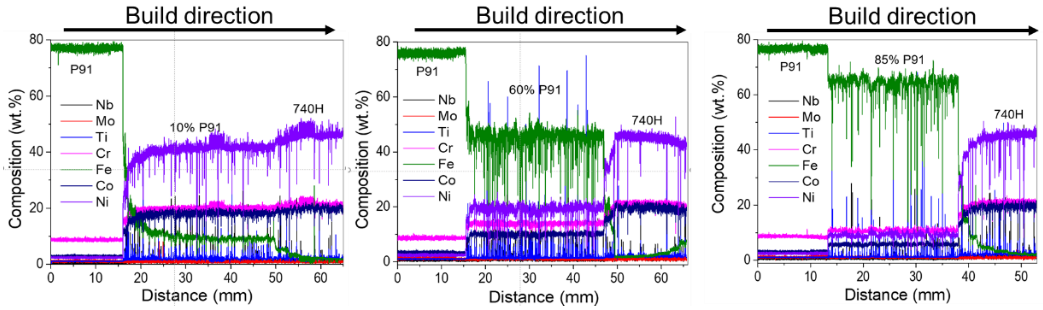

Figure 98. Composition profiles obtained along the build direction using EDS for 10, 60 and 85 wt.% graded alloys.

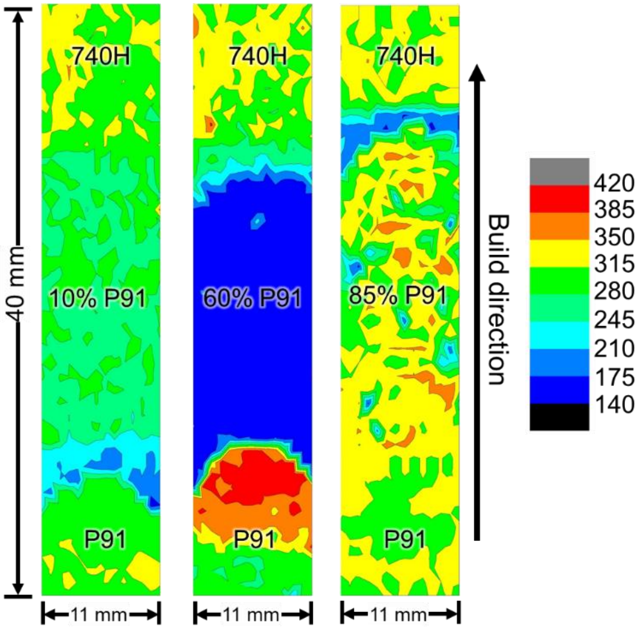

Figure 99. Microhardness maps obtained along the build direction for 10, 60 and 85 wt.% graded alloys.

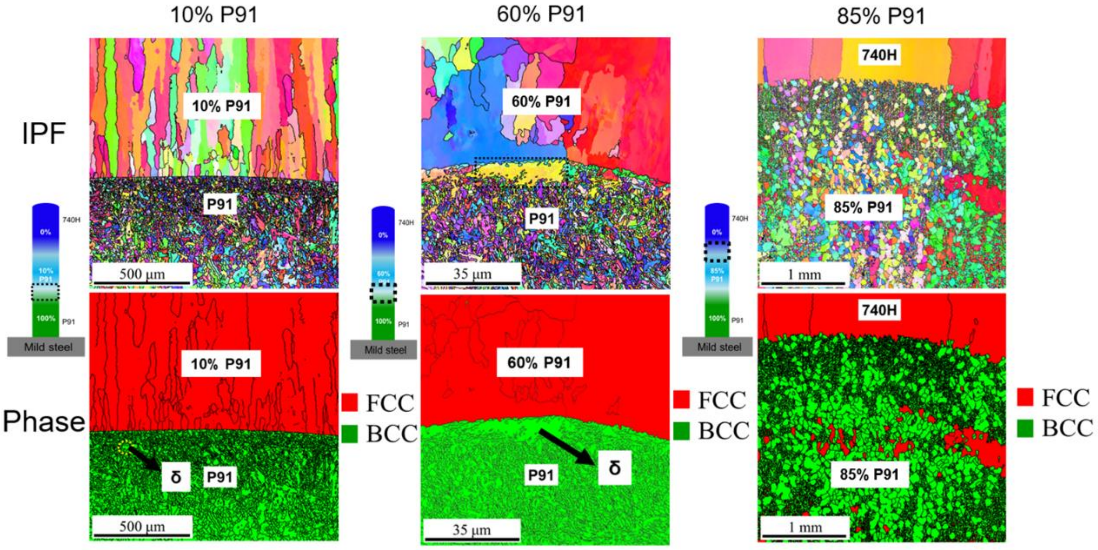

Figure 100. IPF and phase maps at different interfaces to identify the grain structure and phase of 10, 60 and 85 wt.% graded alloys.

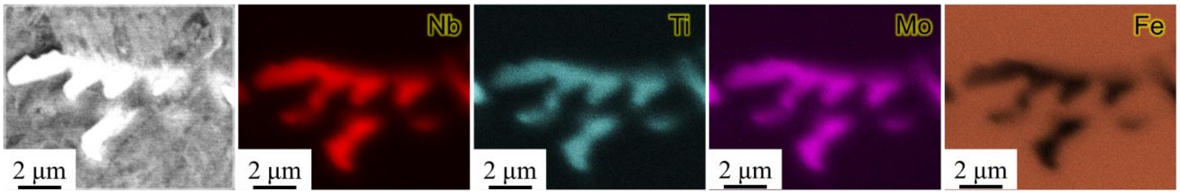

Figure 101. EDS area scan in the region consisting of the Laves phase rich in Nb, Ti and Mo.

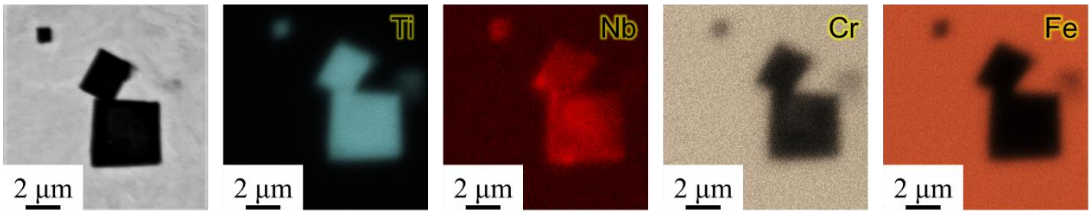

Figure 102. EDS area scan in the region consisting of the MC carbide rich in Nb and Ti.

Similarly, the as-built structure of the linear gradient build was also characterized. The composition profile obtained using EDS line scan along the build direction in the XZ plane is shown in Fig. 103. It can be observed that the composition variation for the major elements (Fe, Ni, Co and Cr) is step-wise till 20 wt.% P91 and each layer is clearly visible. The 10 wt.% P91 layers get blended with the pure 740H, probably due to excessive diffusion and nearly close composition for these 2 different layers. The spikes in the composition profile corresponds to the presence of secondary phases. The upward spike in Nb and Ti denotes the presence of either MC (M: Nb, Ti) carbide or Laves phase. The corresponding downward spikes in Fe and Ni indicates the depletion of these elements in the secondary phases. The hardness map was generated by performing series of indents in the as-polished XZ plane along the build direction as shown in Fig. 104. It can be observed from the hardness map that there exists a thick band with high hardness, that corresponds to the 90 wt.% P91 layer. On further probing into that region, it was found to have high amount of carbides with cuboidal morphology as shown in Fig. 105(a). The blue region was found to have an FCC matrix with typically no secondary phases such as carbides or Laves phase (Fig. 105(b)). The composition was between 60-80 wt.% P91 in that region. Between 0 and 50 wt.% P91, the hardness starts to increase gradually and reach the typical hardness for 740H superalloy. Further, electron backscattered diffraction (EBSD) was performed to generate the inverse pole figure (IPF) and phase maps along the build direction of the linear gradient block as shown in Figs. 106 and 107, respectively. It was found that from pure P91 to 90% P91 layer, the matrix is typical lath type martensitic microstructure. From 80% P91, the microstructure is columnar till it reaches the pure 740H superalloy. The corresponding phase map shows that till 90% P91 the matrix has BCC structure and further it becomes FCC structure. A two-phase region of small width is also found in between in the phase map (Fig. 107).

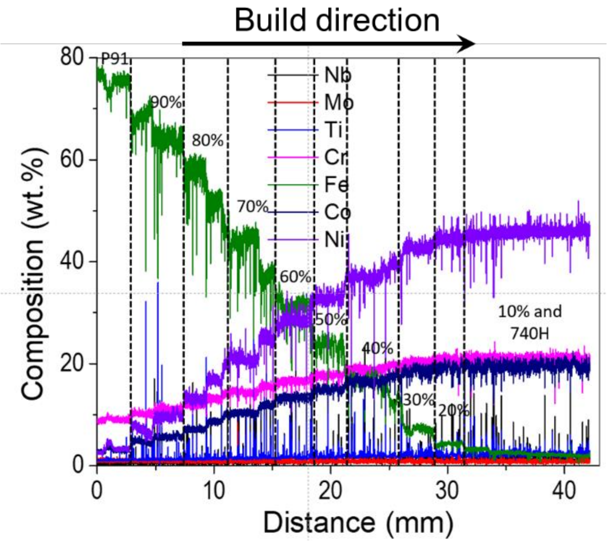

Figure 103. Composition profile along the build direction for the linear gradient build obtained using EDS.

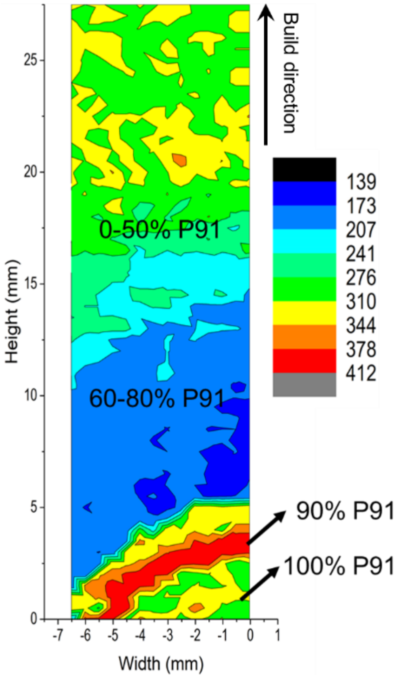

Figure 104. Hardness map along the build direction of the linear gradient build.

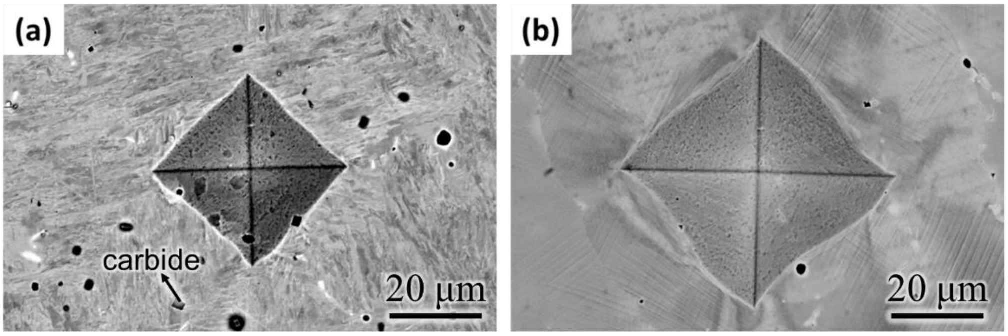

Figure 105. BSE-SEM micrographs for (a) 90% P91 with blacks regions indicating the presence of carbide and (b) 60% P91 showing the absence of secondary phases.

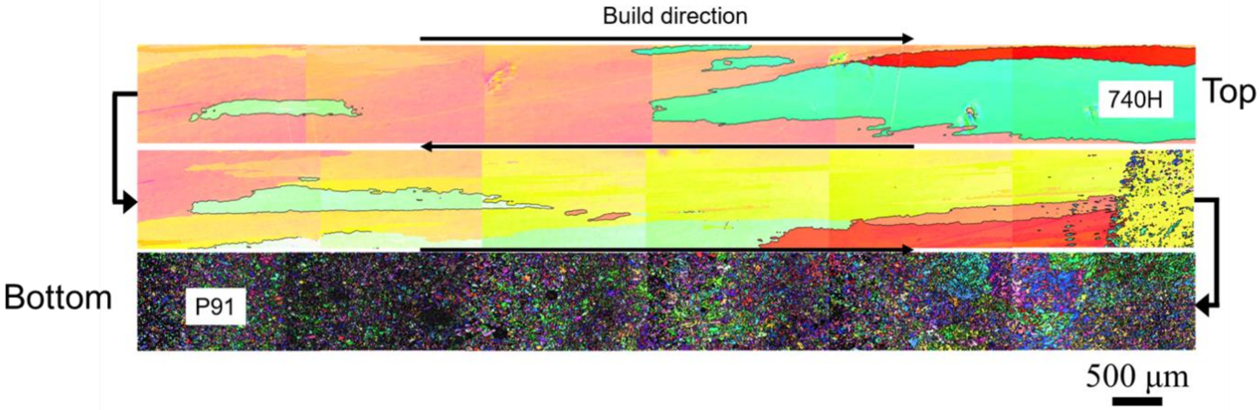

Figure 106. IPF map obtained using EBSD along the build direction of the linear gradient build.

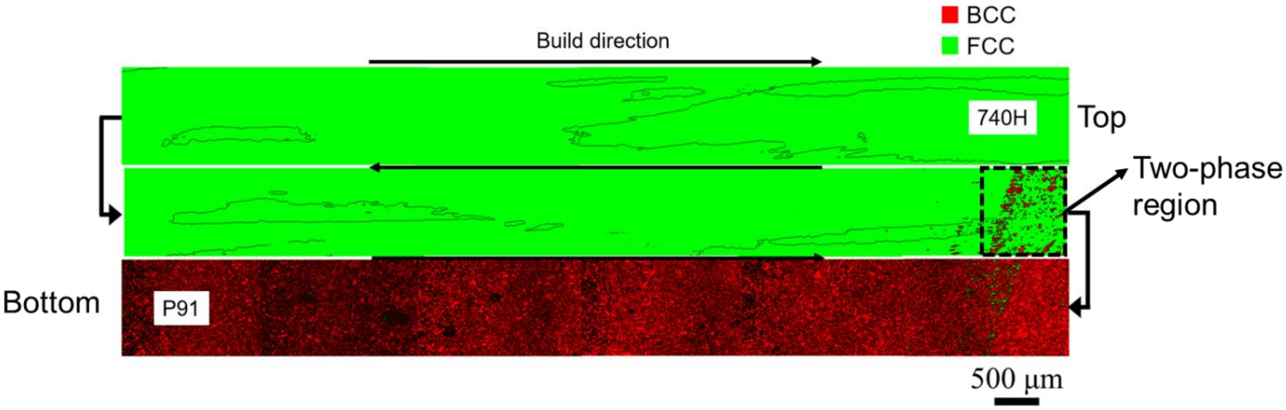

Figure 107. Phase map obtained using EBSD along the build direction of the linear gradient build with a two-phase region in the middle.

Post-Heat treatment design for graded alloys with interlayer

Homogenization is the first step of post-heat treatment which is used for dissolving the deleterious phases present in the as-built sample into the matrix. It is also known to relax the residual stresses that pile up during the additive manufacturing process. Hence, based on the knowledge of the post-heat treatment designed for the sharp gradient sample (G7, 740H deposited over P91), 10, 60 and 85 wt.% P91 graded alloy samples were heat treated at 1200°C for 1 hour followed by water quench, in order to maintain similar heat treatment for all the graded alloys. However, after viewing the samples under the SEM in back-scattered electron (BSE-SEM) mode, it was found that in the P91 block, close the interface between P91 steel and graded alloy, secondary phase formation was found in 10% and 60% P91 samples, as shown in Fig. 108. In order to identify the nature of the secondary phase, electron backscattered diffraction (EBSD) scans were performed, and the inverse pole figure (IPF) and phase maps are shown in Fig. 109. From these maps, it can be confirmed the secondary phase that formed in the P91 block is δ-ferrite, due to the absence of high angle grain boundaries (the black lines in IPF and Phase maps). The formation of δ-ferrite is deleterious for the mechanical performance of the material. Moreover, it was found that there is segregation of Si at the interface between P91 steel and graded alloy as well as the interface between graded alloy and 740H superalloy as shown in the EDS area maps in Fig. 110. These two features observed after homogenization at 1200°C for 1 hour are undesirable for the performance of this material in a A-USC power plant. In order to circumvent this problem, the homogenization temperature was reduced to 1150°C, while the time was maintained to be 1 hour, followed by water quench. From the SEM micrographs shown in Fig. 111, by reducing the homogenization temperature by 50°C, the δ-ferrite formation in P91 steel was suppressed. This can be explained based on the equilibrium phase fraction *vs*. temperature plot for P91 steel wire composition. It can be seen that 1200°C is much closer to the calculated δ-ferrite formation start temperature (~1250°C). Hence, it is more likely to form δ-ferrite during homogenization at 1200°C rather than 1150°C. From these observations, it can be inferred that the optimum homogenization temperature and time are 1150°C and 1 hour, respectively for 10, 60 and 85% P91 graded alloys.

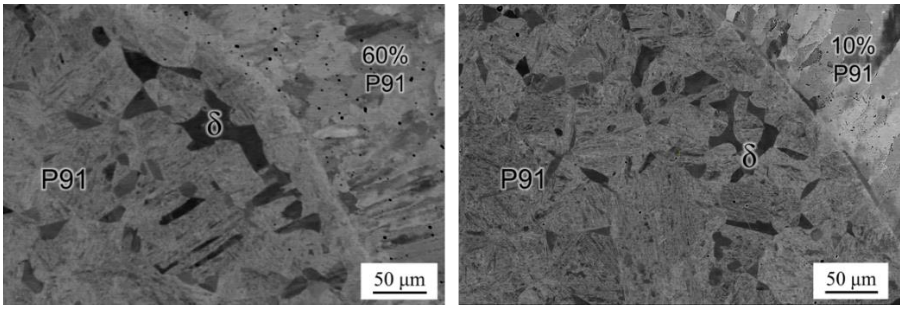

Figure 108. BSE-SEM micrographs showing the formation of δ-ferrite in P91 steel close to the interface between P91 steel and graded alloy after homogenization at 1200°C for 1 hour in 10 and 60 wt.% P91 graded alloy samples.

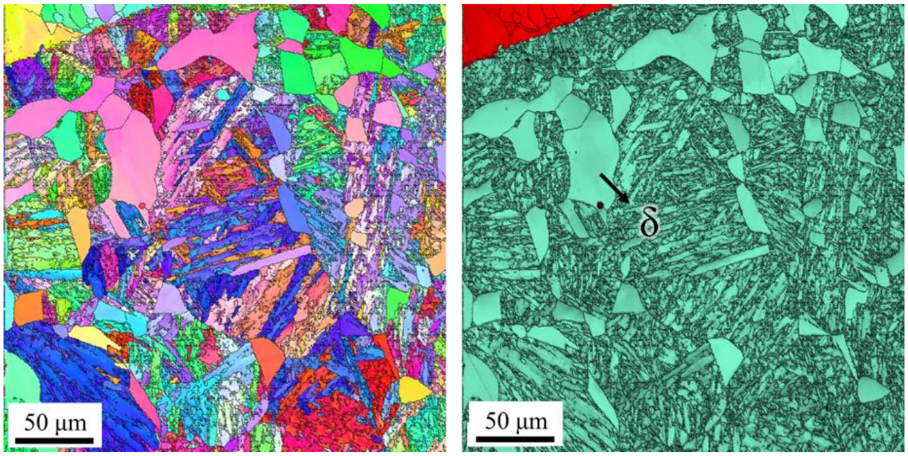

Figure 109. IPF (left) and Phase (right) maps showing the presence of δ-ferrite in the P91 side of the P91/graded alloy interface in 10 wt.% P91 graded alloy sample homogenized at 1200°C for 1 hour.

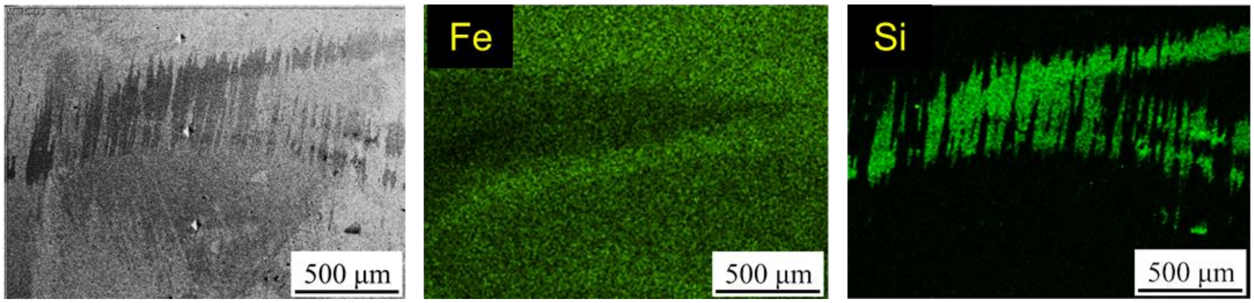

Figure 110. EDS maps showing the segregation of Si at the interface between P91 and graded alloy in 10 wt.% P91 graded alloy sample homogenized at 1200°C for 1 hour.

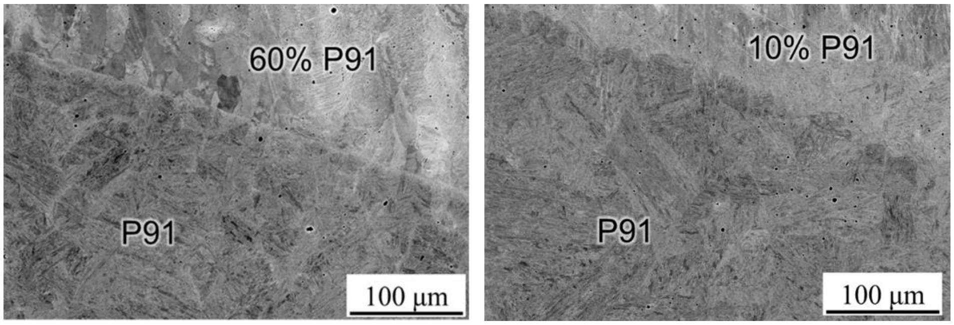

Figure 111. BSE-SEM micrographs showing a clear interface between P91 steel and graded alloy after homogenization at 1150°C for 1 hour in 10 and 60 wt.% P91 graded alloy samples.

After homogenization at 1150°C for 1 hour, aging studies were performed at 760°C for 2, 4, 8 and 12 hours to identify the optimum aging time. An aging temperature of 760°C was chosen based on the optimum aging temperature for sharp gradient and single 740H superalloy builds. After aging the samples, hardness maps were generated using an automated Vicker's hardness tester. Nearly 350 indents were made for each sample with a load of 300 grams and dwell time of 10 seconds. From these hardness maps, the variation in hardness in different regions of the samples can be found which can be correlated with the observations from microstructural characterization. Also, the samples with peak hardness can be identified from these maps. The hardness maps for 10 wt.% P91 samples in aged conditions are shown in Fig. 112. It can be observed that there is a marked variation in hardness in the P91, graded and 740H regions. The P91 steel block becomes softer while, the 740H superalloy block becomes harder as the aging time increases. The 10% P91 graded alloy shows the highest hardness which is uniform after aging for 4 hours at 760°C while, the sample aged for 8 hours was the second hardest. In the 2 hours aged sample, a weak region exists in the P91 steel and graded alloy interface, which is undesirable. Hence, further microstructure characterization was performed for the 4 and 8 hours aged samples. Interestingly, it was observed that the microstructure after aging for 4 and 8 hours, the precipitation behavior is exactly similar to aged 740H on P91 (G7) sharp gradient alloy. The BSE-SEM micrographs of the 10 wt.% P91 samples aged for 4 and 8 hours are shown in Figs. 113 and 114, respectively. Similar to the aged G7 sharp gradient alloy, in the 4 hour aged sample, densely populated Nb-rich carbides were found close to the interface between P91 and graded alloy while sparsely populated Laves phase was observed in the bulk of the graded alloy away from the interface. For the 8 hour aged sample, densely populated Nb-rich carbides were found close to the interface between P9 and graded alloy as well as the bulk of the graded alloy, with minor amount of Laves phase in the bulk, away from the interface. Based on the same argument for G7 sharp gradient alloy, the optimum aging time for 10 wt.P91 graded alloy sample is 2 hours.

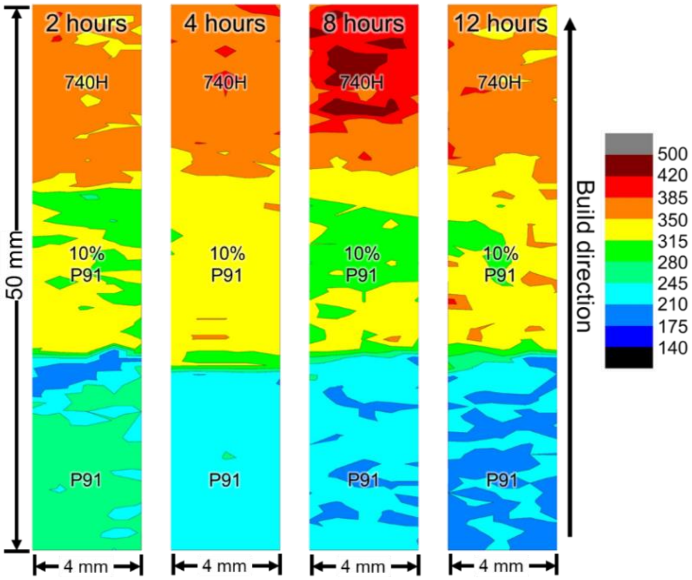

Figure 112. Hardness maps along the build direction for 10 wt.% P91 graded alloy aged at 760ºC for different time period.

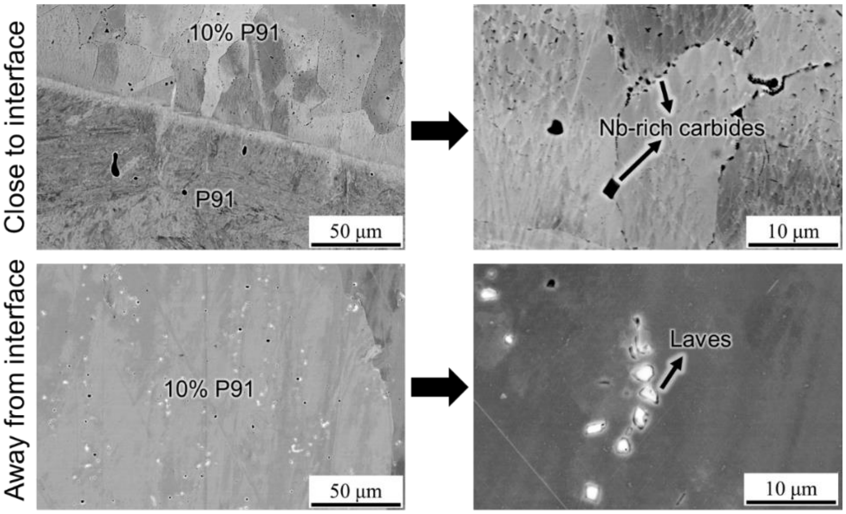

Figure 113. BSE-SEM micrographs for graded alloy with sharp interface aged at 760ºC for 4 hours. (a) Interface between P91 and graded alloy showing the presence of black precipitates in the graded alloy close to the interface, (b) Middle of the 10% P91 graded alloy block farther from the interface showing the presence of white precipitates, (c) Closer look at the black precipitates near the interface showing the presence of two morphologies namely, small and continuous precipitates and blocky square shaped precipitates and (d) Closer look at the white precipitates that form farther away from the interface with irregular morphology.

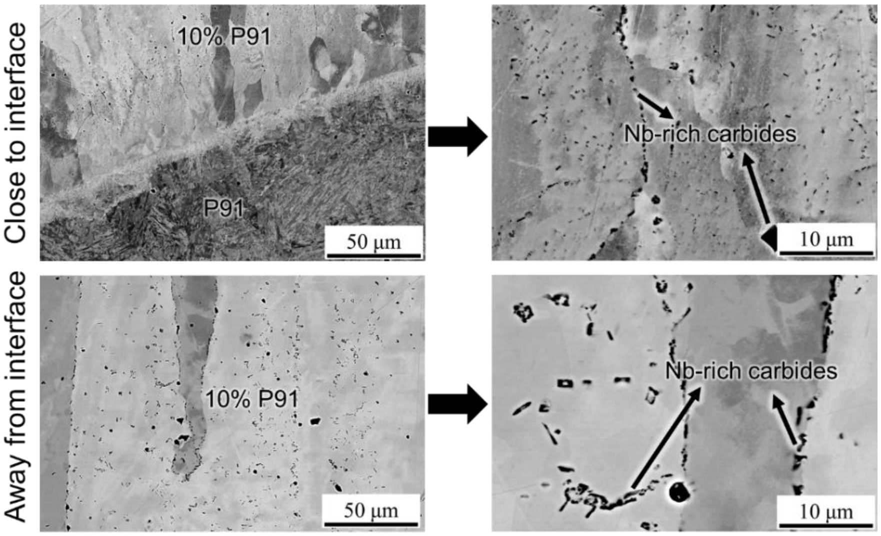

Figure 114. BSE-SEM micrographs for 10% P91 graded alloy samples aged at 760ºC for 8 hours. (a) Interface between P91 and graded alloy showing the presence of black precipitates in the graded alloy close to the interface, (b) Middle of the 10% P91 graded alloy block farther from the interface showing the presence of small black precipitates, (c) Closer look at the black precipitates near the interface showing the presence of two morphologies namely, small and continuous precipitates and blocky square shaped precipitates and (d) Closer look at the black precipitates that form farther away from the interface with irregular morphology.

The hardness maps for the 60 wt.% P91 graded alloy samples after aging are shown in Fig. 115. It is clearly evident from these maps that the hardness of the 60 wt.% P91 graded alloy blocks do not improve even after aging. Hence, none of the aging time could be considered as an optimum one. This observation is consistent with the equilibrium phase fraction vs. temperature calculation at 760ºC for different graded alloy compositions as shown in Fig. 92(b). Since there are no effective strengthening precipitates predicted for the 60 wt.% P91 graded alloy, the hardness of this alloy is not expected to improve even after post-heat treatment. This proves that the design of graded alloys using CALPHAD-based ICME approach is more reliable. The hardness maps for the 85% P91 graded alloy samples after aging at 760ºC for different time period are shown in Fig. 116. The interface between the graded alloy and the 740H superalloy is weak in aged condition similar to the as-built condition. Moreover, the 2 hours aged sample showed the highest hardness for both the graded alloy and P91 blocks. However, the width of the weak interface between the graded alloy and 740H superalloy reduced as the aging time was increased while the hardness of the P91 and graded alloy reduced. As a tradeoff, after 8 hours of aging, the width of the weak zone close to the interface has reduced and the hardness of P91 steel is not reduced considerably as in the case of the 12 hour aged sample. Though, the hardness of P91 is higher after 4 hours of aging, the width of the weak zone is still thick. Hence, for the 85 wt.% P91 graded alloy, the optimum aging time at 760ºC is 8 hours.

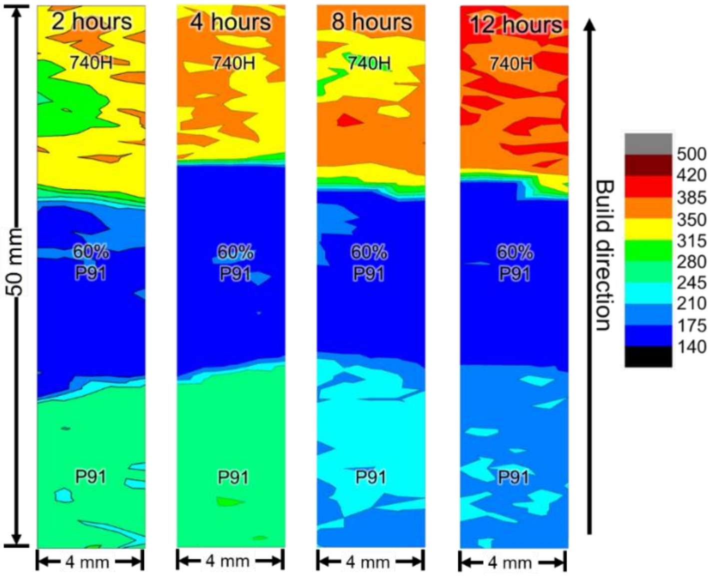

Figure 115. Hardness maps along the build direction for 60 wt.% P91 graded alloy aged at 760°C for different time period.

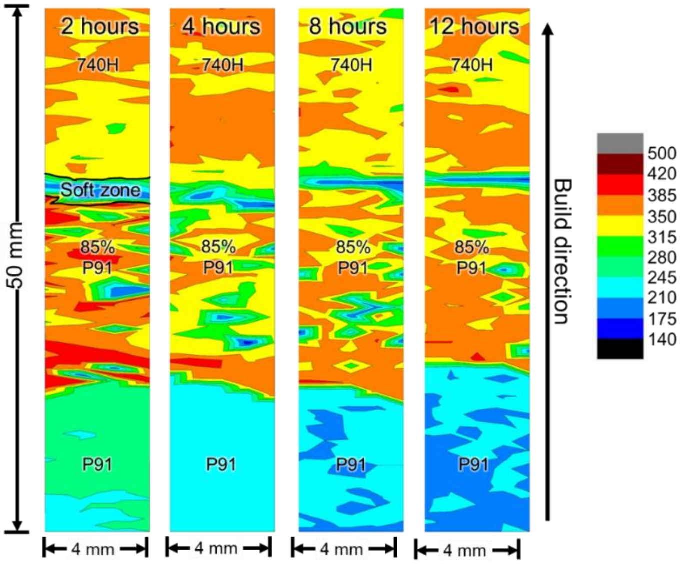

Figure 116. Hardness maps along the build direction for 85 wt.% P91 graded alloy aged at 760°C for different time period.

In order to evaluate the effectiveness of the designed post-heat treatment, tensile tests were performed for 60 and 85 wt.% P91 samples in both as-built and heat treated conditions. Though, no optimum aging time could be identified for 60 wt.% P91 graded alloy sample, a 8 hour aging treatment was performed in order to be similar with the optimum aging time identified for 85 wt.% P91 graded alloy. Tensile bars of nearly 65 mm length with a gauge length of 25 mm were extracted along the building direction as shown in Fig. 117. The stress-strain curves obtained for different conditions are shown in Fig. 118 and the tensile properties along with the location of failure are listed in Table 11. It is clearly evident that in the yield strength and ultimate tensile strength does not improve after post-heat treatment. However, the ductility is very high in the as-built condition which reduces after post-heat treatment probably due to the precipitation of γ' in the 740H block, which induces a hardening effect. The location of failure remains the same before and after the post-heat treatment for the 60 wt.% P91 graded alloy sample. On the other hand, there is considerable improvement in the yield strength and ductility of 85 wt.% P91 after post-heat treatment. This proves that the post-heat treatment designed for this alloy is highly effective. Moreover, the location of failure changed from the interface between 85 wt.% P91 graded alloy in the as-built condition to the P91 block in the post-heat treated condition, proving that the designed optimum post-heat treatment has strengthened the 85 wt.% P91 graded alloy, thus avoiding failure. The long aging time of 8 hours is not suitable for the P91 block and hence, it fails well before the graded block in the post-heat treat sample.

From the post-heat treatment design for the 10, 60 and 85 wt.% P91 graded alloys, it can be inferred that the 10% P91 graded alloy will suit better for the A-USC application. The 60 wt.% P91 graded alloys in weaker in comparison with the P91 steel and 740H superalloy and hence, it is expected to fail in the graded alloy portion when put in service. Moreover, the interface between the 85 wt.% P91 graded block and the 740H superalloy is weak even after aging and hence, there is a possibility for early failure at the interface even though the P91 block fails before it. Since there are no major weak regions found after aging 10% P91 graded alloy, this alloy will be further tested for determining the creep resistance and compared with the sharp gradient (740H over P91) build at different stresses and temperatures.

Figure 117. Tensile bars extracted from the 60 and 85 wt.% P91 builds for mechanical testing.

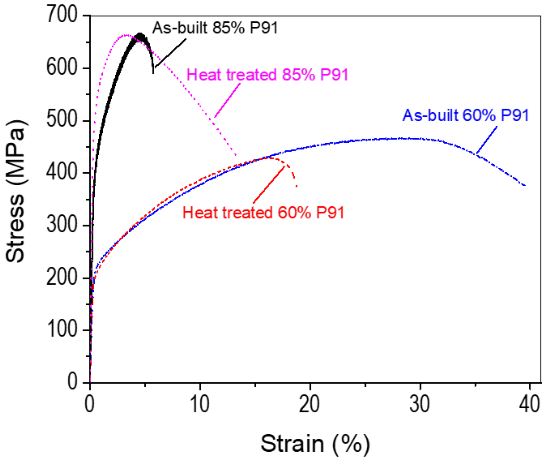

Figure 118. Stress-strain curves obtained for the 60 and 85 wt.% P91 builds in as-built and heat-treated conditions.

Table 11: Tensile properties of as-built and post-heat treated 60 and 85 wt.% graded alloys.

Material	***Condition***	***YS (MPa)***	***UTS (MPa)***	***Elongation (%)***	***Location of failure***
60 wt.% P91	*As-built*	*219*	*459*	*33*	*60 wt.% P91 block*
	Heat treated	*212*	*440*	*21*	*60 wt.% P91 block*
85 wt.% P91	*As-built*	*419*	*665*	*6.5*	*Interface between 85 wt.% P91 and 740H*
	Heat treated	*538*	*667*	*13*	*P91 block*

3.4.4 Design of dissimilar alloy interface

For the AM of dissimilar alloys, it is important to design the gradient zone. We compare two designs namely, sharp and locking structures as shown in Fig. 119. For these preliminary simulations, the interface region is defined as same material property as structural steel but with reduced ultimate tensile strength. In the future, the actual materials property of the P91 steel, In740H and interface properties from ICME simulations. A simple uni-axial tensile simulation is setup to identify the stress-strain response due to changes in the geometrical design. The failure of the specimen at ultimate tensile load is simulated using the APDL command *ekill*. This command removes the element from the model when it reaches the failure criterion. The model, however, continues the load incrementation and solution after removal of the element. The distribution of equivalent plastic strain and stress for sharp and locking interface designs are shown in Fig. 120. It is evident that introduction of a locking design in the interface results in reduction of the equivalent stress by ~5.26%. The stress-strain variation between sharp and locking interface designs is also compared in Fig. 121. It is evident that introduction of geometrical complexity at the interface can improve ductility and delay failure. This information can be used to geometrically design the interface composed of graded alloy composition with different mechanical strength compared to the alloys used.

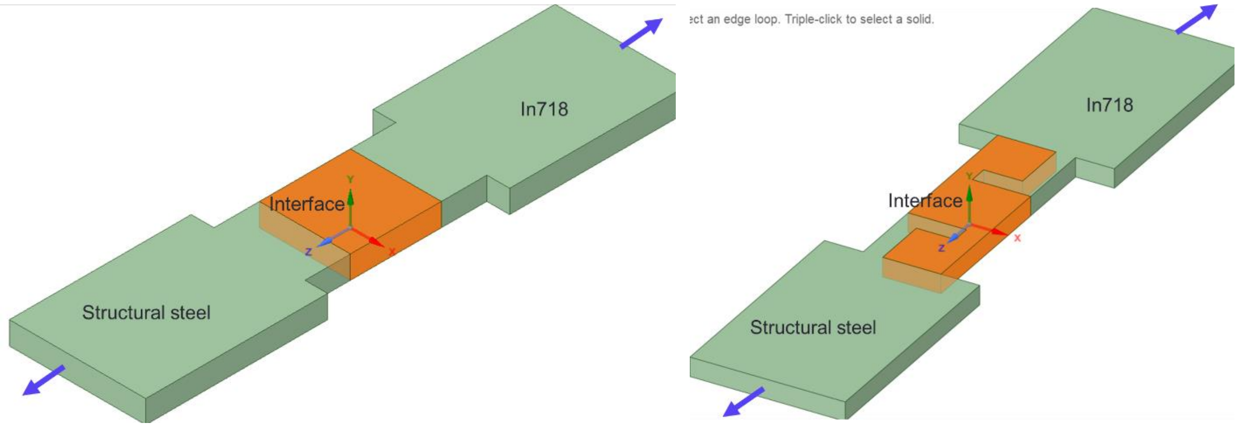
ect an edge loop. Triple-click to select a solid.

(a) (b)

Figure 119. (a) Sharp, (b) Locking interface designs.

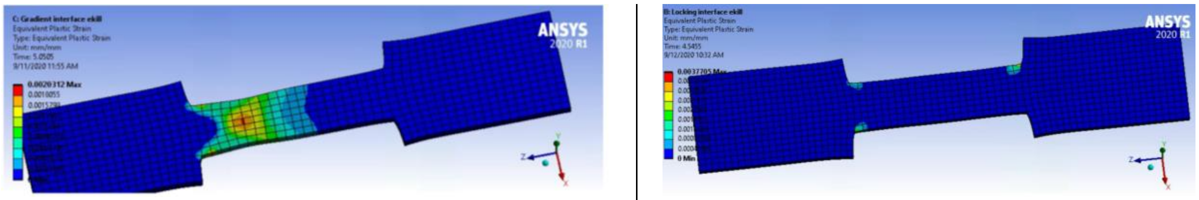

Equivalent plastic strain Equivalent plastic strain

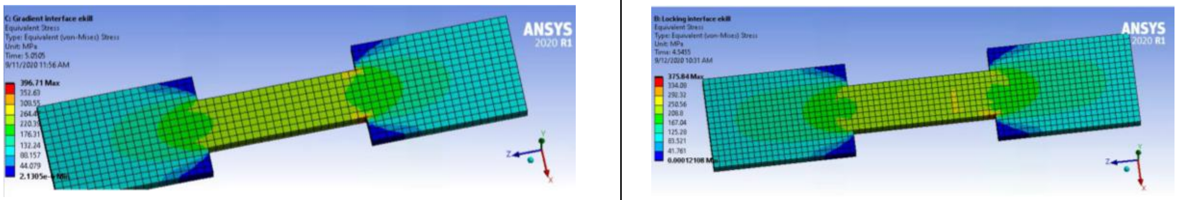

Equivalent stress Equivalent stress

(a) (b)

Figure 120. Distribution of equivalent plastic strain and stress for (a) Sharp, (b) Locking interface designs.

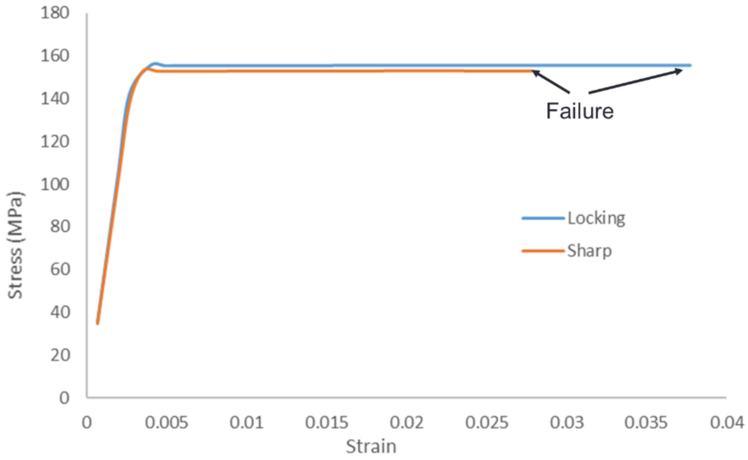

Figure 121. Comparison of stress-strain variation between sharp and locking interface designs.

Ductile Damage model

To include the plastic deformation and actual mechanical behavior of the alloys ductile damage model is developed using the commercial FEA solver Abaqus/CAE 2019. The damage model simulates the tensile tests conducted on the AM specimens build using single alloys (IN740H and P91). Additionally, the tensile tests on heat treated single alloys are also simulated and compared with experimental results for calibration of the damage model. The ductile damage model is a phenomenological model for predicting the onset of damage due to nucleation, growth, and coalescence of voids. It assumes that the equivalent plastic strain at the onset of damage $(\bar{\varepsilon}_D^{pl})$ is a function of stress triaxiality (η) and strain rate $(\dot{\bar{\varepsilon}}^{pl})$ and is given as:

$$\bar{\varepsilon}_D^{pl}(\eta, \dot{\bar{\varepsilon}}^{pl}), \eta = p/q \tag{14}$$

where, p is the hydrostatic stress, and q is the Mises equivalent stress. Damage is initiated at:

$$w_D = \int \frac{d\bar{\varepsilon}^{pl}}{\bar{\varepsilon}_D^{pl}(\eta, \dot{\bar{\varepsilon}}^{pl})} = 1 \tag{15}$$

where, w_D is a state variable increasing monotonically with plastic deformation. In the present study, the damage model is applied in conjunction with the Mises plasticity model. Subsequently, damage evolution is modelled which describes the rate of degradation of the material stiffness once the corresponding initiation criterion (described by Eq. 10) has been fulfilled. At any given time during the analysis the stress tensor (σ) in the material is given by the scalar damage equation:

$$\sigma = (1 - D)\bar{\sigma} \tag{16}$$

where, $\bar{\sigma}$ are the stresses that would exist in the material in the absence of damage. As load is increased, the material point loses its load-carrying capacity when $D = 1$. By default, an element is removed from the mesh if all the section points at any one integration location have lost their load-carrying capacity.

Model calibration

Table 12: Material properties used for P91 and IN740H

P91

Density	7800 kg/m^3	
Young's modulus	2.10E+05 MPa	
Poison's ratio	0.3	
Ductile damage		
Fracture strain	Stress triaxiality	Strain rate
0.8	1	1
Damage evaluation		
Displacement at failure = 0.05		

IN740H

Density	8120 kg/m^3	
Young's modulus	2.25E+05 MPa	
Poison's ratio	0.3	
Ductile damage		
Fracture strain	Stress triaxiality	Strain rate
0.6	1.35	1
Damage evaluation		
Displacement at failure = 0.08		

The stress-strain measurement from ASTM standard tensile bar fabricated using IN740H and P91 were compared with the stress-strain results predicted by the ductile damage model. Fig. 122 illustrates the tensile test simulation as well as the calculation of stress and strain from the model. Prior to designing the interface between dissimilar alloys IN740H and P91, the model is calibrated for as built and heat treated IN740H and P91. The material property input to the model is listed in Table 12. Additionally, a temperature and strain rate independent Johnson-Cook hardening law, is input for calibration of the model. For each as built and heat treated IN740H and P91 builds the yield stress (σ_{YS}) is fitted with different values of A, B and n. The calibrated results for as built and heat treated IN740H and P91 alloys are shown in Fig. 123.

$$\sigma_{YS} = [A + B(\bar{\varepsilon}^{pl})^n] \tag{17}$$

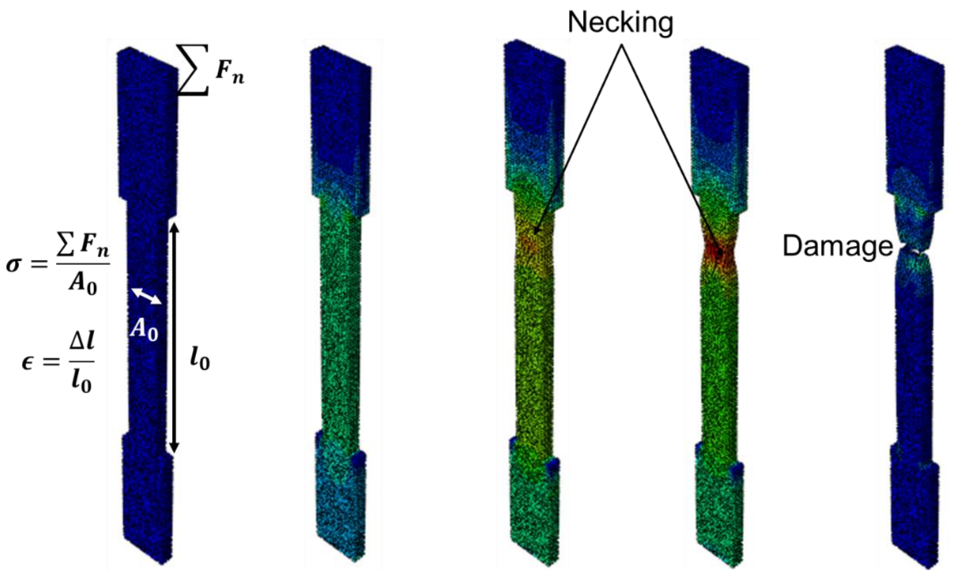

Figure 122. Tensile test simulation results at different instants.

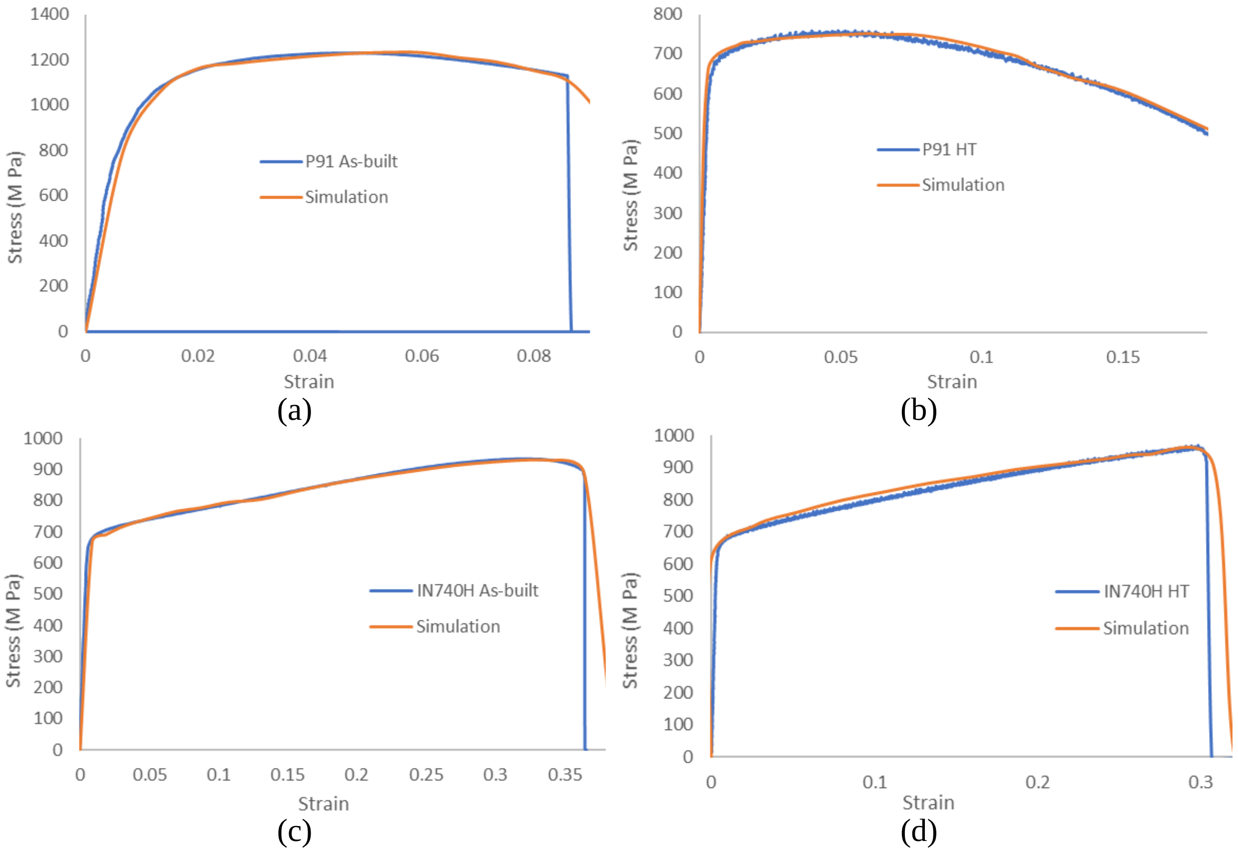

(a) (b)

(c) (d)

Figure 123. Model calibration for (a) P91 As-built, (b) P91 Heat Treated, (c) IN740H As-built, (d) IN740H Heat Treated.

Design comparison

For the AM of dissimilar alloys, it is important to design the interface zone to improve the static load carrying capacity of the component. In the present study, we compare the effect of introducing a locking structure design joining IN740H and P91 alloys as shown in Fig. 124. Figure 124(a) (Interface_1) considers the tensile bar with standard ASTM dimensions, while a non-standard tensile bar size (Interface_2) is considered in Fig. 124(b). Figures 124(a) and (b) assumes perfect bonding between IN740H and P91. However, actual depositions indicated the presence of dilution zone (brittle phase) appearing between IN740H and P91. Therefore, in Fig. 124(c) a sharp interface design is also considered including a brittle phase between the dissimilar alloys. A reduced value of ultimate strength for the brittle phase is based on the proportional decrease in its hardness from IN740H. In the future, the actual materials property of the gradient alloy composition (arrived from ICME simulations) for the interface will be considered.

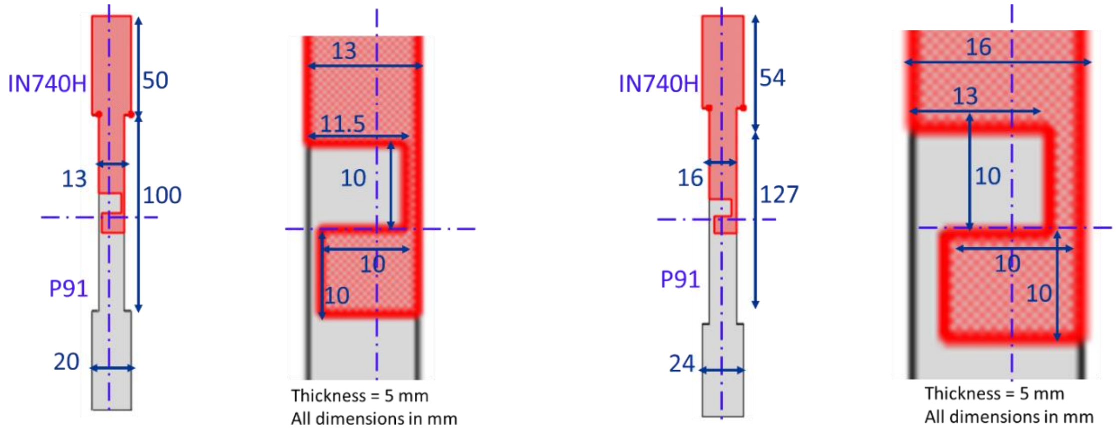

Interface_1
(a)

Interface_2
(b)

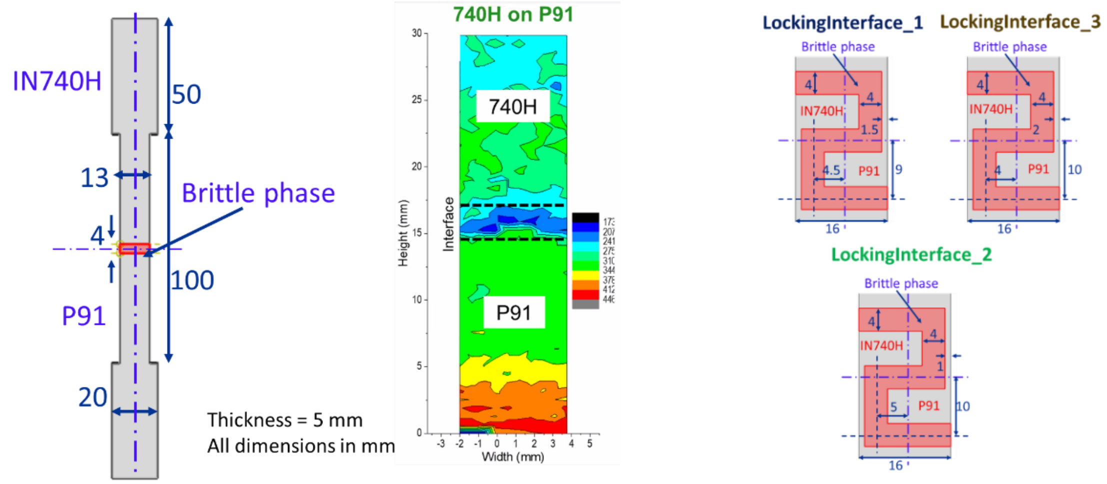

(c)

(d)

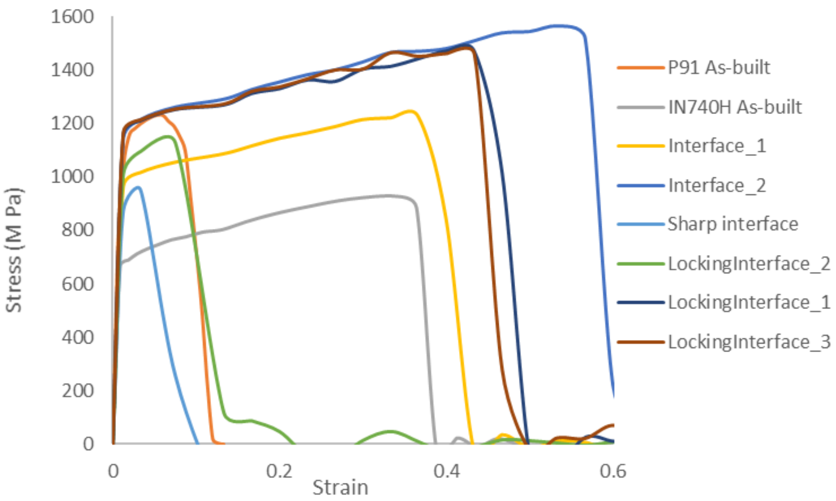

(e)

Figure 124. (a) ASTM standard, (b) non-ASTM standard tensile bar with locking design, and (c) ASTM standard tensile bar with shar interface, (d) 3 different interlocking designs at the interface for non-ASTM standards, (e) Stress-strain comparisons for different interface designs with P91 and IN740H as-built alloys.

Figure 124(d) shows 3 different interlocking designs for the interface considering the aspects of manufacturability in the designs. The stress-strain variations for different interface designs are compared with the P91 and IN740H as-built alloys in Fig. 124(e). The locking design can take advantage of higher ductility of IN740H and higher strength of P91 as compared to the sharp interface design. The perfect bonding assumption between the dissimilar alloys results in increased plasticity for Interface_2 (non-ASTM standard) design.

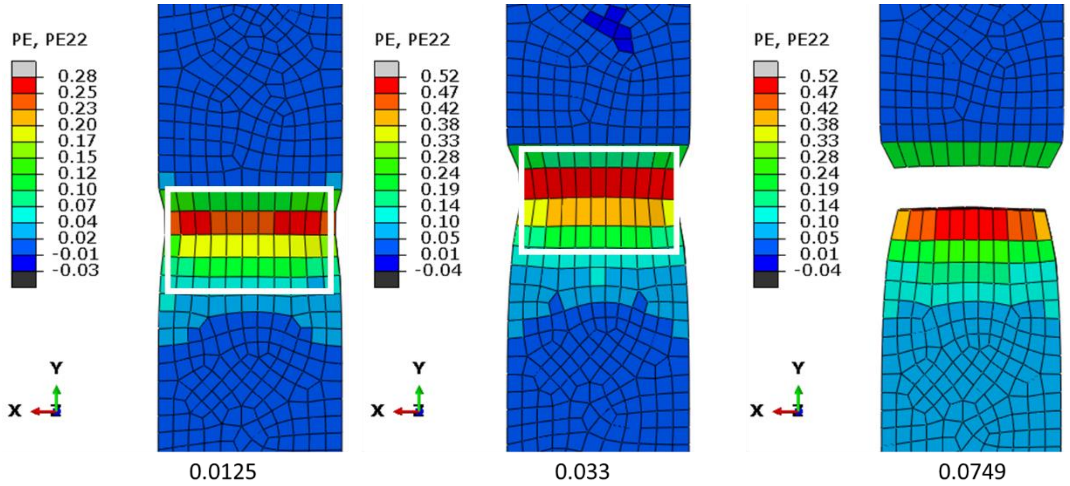

Figure 125. Plastic deformation in sharp interface.

The comparison of plastic deformation between sharp and locking interface design is studied in Figs. 125 and 126. In sharp interface design the necking phenomena starts at lower strain value (0.0125) and the reaction load distributes to nearby brittle phase elements resulting in failure at lower strain (0.0749) due to lower ultimate strength in brittle phase compared to P91. On the other hand, introduction of a locking interface design leads to initial elongation in IN740H at lower strain (0.166). As the load is increased, the necking phenomena transfers to the interface zone to redistribute reaction load (see Fig. 126(a)). Subsequently, the reaction load can be gradually redistributed to P91 to cause failure at higher strain (0.468) (see Fig. 126(b)). Thus, it is evident that the introduction of a locking interface design improves the static load carrying capacity of the component. In the future, the mechanical (stress-strain) response due to the introduction of gradient composition in the interface will be studied and further improvements in the design (if necessary) will be incorporated.

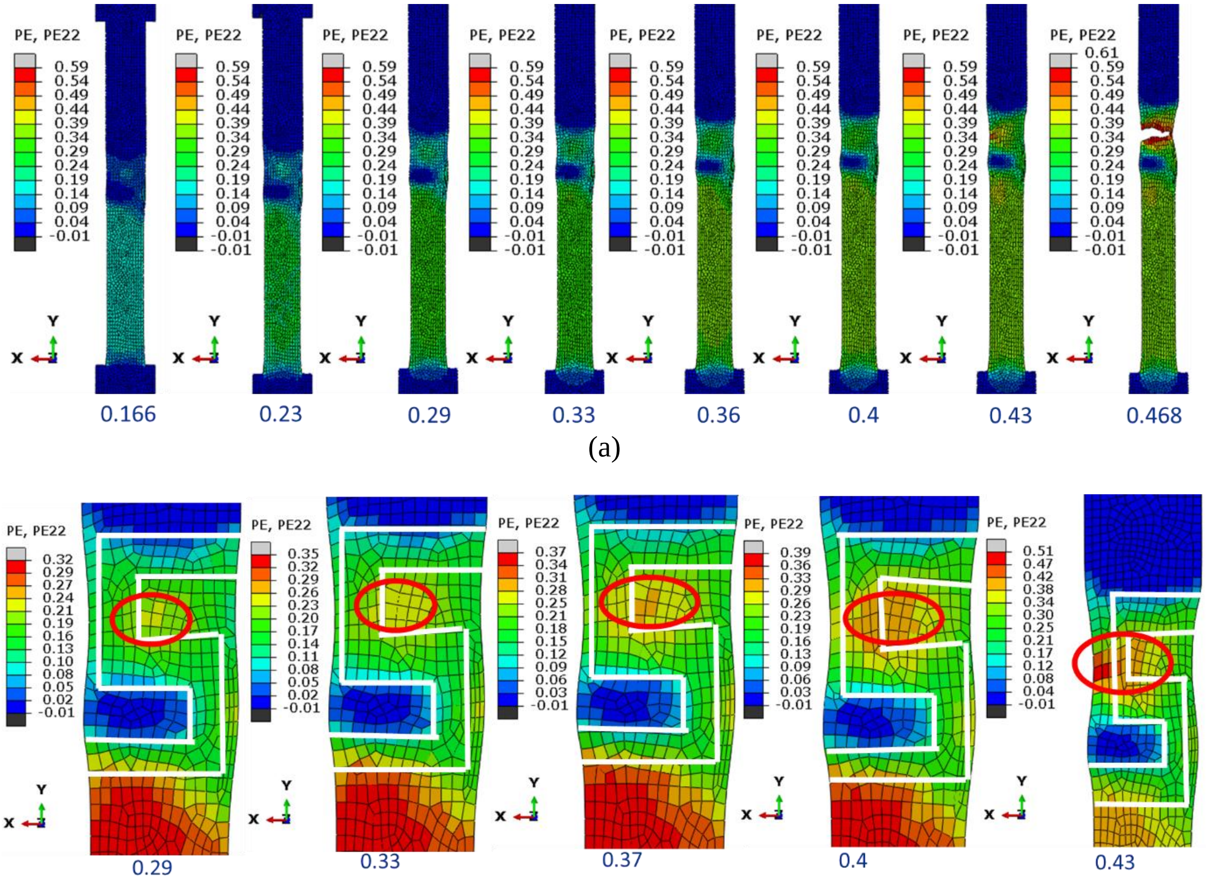

(a)

(b)

Figure 126. Plastic deformation in LockingInterface_1 design (a) deformation of entire tensile bar, (b) deformation of the interface zone at different strain values.

Modification of Interlocking Design

Previously, ductile damage model was developed for single alloy builds (IN740H and P91) using the commercial FEA solver Abaqus/CAE 2019. The model was also calibrated by comparing with the experimental stress-strain response of the single alloy builds. Additionally, a locking structure design joining IN740H and P91 alloys was introduced. Different tensile test specimens (ASTM standard and nonstandard) with locking structure were compared with sharp interface design to understand the mechanism of failure due to the presence of dilution zone (brittle phase) appearing between IN740H and P91. The study revealed that introduction of a locking interface design leads to initial elongation in IN740H at lower strain (~0.166). Subsequent increase in static load redistributes the reaction load from the interface to P91 leading to failure at much higher strain (~0.468). In the previous study LockingInterface_1 design, as shown in Figure 41, was used for understanding the failure mechanism. In this report a modified design, LockingInterface_4 as shown in Fig. 127, has been suggested for AM. LockingInterface_4 is shorter in size with similar size of the gradient interlock zone.

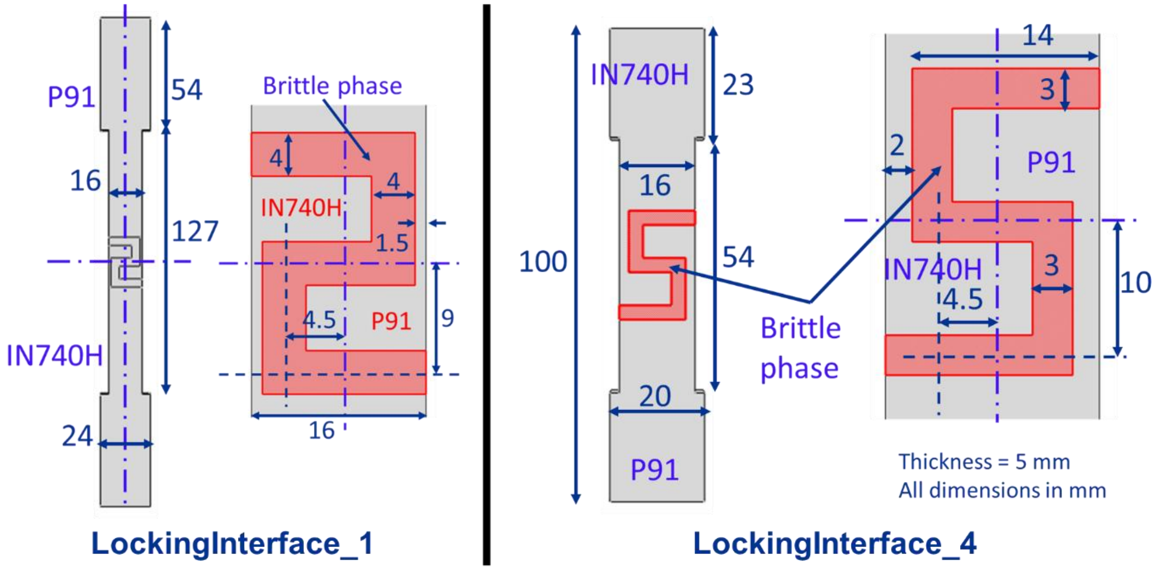

Figure 127. Non-ASTM standard tensile bar with locking design (a) LockingInterface_1, and (b) LockingInterface_4.

A comparison of the plastic deformation between LockingInterface_1 and LockingInterface_4 is presented in Figs. 128(a) and 128(b). The initial elongation in IN740H initiates at lower strain (0.0125) in LockingInterface_4 compared to LockingInterface_1 (at 0.166 strain). This can be attributed to the shorter gauge length of LockingInterface_4. Like LockingInterface_1, the reaction load redistributes in the P91 zone in LockingInterface_4. Additionally, although the LockingInterface_4 improves the strength by merely ~1%, it reduces the ductility by ~50%, as seen in Fig. 128(c). However, from a manufacturing perspective the relatively wide flanges and the gauge section compared to the length, provides improvement in introducing gradient alloy compositions in the interlocking zone during deposition. Therefore, in the future, the stress-strain response due to the introduction of gradient composition in the interlocking zone will be compared with experimental results and further improvements in the design (if necessary) will be incorporated.

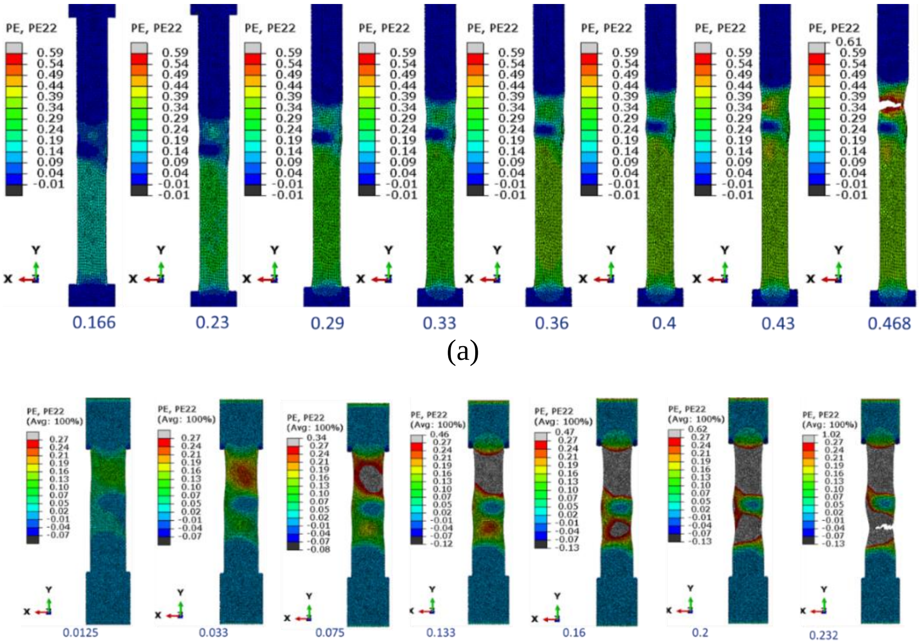

(a)

(b)

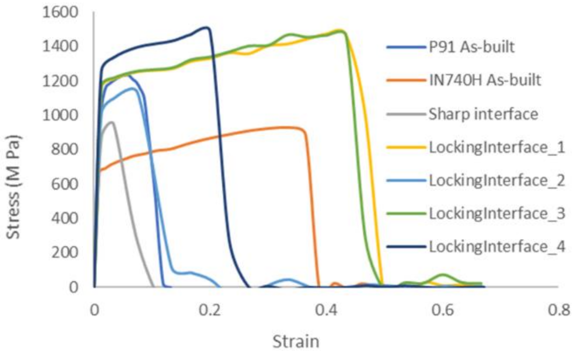

(c)

Figure 128. (a) Plastic deformation in entire tensile bar (a) LockingInterface_1 design, (b) LockingInterface_4 design, and (c) Stress-strain comparisons for different interface designs with P91 and IN740H as-built alloys.

Interlocking Design: Comparison with experimental results

In addition to the blended alloy compositions, fabrication was completed for a sample which includes a dissimilar material joint/shape including an interlocking feature. This interlock, rather than an an abrupt transition between the two alloys, aims to avoid brittle behavior at the interface. The design suggested by Pitt is shown in Fig. 129. Here, the right section of the sample (shown as a tensile bar, designed to test across the material interface) is P91, while the left is IN740H. The red section is the region where dilution will likely occur between the two materials.

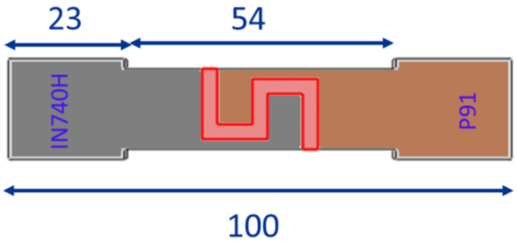

Figure 129. Proposed interlock design for tensile bar with dissimilar material joint.

To achieve this shape, the middle section of the deposit fill pattern was modified as shown in Fig. 130. Base layer (P91) and upper layers (IN740H) remained similar to previous deposits, with matching deposition conditions. The middle section utilized the fill pattern shown below. To achieve the left and right interlock shapes, the below pattern was alternated. First, 5 layers of a right-hand interlock continued to deposit the P91 along the blue line of the pattern, with IN740H in the remaining bulk. Later, the interlock was switched to left side, with IN740H as the blue line, for an additional 5 layers. This serves to generate the structure shown in Fig. 129.

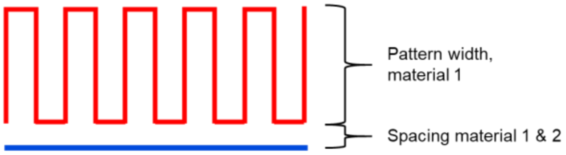

Figure 130. Fill pattern used to generate the interlock structure, in the middle of the deposit.

In the above pattern, the blue line travel speed was 3 mm/s (slower, to ensure good fusion with the remainder of the fill pattern), while the red pattern travel speed was the standard 5 mm/s. Red pattern width was reduced to 8.5 mm width, with the same 3mm stepover as before. Spacing between material 1 & 2 was 3 mm, matching the raster pattern spacing. The interlock samples were sectioned into tensile bars via electrical discharge machining (EDM) and submitted for further mechanical testing.

The tensile test results of the locking interface designed based on the FE analysis are compared with the FE simulation results. The FE analysis were conducted in the using the commercial FEA solver Abaqus/CAE 2014. The geometrical specifications of the non-standard tensile test specimen along with the size of the interface zone is shown in Fig. 131. The hardness data of the interface zone was measured by Dr. Xiong's group. For the ductile damage model, the approximate relation Yield strength (MPa) = 9.81*Hardness in HV/3, was used in the calibrated ductile damage model.

A comparison of the stress-strain comparisons for the interface design (tensile test result and FE simulation) with P91 and IN740H as-built alloys is provided in Fig. 132(a). The FE simulation predicts higher yield stress (~12.09%) for the interface design compared to the experimental tensile test results. Additionally, for the FE simulation the ultimate tensile test (UTS) is ~5.88% higher than the UTS measured for the experimental tensile test results. A comparison of the plastic deformation from the FE analysis for the interface design is provided in Fig. 132(b). It is evident that the failure initiates at the P91-interface boundary as highlighted in Fig. 132(b).

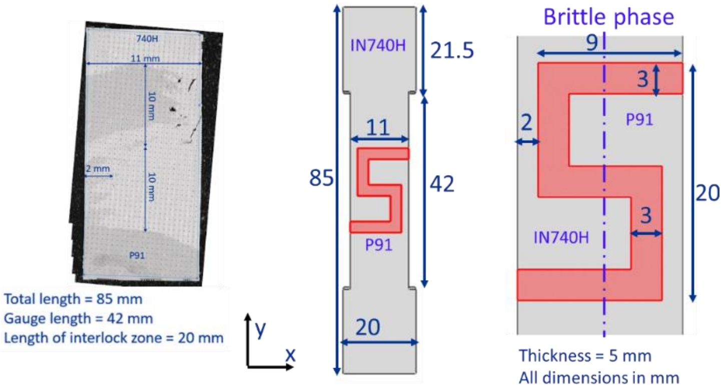

Figure 131. Non-ASTM standard tensile bar with locking interface design.

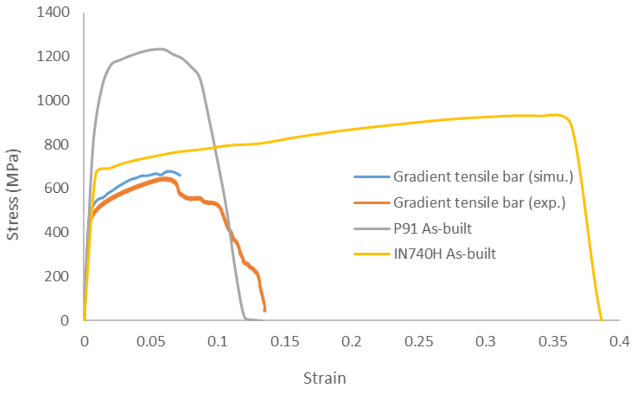

(a)

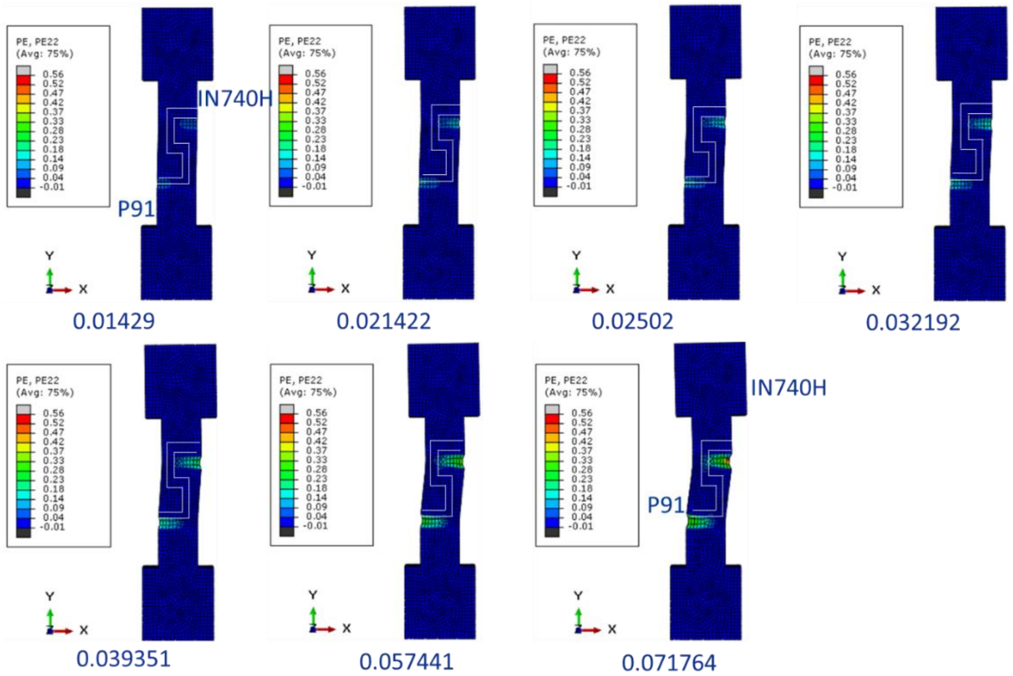

(b)

Figure 132. (a) Stress-strain comparisons for the interface design (tensile test result and FE simulation) with P91 and IN740H as-built alloys (b) Plastic deformation in entire tensile bar.

3.5 Graded alloy design optimization and performance evaluation

3.5.1. Data driven design of graded alloy using machine learning and genetic algorithm

For the design of new graded alloy, we firstly built the gradient alloy with 0, 10, 20, … 100 % P91 content using WAAM. Then, we measured the hardness, porosity, cracks, and compositions, and used different modeling tools to predict the phase fractions, martensitic start temperatures, etc., to build the database for the machine learning model. Later, the genetic algorithm is employed to optimize the materials descriptor set in order to get the most accurate machine learning model. Lastly, we predicted the gradient alloy property like the hardness and porosity, verified the design using experiments, and discovered the location-specific properties. The framework used is shown as a schematic in Fig. 133.

Figure 134 shows three different sampling tracks along the building direction. It is found that the properties of the material do not only change along the building direction with different P91content but also vary with different locations that are vertical to the building direction. For example, the matrix phase gradually changes from martensite to austenite with more 740H content and the track 1 matrix changes to austenite earlier than track 3. Such a variation reveals that the additive manufactured component has location-specific properties, and it provides a diverse dataset with more than 400 data points. In addition to the experimental results, we also calculated the phase information and thermodynamic properties. The simulated results match well with the experiments, implying that we could use the simulated results as materials descriptors to model the performance of the material.

After adding simulated results to the dataset, we have more than thirty materials descriptors. In order to build an accurate model, we adopted the genetic algorithm (GA) to optimize the selection of descriptors, and the results are available in Fig. 135. Compared with the model with only composition as the material descriptors, the root mean squared error (RMSE) of models with calculated properties decreased dramatically, showing that adding the calculated descriptors is beneficial for the machine learning model. We optimized the model performance three times for the hardness and porosity model, respectively. As the GA iterates, the RMSE keeps decreasing until the model performance reach a plateau, and the performance of all three models is similar. This result indicates that the GA can effectively search for the optimized set of material descriptors.

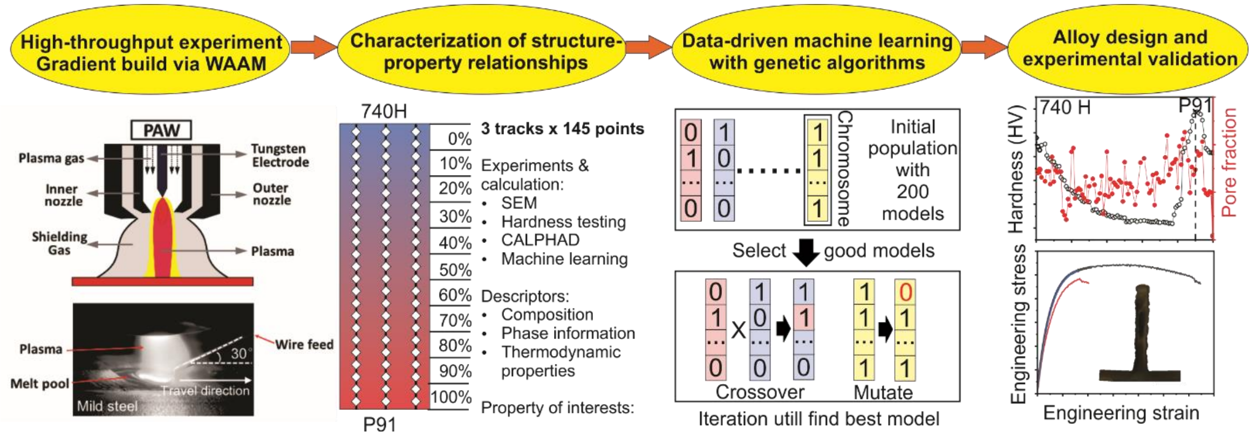

Figure 133. Flow chart of machine learning alloy design using database established via WAAM and high-throughput experiments and calculation.

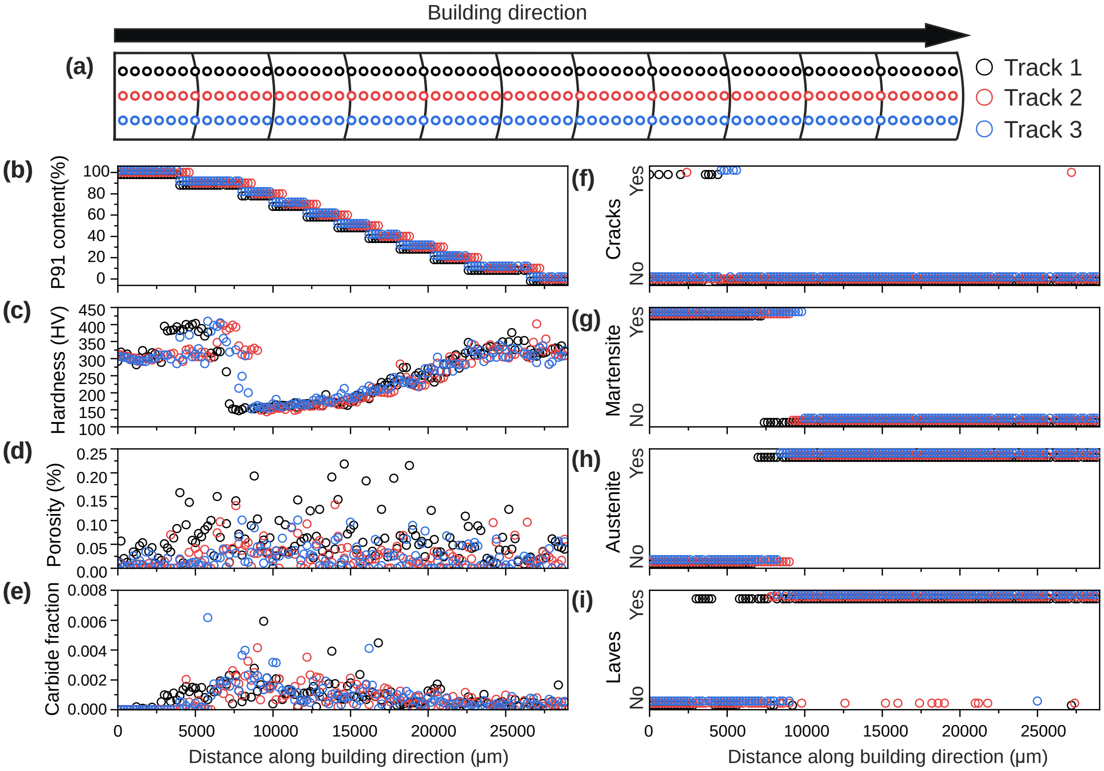

Figure 134. High-throughput experimental results along building direction. (a) Schematics of the build and three testing tracks (b) P91 content, (c) Vickers hardness, (d) Porosity, (e) carbide fraction, (f) If cracks are introduced during hardness test, (g) Martensite distribution, (g) Austenite distribution, (i) Laves phase distribution.

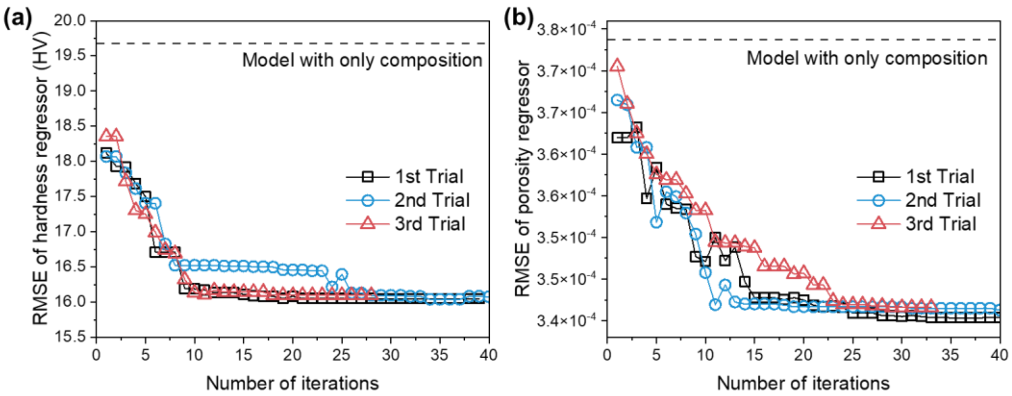

Figure 135. The model performance as a function of genetic algorithm iterations. (a) hardness model, (b) porosity mode. The dashed line is the models trained with only alloy composition, while the colored lines are models trained with the composition and calculated descriptors.

Moreover, the GA also helps researchers determine what features are helpful in predicting target properties and find the potential physical link between the descriptors and properties. We counted how many times a materials descriptor has been selected for machine learning models and summarized the results in Fig. 136 (a). Those features are categorized into composition, phase, and thermodynamic properties. For predicting hardness, it is found that Fe, Ni, Si, Mn, N, Martensite, and Laves phase fractions have been selected more than twice during the three trials, while the Si, Al, Ti, Nb, Cu, Laves and MX (carbides or nitrides) phase fractions, thermal expansion coefficient (TEC), latent heat, and heat capacity (Cp) are the most important descriptors. Below is a case study explaining why GA-selected features help us understand the underlying physics relationship. For example, Laves phase has been selected in the porosity model because Laves phase is often associated with the pore formation, as shown in Fig. 136(b). This phenomenon may be caused by the remelting of low melting temperature phase e.g. laves during cyclic heating and cooling process [14]. Moreover, the MX phase fraction is also selected for predicting porosity prediction. In order to explain this phenomenon, we summarized the accuracy of phase labeling with more than 100 labeled black features, and the results are plotted as the confusion matrix in Fig. 136(c). The confusion matrix shows that 23 % MX will be labeled as pore, which will lead to the correlation between porosity and MX phase fraction.

Based on the data collected for the gradient build and the genetic algorithms, data-driven models have been developed to calculate the hardness variation and pore fraction along with the gradient composition. Based on the calculated results (Fig. 137), it is found that the hardness will firstly decrease with the addition of P91 to 740H. However, after reaching 80 wt.% P91, the hardness will drastically increase to a peak and drop as the composition is close to P91. Moreover, it is found that 90% P91 composition exhibits the highest hardness and a relatively low pore fraction compared to P91, 740H, and other gradient alloys. As a result, we select this composition as the new composition for alloy used in the as-built condition. Moreover, the entropy of the gradient alloys and phases at 1200˚C have being calculated using different thermodynamic databases. As shown in Fig. 137(b), all results show a similar trend that the entropy will reach the maximum value near 26% P91. Since the high entropy often lead to good properties, the 26% P91 alloy is also selected for printing and further study.

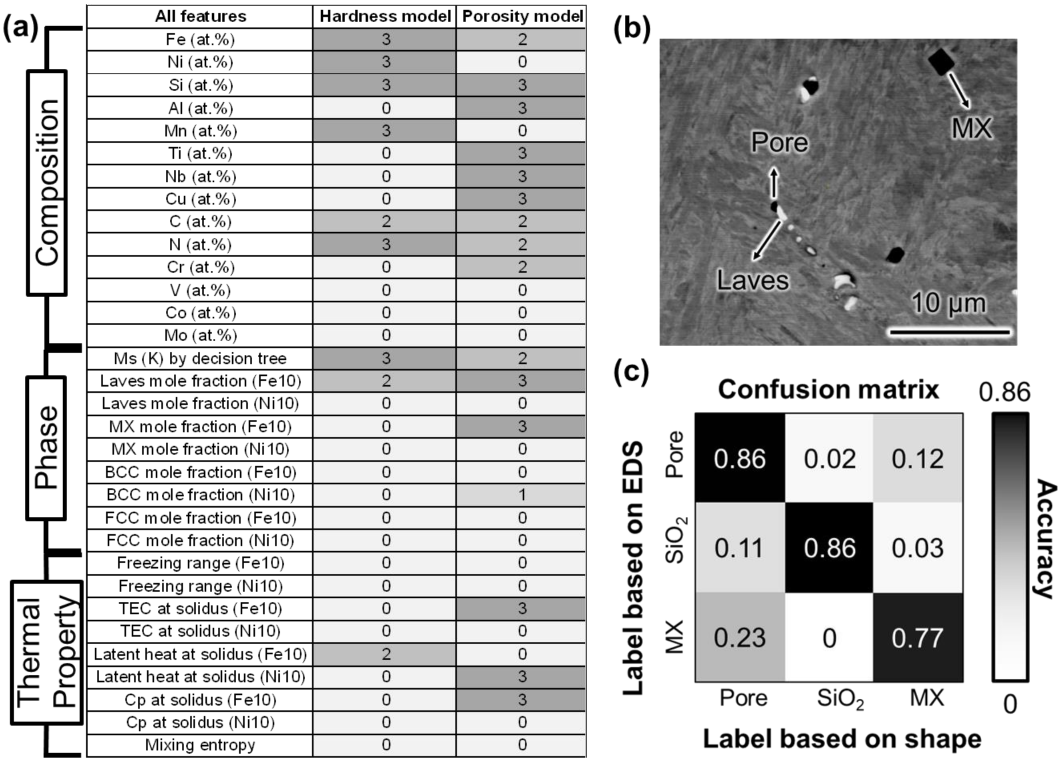

All features	Hardness model	Porosity model
Fe (at.%)	3	2
Ni (at.%)	3	0
Si (at.%)	3	3
Al (at.%)	0	3
Mn (at.%)	3	0
Ti (at.%)	0	3
Nb (at.%)	0	3
Cu (at.%)	0	3
C (at.%)	2	2
N (at.%)	3	2
Cr (at.%)	0	2
V (at.%)	0	0
Co (at.%)	0	0
Mo (at.%)	0	0
Ms (K) by decision tree	3	2
Laves mole fraction (Fe10)	2	3
Laves mole fraction (Ni10)	0	0
MX mole fraction (Fe10)	0	3
MX mole fraction (Ni10)	0	0
BCC mole fraction (Fe10)	0	0
BCC mole fraction (Ni10)	0	1
FCC mole fraction (Fe10)	0	0
FCC mole fraction (Ni10)	0	0
Freezing range (Fe10)	0	0
Freezing range (Ni10)	0	0
TEC at solidus (Fe10)	0	3
TEC at solidus (Ni10)	0	0
Latent heat at solidus (Fe10)	2	0
Latent heat at solidus (Ni10)	0	3
Cp at solidus (Fe10)	0	3
Cp at solidus (Ni10)	0	0
Mixing entropy	0	0

	Pore	SiO_2	MX
Pore	0.86	0.02	0.12
SiO_2	0.11	0.86	0.03
MX	0.23	0	0.77

Figure 136. (a) Materials properties selected by GA models, numbers in the cell is the times of the feature has been selected by GA during the three trials (b) SEM image showing the relationship between Laves phase and pore. (c) Confusion matrix showing the relationship between carbides and pore.

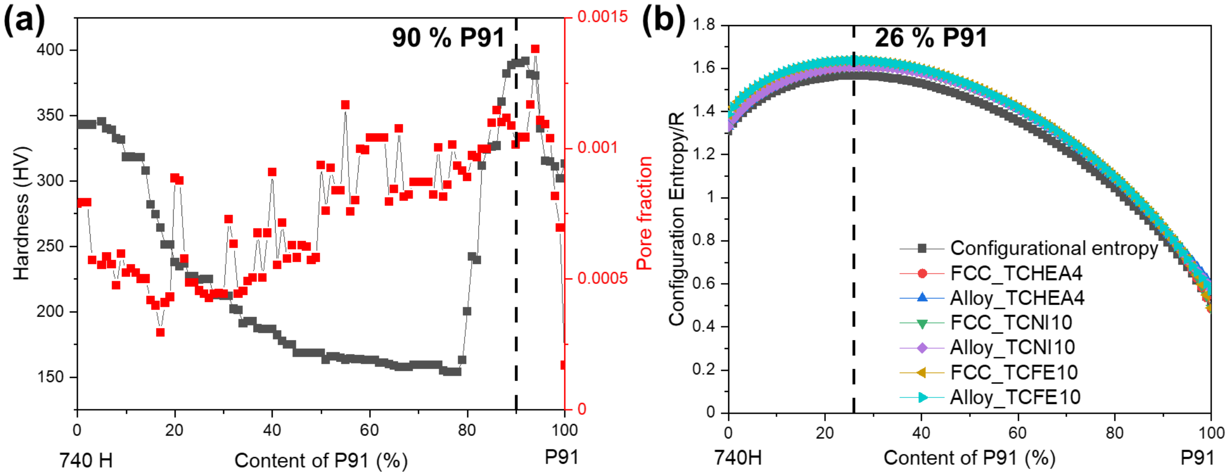

Figure 137. (a) Prediction of the hardness and pore fraction for gradient alloy using data driven model, (b) Prediction of the entropy change for gradient alloy.

3.5.2. WAAM of computationally designed graded alloy

Several new designs for gradient and blended-alloy compositions were developed based on earlier results and modeling team efforts. Among these are several large blocks to be deposited via WAAM, which include a constant blend of P91 steel and IN740H throughout. Each block is designed with a different ratio of the two materials, as a means to test various heat treatments, explore microstructure, and mechanical properties as shown in Fig. 138.

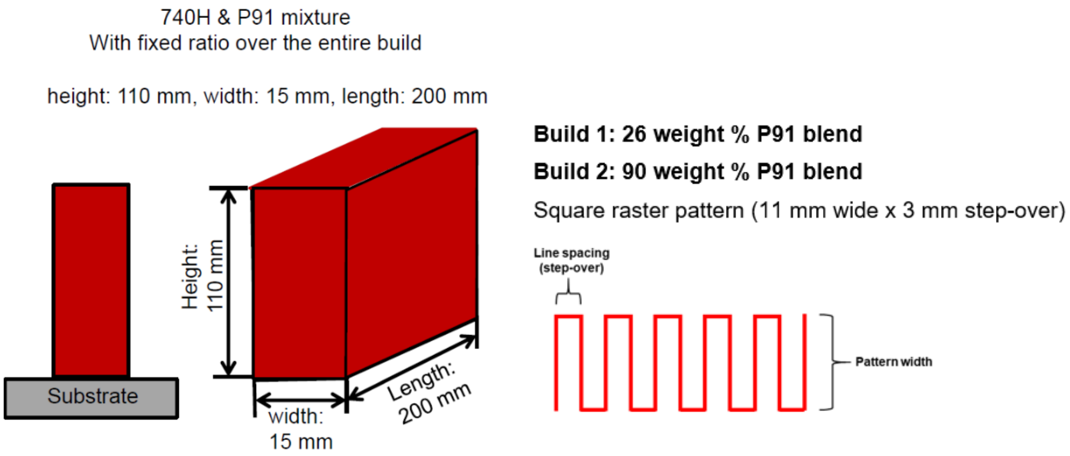

Figure 138. Blended material composition for graded alloy samples.

For these sample builds, the deposition parameters remain the same as previous bulk sections fabricated from both single and gradient compositions. The base layer is produced at slightly elevated power and slower travel speed, to ensure good fusion to the substrate. The wire feed ratios for both builds are shown below, which are set to achieve the desired wt.% throughout the sample. Recall, the wire diameters are 0.035-inch for the P91 steel, and 0.039-inch for the IN740H, along with their slight differences in density, which was taken into account when calculating required feed rates.

- **Build 1: 26% P91 blend**
  - 0.82 m/min P91 + 1.80 m/min IN740H
- **Build 2: 90% P91 blend**
  - 2.83 m/min P91 + 0.24 m/min IN740H
- **Deposition parameters for both samples:**
  - 166 Amp main current, 5 mm/s travel speed, square raster pattern 11mm x 3mm
  - Interpass temperature < 175°C before beginning next layer

The resulting bulk coupons for the deposits are shown in Fig. 139.

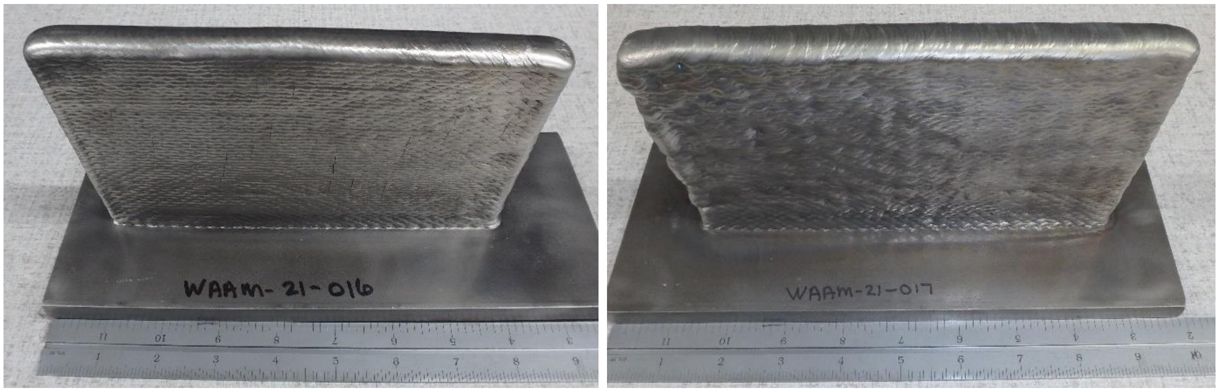

Figure 139. Final build fabricated using WAAM for 26 wt.% P91 (left) and 90 wt.% P91 (right).

Characterization of as-built 90 wt.% P91 graded alloy

The SEM micrographs obtained using the BSE showed that the matrix was martensite and there were two types of secondary phases namely, carbides and Laves phase as shown in Figure 140. The carbides were rich in Ti while the Laves was rich in both Nb and Ti. It was also found that the carbides were dispersed throughout the sample and in higher volume fraction than the Laves phase. While the Laves phase was found mainly in the PAG boundaries indicating that there is segregation of Nb along these grain boundaries during the transformation. From Fig. 141, the IPF and the reconstructed PAG maps prove that Laves phase precipitates predominantly along the PAG boundary.

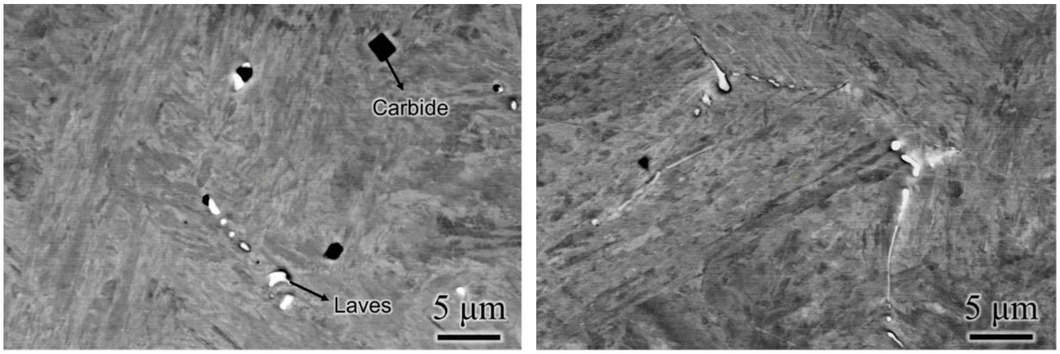

Figure 140. BSE-SEM micrographs showing the presence of carbide and Laves phase in a martensitic matrix of the 90 wt.% P91 build.

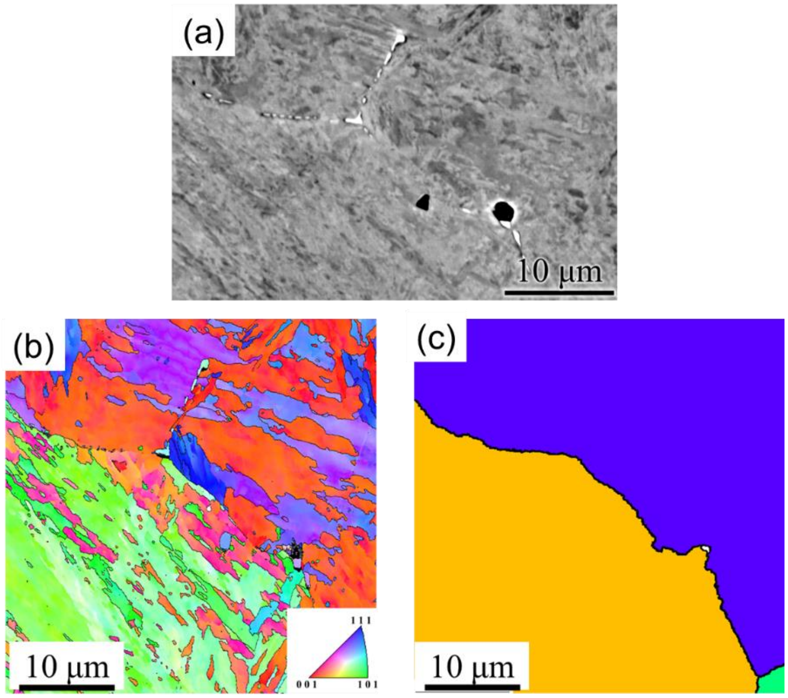

Figure 141. (a) BSE-SEM micrograph, (b) IPF map and (c) reconstructed PAG map showing that the Laves phase precipitates predominantly in the PAG boundary in the as-built 90 wt.% P91 build.

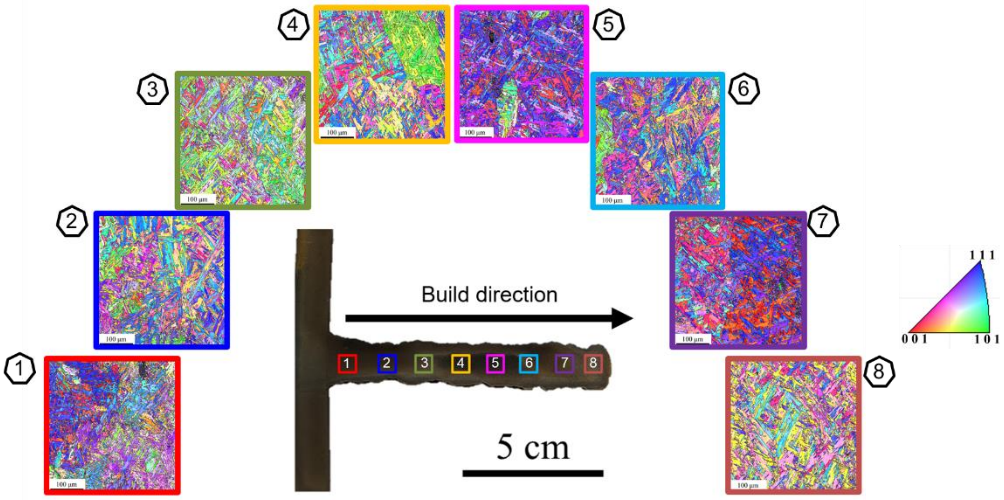

Figure 142. IPF maps from different regions of the as-built 90 wt.% P91 sample along the build direction showing that the matrix is martensitic.

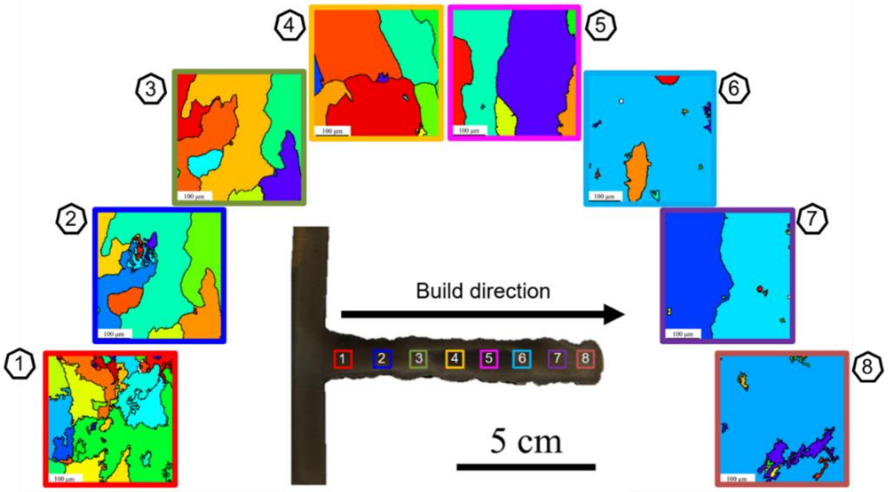

Figure 143. Reconstructed prior austenite grain maps from different regions of the 90 wt.% P91 sample along the build direction showing that the PAG size increases as the build height increases.

To further understand the grain structure along the build direction, EBSD was performed in different locations as shown in Figure 142. The matrix was completely martensitic along the build direction. Moreover, the prior austenite grains were reconstructed using the ARPGE software using the EBSD data as input as shown in Figure 143. It was found that the prior austenite grain size increases as the build height increases. This is mainly dure to the repeated thermal cycling in the bottom layers which refines the grains while, the number of thermal cycles the top layers are subjected to is lesser. The hardness map was obtained for the as-built sample as shown in Figure 144. It was found that the hardness was uniform throughout the sample and the average hardness (356 HV) is close to the hardness used as input for the modelling using machine learning.

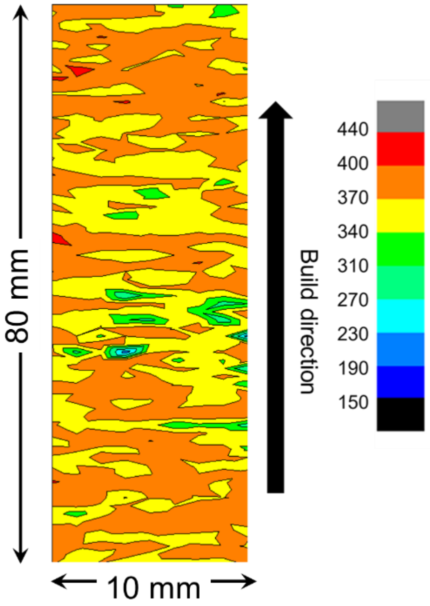

Figure 144. Hardness map obtained for the as-built 90 wt.% P91 graded alloy along the build direction.

The 90 wt.% P91 has been manufactured by WAAM, and its mechanical property is measured by tensile test, which is listed in Fig. 145. There is a significant variation in the performance of the sample cut from the WAAM build alloy. For test 1, the strength, UTS, and Elongation are good, while tests 2 and 3 have no ductility. Based on Figs. 145(b, c), we found that test 1 fracture surface shows more dimples than the fracture surface of test 3. In order to investigate the cause of the difference, we characterize the microstructure of the build. Figs. 145(d-f) show the microstructure at the bottom, middle and top, respectively. The bottom part shows spherical gas pores, which are caused due to the trapped gas [15]. However, lack of fusion pores is noticeably observed in the middle part due to the input energy that fails to fully melt the materials and leaves large and irregular voids [16]. Moreover, cracks and pores are also found in the middle part, which may be caused by the localized residual stress and remelting low melting point secondary phase during the cyclic heating and cooling process [14]. Figs. 145(g-h) are obtained from the part below the gauge section of test 1 and test 2, which show the printability variation along with the length direction. The test 3 sample that locates close to the center shows lack of fusion pores, and it has higher porosity compared with test 1 tensile bar that is close to the edge of the build. Thus, we can claim that the porosity is higher in the middle, while it is smaller in the bottom and the edge, which is illustrated in Fig. 145(i). Since high porosity will decrease the ductility and strength [17], the difference of strength and ductility maybe attributed to the site-specific porosity, i.e., printability. It is generally believed that both the materials intrinsic property and thermal history can affect printability. Since the build has a uniformed composition, the difference of porosity should be caused by the different thermal profile at different locations even with the same processing parameters. A similar phenomenon has been reported in Inconel 718 manufactured by directed energy deposition [18]. Thus, it is suggested that we should monitor the thermal profile at different locations and add this information to the machine learning model to build the alloy with controlled thermal history and uniform properties.

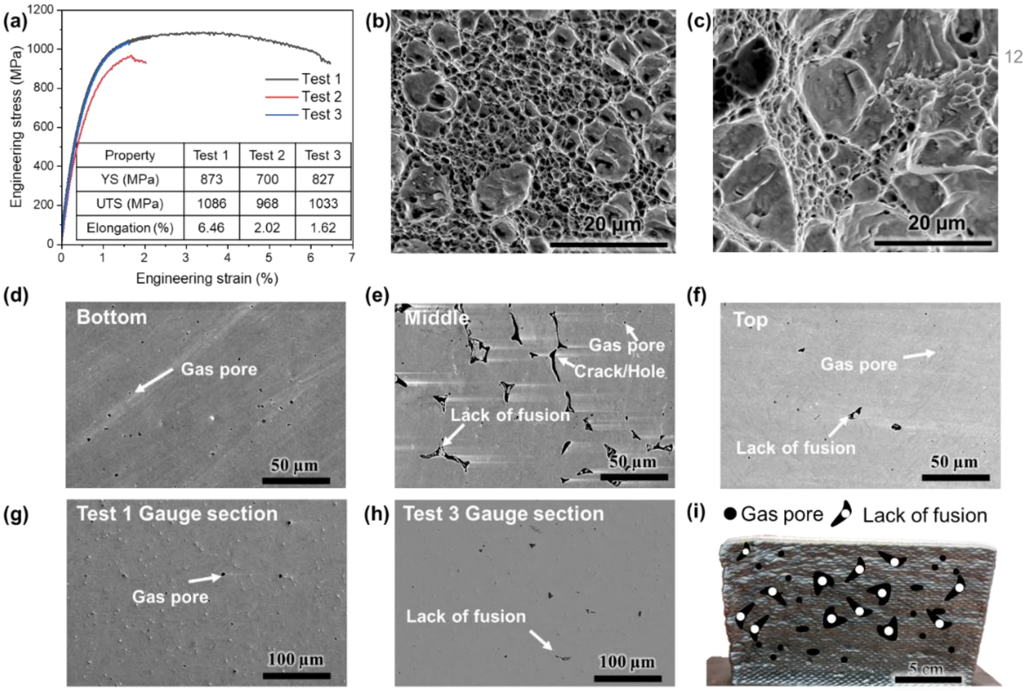

Figure 145. Uncertainty of the tensile property and microstructure of as-build 90 wt.% P91 alloy. (a) Uniaxial tensile strain-stress curves of the as-build samples. (b) SEM image of the test 1 fracture, (c) SEM image of the test 3 fracture, SEM image showing the difference of porosity at (d) bottom (e) middle (f) and top of the 90% P91 build, SEM image of (g) test 1, (h) test 3 gauge length part of the 90% P91 build, and (i) schematics showing the variation of pores at different locations. All SEM images are obtained using secondary electron mode.

Location-specific solidification cracking in 26 wt.% P91 graded alloy

Fig. 146 shows the SE-SEM micrographs of the cracks of varying lengths from different locations of the sample. It can be observed that the longest cracks were observed in the Top portion of the sample and the crack length decreases in the Middle region. No cracks were observed in the Bottom region of the sample. It is to be noted that cracking was observed only after deposition of the first 15 layers during the WAAM processing, although, in total, there are 58 layers to accomplish the build. The inverse pole figure (IPF), kernel average misorientation (KAM) and phase maps obtained from the cracked region in the top and middle portions of the sample using EBSD are shown in Fig. 147. It is evident from the IPF map that the grain structure is columnar, and the crack is intergranular since it propagates along the grain boundary. Moreover, the grains are coarser in the middle portion since it has undergone multiple thermal cycling during the deposition in comparison with the top section of the sample. KAM represents the residual stresses qualitatively and is defined as the average misorientation around a point corresponding to a defined set of nearest neighbors. Therefore, we applied it to gain more insight into the crack formation at locations 1 and 2. From the KAM maps (Figs. 147(c) and 147(d)), it can be observed that the region around the crack has a very high misorientation angle (red points with KAM ~ 5° and the yellow regions with KAM ~ 3-4° surrounding the crack) in comparison with the surrounding matrix implying that the residual stresses are high near the cracked region. It is also evident that the grains in the top portion of the sample have higher KAM (green regions with KAM ~ 2-3°) within the grains in comparison with the Middle portions (blue regions with KAM ~ 0°) within the grains. This is because the middle portion undergoes a larger number of heating and cooling cycles that annihilates the residual stresses while the top layers are subjected to lesser thermal cycling leading to higher residual stress within the grains. From the phase maps (Figs. 146(e) and 147(f)), it is evident that the 26 wt.% P91 alloy has a single-phase FCC structure. Figs. 148 and 149 show the composition maps for the major (Ni, Fe, Cr, and Co) and minor (Cu, Mo, Nb, and Ti) alloying elements from the cracked regions in the top and middle sections of the sample, respectively. The composition maps for Cu and Nb clearly show that the extent of segregation varies in different sample locations. The Cu segregation is higher in the top portion of the sample but is lower in the middle portion. Thus, it is clear that the extent of Cu segregation increases as the build height increases. On the other hand, Nb segregation is found to be more pronounced in the middle section but to a lesser extent in the top portion of the sample. Therefore, it can be inferred that the difference in length of the cracks and extent of segregation of the minor alloying elements such as Cu and Nb will lead to varying solidification cracking susceptibility along the build direction, which will be estimated using computational techniques as explained further.

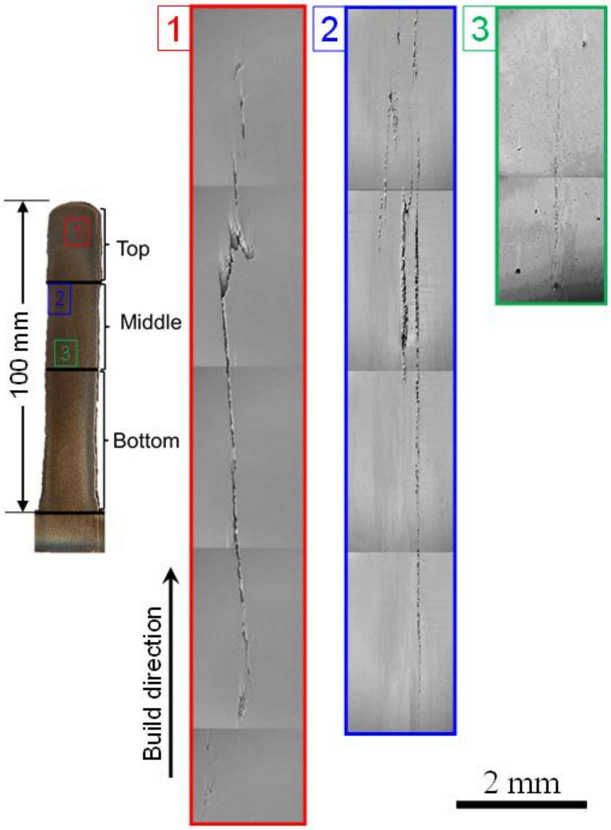

Figure 146. SE-SEM micrographs showing cracks of varying length from different locations of the 26 wt.% P91 sample along the build direction.

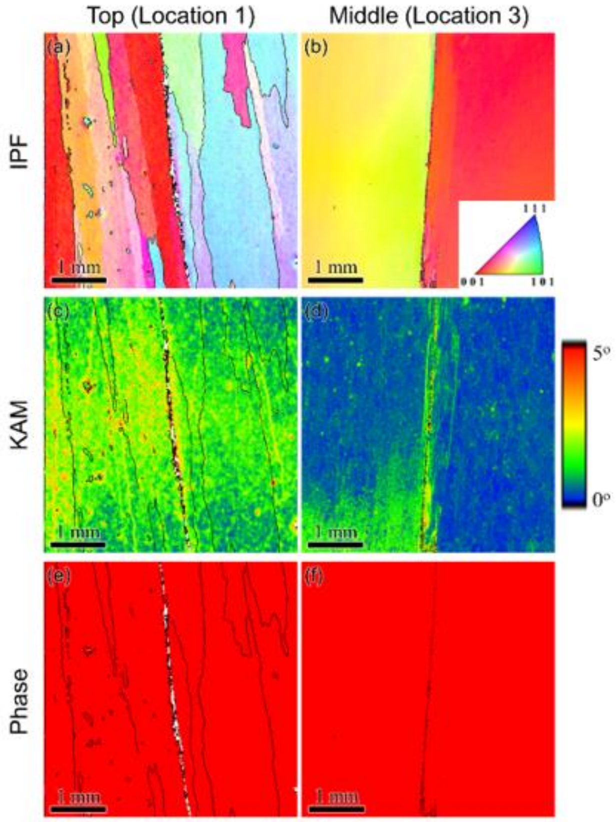

Figure 147. (a, b) IPF, (c, d) KAM and (e, f) Phase maps from Locations 1 and 3 (shown in Figure 2) from the Top and Middle sections, respectively, showing that the cracks are intergranular with high KAM around the crack.

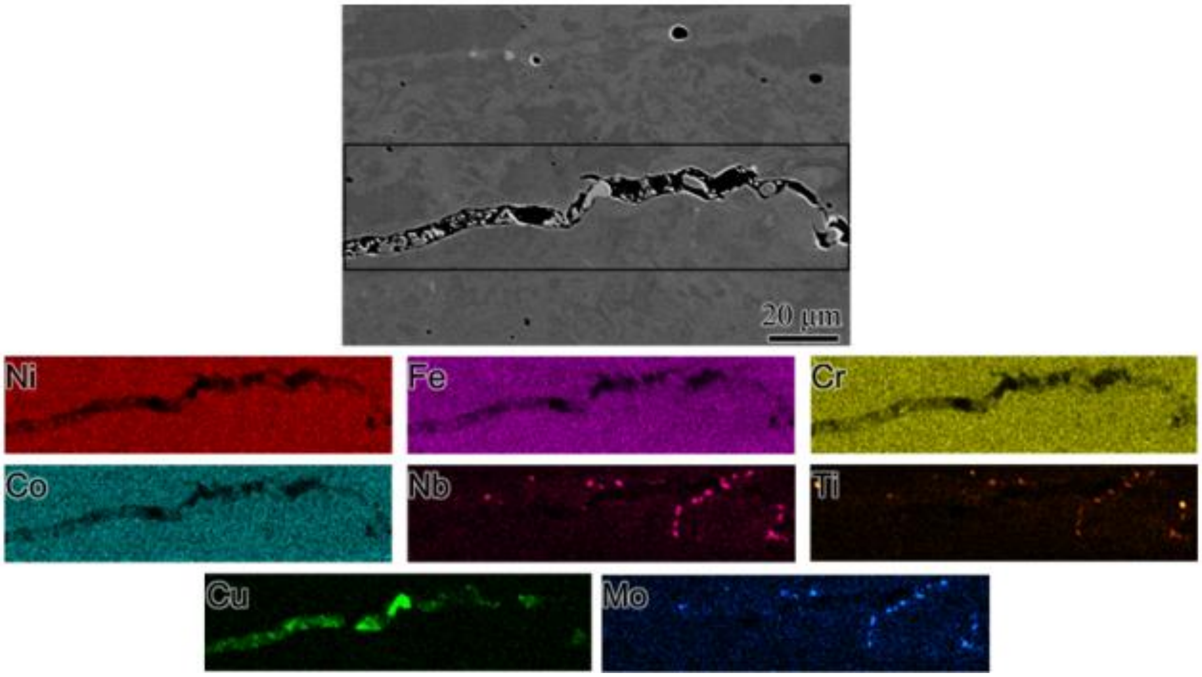

Figure 148. BSE-SEM micrograph along a crack from the Top portion (Location 1 in Figure 132) of the sample and their corresponding composition maps for major (Fe, Ni, Co, Cr) and minor (Nb, Ti, Mo, Cu) alloying elements.

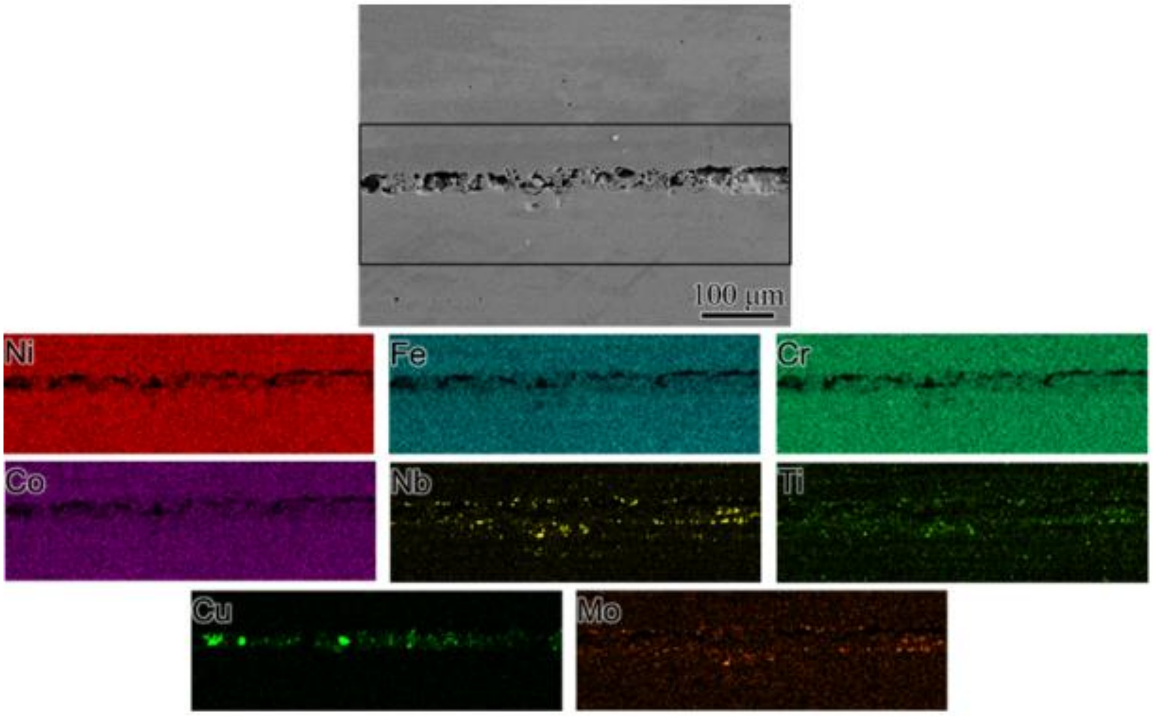

Figure 149. BSE-SEM micrograph along a crack from the Middle portion (Location 1 in Figure 132) of the sample and their corresponding composition maps for major (Fe, Ni, Co, Cr) and minor (Nb, Ti, Mo, Cu) alloying elements.

To estimate the location-specific solidification cracking susceptibility in the 26 wt.% P91 alloy processed using the WAAM technique, the Kou criterion coupled with DICTRA simulations were used. The solidification cracking susceptibility was evaluated using the Kou criterion [19] coupled with one-dimensional DICTRA simulations. The input parameters required for the DICTRA simulations, i.e., the cell size and cooling rate, from each section of the build, were obtained by observing the microstructure under the SEM in SE mode. The samples used for SEM were etched by immersing in a solution consisting of 4.8 grams of $CuCl_2$, 4 mL of water, and 48 mL of HCl for nearly 25 seconds. The secondary dendrite arm spacing (SDAS) was measured from the SEM micrographs using the ImageJ software. The cell size for the DICTRA simulation for the top, middle and bottom regions was considered as half the SDAS size. In order to determine the location-specific cracking susceptibility, the cooling rate in different regions needs to be identified. Therefore, the cooling rate was determined from the SDAS using the following relation determined for Inconel 625 by Tinoco *et al*. [20]:

$$\lambda = 58.02\, R^{-0.312} \qquad (18)$$

where, λ is the SDAS, and R is the cooling rate. The cooling rate from different regions determined using Eqn. (14) was incorporated, and a linear grid with 100 points was used for these simulations. The solid fraction calculated as a function of temperature from the DICTRA simulations was used for determining the solidification cracking susceptibility using the Kou criterion by finding the maximum in the slope of the temperature *vs*. square root of the solid fraction curve [21]. For computing the derivative to determine the slope, a three-point central Lagrange polynomial differentiation similar to the method reported by Sargent *et al*. [22].

The SDAS was determined from the etched microstructure of the sample, as shown in Fig. 150(a). The compositions determined using EDS from different regions are listed in the table embedded in Fig. 150. It can be observed that the concentration of Nb varies significantly in different locations. Nb enrichment can be observed in the interdendritic region (Point 2 in Fig. 150(a)) in comparison with the dendrites (Point 1 in Fig. 150(a)) including the primary and the secondary ones. However, the white precipitates found in the interdendritic region have a higher Nb content along with Ti and Mo. These precipitates correspond to the Laves phase (Point 3 in Fig. 150(a)). Due to the increased enrichment of Nb towards the end of solidification, the Laves phase is expected to form in the interdendritic region. Moreover, Laves phase was found to be one of the solidifying phases towards the end of solidification from the Scheil solidification curve obtained for the nominal composition of 26 wt.% P91. The SDAS calculated using the etched micrographs and the cooling rate calculated using Eqn. (14) are shown in Figs. 150(b) and 150(c), respectively. An inverse correlation was observed between the SDAS and the cooling rate. It is to be noted that though, a constant interpass temperature (175°C) was maintained during the deposition of each layer to control the bulk cooling rate, the local cooling rate was found to vary considerably leading to variation in microstructural features along the build direction. The estimated cooling rate and SDAS were used as inputs for the DICTRA simulation.

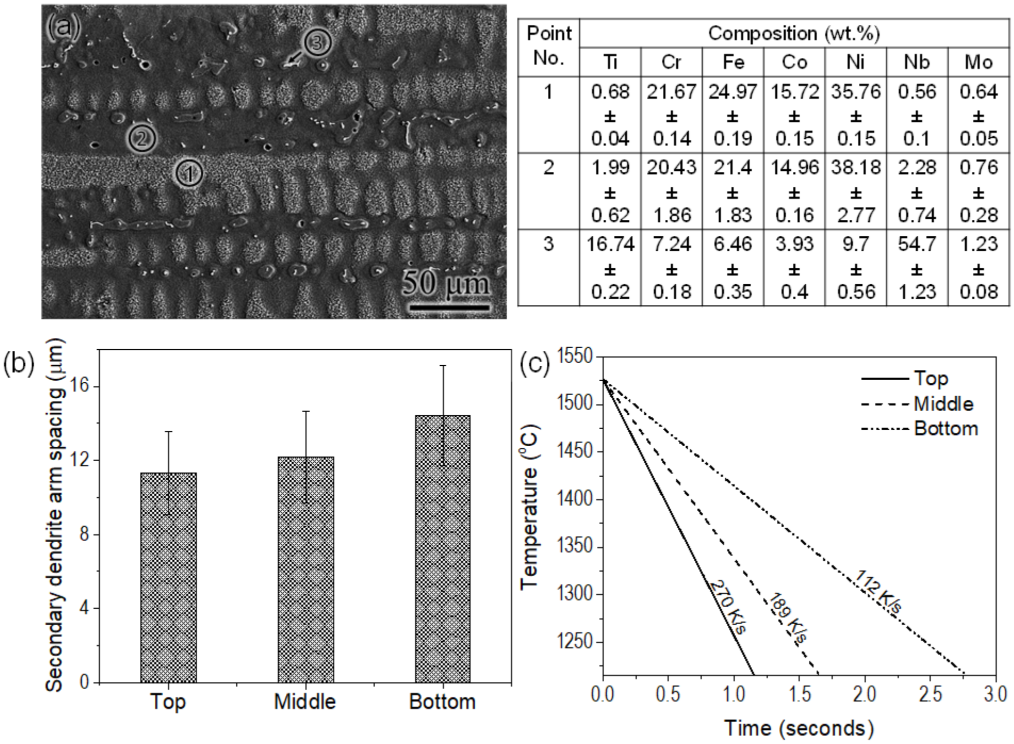

Point No.	Composition (wt.%)						
	Ti	Cr	Fe	Co	Ni	Nb	Mo
1	0.68 ± 0.04	21.67 ± 0.14	24.97 ± 0.19	15.72 ± 0.15	35.76 ± 0.15	0.56 ± 0.1	0.64 ± 0.05
2	1.99 ± 0.62	20.43 ± 1.86	21.4 ± 1.83	14.96 ± 0.16	38.18 ± 2.77	2.28 ± 0.74	0.76 ± 0.28
3	16.74 ± 0.22	7.24 ± 0.18	6.46 ± 0.35	3.93 ± 0.4	9.7 ± 0.56	54.7 ± 1.23	1.23 ± 0.08

Figure 150. (a) SE-SEM micrograph showing the etched microstructure from the top portion of the sample with the secondary dendrites and the composition of points 1, 2 and 3 measured using EDS as well as (b) SDAS calculated from the etched microstructure and (c) cooling rate calculated using the SDAS from different locations of the sample.

The temperature *vs*. solid fraction curves obtained using DICTRA simulation for different locations shown in Fig. 151(a) are compared with the prediction using the Scheil modeling and equilibrium calculations for the alloy containing 26 wt.% P91. The solidus temperature varies significantly as the calculation method varies, mainly because of the difference in cooling rate assumed for different calculations. The cooling rate assumed in equilibrium calculation is the least with complete diffusion in both solid and liquid during solidification, due to which the solidus temperature is the highest amongst the different calculation methods. On the other hand, the Scheil model shows the lowest solidus temperature since it assumes a faster cooling rate with complete diffusion in the liquid and negligible diffusion in the solid. The solidus temperatures calculated using the one-dimensional DICTRA simulations are in between the equilibrium and Scheil calculations since the cooling rate is intermediate. Moreover, it could be seen that the solidus temperature increases from the top to bottom sections since the cooling rate increases. The solidification cracking susceptibility, which is the maximum in the slope of the temperature *vs*. fraction of solid curve ($dT/df_s^{0.5}$) obtained using the DICTRA simulations as per the Kou criterion from various sample locations shown in Fig. 151(b). The cracking susceptibility is the highest in the top portion of the sample with the highest cooling rate. Solidification cracking susceptibility decreases as the cooling rate decreases in the middle and bottom portions. The calculated solidification cracking susceptibility also correlates well with the cracking behavior characterized from different sample portions (Fig. 146).

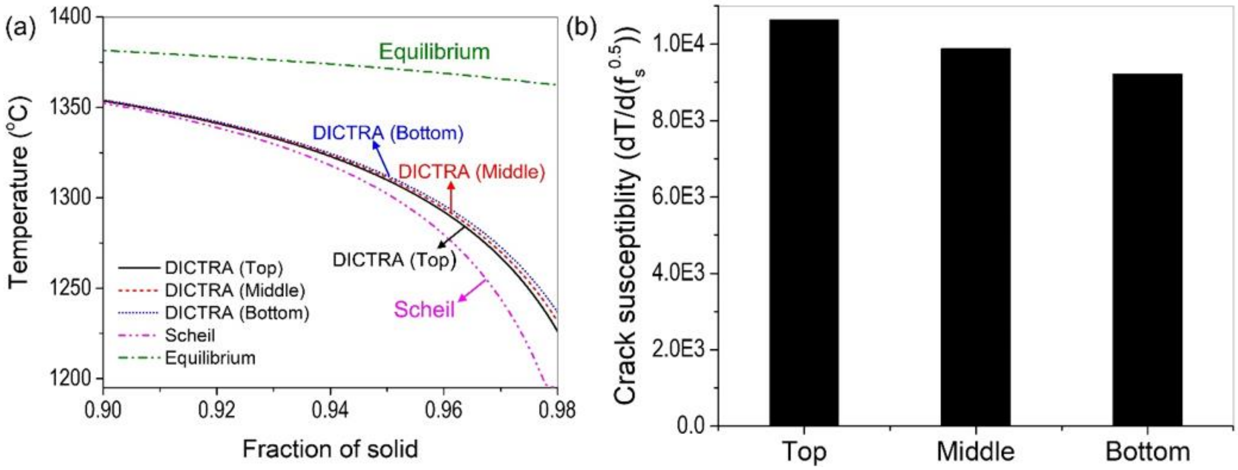

Figure 151. (a) Temperature vs. fraction of solid curves obtained using equilibrium, DICTRA and Scheil calculations at the end of solidification showing the difference in solidus temperatures at ~98% solid fraction and (b) solidification cracking susceptibility calculated from different locations of the sample using the Kou criterion coupled with DICTRA calculations.

It is evident that the solidification cracking susceptibility is highly location-specific for the 26 wt.% P91 sample fabricated using WAAM. It is also clear that the cooling rate plays a major role in inducing the location-specific cracking behavior since the top portion with the highest cooling rate had the longest crack. In addition, a difference in the extent of segregation of minor alloying elements such as Nb and Cu was also observed in different portions of the sample. However, the role of segregation on the solidification behavior needs to be probed further to identify their role in the location-specific cracking behavior. Therefore, the composition from several points within and around the cracks was measured using EDS from different sample locations and used as input for Scheil simulations. The solidification range calculated for each point from different locations is shown in Fig. 152. From these EDS measurements it was observed that there is a varying degree of enrichment of Nb and Cu compared to the nominal composition of these elements for 26 wt.% P91 graded alloy. In comparison with the top and middle part, the bottom region has the lowest enrichment of Nb (nearly 2.5 wt.%) and Cu (~0.4 wt.%), along with a lower solidification range, i.e., temperature difference between liquidus and solidus. However, in the top and middle regions, the enrichment of Cu and Nb rises rapidly. The composition of Cu was found to be up to 87 wt.% in both the regions, while the extent of enrichment of Nb is lesser in the Top region (~27 wt.%) in comparison with the middle region (~56 wt.%), which correlated well with the composition maps for Nb from these regions. Moreover, it can be observed that the enrichment of Nb and Cu are likely to increase the solidification range. The increase in solidification range due to the increase in Nb content is more pronounced than the segregation of Cu. As the Nb content reaches close to 60 wt.%, the solidification range is as high as 1133 K, while as the Cu content becomes higher, the solidification range is up to 681 K. It is to be noted that the effect of other minor alloying elements such as Mo and Ti also play a role, although not as noticeable as Nb. For instance, in the top region, a wide solidification range (848 K) was observed at a point where the Cu content was intermediate (~30 wt.%) in comparison with the maximum enrichment while the Nb and Mo content was almost equal (~2.5 wt.%). It was also observed that Mo affects the solidification range significantly if it is equal to the composition of Nb along with higher Cu content. This proves that the effect of Mo is not as significant as Nb in affecting the solidification range.

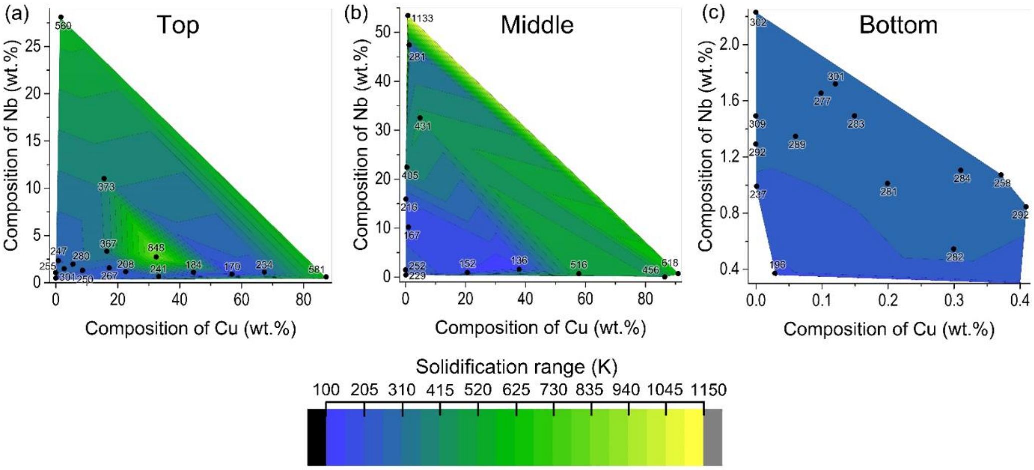

Figure 152. Solidification ranges obtained using Scheil simulations as a function of Nb and Cu content from different points at (a) bottom, (b) middle and (c) top regions of the 26 wt.% P91 build.

3.5.3. Performance evaluation for graded alloys with interlayer

Creep resistance

Based on previous results, a third generation of specimens were chosen to test gradients/joints between the P91 and IN740H. These bulk deposits were selected in order to extract mechanical test specimens. Two interface designs were selected, which are shown schematically in Fig. 153. One design includes a sharp interface between the two materials. The base layers are P91, while the upper layers IN740H. The interface between the two is located at the middle of the deposit (in the z-height direction), to occur in the middle of test specimens later extracted. The second design includes an intermediate zone with gradient composition. This intends to mitigate the sharp transition, by using a blended composition of 10% P91 (by weight) + 90% IN740H for several layers deposited prior to switching to IN740H. The resulting intermediate block build is also shown in the figure below after deposition was completed. Slight differences in appearance are noted in the lower and upper sections, due to the different melt pool behavior of each section/material in the final sample.

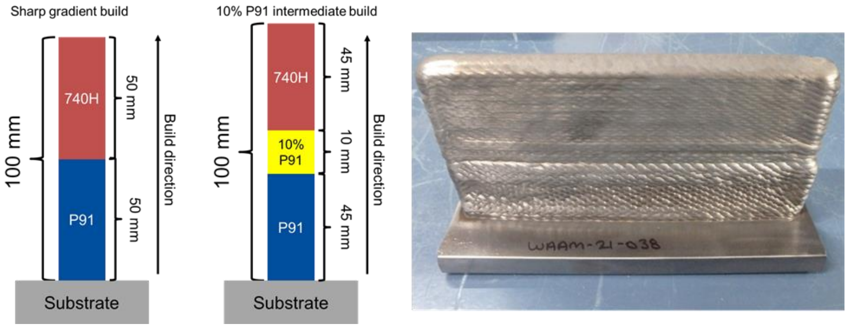

Figure 153. Schematics of the two interface builds, along with the finished build for the 10% P91 intermediate block deposit.

At the interface between P91 and IN740H (and between bottom, middle, and top of the intermediate block build), the bulk sample was allowed to cool to room temperature prior to resuming deposition. This was prescribed to reduce dilution between the dissimilar materials. Deposition parameters for each material match those from prior deposits, to maintain consistency across samples. Conditions for both blocks are shown below. Both builds utilized a square raster pattern, with pattern width 12mm and line spacing (step-over) of 3mm. Travel speed was 5 mm/s in bulk layers, while base layers near substrate are slightly slower for improved fusion to the substrate.

Sharp gradient build

Layers have 60 seconds wait before resuming subsequent layer, unless noted

Layers 1 through 26: P91 only
(P91 wire feed = 3.1 m/min)

- Layer 1: 225A, 3.5 mm/s travel speed
- Layer 2: 215A, 4 mm/s travel speed
- Layer 3: 205A, 5 mm/s travel speed
- Layer 4: 195A
- Layer 5: 175A
- Layer 6 through 26: 166A
    - Stop and wait until part is at 75°F

Layers 27 through 55: Inconel 740H only
(IN740H wire feed = 2.44 m/min)

- Layer 27: 205A, 5mm/s travel speed
- Layer 28: 195A
- Layer 29: 175A

Layers 30 through 55: 166A

10% P91 intermediate build

Layers have 60 seconds wait before resuming subsequent layer, unless noted

Layers 1 through 23: P91 only
(P91 wire feed = 3.1 m/min)

- Layer 1: 225A, 3.5 mm/s travel speed
- Layer 2: 215A, 4 mm/s travel speed
- Layer 3: 205A, 5 mm/s travel speed
- Layer 4: 195A
- Layer 5: 175A
- Layer 6 through 23: 166A
    - Stop and wait until part is at 75°F

Layers 24 through 28: 10% P91
(P91 at 0.31 m/min + IN740H 2.19 m/min)

- Layer 24: 205A, 5mm/s travel speed
- Layer 25: 195A
- Layer 26: 175A
- Layers 27 & 28: 166A
    - Stop and wait until part is at 75°F

Layers 29 through 55: Inconel 740H only
(IN740H wire feed = 2.44 m/min)

- Layer 29: 205A, 5mm/s travel speed
- Layer 30: 195A
- Layer 31: 175A

Layers 32 through 55: 166A

Both samples were sent for machining and subsequent heat treatment. Cylinders were extracted via EDM, oriented in the z-direction (build height) as shown in Fig. 154. These cylinders were roughly 15 mm diameter. Cylinders were subsequently subjected to their optimized post-heat treatment in Pitt. Upon returning from heat treatment, it was noted that several specimens exhibited longitudinal cracks. One such cracked specimen is shown in the below figure. Cracked specimens were not utilized for subsequent machining and testing. A selection of the remaining specimens is also shown below. The interface between P91 and IN740H is evident, due to the different coloration occurring during heat treatment. Each material shows slightly different oxidation behavior. This oxide layer was removed during the following machining steps. The heat treated gradient builds (both sharp and 10% P91) were machined after heat treatment, into creep / stress rupture specimens. The specimen geometry is shown in Fig. 153. In addition to the sharp and 10% P91 gradient specimens, several specimens from single material P91 and IN740H WAAM deposits were also heat treated and machined for testing, to provide a single material baseline.

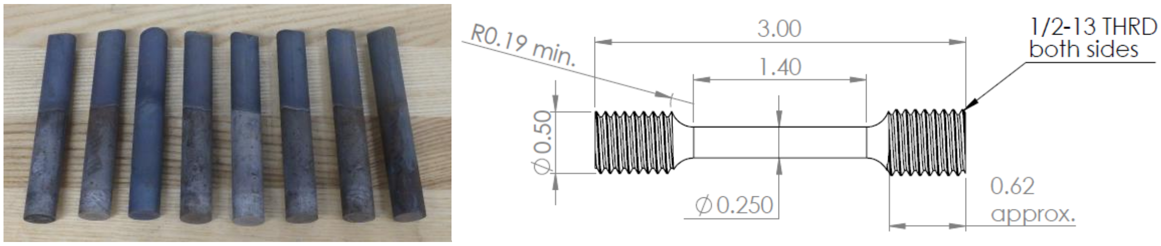

Figure 154. (Left) Gradient specimens after heat treatment to study the creep behavior, (Right) Specimen geometry for stress rupture testing.

Preliminary stress rupture testing was conducted for these materials at a range of test conditions, based on material. As P91 shows lower strength at temperature compared to IN740H, different conditions were required for the two materials. For the gradient compositions, it was anticipated failure would occur in the P91 side of the deposit, or within the dilution / gradient zone at the center of the specimen. This serves to demonstrate the ability for WAAM to generate joints between these dissimilar materials. The time taken for failure is noted after the stress rupture test. In addition, the literature reported creep test results for P91, 740H and P92/740H joints fabricated using other techniques are collected to compare with the WAAM manufactured samples. To compare the stress rupture data of samples tested in different temperatures, the Larson-Miller parameter that based on the Arrhenius rate equation has been calculated and summarized in the plots to show the creep resistance of WAAM manufactured alloys.

Figure 155 shows the comparison of the rupture life by calculating the Larson Miller parameter with the equation $T(\ln(t_r) + 25)$, where the T is the temperature in unit Kelvin, and t_r is the rupture life in hours. At the same applied stress, a higher Larson-Miller parameter indicates a higher rupture life for a given temperature. Clearly, the dissimilar material P91 steel and Inconel 740H manufactured by WAAM shows comparable creep rupture properties to the P91 [23, 24], P92 [24], and P92/740H [25] weldment reported in the literature, indicating that the creep deformation and fracture of the dissimilar gradient build mainly depends on the P91 side rather than the Inconel 740H side. Moreover, the performance of sharpy gradient is slightly better than using 10 wt.% P91 at an interlayer. This is probably because of the 10 wt.% P91 has less reduced fraction of γ' to pin the grain boundary as indicated in the CALPHAD model prediction shown as Fig. 92(b), which worsen the creep resistance.

The P92 alloy is modified based on P91 alloy by adding W to strengthen the material, which enables an 10-20% higher creep strength in 100,000 h at 600°C compared with P91. In the Fig. 155, we also observed that the P92 shows better performance than literature reported P91. However, the WAAM manufactured P91 steel shows significant higher Larson-Miller parameter to the P91 and P92 at the same applied stress, indicating that WAAM method leads to better high-temperature mechanical property and creep resistance than conventional welding. Thus, WAAM may serves as a promising method for manufacturing power plant components in the future for more rupture life and thinner component.

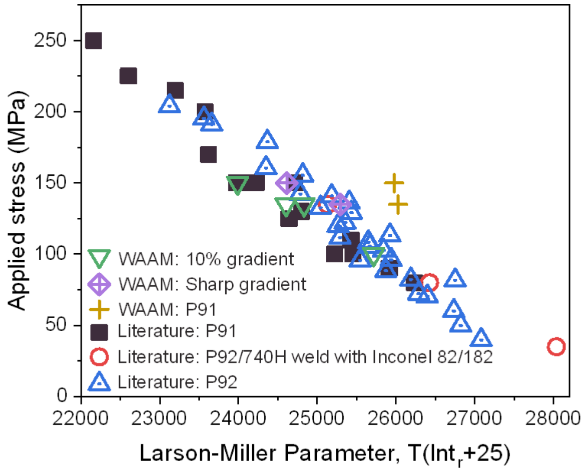

Figure 155. Comparison of creep rupture property between the WAAM manufactured samples in this project and literature reported P91, P92 and P92/740H weldment using Larson-Miller parameter.

Oxidation resistance

In order to evaluate the performance in an oxidizing atmosphere, the oxidation resistance for WAAM manufactured P91 steels, cast and 740H superalloy as well as 10 wt.% P91 graded alloy sandwiched between P91 steel and 740H superalloy were evaluated in air atmosphere at 800°C for 100 hours. Due to the low standard free energy of formation (Fig. 156) and low diffusion coefficient of iron ions in Cr_2O_3, Al_2O_3, SiO_2, these solutes (Cr, Al, Si) are added to form stable, slowly growing external oxide to prevent oxidation in Fe-based alloys at high temperature [26]. This process is known as selective oxidation. The conventional critical Cr concentration is 12 wt.%, above which the condense protective chromia will form on the steel surface when exposed to dry air [27]. However, it was found that the 12 wt.% Cr steel does not have qualified creep resistance under high temperature and therefore the 9 wt.% Cr steels such like P91 become popular because of higher creep strength and lower alloy cost. The oxidation behavior of cast P91 and other Fe-9Cr-X alloy exposed to different environments were investigated by several researchers previously [27-30]. However, few studies are available that evaluated the effect of manufacturing method on the oxidation behavior of P91. In our study, the oxidation behavior of Cast P91 and WAAM alloys in air are compared.

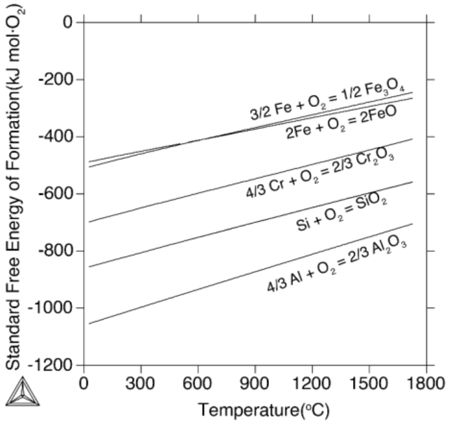

Figure 156. Standard free energy of formation of Fe, Cr, Al, Si oxides versus temperature.

The alloys were ground to 1200 grid surface finish, cleaned with ethanol and dried by pressured air prior for oxidation experiment. The samples were oxidized at 800ºC in air for 100 hours. The heat treatment was carried out in a horizontal furnace equipped with quartz tube. The oxidized samples were analyzed by scanning electron microscope (SEM) and Energy-dispersive X-ray spectroscopy (EDS) to characterize the nature of oxide formed on the surface as well as the cross-section. In Fig. 157, the images and SEM micrographs of WAAM P91 after oxidation are presented. Two different oxidation products (black and grey oxide) are observed on surface with varying morphologies. EDS results confirms that the white oxidation product is the Fe3O4 phase which has a spinel structure, and the black oxidation product is (Fe, Cr)-rich oxide which could also possess a spinel structure. It is obvious that WAAM P91 has less fraction of grey oxide on the surface, which means better oxidation behavior because the grey oxide layer consumes the Fe, which is the major alloying element. While Cr is added specifically for improving the oxidation resistance to form passive oxide layer, Cr is expected to be consumed the most to improve the oxidation resistance. Moreover, a V-Mn rich product is observed on the surface of WAAM P91 (Fig. 158). It was not understood how this product formed and no paper reported this phenomenon before. Cross-sections of oxidized WAAM P91 are shown in Fig. 159. Iron oxide nodules were observed between discontinuous thin Cr-Mn rich oxide layer. The chemical composition of spinel (M_3O_4) and corundum (M_2O_3) under different oxygen activity calculated using Thermo-Calc are shown in Fig. 160. It was found that Mn is stable in the spinel phase (M_3O_4) but not in corundum (M_2O_3), which means the Cr, Mn-rich oxide layer observed in P91 is most likely spinel phase ($(Fe, Cr, Mn)_3O_4$).

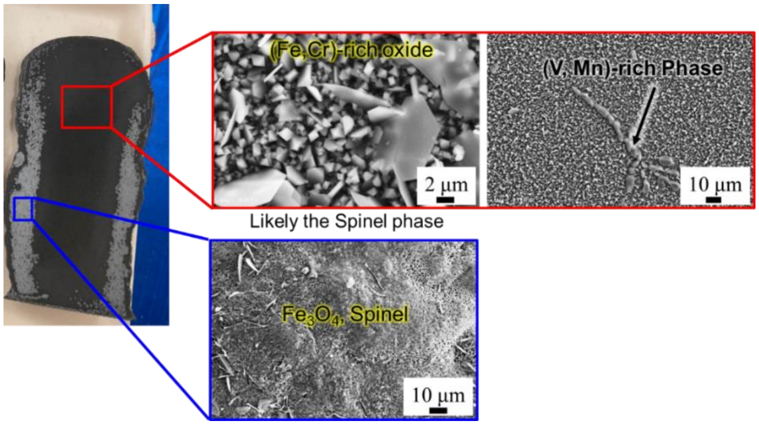

Figure 157. Image of the oxidized surface and SEM micrographs of oxidized WAAM P91 steels showing the presence of 2 different oxides after oxidation at 800ºC in air for 100 hours.

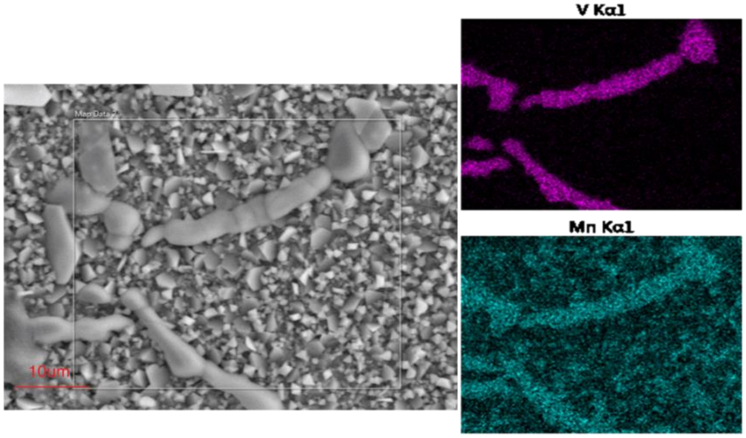

Figure 158. Vanadium and Manganese-rich product on the surface of oxidized WAAM P91 identified using EDS.

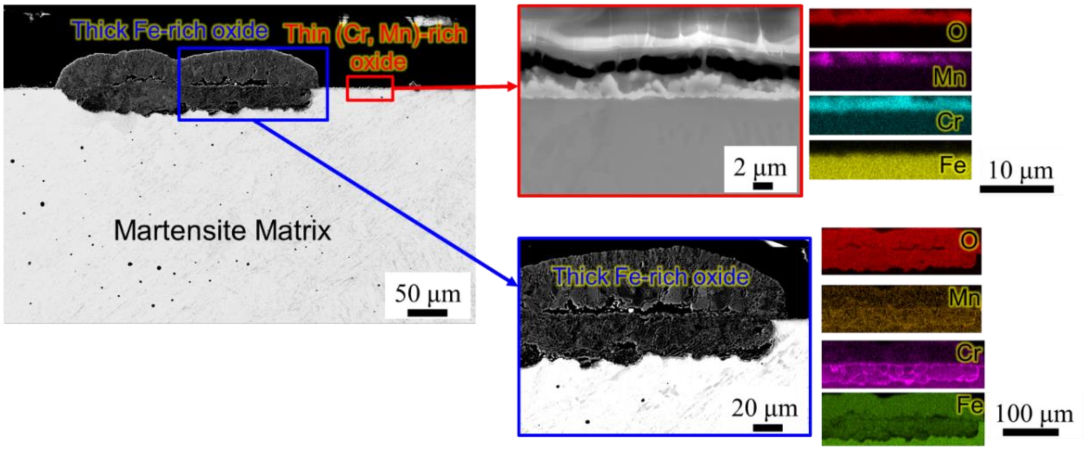

Figure 159. BSE-SEM micrograph and composition maps obtained using EDS in the cross-sections of WAAM P91 steel oxidized at 800°C for 100 hours.

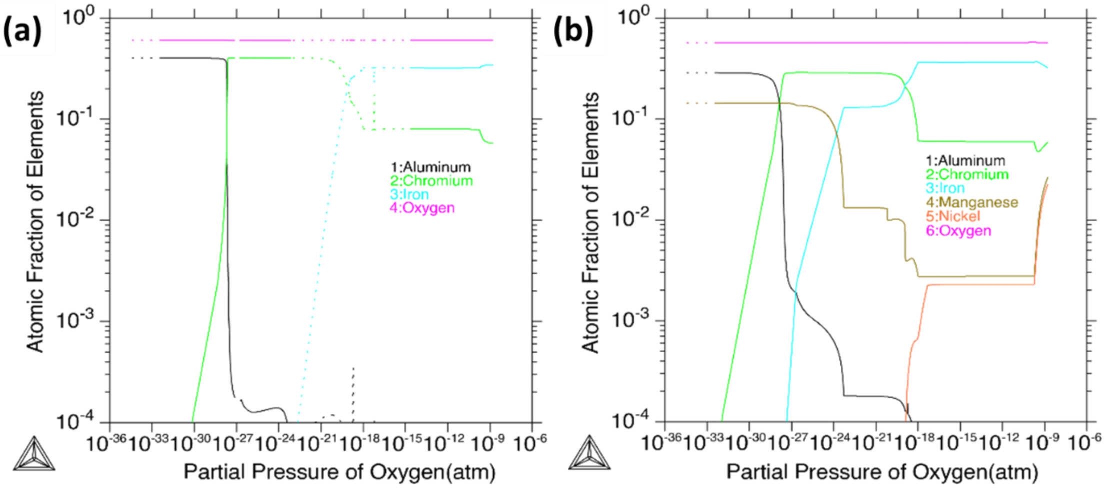

Figure 160. The chemical composition of (a) corundum (M_2O_3) and (b) spinel (M_3O_4) versus oxygen activity at 800°C calculated using Thermo-Calc.

Similar experiments were performed for WAAM 740H superalloy. After oxidation, it was found that 100 hours were not sufficient to form a thick oxide layer in the 740H superalloy to perform in-depth studies due to the superior oxidation resistance of 740H superalloy. Due to experimental limitations, the maximum time up to which the oxidation experiments can be performed is 100 hours. However, from the SEM micrographs from the surface of oxidized WAAM 740H superalloy, it was evident that the γ matrix was completely covered with Cr_2O_3, while there small nodules of TiO_2 along the build direction as shown in Fig. 161. The Laves phase that precipitates in the interdendritic region typically oxidizes to form TiO_2 which is present as a series of nodules along the build direction.

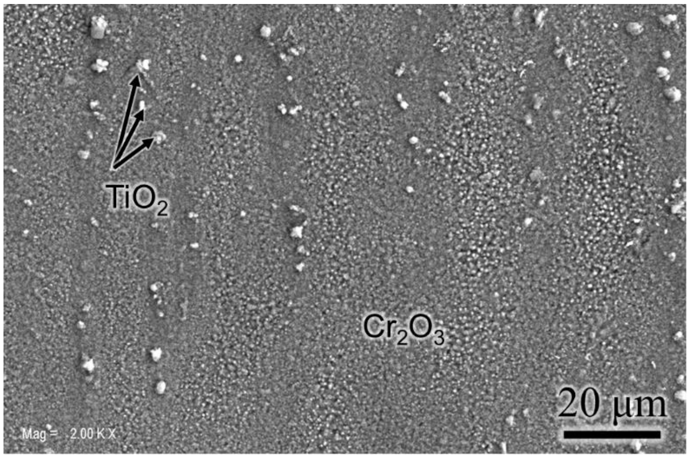

Figure 161. BSE-SEM micrograph of the oxidation surface of WAAM 740H superalloy showing a uniform layer of Cr_2O_3 *with nodules of* TiO_2 *after oxidation at 800°C for 100 hours.*

Interestingly, the 10 wt.% P91 sample showed varying oxidation behavior in different parts of the sample as summarized below. With SEM and EDS, we identified that the interface between P91 and graded alloy suffers from severe oxidation in comparison with the monolithic P91 and graded alloy blocks, as demonstrated in Figs. 162 and 163. Figure 162(a) presents a secondary electron SEM image of the interface. As can be seen, a significantly thicker layer of oxide is generated along the interface, compared with the light oxidation on the monolithic blocks, demonstrating a preferred oxidation along the interface. The corresponding EDS maps (Fig. 162(b)) indicates that the interfacial oxides are enriched with Fe and Co, while Cr and Ni are barely present. For a better understanding of the oxidation along the interface, cross-section SEM and EDS analysis was performed to reveal the penetration of oxides along the boundary into the subsurface, as shown in Figs. 162(c-d). As it can be seen, the interfacial oxidation rigorously develops into the subsurface region as deep as 105µm, while the oxidation on the uniform P91 and 10 wt.%P91 surfaces away from the interface penetrates only about 2-10 µm into the surface.

Figure 163 presents SEM and EDS analysis of the cross-sectional morphologies and chemical features of oxides from the uniform regions of 10wt.%P91 and P91. Different from the accelerated oxidation kinetics along the interface, the monolithic block exhibit thin, uniform oxide layers. The uniformity of the oxide layers indicates that the oxidation proceeds via the near equilibrium interdiffusion between the oxygen from the environment and the alloy substrate. Figures 163(a-b) present an SE-SEM view and the associated EDS mapping of the 10 wt.% P91 part after oxidation, showing the formation of an oxide layer of ~10 µm. The range of the oxide layer is clearly indicated by the oxygen EDS map in Fig. 163(b). In the oxide layer, Co is enriched on the outmost surface with iron underneath, indicating that higher kinetics of outward migration and oxidation of cobalt. An internal oxide layer enriched with Cr was detected beneath the Fe-rich layer, confirming the inward diffusion of oxygen toward the bulk of the material. The clear depletion zone of Cr could be observed beneath the internal oxides. The oxidation shown in Figs. 163(a-b) is comparable to the breakaway oxidation of steels, which occurs due to the failed formation of a protective Cr_2O_3 layer on the outermost surface. Without the formation of a dense, continuous Cr_2O_3 layer, Fe from the material reacts with oxygen from the environment, leading to the formation of Fe-rich oxides. Afterwards, Fe-rich oxide further reacted with incontiguous Cr_2O_3 oxide and formed (Fe, Cr)-rich spinel phase, which is not protective and therefore cannot prohibit the formation of (Fe, Co)-rich oxides at outer layer that has resulted from outer diffusion of Fe and Co. Contrary to the failed formation of a protective Cr-rich layer in the 10 wt.% P91 part, a dense, continuous Cr-rich oxide layer was formed in the P91 part, as shown in Figs. 163(c-d). The successful formation of the Cr-rich oxide layer can be attributed to significantly higher chemical diffusivity of Cr in Fe-based alloys than that in Ni-based alloys. Due to the lack of experimental data for 10 wt.% P91, thermodynamic calculations were employed to calculate the chemical diffusivity of this material. The chemical diffusivity of Cr in 10 wt.% P91 is 5.88E-18m^2/s and is 5.21E-16m^2/s in P91 steel. In both P91 and 10 wt.% P91 alloys, Cr-rich oxides form firstly during oxidation due to low Gibbs free energy, depleting Cr near the surface, resulting in a composition gradient. This depletion could be supplemented promptly in P91, not in 10 wt.% P91, due to distinct chemical diffusivity of Cr in these materials, and therefore forms visible Cr depletion zone in the graded alloy under EDS (Fig. 163(b)).

We performed XRD analysis on the welded parts, using a point source with diameter of 2mm to collect signals in the interface between P91 steel and 10 wt.% P91 graded alloy along with the constituent materials included, as shown in Fig. 164. The FCC matrix phase of the 10 wt.% P91 part and the BCC matrix phase of the P91 part are readily visible in the XRD pattern, indicating that the XRD scan collects signals from both the P91 and 10 wt.% P91 blocks. Diffraction peaks of Cr_2O_3 were detected, suggesting that Cr-rich oxides observed on the surface of P91 steel is Cr_2O_3. The spinel phase was also detected by XRD. Except Cr-rich oxides, we also observed (Fe, Cr)-rich, (Fe, Co)-rich, and (Cr, Mn)-rich oxides by EDS (Figs. 162 and 163). Since the atomic radius of Cr, Mn, Fe and Co are similar, the spinel phases containing these elements have similar lattice parameters, leading to overlapping diffraction peaks in the XRD pattern.

Besides the selective oxidation at the interface, we found that the grain boundary also promotes the inward diffusion of oxygen and the associated oxidation, as demonstrated by the SEM and EDS analysis of 10 wt.% P91 surface as shown in Fig. 165. A similar oxidation behavior along the interface and the grain boundary confirms that the defect-accelerated inward diffusion of oxygen plays the critical role in determining the development of oxides into the subsurface region. As shown in the EDS maps in Fig. 165(b), concentrated distributions of Al and O are observed along the grain boundaries, indicating the preferred formation of Al_2O_3 along the grain boundaries. By contrast, the Cr- and Mn-rich oxides form a uniform shell on the material surface, comparable to the near-equilibrium oxidation shown in Fig. 163. The different oxidation kinetics of the metallic elements can be attributed to their different diffusion kinetics. Mn diffuse fast from the alloy into the surface to react with the oxygen in the environment in comparison with Al and Cr. By contrast, Al diffuses slow, preventing it to reach the surface. Instead, the oxygen from the environment diffuses along the grain boundary into the subsurface region to combine with Al, leading to the formation of Al_2O_3 along grain boundaries. EDS results (Fig. 165(b)) show that internal oxidation zone is consistent with Al-rich oxides. Even though, continuous (Mn, Cr)-rich spinel phase were formed on the surface initially, the internal diffusion of oxygen was not prohibited. It may be due to the defects present in the AM alloys resulting from cyclic heating and cooling process, which provides a fast pathway to this process. Low chemical diffusivity makes it difficult to supplement Cr near the surface after oxidation, and therefore the reactions between Al, of which the oxide has second lowest Gibbs energy, and internal diffused oxygen happened, forming Al-rich oxide along grain boundaries.

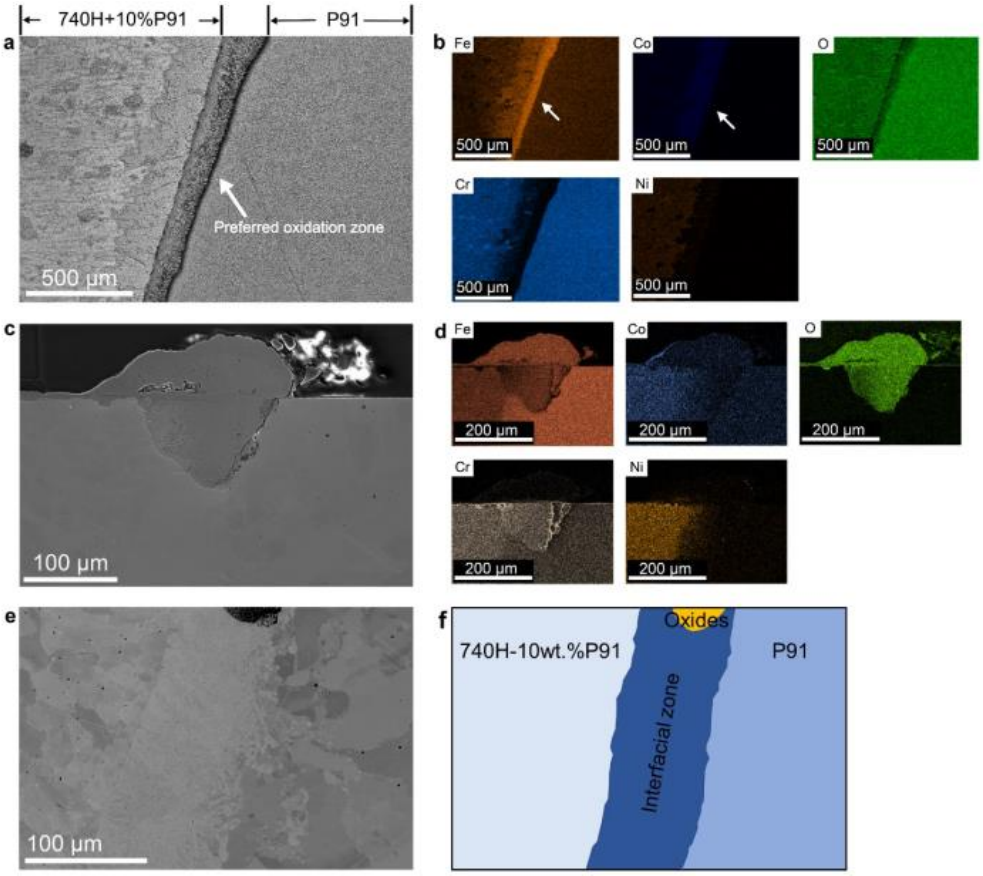

Figure 162. (a, b) SEM-SE image and EDS mapping of the interfacial region, showing a preferred generation of Fe- and Co- rich oxides. (c, d) Cross-section SE-SEM image and corresponding composition maps of the oxide strip shown in (a, b), indicating that the interface promotes the inward diffusion of oxygen and thus the associated metal oxidation, (e, f) BSE-SEM image of the interface and the associated schematic.

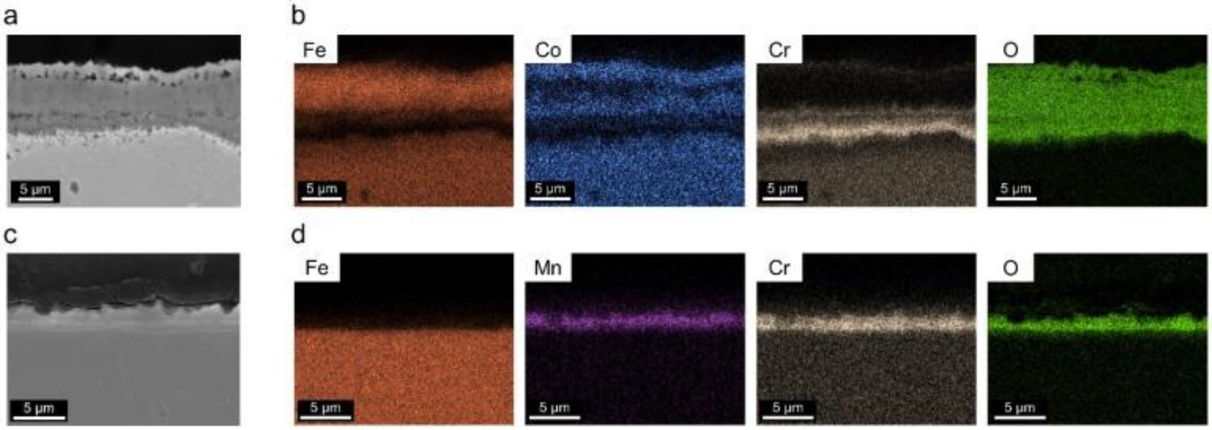

Figure 163. (a) SE-SEM image and (b) composition maps for 10 wt.%P91 graded alloy away from the interface, (c) SE-SEM image and (d) composition maps for P91 steel part away from the interface.

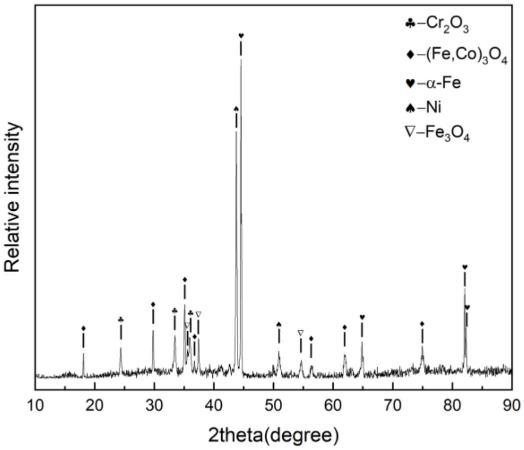

Figure 164. X-ray diffractogram obtained using a point source in the region close to the interface between the 10 wt.% graded alloy and P91 steel.

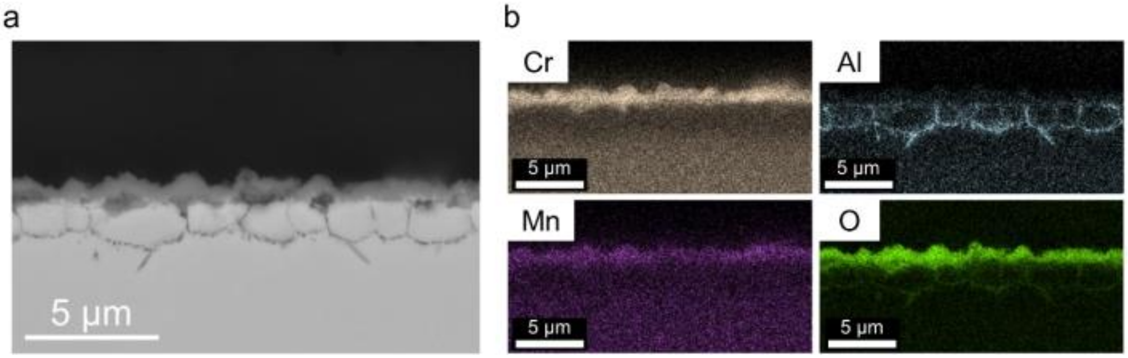

Figure 165. SEM image and the associated composition maps for the 10 wt.% P91 graded alloy away from the interface showing preferential oxidation of Al in the grain boundaries.

Feasibility evaluation

Overall, this effort demonstrated feasibility for additively manufactured materials suited for power generation applications. Several multi-material and gradient combinations were explored, including joints between P91 steel and Inconel 740H superalloy. This provides a method for integrating both materials in future designs, to improve both performance and cost. Furthermore, the results serve to calibrate and validate the ICME tools developed by the modeling team.

WAAM method was demonstrated using a dual wire feed configuration, enabling gradients and seamless transitions between both materials. The deposition parameters developed can be easily transitioned to fabrication of larger parts/geometries. For example, two variable diameter pipe/tube sections are shown in Fig. 166, printed with a high-strength low alloy steel. In the future, designs such as this could be printed via WAAM, and include multiple materials based on local demands for strength, oxidation performance, and cost.

Figure 166. Variable diameter tube/pipe sections, deposited via WAAM using a high-strength low alloy steel. Shows feasibility of 3D printed components for power applications.

3.6 Milestones achieved for each task

The milestones achieved for each task according to the SOPO are listed in Table 13. (see the last page of the report).

3.7 Training and professional development provided

Under the supervision of PI Xiong, microstructure characterization training was conducted to three postdoctoral associates. One Ph.D. student was trained to perform calculations for gradient alloys, such as the creep model, microstructure prediction, Scheil calculation, and so forth.

One Ph.D. student was instructed by co-PI Dr. Albert To on WAAM simulation by using ANSYS APDL. Technical training was provided to a postdoc on crystal plasticity modeling for the prediction of mechanical properties by Dr. To.

3.8 Dissemination

3.3.1. Journal publications

1. Sridar, S., Sargent, N., Wang, X., Klecka, M.A., Xiong, W., *Determination of Location-Specific Solidification Cracking Susceptibility for a Mixed Dissimilar Alloy Processed by Wire-Arc Additive Manufacturing*. Metals, accepted for publication (2022) (preprint doi: 10.20944/preprints202201.0370.v1).
2. Sridar, S., Klecka, M. A., Xiong, W., *Interfacial characteristics of P91 steel-Inconel 740H bimetallic structure fabricated using wire-arc additive manufacturing*. Journal of Materials Processing Technology, 300 (2022), 117396 (doi: 10.1016/j.jmatprotec.2021.117396).
3. Li, K., Klecka, M. A., Chen, S., Xiong, W., *Wire-arc additive manufacturing and post-heat treatment optimization on microstructure and mechanical properties of Grade 91 steel*. Additive Manufacturing, 37 (2021), 101734 (doi: 10.1016/j.addma.2020.101734).
4. Paul, S., Liu, J., Strayer, S. T., Zhao, Y., Sridar, S., Klecka, M. A., Xiong, W., & To, A. C., *A Discrete Dendrite Dynamics Model for Epitaxial Columnar Grain Growth in Metal Additive Manufacturing with Application to Inconel*. Additive Manufacturing, 36 (2020), 101611 (doi: 10.1016/j.addma.2020.101611).
5. Jimenez, X., Dong, X., Paul, S., Klecka, M. A., To, A. C., *Residual Stress Modeling with Phase Transformation for Wire Arc Additive Manufacturing of B91 Steel*. JOM, 72 (2020), 4178–4186 (doi: 10.1007/s11837-020-04424-w).

3.3.2. Conference presentations

1. [Invited Talk] Wei Xiong, “Wire-Arc Additive Manufacturing of Alloy Components from Traditional Alloys to Functionally Graded Materials”, International Conference on Additive Manufacturing, JW Marriott - Anaheim, CA, USA, Nov 1-5, 2021
2. [Invited Talk] Wei Xiong, “ICME Gap Analysis for Materials Design and Process Optimization in Additive Manufacturing”, Symposium: Additive Manufacturing of Metals: ICME Gaps: Material Property and Validation Data to Support Certification, MS&T 2021, Columbus, Ohio, USA, Oct 17-21, 2021
3. [Invited Talk] Soumya Sridar, Xin Wang, Michael Klecka, Wei Xiong, “*Wire-arc additive manufacturing of functionally graded alloy from Inconel 740H superalloy to P91 steel guided by the CALPHAD-based ICME approach*”, IMAT 2021, St. Louis, MO, USA, September 13–16, 2021
4. Xin Wang, Soumya Sridar, Michael Klecka, Wei Xiong, “*Design of Wire-arc Additive Manufacturing of Functionally Graded Alloy from P91 Steel to Inconel 740H Superalloy Using High-throughput Method*”, Materials Science & Technology 2021, Columbus, OH, USA, October 17–21, 2021
5. Soumya Sridar, Xin Wang, Michael Klecka, Wei Xiong, “*Wire-Arc Additive Manufacturing of Inconel 740H – P91 steel bimetallic structure: Microstructure Characterization and Post-Heat Treatment Design*”, Materials Science & Technology 2020, Pittsburgh, PA, USA, November 2–6, 2020 (Virtual)
6. S. Paul, J. Liu, Y. Zhao, S. Sridar, M. A. Klecka, W. Xiong, and A. C. To, “*A discrete dendrite dynamics model for fast epitaxial columnar grain growth in metal additive manufacturing*,” MS&T20 Virtual, November 2-6, 2020.
7. S. Paul, Q. Chen, X. Wang, W. Xiong, and A. C. To, “*Part-scale coupled process-microstructure model for additive manufacturing of nickel alloy*,” 2019 Annual International Solid Freeform Fabrication Symposium, Austin, TX, August 12-14, 2019.

8. A. C. To, S. Paul, Q. Chen, J. Liu, Y. Zhao, and W. Xiong, "*Part-scale process-microstructure simulation during laser power bed additive manufacturing*," 15th US National Congress of Computational Mechanics, Austin, TX, July 28 – August 1, 2019.

REFERENCES

[1] http://www.specialmetals.com/assets/smc/documents/alloys/inconel/inconel-alloy-740-h.pdf

[2] Coleman, K. and Newell, W.F. Jr., "P91 and Beyond," Welding Journal, August 2007.

[3] C. Pandey, M.M. Mahapatra, P. Kumar, J.G. Thakare, Characterization of weld fusion zone for TIG welded P91and P92 steels, *Arch. Metall. Mater.* **63** (2018).

[4] C. Cayron, ARPGE: a computer program to automatically reconstruct the parent grains from electron backscatter diffraction data, *J. Appl. Crystallogr.* **40** (2007) 1183–1188.

[5] C. Cayron, B. Artaud, L. Briottet, Reconstruction of parent grains from EBSD data, *Mater. Charact.* **57** (2006) 386–401.

[6] X. You, Y. Tan, J. Li, P. Li, C. Dong, S. Shi, J. Liao, S. Qin, Effects of solution heat treatment on the microstructure and hardness of Inconel 740 superalloy prepared by electron beam smelting, *J. Alloys Compd.* **638** (2015) 239–248.

[7] A. Zieliński, M. Sroka, T. Dudziak, Microstructure and Mechanical Properties of Inconel 740H after Long-Term Service, *Materials (Basel).* **11** (2018) 2130.

[8] W. Zhang, J. Lu, J. Wang, L. Sang, J. Ma, Y. Zhang, Z. Zhang, In-situ EBSD study of deformation behavior of Inconel 740H alloy at high-temperature tensile loading, *J. Alloys Compd.* **820** (2020) 153424.

[9] J. Liu, W. Xiong, A. Behera, S. Thompson, A.C. To, Mean-field polycrystal plasticity modeling with grain size and shape effects for laser additive manufactured FCC metals, *Int. J. Solids Struct.* **112** (2017) 35–42.

[10] R.C. Reed, T. Tao, N. Warnken, Alloys-by-design: application to nickel-based single crystal superalloys, *Acta Mater.* **57** (2009) 5898–5913.

[11] M.S.A. Karunaratne, R.C. Reed, Interdiffusion of the platinum-group metals in nickel at elevated temperatures, *Acta Mater.* **51** (2003) 2905–2919.

[12] A. Janotti, M. Krčmar, C.L. Fu, R.C. Reed, Solute diffusion in metals: larger atoms can move faster, *Phys. Rev. Lett.* **92** (2004) 85901.

[13] S. Paddea, J.A. Francis, A.M. Paradowska, P.J. Bouchard, I.A. Shibli, Residual stress distributions in a P91 steel-pipe girth weld before and after post weld heat treatment, *Mater. Sci. Eng. A.* **534** (2012) 663–672.

[14] J. A. Dantzig & M. Rappaz, *Solidification: -Revised & Expanded*. (EPFL press, 2016).

[15] D. Bourell *et al.*, Materials for additive manufacturing. *CIRP Ann.* **66**, 659–681 (2017)

[16] F. H. Kim, S. P. Moylan, E. J. Garboczi, J. A. Slotwinski, Investigation of pore structure in cobalt chrome additively manufactured parts using X-ray computed tomography and three-dimensional image analysis. *Addit. Manuf.* **17** (2017) 23–38.

[17] D. K. Leigh, D. L. Bourell, J. J. Beaman Jr, Effect of in-plane voiding on the fracture behavior of laser sintered polyamide. in *International Symposium on Flexible Automation* vol. 45110 411–417 (American Society of Mechanical Engineers, 2012).

[18] X. Xie, *et al.* Mechanistic data-driven prediction of as-built mechanical properties in metal additive manufacturing. *npj Comput. Mater.* **7** (2021) 1–12.

[19] S. A. Kou, criterion for cracking during solidification. *Acta Mater.* 88 (2015) 366–374.

[20] J. Tinoco; H. Fredriksson, Solidification of a Modified Inconel 625 Alloy under Different Cooling Rates. *High Temp. Mater. Process.* 23 (2004) 13–24.

[21] S. A. Kou, Simple Index for Predicting the Susceptibility to Solidification Cracking. *Weld. J.* **94** (2015) 374–388.

[22] N. Sargent, M. Jones, R. Otis, A. A. Shapiro, J.-P. Delplanque, W. Xiong, Integration of Processing and Microstructure Models for Non-Equilibrium Solidification in Additive Manufacturing. *Metals*, **11** (2021) 570.

[23] A. Miyakita, K. Yamashita, G. Taniguchi, T. Suga, Creep-rupture life prediction for 9Cr-1Mo-Nb-V weld metal. *ISIJ Int.* **55** (2015) 2189–2197.

[24] F. Ren, X. Tang, H. Lu, Life assessment of Grade 91 steel using Larson-Miller parameter. in *AIP Conference Proceedings* vol. 1971 20019 (AIP Publishing LLC, 2018).

[25] K.-Y. Shin *et al.* Transition of creep damage region in dissimilar welds between Inconel 740H Ni-based superalloy and P92 ferritic/martensitic steel. *Mater. Charact.* **139** (2018) 144–152.

[26] Neil Birks, Gerald H. Meier, Frederick S. Pettit, *Introduction to the high temperature oxidation of metals*, (Cambridge University Press, 2006).

[27] G. H. Meier et al., Effect of Alloy Composition and Exposure Conditions on the Selective Oxidation Behavior of Ferritic Fe–Cr and Fe–Cr–X Alloys, *Oxid Met* **74** (2010) 319–340.

[28] N. Mu, K. Y. Jung, N. M. Yanar, G. H. Meier, F. S. Pettit, and G. R. Holcomb, Water Vapor Effects on the Oxidation Behavior of Fe–Cr and Ni–Cr Alloys in Atmospheres Relevant to Oxy-fuel Combustion, *Oxid Met*, **78** (2012) 221–237.

[29] D. Zhang, G. Liu, G. Zhao, and Y. Guan, Cyclic oxidation behavior of Fe-9Cr-1Mo steel in water vapor atmosphere, *J. Cent. South Univ. Technol*., **16** (2009) 535–540.

[30] K. Kaya, S. Hayashi, and S. Ukai, High-temperature Oxidation Behavior of 9Cr Ferritic-steel in Carbon Dioxide, *ISIJ Int*., **54** (2014) 1379–1385.

Table 13: Summary of achievement of this project based on milestones and tasks

MILESTONE TITLE/DESCRIPTION	VERIFICATION METHOD	COMMENTS (PROGRESS TOWARD ACHIEVING MILESTONE, EXPLANATION OF DEVIATION FROM PLAN, ETC.).
Task 1. Conduct project management and planning	N/A	Pitt and RTRC worked the technology maturation plan,
Task 2. Develop process-structure models for the WAAM technique		
Task 2.1. Establish process-structure models for alloys with uniform composition	Mechanical experiments by RTRC and mechanical modeling by Pitt	Pitt identified the suitable process-scale thermal -model for WAAM (Sec. 3.3.1) and parallelly, RTRC performed the heat source calibration by measuring the temperatures during deposition using thermocouples (Sec. 3.3.2). Finite element based detailed thermal model to predict the temperature distribution for single alloy deposition was developed and these temperature results were also compared with thermocouple measurements for validation of the model. Similarly, finite element based detailed mechanical model to predict the stress distribution (Sec. 3.3.4) and grain texture prediction using the Discrete Dendrite Dynamics (DDD) model (Sec. 3.3.5).
Task 2.2. Build alloy samples with uniform composition for model calibration and perform tests	N/A	WAAM feedstock materials of Inconel 740H and ER90S-B91 (T91) steel were procured, and several builds were deposited to determine the optimum parameters by RTRC. Microstructure characterization and post-heat treatment design for the single builds were performed by Pitt (Sec. 3.2.1-3.2.4). Residual stress measurements were performed using XRD to further help in the calibration of the mechanical models (Sec. 3.3.3).
Task 3. Improve ICME models for WAAM technique		
Task 3.1. Model-prediction of microstructure-property relationship for uniform alloy composition	Mechanical experiments by RTRC and microstructure analysis by Pitt. Microhardness were performed and analyzed by Pitt .	The mechanical properties due to variation of grain texture at different locations was predicted using the Crystal Plasticity Finite Element (CPFE) model (Sec. 3.3.6). The variation in grain structure as well as microhardness along the build direction of the single builds was beneficial for further calibrating the developed models for WAAM process.
Task 3.2. Sample manufactured by WAAM technique and its mechanical property results	Mechanical experiments by RTRC and microstructure analysis by Pitt. Microhardness were performed and analyzed by Pitt.	From the optimum printing parameters identified for single build P91 steel and 740H superalloy, larger builds from which full size tensile bars could be extracted were printed by RTRC. Room temperature tensile tests were performed before and after heat treatment for single build P91 steel and 740H superalloy by RTRC (Sec. 3.2.5). These results served as useful results for further calibrating the finite element based mechanical models for the single builds.

MILESTONE TITLE/DESCRIPTION	VERIFICATION METHOD	COMMENTS (PROGRESS TOWARD ACHIEVING MILESTONE, EXPLANATION OF DEVIATION FROM PLAN, ETC.).
Task 4. Extend the developed ICME modeling to the gradient interface modeling for alloy components with graded structure		
Task 4.1. Process-structure-property modeling of graded alloys with gradient composition profile	Microstructure characterization including the scanning electron microscopy, electron back scattered diffraction, etc. and microhardness by Pitt. Mechanical testing by RTRC	The optimum deposition sequence for the deposition of graded alloys with sharp gradient was determined (Sec. 3.3.1) and the reasons for choosing the particular sequence over the other was supported by thermomechanical modeling (Sec. 3.3.2). The post-heat treatment for the build with optimum deposition sequence was developed based on the inputs from the previous design for the single builds. Parallelly, the graded alloy compositions that can act as interlayer for joining P91 steel with 740H superalloy was identified using CALPHAD-based ICME modeling (Sec. 3.3.3).
Task 4.2. Perform experiments for alloys with a gradient composition interface	Microstructure characterization including the scanning electron microscopy, electron back scattered diffraction, etc. and microhardness by Pitt. Mechanical testing by RTRC	The builds with the computationally designed graded alloy interlayer compositions sandwiched between P91 steel and 740H superalloy were printed using WAAM successfully along with a step-wise linear gradient build. The post-heat treatment was designed for the graded alloy interlayer builds with inputs from the previous design for single and sharp gradient builds (Sec. 3.3.3). Tensile properties were determined to understand the effectiveness of the designed post-heat treatment. From the post-heat treatment design, the alloy with optimum microstructure (no visible microstructural irregularities) that can tested further for performance evaluation was identified.
Task 5. ICME modeling framework with topology optimization		
Task 5.1. Topology optimization for interface builds between P91 and 740H	Microstructure characterization including the scanning electron microscopy, electron back scattered diffraction and mechanical testing by Pitt.	Finite element based ductile damage model was identified to predict the mechanical behavior for multi-material deposition and design the interface (Sec. 3.3.4). Microhardness for the optimum sharp gradient build was used as one of the inputs. The designed interface was printed using WAAM by RTRC and the microhardness, microstructure characterization and mechanical testing were performed by Pitt. The experimental and simulations results were compared.

MILESTONE TITLE/DESCRIPTION	VERIFICATION METHOD	COMMENTS (PROGRESS TOWARD ACHIEVING MILESTONE, EXPLANATION OF DEVIATION FROM PLAN, ETC.).
Task 5.2. Mechanical and oxidation testing for alloy components with topology optimization	Microstructure characterization including the scanning electron microscopy, electron back scattered diffraction and mechanical testing by Pitt.	In comparison with the interface designed using the topology optimization, the graded alloy builds with interlayer were found to be more promising and hence, mechanical and oxidation tests were performed (Sec. 3.5.3). In order to compare the performance of the interlayer, the mechanical properties of the graded alloy with sharp interface was also performed.
Task 6. Perform uncertainty quantification for ICME model-prediction and design allowables		
Task 6.1. Sensitivity analysis for uncertainty quantification of ICME models	Microstructure characterization including the scanning electron microscopy, electron back scattered diffraction and mechanical testing by Pitt.	Data driven models were utilized to develop a new graded alloy with the inputs from high-throughput experiments from the linear gradient build (Sec. 3.5.1). In addition, a new composition with high entropy effect was also identified. The new alloy build with composition derived from the data driven model was successful and its microstructure along with mechanical properties were studied (Sec. 3.5.2). However, the new alloy developed based on high entropy effect showed a location-specific solidification cracking susceptibility which was correlated by applying well established models from literature (Sec. 3.5.2)
Task 6.2. Scale-up sample preparation for oxidation and mechanical testing supporting uncertainty quantification	Microstructure characterization including the scanning electron microscopy, electron back scattered diffraction, etc. and microhardness by Pitt. Mechanical testing by RTRC	RTRC performed multi-material builds which were being subjected to creep experiments at different conditions. The new builds were scaled up such that bigger samples can be extracted and the variation in properties along the build if any could be identified (Sec. 3.5.3). In addition, a large-sized multi-material tube with dimensions similar to that employed in a power plant was printed using WAAM to show the feasibility of using this technique for real-time application (Sec. 3.5.3).